DAMAGE DETECTION USING SELF-SENSING COMPOSITES

Shoaib Ahmad Malik

A dissertation submitted to the

The University of Birmingham

for the degree of

Doctor of Philosophy

School of Metallurgy and Materials

College of Engineering and Physical Sciences

University of Birmingham

January 2011

UNIVERSITY^{OF} BIRMINGHAM

University of Birmingham Research Archive

e-theses repository

Abstract

The primary aim of this research programme was to enable damage detection in glass fibre reinforced composites using the reinforcing fibres as the sensing element. In other words, E-glass fibres were used as light guides to detect the fracture of individual fibres, when loaded in tension. This was achieved by monitoring the transmitted light intensity through the reinforcing glass fibres.

Two types of glass fibres and matrices were evaluated. In the case of glass fibres, E-glass and custom-made small-diameter (12 µm) optical fibre (SDOF) were used. Three types of low refractive index resin systems with specified failure strains were also used.

The basic technology involved illuminating one end of the fibre bundle or composite with a white light or laser source and the opposite end was imaged using a high-speed CCD camera. However, in order for this self-sensing technology to be realised, it was necessary to develop and optimise the following aspects:

End-tabs: Custom designed end-tabs were used to prevent the glass fibres from being damaged during tensile loading.

Sample preparation: A resin-injection technique was developed to enable void-free composites to be fabricated.

Equipment Integration: Procedures were developed to enable the high-speed camera to be triggered, when the first acoustic emission (AE) emanating from a fibre fracture was detected with a pair of piezoelectric transducers. The load-data from the tensile test machine was inputed into the AE data acquisition system. This self-sensing technique was used to study the fracture behaviour of E-glass fibre bundles and composites.

Image analysis: It was necessary to develop appropriate image analysis routines to register and monitor the light transmission characteristics of each fibre in the bundle and composite.

Acoustic emission monitoring of fibre bundles revealed that there were two types of failures occurring in a bundle, a lower amplitude of the acoustic emission signal (AES)

related to the inter-fibre friction and a high amplitude of the AES to fibre fractures. This characteristic was also confirmed by a Weibull statistical analysis where it was demonstrated that a two parameter distribution was present corresponding to two different flaw distributions. In the case of self-sensing composites, it was found that the specific failure modes in the composites (matrix failure, fibre fracture, debonding) generate their characteristic amplitudes of the AES and frequencies. These failure modes were recorded and correlated to the tensile test data.

It was demonstrated that the attenuation of transmitted light can be related to the fracture of fibres in the bundle or a composite test specimen. It was found that the image analysis routines were capable of identifying and tracking the survival or fracture of each fibre in the bundle or composite. The results obtained from mechanical loading, acoustic emission and images analysis were cross-correlated. Here it was shown that the transmitted light intensity decreased as a function of tensile loading. Rapid attenuation in the transmitted light intensity was observed just prior to the onset of catastrophic failure. The images captured by the high-speed camera were correlated to the fracture of the individual filaments via acoustic emission.

Dedication

To my Abu

and my dearest Ammi Ji whose unconditional love and prayers remain my unremitting source of strength

&

To my beloved wife (Sidra) and son (Aayan), for your extreme patience and love during this time

Acknowledgements

I extend my gratefulness and thanks to those who have played a vital role not only in the research work but also throughout my life, my parents. My deepest gratitude is to my parents, for their unconditional love and prayers; "without you and your struggle I cannot excel in my career, it is indeed all your prayers and hard work that I have reached this stage". *Ammi ji*! Your prayers and blessings always protected, helped and guided me through difficult times. Thank you.

I would like to give my special gratefulness to my wife Sidra Noor Malik and our lovely son Aayan Ahmad Malik for always being there for me. Thank you for your extreme

patience, sharing my difficulties, supporting me with endless love and encouragement to realise this dream.

I am grateful to all my family members, my brothers and sisters for supporting me throughout the course of my work.

Table of Contents

List of Figures

List of Tables

List of Symbols

The symbols listed below represents the nomenclature used throughout the text.

E	Modulus of elasticity (N/m^2)
E_x	Modulus of elasticity in the x-direction (N/m^2)
E_y	Modulus of elasticity in the y-direction (N/m^2)
E_z	Modulus of elasticity in the z-direction (N/m^2)
ν	Poisson's ratio
G_f	Modulus of rigidity of the fibre
E_f	Modulus of elasticity of the fibre
ν_f	Poisson's ratio for the fibre
G_m	Modulus of rigidity of the matrix
E_m	Modulus of elasticity of the matrix
ν_m	Poisson's ratio of the matrix
V_f	Fibre volume fraction
V_m	Matrix volume fraction
A_f	Area of fibres in the lamina
r_f	Radius of one fibre
l_{ce}	Critical length
σ_1	Stress in the composite
σ_m	Stress in the fibre
σ_m	Stress in the matrix
σ_{mu}	Ultimate failure stress of the matrix
σ_{fu}	Ultimate failure stress of the fibre
ε_{fu}	Ultimate strain of the fibre
ε_{mu}	Ultimate strain of the matrix

σ_{mfu}	Matrix stress at the onset of fibre cracking
σ_{fmu}	Fibre stress at the onset of matrix cracking
dp	Penetration depth
n	Refractive index
NA	Numerical aperture
λ	Wavelength
RFLG	Reinforcing fibre light guides
AES	Acoustic emission signal
SDOF	Small-diameter optical fibres

1 Introduction

1.1 Background

Fibre-reinforced composites (FRC) are used extensively in numerous industries due to their characteristic properties such as low density, high-strength, high stiffness-to-weight ratio and design flexibility [1, 2]. This class of materials also has good fatigue and corrosion resistance [3]. On the other hand, FRC are vulnerable to different damage mechanisms, particularly by impacts, even at low energies [4]. Impact-based problems are also significant for civil engineering applications where FRC are being used in the construction of bridges and to strengthen concrete columns. Therefore, there is a growing interest in developing techniques for damage detection in FRC [5, 6].

Considerable progress has been made recently in the design and deployment of novel and elegant optical fibre-based sensor systems [7]. However, the outer diameters of conventional optical fibres are 125 μm in comparison to the 15 (±3) μm diameter of reinforcing E-glass fibres. This diameter mismatch can introduce significant distortions in the relative orientations of the reinforcing fibres; this can cause the degradation of specified properties in the composite material [8]. The relative orientation of the reinforcing fibre and optical fibre can also result in resin-rich regions, which can affect the mechanical properties of the host material.

A potential solution to the above mentioned concerns is to convert the reinforcing fibres into light guides (RFLG). Quartz and E-glass fibres are ideal candidates for this application. It has been demonstrated previously that conventional reinforcing fibres such as quartz and E-glass fibres can be used as light-guides to enable chemical process monitoring [8] during the processing of thermosetting resins and composites [9]. Since the

reinforcing fibres can be used as pseudo light-guides, it has been demonstrated that the light transmission characteristics through the reinforcing fibres can be used for detecting fibre fractures in a composite material [10]. Hence, there is significant commercial and technical merit if conventional reinforcing fibres can be used for damage detection.

Self-sensing composites and RFLGs can provide unambiguous information regarding their continuity or integrity. In other words, fibre fracture results in a significant attenuation of the transmitted light intensity. However, this may require access to the ends of the fibres. This is not a prerequisite since it has been demonstrated previously that through-thickness illumination can be used [10]. It was also established that the severity of impact damage can be inferred by assessing the magnitude of the light bleeding from the fractured fibres in a 16-ply glass fibre composite manufactured from E-glass/Fiberdux 913 [11].

A limitation of self-sensing composites and fibres is that the light-guiding properties will only be maintained if the refractive index of the resin is lower than that of E-glass (1.56 at 20 ºC and 589.6 nm). This is not a major concern because resin systems with the required refractive index range can be obtained from commercial sources.

In the present study, a damage detection technique based on the concept of self-sensing composites was developed. The fracture of un-impregnated fibre bundles and composites was monitored during tensile loading using a high-speed camera; conventional acoustic emission transducers were used to trigger the high-speed camera. The change in light intensity due to the applied mechanical loading was analysed using image analysis techniques.

1.2 Aims of the Study

The aim of this study was to convert conventional reinforcing E-glass fibres into light guides (RFLG) and to develop a technique to enable damage detection in a glass fibre composite using high-speed photography. The conventional reinforcing fibres were first converted into light guides by preparing the ends of the fibre bundles for efficient light coupling into and out of the fibre bundles. Then the suitability of using the RFLGs for damage detection within a composite was investigated. Composites were manufactured using commercially-available low-refractive index resins. The RFLGs were also used *in-situ* to detect the damage in the composite during mechanical testing. Image analysis was performed on the images taken by a high-speed camera. Damage detection using conventional acoustic emission monitoring was also employed. Finally, cross-correlation between different modes of testing and analysis, i.e. image analysis, acoustic emission and load/strain data was demonstrated.

This project was funded jointly by the Engineering and Physical Sciences Research Council (EPSRC) and the Ministry of Defence (MoD), UK, via the Joint Grant Scheme. The chemical and cross-linking aspects of the research project were undertaken by a post-doctoral fellow (Dr Liwei Wang). The author was responsible for all aspects related to: (i) the design and fabrication of the test specimens; (ii) mechanical testing of fibre bundles and composites; and (iii) the development of the image analysis routines.

1.3 Industrial Relevance

The self-sensing composites concept will have a direct and significant impact in the majority of the industries associated with the use of advanced fibre reinforced composites. For example, industries associated with producing glass fibres and those involved with

formulating chemicals for surface treatments and producers of the resin matrix will benefit from rapid and cost-effective information on the effectiveness of their products. These parties will have quantifiable information on the chemistry at the interface. Manufacturers will have a simple tool to assess new products and also to possibly reduce the time-to-market. This is likely to give them a competitive edge. End-users and researchers will be able to correlate directly, surface treatments and processing methodology to the resultant mechanical properties. The latter will be possible because the developed technique in this study will enable the failure sequence of the fibres to be studied in real-time. The self-sensing concept will eventually enable a deeper understanding of failure mechanisms in composites.

1.4 Structure of the Thesis

The structure of the thesis is as follows:

Chapter 1: Introduction

Chapter 2: Literature review

The main topic considered is damage detection techniques for fibre reinforced composite materials. Basic information on the types of common fibres, matrices and the composite materials and relevant aspects of their properties have been included.

Chapter 3: Experimental

All the practical work undertaken on the fabrication, testing and experimental setup for self-sensing composites is described in this chapter. It also includes the experimental methods developed for the fabrication of void-free composites.

Chapter 4: Results and discussions

This chapter consists of four main sections: (i) Quality of samples and assessment procedures; (ii) Tensile testing of neat resins; (iii) Tensile testing of fibre bundles and composites; and (iv) Acoustic emission monitoring, and the high-speed photography to detect fibre fracture.

Chapter 5: Conclusions

The conclusions drawn from the results are summarised in this chapter.

Chapter 6: Recommendations for further research

Recommendations for further work are discussed in this chapter.

2 Literature Review

2.1 Fibre Reinforced Composite

A fibre reinforced composite (FRC) consists of the reinforcing members that are bonded together and fixed in place by the matrix [12-14]. In this combination, the fibres and the resin (matrix) retain their chemical and physical identities but produce a combination of structural properties that cannot be obtained by the constituents alone. Fibre reinforced composite materials offer a combination of high modulus and strength that are not possible with conventional engineering materials with the same specific density.

Historically, the concept of fibre reinforcement has existed for centuries [15]. Straw-reinforced clay bricks were used in ancient Egypt. Iron rods were used as reinforcement for masonry applications in the nineteenth century, that lead to the development of steel-reinforced concrete. Phenolic resin that was reinforced with asbestos fibres was introduced at the beginning of the twentieth century [2]. In 1942, the first fibre glass boat was made; also, the use of reinforced plastics in aircraft and electrical components commenced at this time. Filament winding was invented in 1946 and than subsequently incorporated into missile and aerospace applications in the 1950s [16]. In the early 1960s a major advancement was made by the introduction of the first boron and the high-strength carbon fibres that eventually resulted in the applications of advanced composites to aircraft components by 1968. Metal matrix composites such as boron/aluminium were introduced in 1970 [12]. DuPont developed Kevlar (or aramid) fibres in 1973. Applications of composites expanded widely to the aircraft, automotive, sporting goods and biomedical industries in the late 1970s. The use of high modulus fibre was begun in 1980. Now, emphasis is being placed on the development of newer metal/matrix and ceramic/matrix composites, as well as carbon/carbon composites for high temperature applications. New

avenues are being explored for the use of composite materials [14], including underground pipes, ground vehicles, aircraft and aerospace structures, automotive components, sports equipment and biomedical products which are designed to have a better mechanical performance and/or environmental stability coupled with low-weight.

2.2   Constituents of Fibre Reinforced Composites

In its most basic form, a composite material is one which is composed of at least two elements working together to produce material properties that are different from the properties of those elements on their own [13-15]. The following section provides information on the constituents of FRC, and a review of the constituents that are of direct relevance to the current study, i.e. glass fibres and thermosetting resins.

2.2.1   Fibres

Fibres are one of the main constituents of fibre reinforced composites; their primary function is to bear the load applied to the composite material. Fibres may be long (continuous) or short depending upon the end-use application. In general, there diameters are in the range of 7-15 µm and are supplied in the form of bundles or tows. An effective component to be manufactured, proper selection of the type, volume fraction and orientation of fibres are very significant because they affect the following properties of composite materials [2, 17-19].

- Tensile and compressive moduli.

- Tensile and compressive strengths.

- Fatigue properties.

- Electrical and thermal conductivities.

The common types of reinforcement include glass, carbon, Kevlar® etc depending upon the material properties required and end-use applications. The focus of this thesis is on E-glass fibres therefore, the E-glass fibres will be discussed in detail. Recommended reading for different types of fibres include Hull [2], Harris [1] and Gay [14]. The properties of different types of fibres are summarised in Table 2.1.

Table 2.1 Properties of the selected reinforcing fibres [8, 13-16, 19, 20].

Fibre types	Fibre diameter (µm)	Density (kg/m³)	Elastic modulus (GPa)	Tensile strength (GPa)	Poisson's ratio	Elongation to failure (%)	Coefficient of thermal expansion at 20 °C (K⁻¹)
E-glass	10~12	2600	72.4	3.45	0.2	2.8	0.5×10^{-5}
S-glass	10	2800	86.9	4.30	0.22	5.0	0.29×10^{-5}
Quartz	9	2600	73	3.6	0.23	4.6	5.4×10^{-5}
Kevlar®-49	12	1450	131	3.62	0.35	2.8	-0.2×10^{-5}
Carbon-T300	7-8	1750	230	3.20	0.3	1.3	-0.02×10^{-5}

2.2.1.1 Glass fibres

Glass fibres are mostly used for the reinforcement of polymeric matrix composites. Due to their comparatively low-cost they have widespread use in different industries [19]. Other important characteristics include; a high tensile strength, high chemical resistance and excellent insulating properties. The disadvantages when compared to carbon fibres are a low tensile modulus, relatively high specific density and abrasion issues during handling.

Glass fibres are manufactured by blending quarry products (sand, kaolin, limestone, colemanite) at around 1600 ºC in a furnace to produce the liquid glass [13]. This liquid is passed through micro-fine bushings, of specified diameters (7-24 µm) and simultaneously

8

cooled below its melting point to become rigid without crystallising [13, 15]. Glass can be classified in different grades by composition as shown in Table 2.2. The major constituent of glass is silica (SiO_2). The properties of the glass can be varied and adjusted by the addition of modifying ingredients such as metallic oxides. The glass filaments are coated with a "size" to protect the glass from abrasion. Coupling agents are also applied to improve the bonding with the matrix. The internal structure of glass fibres is a three dimensional network of different constituent atoms without any regular order. These can be classified as amorphous and isotropic as they have the same properties in all directions.

Table 2.2 Typical composition for glass fibres (by weight percent) [15].

	SiO_2	Al_2O_3	CaO	MgO	Ba_2O_3	Na_2O
E-glass	52.4	14.5	17.2	4.6	10.6	0.8
S-glass	64.4	25	----	10.3	----	0.3
C-glass	64.4	4.1	13.4	3.3	4.7	9.6

The following section presents a brief commentary on the different grades of glass fibres.

E-glass: Good tensile and compressive strength and stiffness, good electrical properties and relatively low-cost but impact resistance is relatively poor [15]. E-glass is the most common form of reinforcing fibre used in polymer matrix composites.

R, S or T-glass: These fibres are high-strength fibres required by the aerospace and defence industries. R, S or T-glass are manufacturers' trade names for glass fibres having a higher tensile strength and modulus than E-glass. Higher ILSS (inter-laminar shear strength) and strength properties are achieved through a smaller filament diameter [15].

C-Glass: This is used in chemical applications, providing greater corrosion resistance than E-glass. C-glass is mainly used in the form of a surface tissue in the outer layer of laminates used in chemical water pipes and tanks.

E-glass fibre is available in the following forms [14]:

Strand: Strands are compactly associated bundles of filaments. These are rarely used commercially and are usually twisted together to form yarns.

Yarns: A closely associated bundle of twisted filaments or strands. Each filament diameter in a yarn is the same and is usually between 7-13 μm.

Rovings: Rovings are loosely associated bundles of untwisted filaments or strands. Each filament diameter in a roving is the same and is usually between 13-24 μm. The continuous strands are then wound to form a cylindrical wheel and are used for specific applications such as in filament winding.

Tex: Tex is a unit of measure for the "linear" mass density of fibres and is defined as the mass of fibres in grams per 1000 metre [15].

2.2.2 Matrix

The matrix is the second major constituent of fibre reinforced composite materials and the functions of a matrix in a composite material [2] are; to transfer load between the fibres, to protect the fibres from an adverse environment and mechanical abrasion during service and handling. Matrix materials are generally polymers, ceramics or metals.

Matrix materials for polymer composites can be broken down into two groups, namely: thermoplastics and thermosetting resins both of which have been widely used as matrices in high performance composite applications [14]. The important difference between the

two materials is where the forming and the shaping of a thermosetting plastic take place in a simultaneous irreversible chemical reaction; whereas thermoplastics have the advantage of being able to be softened and shaped when heated and this process can be repeated without chemical degradation, if required [1, 2].

Table 2.3 Properties of selected matrix materials [13].

Resins types	Density (kg/m^3)	Elastic modulus (GPa)	Shear modulus (MPa)	Poisson's ratio	Tensile strength (MPa)	Elongation (%)	Coefficient of thermal expansion at 20 ℃ (K^{-1})
Epoxy	1200	2.6-3	1.6	0.4	40-80	2-5	11x10^{-5}
Phenolic	1300	2.7-4.1	11	0.4	35-60	2.5	1x10^{-5}
Polyester	1200	1.8-3.5	14	0.4	40-90	2-4.5	8x10^{-5}
Vinyl ester	1150	3-3.5	----	----	55-75	3.5-5.5	5x10^{-5}
Polypropylene	900	1.5-2.0	----	0.4	30	20~400	9x10^{-5}

Thermosetting resins: The most commonly used thermosetting resins include; epoxy, polyester and vinyl ester. The general properties of a few selected resins are presented in Table 2.3. Thermosets are produced when a liquid resin is converted into solid by cross-linking which cures it into a tightly bound 3D network resulting in a solid [13]. The mechanical properties depend on the length of chains and the density of cross-links. Epoxies have good resistance to heat distortion and shrinkage during curing than other thermosets; they can also be semi-cured allowing a prepreg to be made [14, 15]. The epoxy resins have a wide variety of properties that can be adopted to suit a particular application or a composite manufacturing method; for example, prepregs and filament winding predominantly use thermosetting epoxy resins. The disadvantages of epoxy resins are their

relatively high-cost and comparatively long curing time. Thermosetting epoxy resins were selected to fabricate the composite specimens in this current research programme.

In conclusion, the mechanical properties of composites are dependent upon the proper selection of fibres and matrix. The choice of fibres and matrix depends upon several factors; for instance, cost, manufacturing methods, desired properties i.e. strength and stiffness and the end-use application. The matrix performs two basic functions: transfer of load between fibres and protecting them; in general, the mechanical properties of a composite are dominated by the reinforcement.

The objective of the current study was to develop a technique to enable damage detection and *in-situ* monitoring of light through E-glass fibres and composites. Therefore, conventional E-glass fibres and commercially available low-refractive index epoxy system EPO-TEK®-314 were used in this study to manufacture test specimens of self-sensing composites.

The use of reinforcing E-glass fibres as light guides is based upon total internal reflection. Therefore, before discussing damage modes and its detection in the fibre reinforced composites, it was considered necessary to discuss the basic mechanism of light transmission through an optical fibre and various factors that can affect the light transmission.

2.3   Light Propagation in Optical Fibres

Glass fibre reinforcements are designed to achieve certain material and mechanical properties instead of acting as light guides. A review was carried out to appreciate the major factors that influence the propagation of light in a glass fibre. The principle of an optical waveguide and attenuation mechanisms are reviewed in the following sections.

2.3.1 Total internal reflection

The light beam is propagated through an optical fibre due to total internal reflection. Figure 2.1 shows an optical fibre which consists of a cylindrical central core of refractive index n_1 surrounded by a material of lower refractive index n_2 ($n_2 < n_1$). The refractive index of the surrounding air is n_o. A ray of light at an angle of incidence θ_i strikes at point 'A', if the angle of incidence at the core-cladding interface is greater than the critical angle $\theta_{critical}$, then the light ray will undergo total internal reflection and will be reflected back into the core of the optical fibre [21-23]. The critical angle $\theta_{critical}$ is given by [21, 22, 24]:

$$\sin \theta_{critical} = \frac{n_2}{n_1} \qquad \text{2-1}$$

Since the core has cylindrical symmetry, this ray will also undergo total internal reflection at the lower interface at point 'B', and therefore, be guided through the core by repeated total internal reflections (point 'C' and so on).
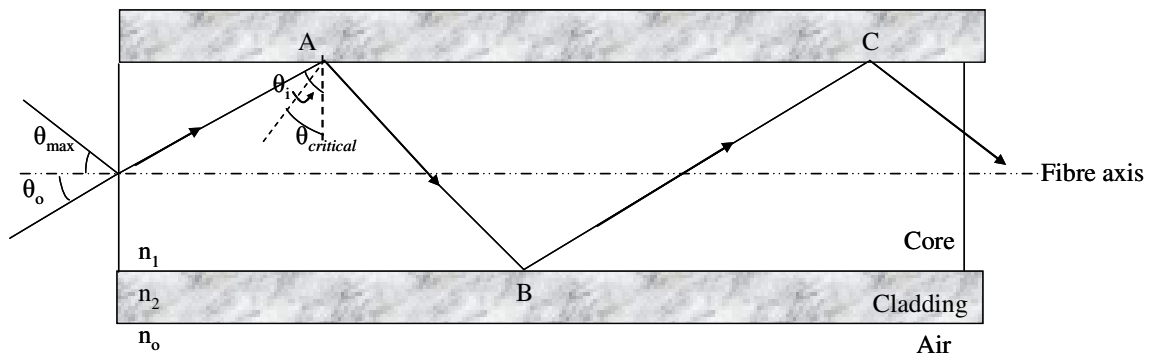
Figure 2.1 Schematic illustration of total internal reflection through an optical fibre [21, 22].

The numerical aperture (NA) defines an acceptance cone within which all rays are captured and it is an important factor for estimating the light that can be accepted into the fibre.

Generally, a higher NA indicates a higher source-to-fibre coupling ability. NA is defined as [21]:

$$NA = \sin\theta_{max} \qquad\qquad 2\text{-}2$$

Thus, if a cone of light is incident on one end of the fibre, it will be guided through the fibre, if the semi-angle of the cone is lower than θ_{max} [22]. Referring to Figure 2.1, θ_{max} is the maximum angle at which the ray entering the fibre undergoes total internal reflection [21, 22]:

$$\sin\theta_{max} = (n_1^2 - n_2^2)^{1/2} \qquad\qquad 2\text{-}3$$

The amount of light accepted, must be a function of the quantity of light incident on the fibre. Therefore, the light acceptance (LA) is given by [21]:

$$LA = f(\sin\theta_{max})^2 = f(n_1^2 - n_2^2) = f(NA) \qquad\qquad 2\text{-}4$$

2.3.1.1 Light loss mechanisms

Total internal reflection was discussed previously and it assumed that no optical power loss takes place at the fibre-coating interface. However, light is lost as it travels through the fibre. This loss, commonly called attenuation, is expressed as the ratio of the output-to-input power levels per unit length of fibre by [21]:

$$Attenuation = -\left(\frac{10}{L}\right)\log_{10}\left(\frac{power_{out}}{power_{in}}\right) \qquad\qquad 2\text{-}5$$

where, if L is expressed in metres, the loss is defined in units of decibels per metre (dB/m).

A number of mechanisms that relate to a wide range of material and manufacture parameters may contribute to the losses in an optical fibre. These mechanisms are categorised as either intrinsic or extrinsic losses [21-23, 25]. The former arises from the fundamental material properties of the glasses and imperfections in the fabrication process. On the other hand, extrinsic losses can be introduced as a result of bending the fibres. In addition, evanescent loss associated with total internal reflection cannot be neglected, in the current case, where the matrix serves as the cladding for the E-glass fibres [21].

2.3.2 Intrinsic loss

With reference to the light transmission characteristics, there are two sources of intrinsic loss in the glass fibre: the absorption mechanism, Rayleigh and Mie scattering mechanisms, which are discussed in the following sub-sections.

2.3.2.1 Absorption

An absorption loss in a glass arises from both the intrinsic structure of the material and impurity-based absorption. The various atomic structures only absorb electromagnetic radiation at particular wavelengths and as a result, the attenuation due to absorption is wavelength dependent [22, 26]. Pure silica has little intrinsic absorption in the near-infrared region due to its basic material structure. However, it does have two major intrinsic absorption mechanisms. There is a fundamental absorption in the ultraviolet wavelength region due to an electronic transition. Absorption from molecular vibrations within the glass is observed in the infrared and far-infrared region. E-glass fibre contains some metal oxides (see Table 2.2), which serve to change or modify the basic properties of glass. In some cases, they become part of the silica network or in other cases disrupt it. For example, the addition of sodium tends to break up the Si-O network and results in a change of its molecular vibration mode [21]. Also some oxides shift the absorption edge, for

example, B_2O_3 shifts the infrared absorption edge to a shorter wavelength. In addition, some oxides exhibit very strong absorption bands in the visible and near-infrared [21].

Water can also be considered as an impurity in the glass fibre structure; since the opportunity for the entrapment of water by chemical or mechanical means is relatively high when the fibres are formed [21, 23, 24]. Some of the oxides in glass, such as SiO_2, Fe_2O_3 and Al_2O_3, form links to hydroxyl groups during contact with water; later, these can leach out other species in glass such as Na and Ca to leave a weak porous surface. The absorptions from water exist at wavelengths of 1383 nm, 1250 nm and 950 nm [21].

2.3.2.2 Scattering

Scattering is another major constituent of intrinsic loss and results from density and composition variations. This is a phenomenon inherent in all glasses, because all the fibres contain defects that scatter light. In all types of glass, the scattering centres are primarily impurities such as oxides and transition metal ions, with sizes typically much smaller than the wavelength (e.g. $r/\lambda \ll 1$, 'r' is the average radius of the scatterer). If the size of the defect site is less than one-tenth of the wavelength of the light, the phenomenon is termed Rayleigh scattering, where light is scattered in all directions by minute variations in atomic structure. As shown in Figure 2.2, some of the scattered light will continue to be transmitted in the forward direction; some will be lost into the coating because the angle of incidence is smaller than the critical angle. Some will be scattered in the reverse direction by total internal reflection.
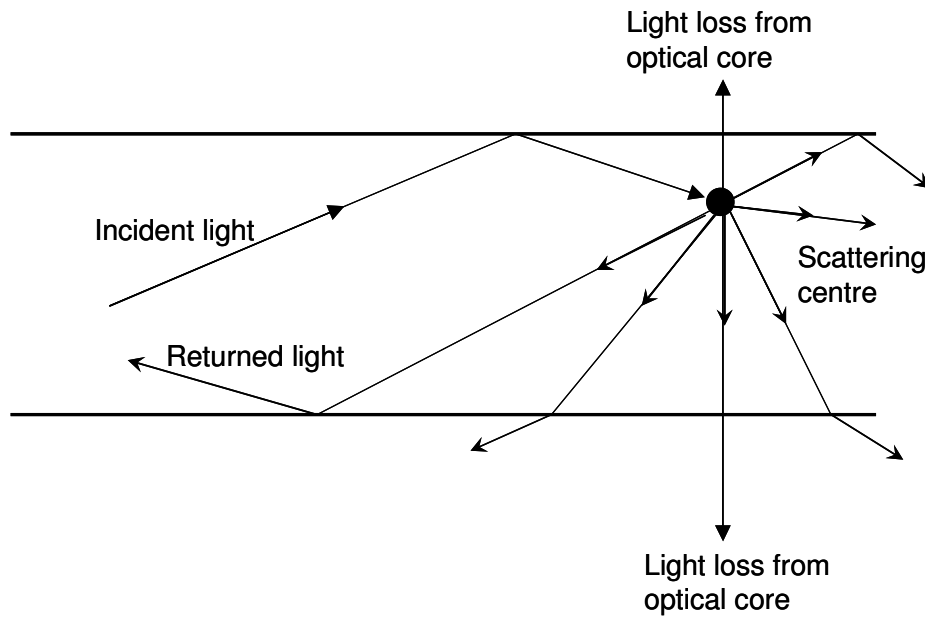
Figure 2.2 Schematic illustration of Rayleigh scattering in an optical fibre [21].

Mie-scattering occurs when the relative dimensions of the random compositional in-homogeneities are comparable to the wavelength of the propagating light. Examples of factors that can give rise to Mie-scattering include irregular dimensions and geometric symmetry within the optical fibre core and cladding, localised strain fields, voids and the refractive-index-variations along the length of the fibre.

2.3.2.3   Evanescent loss

Another contributor to optical loss associated with total internal reflection is due to the evanescent field. Figure 2.3 shows a diagrammatic representation of the evanescent field. Here light is shown to be incident at the interface between the fibre with a high refractive index (n_1) and coating with low refractive index (n_2). When the incidence angle is greater than the critical angle, total internal reflection occurs. The incident light and the reflected light interact resulting in a standing wave close to the interface. This standing wave decays exponentially away from the interface into the coating. The depth of penetration, d_p is the

distance from the surface over which the electric field of the standing wave disturbance decays to l/e of its value at the interface, is given by [23]:

$$d_p = \frac{\lambda}{2\pi n_1 \left(\sin^2 \theta - \sin^2 \theta_c \right)^{1/2}}$$ 2-6

where, θ is the incidence angle and λ is the wavelength of the light; the other terms were defined previously.

The existence of the evanescent field indicates that the light is transmitted into the coating, which underlines the importance of the choice of coating materials. It requires the following [21, 22]:

  i. The coating should not have any significant absorption band at the wavelength range of the incident light.

  ii. The coating thickness (at least 2 µm) must be present to allow the evanescent field to decay to a low value.
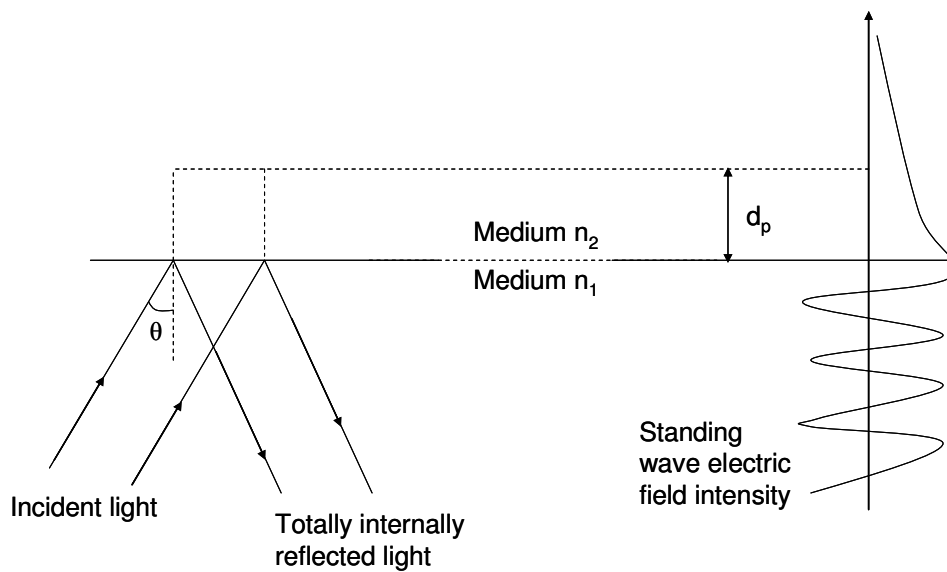
Figure 2.3 Schematic illustration of the evanescent field generated during total internal reflection [21].

2.3.3 Extrinsic loss mechanisms

Loss of the light from the glass fibre can also be induced by bending the fibre. This is a very important loss mechanism as its presence or absence is dependent on the fibre user. In fact, there are two types of bending loss that are associated with two different mechanisms, macro-bending loss and micro-bending loss.

2.3.3.1 Macro-bending loss

Macro-bending loss is the loss observed when the fibre is bent to a relatively large radius [21, 22]. A schematic illustration of severe bending of a fibre is presented in Figure 2.4 and it is clear that light can be lost when the angle of incidence is smaller than the critical angle. This type of macro-bending is common but is obviously more pronounced when fibres with a low numerical aperture are used, since the critical angles are larger [21, 22].
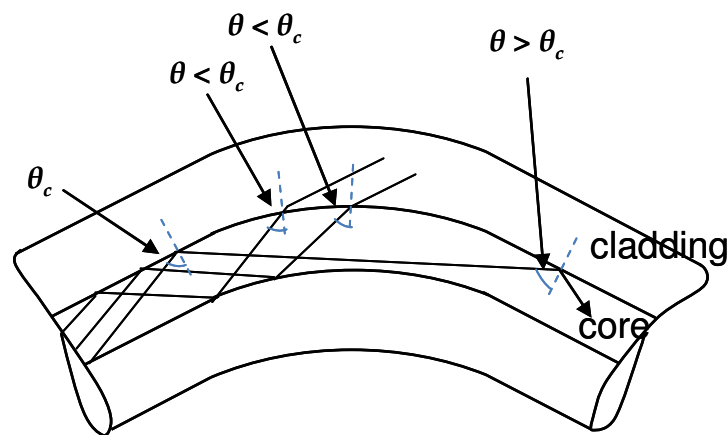
Figure 2.4 Schematic illustration of macro-bending loss [21].

2.3.3.2 Micro-bending loss

Micro-bending loss is the attenuation associated with small perturbations of the fibre. It is normally seen where the core-cladding interface is not a smooth surface, as shown in Figure 2.5. Such defects can create a rippling effect resulting from deformation and

damage to the core-cladding interface, which can alter the transmission of light and increase the light loss. Micro-bending also encompasses small amplitude random bends and compression of the fibre surface.
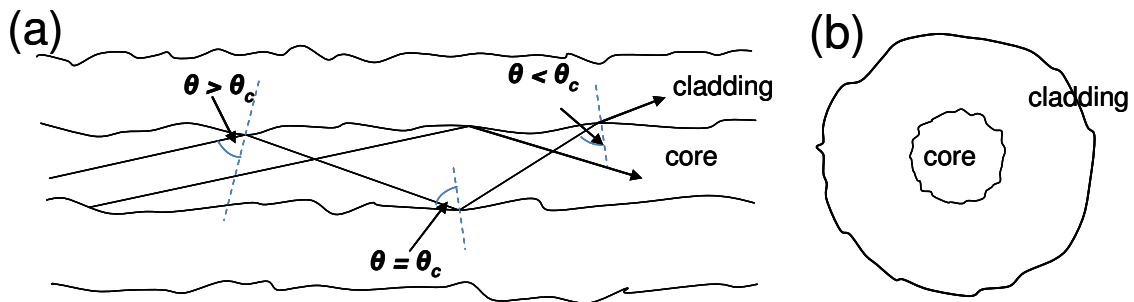
Figure 2.5 Schematic illustration of micro-bending loss: (a) Longitudinal view; and (b) Transverse view of the fibre [21].

For the glass fibres used in this study, the micro-bending loss was an issue as they were supplied with a twist. Therefore, during the fabrication of RFLGs, effective measures were adopted to keep the fibre straight to minimise the optical-losses caused by micro-bending.

In summary, total internal reflection occurs only if the incidence angle is greater than the critical angle. Three light loss mechanisms are likely to be present, intrinsic loss, extrinsic loss and evanescent loss. The intrinsic loss is related the properties of the fibre itself, which cannot be eliminated. The extrinsic loss (bending loss) can be minimised by a proper coating procedure. The evanescent loss can be reduced by using a suitable coating material with sufficient thickness.

2.4   Damage in Fibre Reinforced Composite Materials

In its most basic form a composite material is one that is composed of at least two elements working together to produce material properties that are different from the properties of those elements on their own [27]. The combined performance of the matrix and the fibres is governed by the interfacial bond between them. The fracture of reinforced composites can be caused by the failure of its constituents i.e. fibre or matrix or interfacial bond failure [28]. Therefore, the strength of a composite is dependent upon the strength characteristics of the three constituent elements, i.e. fibres, matrix, the bonding between them and the nature and concentration of voids and/or defects. In addition to the interfacial bonding between the fibre and matrix, the bonding between different layers of a composite is also significant [1, 2, 14]. As such, it can result in the failure of the material that is formed by different individual layers stacked on one another to achieve the desired thickness [29].

The mechanical behaviour and failure of a FRC is dependent upon a few additional factors, such as the fibre orientation, the method employed for the manufacturing of the composite, the applied loading, the fibre volume fraction, the architecture of the fibres in the composite and the stacking sequence of the different laminates in the composite material. For example, plain, tri-axial or satin weaves will significantly effect the damage mechanisms of the composites even if the manufacturing methods are similar [5, 15, 16, 18].

The focus of this thesis is on the damage detection of unidirectional E-glass composite material subjected to axial loading. Therefore, the general damage modes of a composite are discussed briefly in the following sections. The fracture behaviour of continuous-fibre composites subjected to axial loading is presented in Section 2.4.1. The general modes of

failure in a FRC can be divided into four categories: (i) fibre fracture; (ii) matrix cracking; (iii) delamination; and (iv) fibre debonding/pull-out [4, 6, 30-36]:

Fibre fracture: The fibres in a composite material are the main load-bearing member and after its failure either in tension or compression, the internal loads are locally redistributed to the neighbouring fibres in the immediate vicinity of the fracture; the final fracture of the composite depends upon the relative strain-to-failure of the fibres and the matrix.
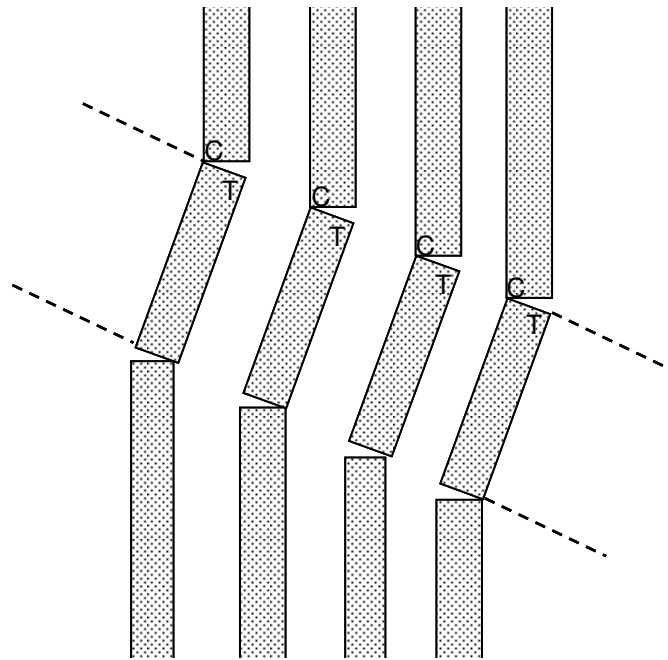
Figure 2.6 Schematic illustration of fibre kinking in the case of brittle fibres, 'C' and 'T' represent compression and tensile failures [2].

Failure in compression is dependent upon the mode of loading, for instance, under axial compression the fibres tend to buckle. The buckling of the fibres is constrained due to neighbouring fibres for composites with a high fibre volume fraction (> 50%) [1, 2, 13-15, 19]. Buckling results in compressive and tensile stresses across different parts of fibre section, leading either to fracture or local distortion. If the applied compressive load is increased further the buckling becomes extensive and the specimen will fracture [2]. Another common type of failure may occur from the onset of local buckling [2]. A kink-

band of misoriented fibres may form as shown in Figure 2.6. The major factors that can influence the onset of this type of instability are fibre volume fraction, fibre misalignment angle and yield strength of the matrix in shear [2, 13, 15].

There is another factor to be considered here, the strength distribution of the fibres. It has been well-established that non-metallic fibres generally have a distribution of strengths [1, 37-41]. The strength distribution is caused by flaws of varying severity within the reinforcing fibres. Flaws can be due to various effects, such as the inclusion of microscopic particles during the production stage, minuscule cracks in the fibre surface or cracks and crystallographic defects within the fibre itself [1]. Flaws can also be introduced or extended during handling and environmental conditions. These flaws are random in nature and are unlikely to be systematically introduced in the same size and position. Therefore, the fibres have a distribution of strengths due to the presence of the randomly oriented surface-flaws. The length of fibres also has an affect on the flaws, i.e. longer the length of the fibres more significant will be the presence of flaws and their affect on the strength distribution.

A commonly used relation for the strength distribution of fibres was proposed by Weibull in 1951 as shown by equation [37]:

$$f(x) = 1 - e^{-\frac{(x-x_u)^m}{x_o}} \qquad \text{2-7}$$

where, 'x' is the parameter of interest, 'x_u' is the lower limit of 'x', 'm' is termed as the Weibull shape parameter and 'x_o' is the Weibull scale parameter. This was developed as a generally applicable theory that could be used in many circumstances in which random effects are involved. To analyse the data, '$ln(ln(1/(1-f(x))))$' is plotted against $ln(x)$. If the

Weibull function applies, the data forms a straight line with a slope of 'm'. Some of the examples used by Weibull follow the basic form of Equation 2.7. These give a straight line when the Weibull distribution curve is plotted. Others take the form of a two parameter distribution, with two straight lines of different slopes. Weibull proposed that this may be due to real effects, such as the dependence of fibre strengths on more than one parameter or for instance a change in surface-flaws to bulk flaws etc.

To analyse the data for the reinforcing fibres, the equation proposed by Weibull takes the form:

$$PF(\varepsilon) = e^{-[L(\frac{\varepsilon}{\varepsilon_o})^m]}$$

$$2\text{-}8$$

where PF is the probability of fibre failure, 'ε_o' and 'm' represent the Weibull scale and shape parameters for strain. 'ε_o' is the failure strain associated with a probability of failure of 0.63 for a unit length of perfect fibre, while 'm' describes the flaw distribution and also determines the coefficient of variation and the magnitude of the size effect at normalized fibre length 'L'.

This relation has been used by several authors, [41-65] to determine the probability of failure for the fibres, using either single fibre tests, fibre bundle tests or the fibre fragmentation test. A few selected papers on this topic are discussed in Section 2.5.5.

Matrix damage: When a composite is loaded in a transverse direction both matrix cracking and fibre–matrix debonding can occur [66]. Small defects present in a ply, such as small regions of fibre–resin debonding, resin-rich regions and voids cause transverse cracks to form [67]. This is mainly due to the application of transverse tensile stresses and in-plane

shear stresses. These cracks extend through the thickness of the ply. Transverse cracks are formed at fibre–resin interfaces and in the resin without interacting with the fibres [6].

Delamination: Delamination is the debonding of different plies within a composite material [66, 68-72]. Delamination is usually caused by the presence of free edges, discontinuities such as matrix cracks, voids and the type of loading, (for example, flexural, impact and cyclic loading) [68, 73-76]. It can result in a significant reduction of the compressive strength. Delamination can be characterised as a function of its initiation point in the material; local delamination (near to the surface of the composite) and global delamination [66]. If the initiation point is near to the surface of the sample, the plies above and below the initiation point separate. Global delamination is a result of internal deformation where the plies move in the same direction when the composite is subjected to compressive loading.
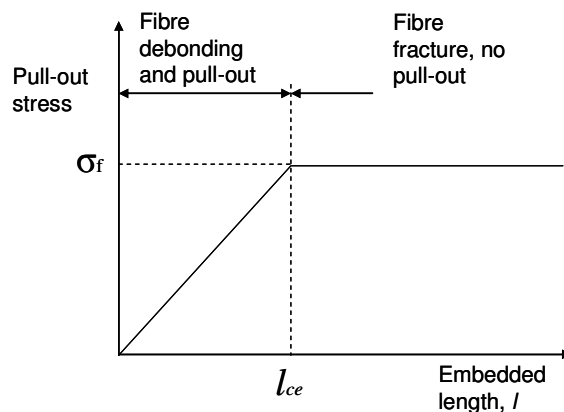
Figure 2.7 A plot of the typical variation in the pull-out stress with embedded length of the fibre [2].

Fibre debonding: Fibre debonding/pull-out is caused by the frictional sliding between the interface of the fibre and matrix [77]. At the tip of an advancing crack, fibres can fracture and fail, if the crack continues to advance along the length of the fibre, the fibre is pulled away from the surrounding matrix. When the tensile strength required for bond failure is

plotted against the embedded length, 'l_e', there is a sharp cut-off due to the fibre fracture before debonding as shown in Figure 2.7. With reference to Figure 2.7, if the applied stress is lower than the fracture strength σ_f of the fibre then fibre debonding and pull-out may occur. The critical length 'l_{ce}', depends on the strength of the bond and is given by:

$$l_{ce} = \sigma_f r / 2\pi \qquad\qquad 2\text{-}9$$

where 'σ_f' is the failure strength and 'r' is the radius of the fibre.

2.4.1   Damage modes in continuous-fibre unidirectional lamina

When a unidirectional lamina is subjected to a tensile stress parallel to the fibre direction, the tensile stress-strain plot is generally linear up to the point of failure. The failure of the lamina will be dependent upon the difference in strain-to-failure of the fibres and the matrix. If the strain-to-failure of fibres is higher than the matrix, the composite will fail catastrophically after a certain number of fibres are fractured. In contrast, if the strain-to-failure of the matrix is higher, than the fractured-fibres will have multiple failures at different locations, and the composite will fracture ultimately [2, 14-16]. This is shown schematically in Figure 2.8 and Figure 2.9. To explain the failure of unidirectional lamina loaded parallel to the fibre direction, it is assumed that both the constituents behave elastically; the interfacial bonding between fibres and matrix is strong (as a consequence, the fibre and matrix experiences the same axial stain); and the specimen fractures in a brittle manner. The stresses in the fibre and matrix are produced with respect to their Young's moduli.

If the matrix has a lower strain-to-failure ($\varepsilon_{mu} < \varepsilon_{fu}$), the stress in the composite is given by the rule-of-mixtures:

$$\sigma_1 = f\sigma_f + (1-f)\sigma_m \qquad\qquad 2\text{-}10$$

where:

σ_1 = Stress in composite lamina in the $0°$,

σ_f = Stress in the fibres,

σ_m = Stress in the matrix,

f = fibre volume fraction.

If the strain is increased above the strain-to-failure of the matrix ε_{mu}, the matrix starts to undergo micro-cracking, that can be seen by the appearance of a 'knee' as shown Figure 2.8c. With a further increase in the applied load, it is progressively transferred to the fibres until the strain in a fibre is less than the ultimate strain of fibres ε_{fu}. At this point the load is carried entirely by fibres with an increase in the stress in the composite. When the applied load reaches the strain-to-failure of the fibres, the final fracture of the composite occurs and the composite failure stress σ_{1u} is given by $f\sigma_{fu}$. In contrast, if the fibres fracture before the matrix cracking is significant enough to transfer all the load to them, then the strength of the composite is given by [2]:

$$\sigma_{1u} = f\sigma_{fmu} + (1-f)\sigma_{mu} \qquad\qquad 2\text{-}11$$

where σ_{fmu} is the stress in the fibre at the onset of matrix cracking ($\varepsilon_1 = \varepsilon_{mu}$).
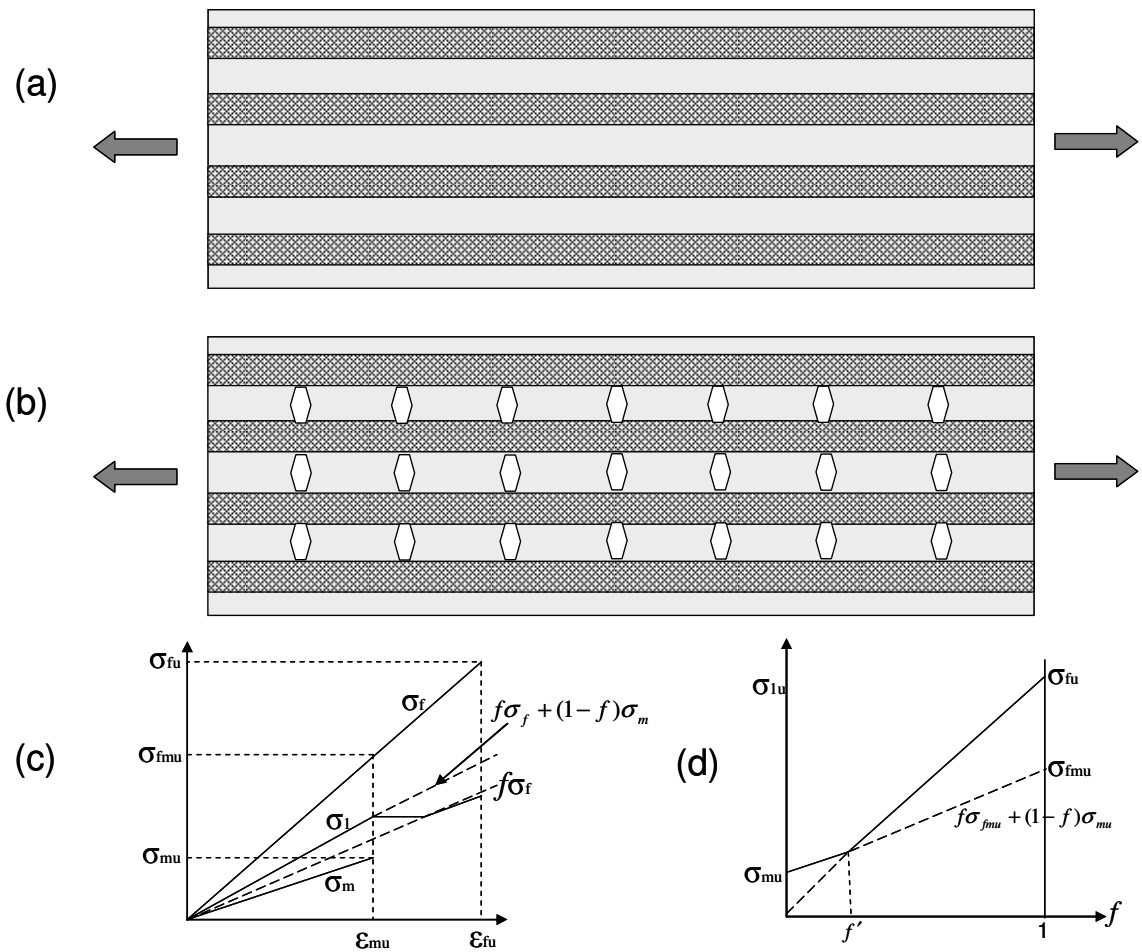
Figure 2.8 Schematic illustrations for the damage mechanism in a continuous-fibre reinforced composites with fibres having a greater strain-to-failure than the matrix: (a) The composite is subjected to tensile load; (b) Matrix show transverse cracking; (c) The respective stress-strain relationship; and (d) The dependence of composite failure stress on the fibre volume fraction [2].
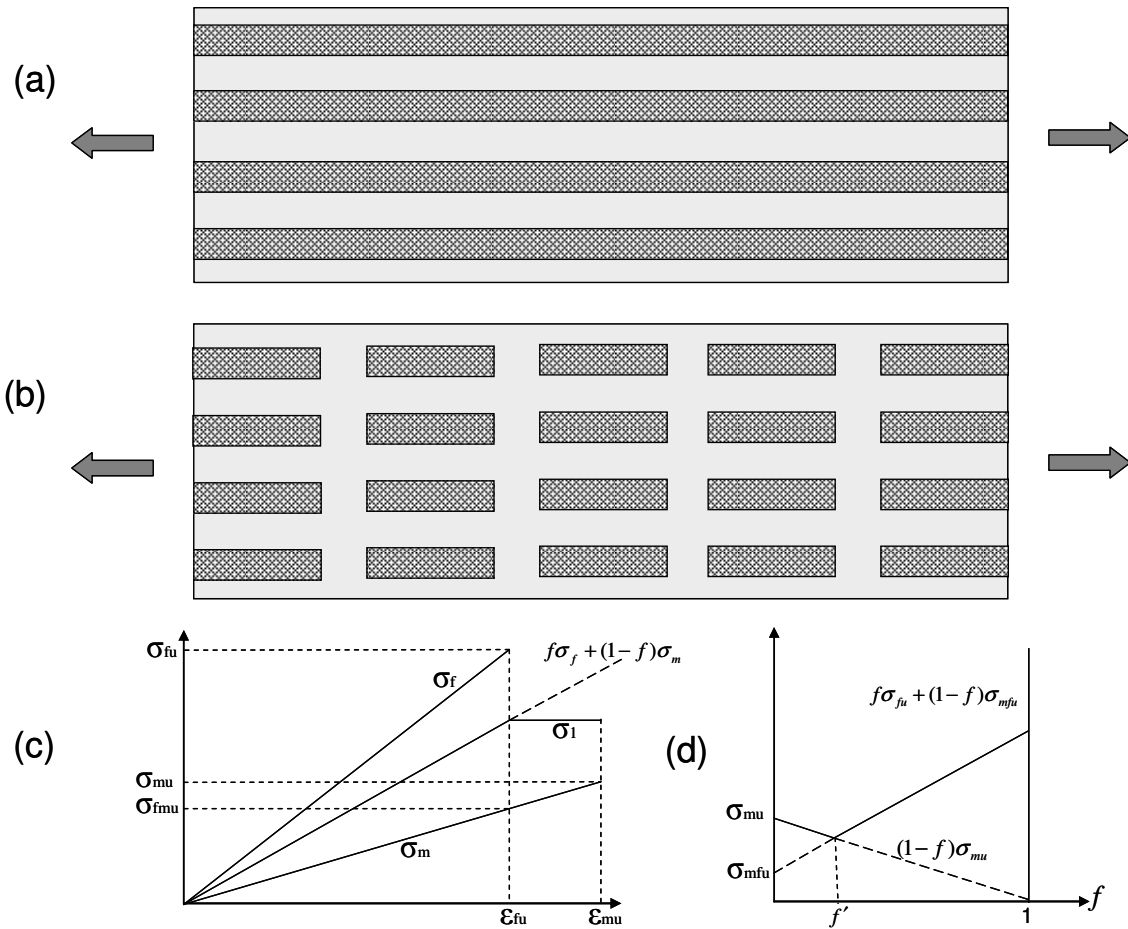
Figure 2.9 Schematic illustrations for the damage mechanism in continuous-fibre reinforced composites with the matrix having a greater strain-to-failure: (a) The composite is subjected to a stress; (b) Progressive failure of the fibres due to the applied stress; (c) The respective stress-strain relationship; and (d) The dependence of the composite failure stress on the fibre volume fraction [2].

A plot of failure-stress as a function of the fibre volume fraction is shown in Figure 2.8d. With reference to Figure 2.8d, the failure stress of the composite is dependent upon the fibre volume fraction, it is clear that at a limiting value of the fibre volume fraction " f' ", the fibres can sustain a fully-transferred load. This value can be obtained by making Equation 2.11 equal to $f\sigma_{fu}$, and f' is given by:

$$f' = \frac{\sigma_{mu}}{\sigma_{fu} - \sigma_{fmu} + \sigma_{mu}}$$

2-12

Now considering the case when the strain-to-failure of the matrix is greater than that of fibres ($\varepsilon_{mu} > \varepsilon_{fu}$), the fibres fail first at a composite strain of ε_{fu}. As the strain is increased further, it causes the progressive fracture of fibres into shorter lengths and the load is transferred to the matrix as shown in Figure 2.9. This process continues until all the fibres have smaller fragments, generally shorter or equal to their critical aspect ratio [2]. The critical aspect ratio is the shortest length of the fibre in the composite, below which the fibre cannot undergo any further fracture [2]. At this point, the fragmentation of the fibres stops and the load is then carried by the matrix. The composite failure stress is given by:

$$\sigma_{1u} = f\sigma_{fu} + (1-f)\sigma_{mfu} \qquad\qquad 2\text{-}13$$

where σ_{mfu} is the matrix stress at the onset of fibre cracking. From Equation 2.13, it is obvious that a lower fibre volume fraction reduces the composite failure stress below that of the neat-matrix. Therefore, the limiting value of the fibre volume fraction f'' is given by equating Equation 2.13 to $(1\text{-}f)\sigma_{mu}$:

$$f'' = \frac{\sigma_{mu} - \sigma_{mfu}}{\sigma_{fu} - \sigma_{fmu} + \sigma_{mu}} \qquad\qquad 2\text{-}14$$

The estimation of the fracture stress of the composite (σ_{lu}) using this approach is appropriate but it involves many assumptions. The effect of the fibre-matrix interface has been ignored and it is assumed that when the fibres are fragmented by the applied tensile stress, the fibres cannot bear any further load. However, the micro-cracking of the matrix does not result in the matrix becoming completely unloaded and similarly, the fibres still carry some stress even after they have broken into short lengths. With reference to Figure 2.9, a change in the slope of the stress-strain curve can be noticed after the "knee", but it does not reduce to zero. These effects arise because the load is transferred across the

interface even after the fibres or matrix fractures. It is also assumed that the fibres have a constant strength and the fibres fail in isolation from each other. As already mentioned that the fibres have a distribution of strengths that can be presented by a two parameter Weibull distribution [44, 49, 51, 65, 78, 79]. This variability of strengths is higher when the fibre displays a low Weibull modulus. This behaviour is discussed in more detail in Section 2.4.2.

In the preceding section, the rule-of-mixtures has been discussed in detail to understand the failure of composite materials [2]; however, other failure criteria for composite materials have been established to study/predict the failure of a composite structure [13-15, 80]. It is outside the scope of the current study to discuss these failure criteria in detail; however a summary is presented in Table 2.4 [80].

The four failure theories presented in Table 2.4 are the most widely used [15]. The applicability of a particular theory depends upon the material properties i.e. ductile or brittle behaviour and the type of loading that governs the failure modes [13, 15, 16, 80]. For example the maximum stress and strain theories are more applicable when brittle behaviour is predominant; the interactive theories i.e. Azzi-Tsai Hill and Tsai-Wu are more applicable when ductile behaviour is prevalent [13-15, 80].

Table 2.4 Summary of four failure criteria of composite materials.

Failure theory	Failure criteria	Description
Maximum stress theory	For tensile stresses: $\sigma_1 \geq F_{1t}$ $\sigma_2 \geq F_{2t}$ For compressive stresses: $\sigma_1 \leq F_{1t}$ $\sigma_2 \leq F_{2t}$	Failure occurs when at least one stress component along the principal material axes exceeds the corresponding strength in that direction.
Maximum strain theory	For tensile strain: $\varepsilon_1 \geq \varepsilon_{1c}$ $\varepsilon_2 \geq \varepsilon_{2c}$ For compressive strain: $\varepsilon_1 \leq \varepsilon_{1c}$ $\varepsilon_2 \leq \varepsilon_{2c}$	Failure occurs when at least one of the strain components along the principal material axis exceeds that of the ultimate strain in that direction.
Azzi-Tsai-Hill theory	$\dfrac{\sigma_1^2}{F_1^2} + \dfrac{\sigma_2^2}{F_2^2} - \dfrac{\sigma_1 \sigma_2}{F_1^2} + \dfrac{\tau_6^2}{F_6^2} = 1$	Failure occurs when the equation is satisfied.
Tsai-Wu failure theory	$F_1\sigma_1 + F_1\sigma_1 + F_1\sigma_1 + F_{11}\sigma_1^2 + F_{22}\sigma_2^2$ $+ F_{66}\tau_6^2 + 2F_{12}\sigma_1\sigma_2 + 2F_{16}\sigma_1\tau_6 + 2F_{26}\sigma_2\tau_6 = 1$	As above.

where;

σ_1=Stress in the fibre direction,

σ_2= Stress in the direction transverse to the fibre,

τ_6= Shear stress,

F_6= Shear strength,

F_1= Ultimate strength in the fibre direction,

F_2 = Ultimate strength in the matrix direction,

ε_1=Strain in the fibre direction,

ε_2= Strain in the matrix direction,

ε_{1t}= Ultimate strain in the fibre direction,

ε_{2t} = Ultimate strain in the matrix direction.

In the next section typical damage mechanisms in a unidirectional E-glass composite material subjected to axial loading are discussed. Generally, the strain-to-failure of the E-glass fibres is higher than the epoxy matrix; therefore, the E-glass composite demonstrates the case where the fracture of the composite is initiated by transverse matrix cracking. However, the distribution in the ultimate strength of fibres causes the weak fibres to fail and the damage in the composite material is initiated by progressive fibre failure.

2.4.2 Damage in unidirectional E-glass composites

The behaviour of a unidirectional composite in the fibre direction, especially the stiffness, is dominated by the fibre properties [2, 80, 81]. To have a clearer understanding of the failure mechanisms and processes within the constituents of the composite, it is essential to study the effect of the type of loading and the properties of constituents i.e. fibre, matrix and the interface. In the case of E-glass epoxy matrix composites, generally, the ultimate strain of the epoxy is lower than the E-glass fibres; therefore, the strength of the composite is dependant on the strength of the fibres [2, 13, 15, 16, 19, 80]. As already mentioned, the glass fibres have a distribution of strengths therefore, the fibres do not fail simultaneously; isolated single-fibre breaks (singlet) occur at the weakest points. A non-uniform stress state is developed around the fibre break as shown in Figure 2.10. This causes an increase in the stress for neighbouring fibres along with the development of an interfacial stress around the broken fibres and adjacent fibres as shown in Figure 2.10. When the load is increased further more single-fibre breaks occur and their effect is to increase the number

of failures of adjacent fibres (i.e. doublets, triplets etc.). These localised failures interact and cause the composite to fail catastrophically. This is illustrated schematically in Figure 2.11. The exact sequence of events and final failure pattern is dependent upon the constituents' properties and the fibre volume fraction.
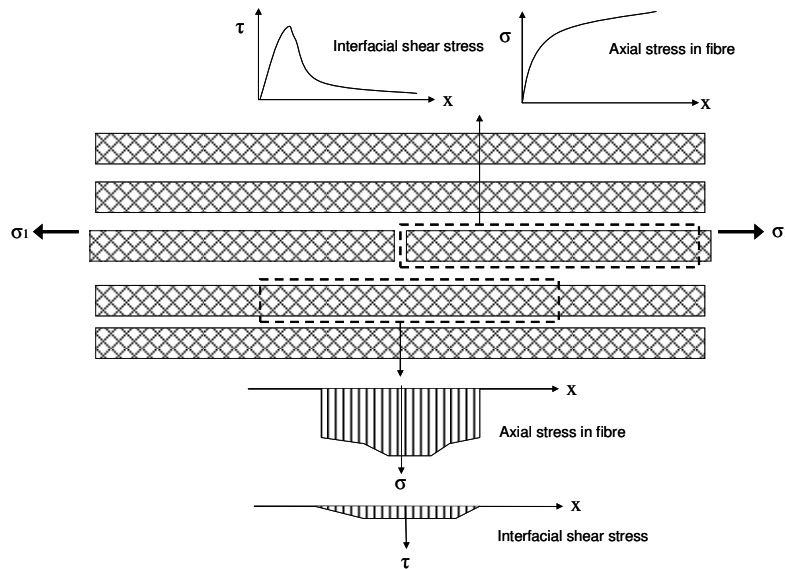
Figure 2.10 Localised stress distribution around a fractured fibre for a unidirectional composite under axial loading [16].
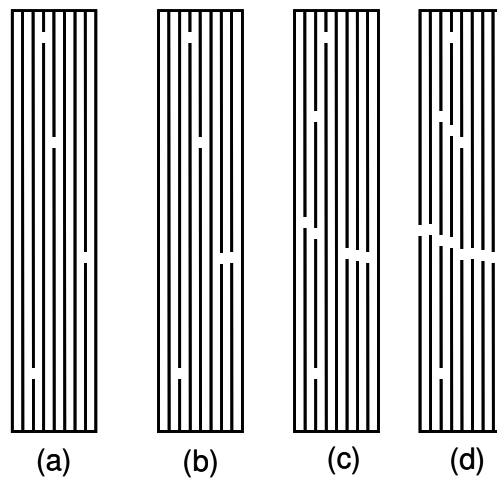
Figure 2.11 Schematic illustration of a failure sequence in a unidirectional composite with fibre-dominated strength subjected to longitudinal loading: (a) Failure is initiated with a single-fibre failure (singlet); (b) The localised stress causes more fibres to fail in the vicinity of broken fibres; (c) More fibres fracture as the loading is increased further; and (d) Finally the unidirectional composite fails catastrophically [16].
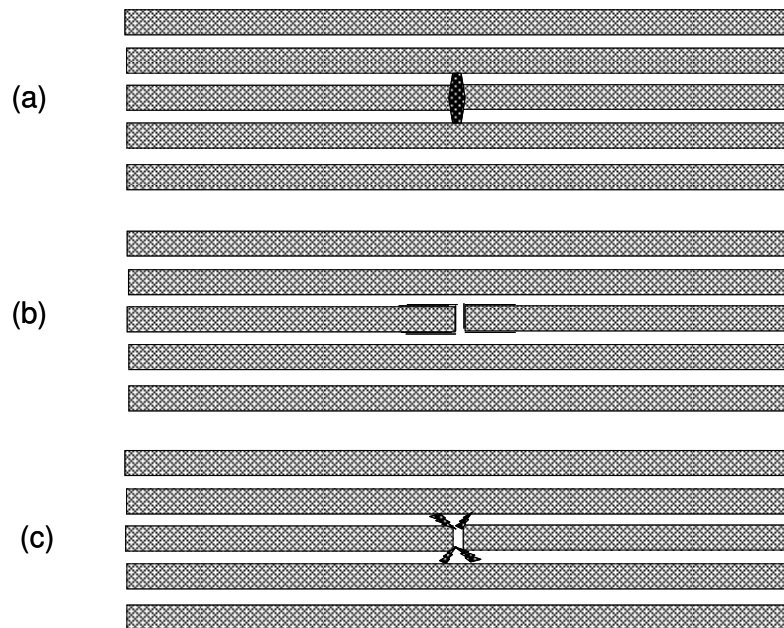
Figure 2.12 Failure mechanisms around a fracture single-fibre in a unidirectional composite under longitudinal tension: (a) Transverse matrix cracking for a brittle matrix and relatively strong interface; (b) Fibre-matrix debonding for a relatively weak interface and/or relatively high fibre ultimate strain; and (c) Conical shear fractures in a relatively ductile matrix [16].

Depending upon the properties of the constituent materials, these fibre breaks produce different types of failure in their vicinity [29, 50, 54, 82-92]. In general, these failure mechanisms take the following forms: (i) transverse matrix cracking in composites with a brittle matrix and a relatively strong interface as shown in Figure 2.12a, (ii) fibre matrix debonding in the case of a relatively weak interface and/or relatively high ultimate fibre strain as shown in Figure 2.12b, and (iii) conical shear fractures in the matrix in the case of a relatively ductile matrix and a strong interface, as shown in Figure 2.12c [16]. Figure 2.12b illustrates the possibility of fibre-matrix debonding if the fibres have a higher ultimate strain. This may be attributed to the fact, that due to the higher ultimate strain of the fibre, the matrix fractures before the fibre. When the applied strain reaches the strain-to-failure of the fracturing fibre, the matrix is incapable of distributing the load and

therefore, fibre-matrix debonding occurs. This is a typical case for E-glass composite materials due to high ultimate strain of fibres (2.2%).

In conclusion, when a load is applied parallel to the fibres, the first fibre failure is at the weakest point. If the stress redistribution associated with this failure is not sufficient to cause adjacent fibres to fail, the applied stress increases and further fractures occur randomly throughout the specimen. However, in general, the redistribution of the stress to the adjacent fibres causes a stress concentration in them and therefore, the progressive fracture of the fibres occurs. It should be mentioned here that generally the failure strength of composites is expected to show much less variability than its constituent individual fibres [1, 15, 16].

The focus of this thesis is on damage detection using E-glass composites and therefore, the following section focuses on a literature review that is limited to damage modes associated with E-glass composites.

Okabe *et al.* [93] investigated the tensile damage process and strength of E-glass fibre reinforced cross-ply laminates, experimentally and numerically. Samples were manufactured using E-glass fibres and epoxy resin (manufacturer code: TX-24235). The stacking sequences of specimens were 0_2, $[0/90_2/0]$, $[0/90_4/0]$ and $[0/90_6/0]$. The specimens were 120 mm long and 5 mm wide with 35 mm end-tabs and a gauge length of 50 mm. An electrical resistance strain gauge was surface-bonded on each specimen. The edges of the specimens were polished to study the transverse cracking of the 90º plies using a video recording system. A Monte-Carlo finite element method based on the experimental results was used to simulate the damage process in the composites. It was concluded that the strength could be estimated from the strength of the 0º ply, independent of the thickness of the 90º ply. The strain was recorded by the strain gauge bonded to the outer ply i.e. 0º ply;

therefore, there were no quantitative results for the stress distribution within the internal plies. The matrix cracks were only developed in the transverse plies due to loading which was obvious since there was no reinforcement in these plies in the loading direction. It was concluded that 90º plies did not contribute significantly to the stiffness of the composite. The results presented might have been more realistic and complete if the stress distribution could have been presented for the 0º plies and at the interface of the 0º and 90º plies. This could possibly be achieved by embedding optical fibre sensors, etc.

Wisnom *et al.* [94] discussed the effect of a transverse compressive strength on unidirectional E-glass composites under flexural loading. Four-point-bending tests were carried out on 32-ply E-glass fibre-epoxy specimens manufactured from Ciba E-glass/913 prepreg. Different lay-up sequences were investigated i.e. $[0]_{32}$, $[0_4(+45/-45)_6]_s$ and $[0/(+45/-45)_7/+45]_s$. Strain gauges (0º/90º) were attached on the opposite faces of the test specimens. The transverse stresses were varied with respect to the layup sequence. It was found that all the flexural specimens with 0º surface plies fractured in a similar manner irrespective of whether the subsequent plies were all 0º or 45º or a combination of both. The failure was mainly on the tension-side of the flexurally-loaded sample. Transverse stresses were calculated from the 90º strain gauges on the surface of the specimen using the stress-strain relations. The stresses within the internal plies i.e. 45º were not reported. Longitudinal tensile strains at failure showed only a small decrease in the presence of the large transverse compressive strains and stresses from the ±45º plies. Finally, it was concluded that transverse compressive stresses have a relatively smaller effect on the longitudinal tensile strength.

Liao *et al.* [95] discussed the environmental degradation of E-glass epoxy composite subjected to longitudinal tension. The specimens were prepared by casting the composite

between two PERSPEX® glass plates (15 x 15 cm). Two metallic spacers, each 2-mm thick were placed along the sides of the glass plates. Approximately 50-60 E-glass filaments were used to make smaller bundles of E-glass fibre. These smaller bundles were wrapped in parallel around the glass plate with double-sided tapes to secure the fibres. A room-temperature curable epoxy resin was introduced from one side of the glass plates. After the composite panel was cured, small specimens with nominal dimensions of 35 mm (length) x 5 mm (width) x 2 mm (thickness) were cut from the composite sheet. Each of these specimens contained 3 to 4 fibre bundles. A small notch approximately 1 mm deep was cut in the centre of each specimen to ensure that the model-composite failed in the centre. These notched specimens were aged in water at 25 ºC for 500 h and 4320 h. The masses of three samples were measured at regular intervals to monitor absorption of moisture. At least 50 measurements were made from samples aged for the same period of time. These samples were tensile-tested to failure after they were aged. A total of 160 individual failed fibres were examined using a scanning electron microscope (SEM). It was concluded that the tensile strength of the E-glass-epoxy composite was degraded when the specimens were aged in water at 25 ºC after 500 h. The results were compared with previous studies of the stress-free aging of E-glass fibres. It was reported that faster *in-situ* strength degradation of glass fibre was noticed in the model-composite. The authors suggested that the moisture-induced tensile stress and the corrosive action of water played an important role in the degradation of the strength of E-glass fibre composites during environmental aging. This paper addressed the issue of the aging of E-glass fibres and its effect on the tensile strength of E-glass composites. Although the samples were tested and then analysed, there was no information about the environmental degradation in real-time. If it was possible to record the information in real-time, the difference between both aging durations i.e. 500 h and 4320 h could have been reported.

Keller *et al.* [96] investigated the fatigue behaviour of pultruded E-glass composite strips. Three different specimen shapes were used as shown in Figure 2.13: (i) plate strips as-delivered; (ii) plates cut into a tapered form; and (iii) plate strips with end-tabs. The basic specimen dimensions were; 500 mm (length) x 100 mm (width) x 5 mm (thickness). Each specimen was instrumented with three electric resistance strain gauges. Two strain gauges were placed on the longitudinal axis (one on each side) and one perpendicular to the loading axis. Axial tension–tension fatigue experiments were performed on the test specimens. It was reported that there was a reduction of 3 – 5% in the ultimate tensile strength per decade of fatigue cycles. A decrease in stiffness up to 50% was observed that could be attributed to the fibre failures during the fatigue loading. In addition, a fatigue limit of approximately 25% of the ultimate tensile strength was observed at ten million cycles. The authors used strain gauges to measure the strain and then studied the fracture of the composites after failure. The decrease in stiffness could have been reported with more confidence if the number of the fractured fibres had been reported quantitatively with respect to the number of cycles during fatigue loading.
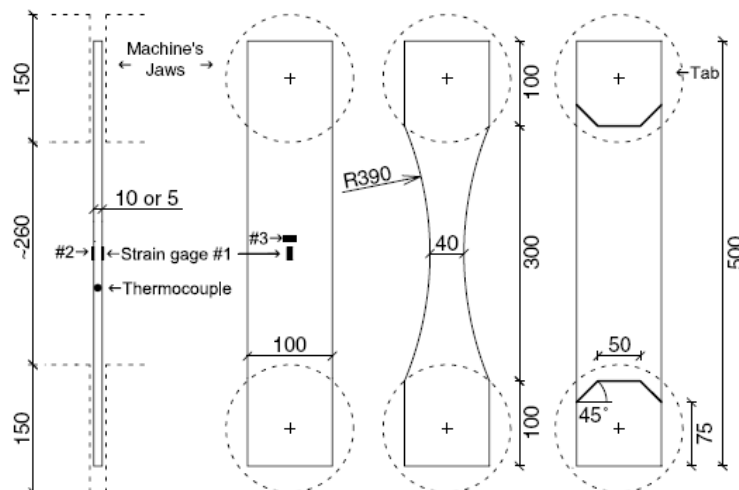
Figure 2.13 Test specimens used by Keller *et al.* with strain gauges and thermocouples: as-delivered; "tapered"; and end-tabbed [96].

Wisnom *et al.* [62] reported on the sample-size effect by means of tensile and four-point-bending tests on specimens manufactured from Ciba E-glass/913 prepreg. The tensile test samples were tapered by dropping-off plies symmetrically within the layup as shown in Figure 2.14. The centre section was eight plies thick, increasing to 15 plies at the ends. Strain gauges were installed on both sides of the tensile test specimens with gauge lengths of 100 mm, 200 mm, 1000 mm. Specimens were loaded to failure with different displacement rates of 0.048, 0.116 and 0.48 mm/s used for the 100, 300 and 1000 mm specimens, respectively. Four-point bending tests were carried out on the 16-ply unidirectional E-glass composite. The specimen dimensions were 60 mm (length) x 5 mm (width) x 2 mm (thickness). They were tested with an outer span of 45 mm, and an inner span of 15 mm as shown in Figure 2.15. Two further sets of the tests were repeated with all the dimensions of the specimen increased by factors of 2 (32-ply specimen) and 4 (64-ply specimen) compared with the initial set.
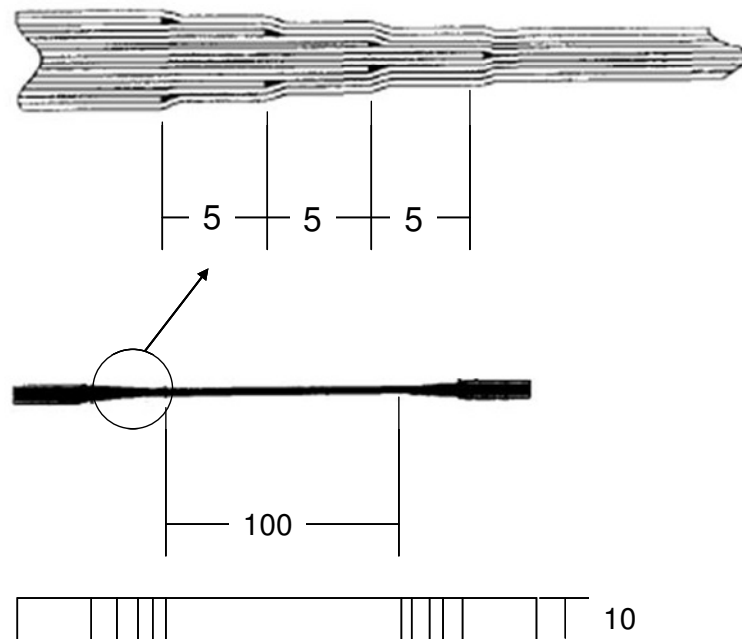
Figure 2.14 Schematic illustration of a tapered-specimen and ply drop-off (with dimensions in mm) used by Wisnom *et al.* [62].
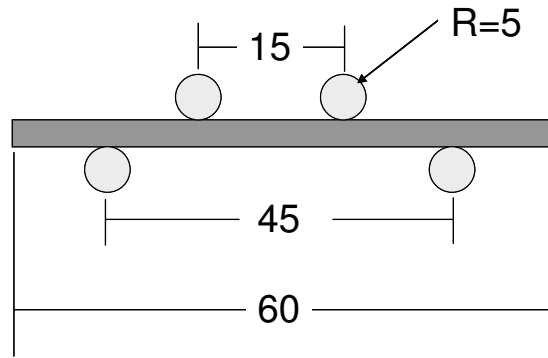
Figure 2.15 Schematic illustration of the four-point-bending test (with dimensions in mm) used by Wisnom *et al.* [62].

It was reported that the new tapered technique caused the specimens to fracture away from the end-tabs. A 7.2% reduction in the strain was reported when the gauge length was increased from 100 mm to 1000 mm. It was suggested that the reduction in the strain was due to the effect of strain energy stored in the specimens that increased with length. The greater release of energy for the longer specimens made it more likely that failure will propagate through the long samples. In the case of flexural tests, fracture occurred on the tensile face for all the samples, with fibres breaking in the centre section between the loading points and splitting-off from the surface to produce a brush-like appearance. For the 16-ply samples the reduction in strain was noticed before the strain-gauge broke, however for the medium (32-ply) and large (64-ply) specimens, the maximum strain was recorded before the maximum load was reached. This could be explained by failure occurring on a ply-by-ply basis, where the effect of one ply failing and splitting-off would have much less effect on the load on a 64-ply specimen than it would be on the specimen with only 16 plies. The maximum strains for failure under flexural loading were compared with the strains at maximum load under tensile loading. It was reported that the bending strains were 16% higher than the corresponding tensile strain-to-failures. This suggested that this reflected a real difference between the two types of failure i.e. failure under flexural and failure under tensile loading.

Iba *et al.* [97] investigated the relationship between the light transmission characteristics and the mechanical properties of unidirectional continuous glass fibre/epoxy composites. The test samples were fabricated using custom-made glass fibres with three diameters of 18, 37, and 50 µm. The glass fibres were fabricated from a bulk glass (Code 1724, Corning Glass Works, NY, USA) with a refractive index of 1.542 (measured at a wavelength of 589.3 nm at 20 ℃). The fibres were embedded into a clear-grade epoxy resin (Epikote 828; Yuka-shell Epoxy Corp., Tokyo) with a refractive index of 1.544 (measured at a wavelength of 589.3 nm at 20 ℃). The fabricated composite samples exhibited fibre volume fractions of 25-45%. The surfaces perpendicular to the fibre axis of the composite samples was polished and the light transmittance was measured in a wavelength range from 200 to 1100 nm (UV (ultraviolet)–VIS (visible)–NIR (near infrared)) using a transmission optical spectrometer. Figure 2.16 show the dimensions of the tensile test specimen, the location of the strain gauge and the polished-end.
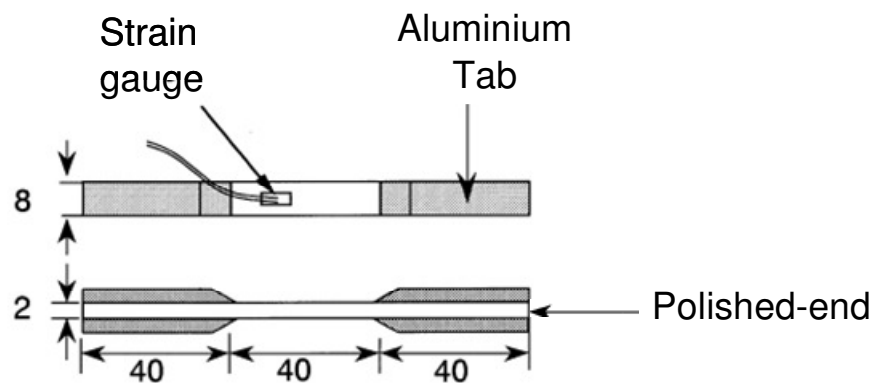
Figure 2.16 Schematic illustration of the test specimen and the polished-end with dimension in mm [97].

It was concluded that the composite demonstrated light transmittance above 50% in the wavelength range from 600 to 1100 nm. The light transmittance of the composite decreased with an increase in the fibre volume fraction and with a decrease in the fibre diameter, respectively. They inferred that the ultimate tensile strength of the composites

increased with an increase of the fibre volume fraction. However, it was difficult to relate the ultimate tensile strength of the composite to the change in fibre diameter due to variation in the data presented. This variation in the data might be attributed to the custom-made glass fibres that did not have any sizing on them. It was suggested that the transmitted light exhibited an opposite tendency to the mechanical properties of the composite, i.e. as the light transmittance through composite specimen decreased (due to an increase in the fibre volume fraction) the strength of the composite increased. It was also suggested that to achieve higher light transmittance in the composite a much closer matching of the refractive indices of the fibre and matrix was required. The light transmission was not monitored *in-situ*, and therefore, there was no information about the light attenuation during the tensile testing. It was reported that the closer matching of refractive indices may result in an increase in transmission of light; this issue can be addressed if the light was launched through the fibres only, instead of the composite test-specimens.

To summarise, the damage behaviour of E-glass/epoxy composites in tension is fibre dominated. The strength of the reinforcing fibres is the main contributor to the ultimate strength of the composite. The epoxy matrix due to its low ultimate strain fails first and therefore, the E-glass composite fails catastrophically when the applied stress reaches the ultimate strength of the fibre. Moreover, E-glass fibres have a distribution of strengths that cause a progressive failure of the fibres and stress concentrations in the fibres adjacent to fractured fibres. The net effect is a varying stress distribution in the vicinity of the fractured fibres that causes more fibres to fail.

The damage in an E-glass composite is a fibre-dominated failure; therefore, there is significant merit in developing damage detection techniques based on the fibre failure. In

the next section, damage detection techniques for composite materials are presented together with their application to different composite materials.

2.5   Damage Detection in Fibre Reinforced Composites

The characterisation of damage in composite materials can be achieved using destructive, non-destructive and *in-situ* techniques such as; Acoustic Emission (AE), Thermography, Ultrasonic C-Scanning and X-Ray radiography, an optical fibre sensing system etc. [4, 32].

In the following sections, a review of the literature relevant to the current study and the damage detection techniques such as optical fibre sensors and acoustic emission are presented.

2.5.1   Optical fibre sensors

An optical fibre is a glass or plastic fibre that transmits light along its length by total internal reflection. Optical fibres are used widely to fabricate sensors to measure parameters such as strain, temperature, and pressure [21]. They can be either surface-bonded or embedded in the composite material. There are many methods of classifying optical-fibre sensors [21-24]. They may be extrinsic, intrinsic, or evanescent sensors. They may be classified with respect to their applications, for instance, embedded, surface-mounted etc. The reinforcing fibre light guides used in this study were based upon the attenuation of light intensity as it propagates through the fibres. Therefore, the sensors based upon this effect may be classified as intensity based sensors.

2.5.2   Intensity-based sensors

A typical intensity-modulated optical fibre sensor system consists of a light source, a sensing device, within which the intensity of light is altered by the measurand in some

way, a detector to measure the intensity of the transmitted signal and optical fibres to carry light between these components [98-100].

2.5.3 Self-sensing fibres and composites

A self-sensing composite is a novel concept in which the reinforcing fibres are used as light guides. This idea can be effectively employed for chemical process monitoring and *in-situ* damage detection.

Damage detection techniques, C-scan, thermography, etc. are well developed [4-6, 30, 101-105] and are in service but they cannot be employed for on site damage detection in fibre reinforced composites. Structural health monitoring of mechanical and civil structures can be accomplished with the use of electrical resistance strain gauges, photo-elasticity, acoustic emission sensing or other traditional methods of non-destructive testing. The deployment of strain gauges can cause experimental errors in service (debonding from a test specimen, difference in stiffness, erroneous transfer of measured strain etc.). In addition electric strain gauges are planar in nature and therefore, provide two-dimensional in-plane strain information.

Optical fibre strain gauges are the next generation of strain measurement devices, since they offer a number of the advantages such as [32, 106, 107];

 i. They can be embedded in a composite specimen during fabrication.

 ii. They are generally smaller and have a diameter of 125 µm for a standard telecom fibre.

 iii. They are more flexible, light weight and resistant to corrosion [108].

iv. They are immune to electromagnetic interference and can be used in different environments [109].

v. They can be multiplexed to predict more than one parameter such as strain, temperature and pressure within a single sensor [110].

On the other hand there are certain limitations and disadvantages associated with optical fibre sensors. For example, the diameter mismatch between the reinforcing fibres (10 µm - 17 µm) and the optical fibres (125 µm - 250 µm), the possible misalignment of the optical fibres from the reinforcing fibre and the embedded optical fibre sensors result in resin-rich areas that can influence the rate of crack propagation [111-114]. Fibre-optic sensors can result in significant alterations of the stress/strain field of the host material and finally the long-term performance of the optical fibre sensor under various loading conditions [114].

Figure 2.17a shows a cross-sectional view of conventional a 125 µm diameter multi-mode optical fibre surrounded by E-glass and custom-made small-diameter optical fibres to illustrate the diameter mismatch between the conventional and reinforcing fibres. Figure 2.17b demonstrates clearly that even if the optical fibre is embedded along the same direction as the reinforcing fibres, significant distortions can be introduced in the plies well-below the location of the optical fibre. The consequence of this is the degradation of specific properties of the composite [8]. However, there is no consensus in the literature on the effects of embedded sensors on the mechanical properties of the host composite [7, 36, 106, 115]. The issues stated above can be addressed if the reinforcing fibres act as optical fibre sensors and therefore, become self-sensing for their respective host material.

(a)   (b)
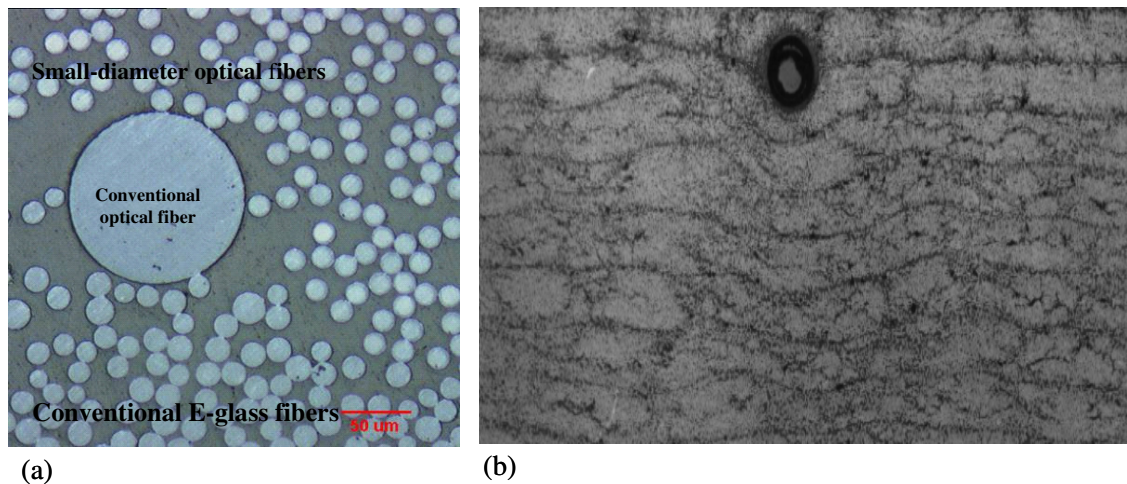
Figure 2.17 (a) Micrograph showing a conventional 125 µm diameter multi-mode optical fibre surrounded by E-glass and small-diameter optical fibres; and (b) Micrograph illustrating the distortions induced in the reinforcing fibres as a consequence of the embedded optical fibre in a unidirectional composite [8].

Martin *et al.* [116] employed custom-made 17/50 µm optical fibres that were integrated into the filament wound tubes at the time of manufacture. The light transmission through each length of the optical fibres was determined with a white-light source and a photo-detector array before and after impact. The filament-wound tubes were impacted by 2, 5, 8 and 10 J using a Rosand instrumented impact falling-weight machine fitted with a 50 mm hemispherical tup. A reduction in light intensity of 40%, 80% and 90% was reported related to the impact of 5, 8 and 10 J, respectively. The optical fibre-based crack detection sensor system was also evaluated for bleeding light after the impact. It was reported that no bleeding light was detected after subjecting the filament wound tube to a 2 J impact. However, the bleeding light was visible in the vicinity of the impact point after 5 J and 10 J impacts.

(a)   (b)
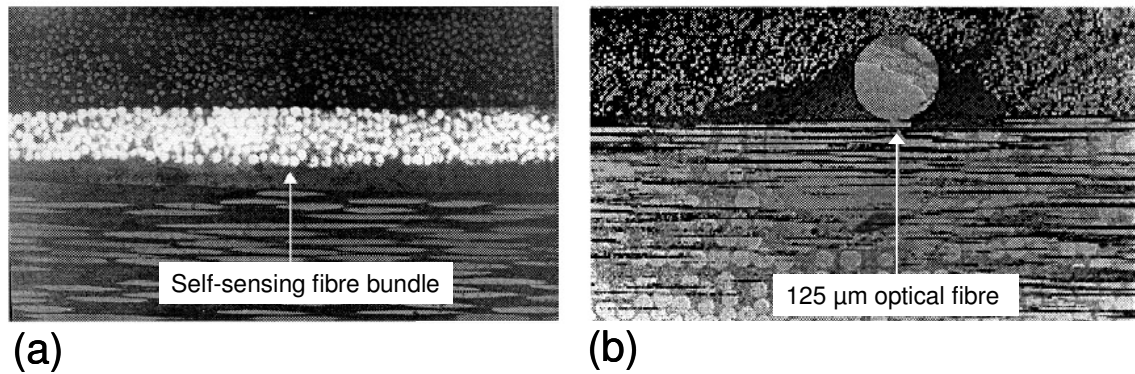
Figure 2.18 (a) Micrograph of a self-sensing composite; and (b) Micrograph of an
embedded 125 µm optical fibre [99].

In 1997, Hayes *et al.* used commercially-available quartz reinforcing fibres in the
development of a novel composite system in which some of the reinforcing fibres acted as
the light guide [8]. Quartz fibres were used as they had comparable mechanical properties
to E-glass fibres. The coating that was applied to the fibres during manufacture was de-
sized by pyrolysis at 700 ºC for 1 hour. The fibres were then re-coated with a silicone
resin. The basic requirement for a conventional light guide is that the refractive index of
the core (E-glass fibres in the current case) be higher than that of the cladding or coating
[10]. Composite panels were produced by a vacuum assisted hand lay-up technique of 300
mm square panels with a ply sequence of [0, 90, 90, 0, 0, 90, 0, 90]$_s$. There was one
reference composite plate, one sample consisting of self-sensing fibres (a micrograph of a
polished transverse section through a self-sensing composite is shown in Figure 2.18a),
and three samples with conventional optical fibres with diameters corresponding to 30 µm,
50 µm and 125 µm diameter. These fibres were introduced between plies 1 and 2 and plies
15 and 16 at a spacing of 10 mm. Figure 2.18b illustrates an embedded, conventional
50/125 optical fibre; the diameter mismatch between the optical fibre and the reinforcing
fibre is obvious. Different samples of each lay-up were impact tested at 2, 4, 6, 8 and 10 J
using a 20 mm hemispherical tup. The results indicated that the self-sensing fibres were

able to detect impact damages as low as 2 J and they were found to be more sensitive than the conventional optical fibres. The RFLGs were capable of detecting the damage and they can cover the larger areas of the structure since the reinforcing fibres were acting as light guides.

The problem with quartz fibres is that they are expensive. Instead of using quartz fibres, the use of E-glass fibres which are significantly cheaper and extensively used in the electrical, aerospace automotive and marine industries as reinforcing fibres has been investigated [11, 117].

In 2003, Kister *et al.* [10] reported that conventional E-glass fibres could be converted into reinforcing fibre light guides by applying an appropriate cladding material. Three classes of cladding materials were evaluated: epoxy, polyurethane and sol–gel. The E-glass fibres used in the study were un-sized and supplied by PPG Industries, UK. The end of the fibre bundle was secured in a heat-shrink tube and potted with a low refractive index resin EPO-TEK®-395 supplied by Promatech, UK. The fibre bundle end was then polished down to a 1 µm diamond-finish using conventional procedures. The effect of fibre end-preparation was also investigated by cleaving the heat-shrink tubing and the E-glass fibres using a fresh portion of a razor blade. It was reported that polishing the fibre bundle down to a 1 µm diamond finish improves the light transmission by more than 200%; and the cleaved fibre bundle ends had achieved more than 400% of light transmission compared to the as-made fibre bundle end. However, the recorded light intensity data was more scattered due to the surface debris caused by the cleaving operation. In addition to launching light through the fibre bundle end, the possibility of launching light through the sample surface was also investigated and similar results were obtained. The effects of using different cladding materials on the conventional E-glass fibres were studied by preparing samples of

20 cm length with different cladding materials including; epoxies (OG-135, OG-136 and OG-137) supplied by Promatech, (UK), polyurethane supplied by AZON (UK), and a sol-gel made from tetra ethoxy silane and polyvinyl alcohol. It was concluded that the E-glass fibres coated with commercially available resins exhibited good light transmission intensities as compared to the sol-gel based coatings. The as-received and coated E-glass fibres were tensile tested to failure with *in-situ* light transmission monitoring. It was reported that for the uncoated-bundle the transmitted light intensity decreases gradually up to 30% of the applied load, a further increase in the applied load causes a rapid attenuation of the light intensity. For the polyurethane coated E-glass fibres bundles, a 39% reduction is observed in the transmitted light intensity just prior to failure. For the epoxy based coatings, more than a 30% decrease in the transmitted light intensity was observed before failure. It was concluded that the conventional reinforcing E-glass fibres can be converted into light guides by the application of a suitable low-refractive index coating. It was also concluded that these light guides can be employed for *in-situ* damage detection.

Kister *et al.* [11] used reinforcing E-glass fibres as light guides to detect damage induced in a composite by impact, indentation and flexure. E-glass fibre-reinforced epoxy resin composite panels were made from unidirectional E-glass/epoxy prepregs, the prepregs were stacked into a 16 ply composite using the lay-up sequence $[0, 90, 90, 0, 0, 90, 0, 90]_s$ and then processed in an autoclave. Conventional E-glass fibres were de-sized and coated with an epoxy and a polyurethane resin so that they could act as reinforcing fibre light guides. The refractive index of the E-glass fibres was 1.56 and the refractive index of the epoxy and polyurethane resins were 1.49 and 1.36, respectively. The RFLGs were placed on the surface of the panels, or between the 4th and 5th plies or between the 12th and 13th plies. The RFLGs were illuminated using a 100 mW solid-state laser operating at 532 nm or a white-light source. A photodiode was used to record the output light intensity and a

CCD camera was used to image the ends of the light guides. The samples for the impact tests were 300 mm x 150 mm and were impacted at 2 J and 10 J using a 20 mm hemispherical tup. The light transmission was measured before and after the experiments using the green laser and photodiode. The indentation tests were performed on samples with dimensions of 300 mm x 100 mm. The samples were indented using the same 20 mm hemispherical tup at a rate of 0.5 mm/minute. The light transmission characteristics were recorded using the photodiode and the CCD camera was used for visualisation. The flexure tests were performed using a 3-point bending fixture. The dimensions of the sample were 60 x 20 x 20 mm and they were loaded at a speed of 0.5 mm/minute. The intensity of the light transmission output was recorded using the photodiode. In all cases, the damaged area of the composites was located by locating the light bleeding from the damaged RFLGs. The impact testing revealed that the two different claddings used were similar in the transmitted light intensity after impacts of 2 J and 10 J. The light transmission of the light guides was attenuated after impact. Despite a significant increase in delamination there was only a slight decrease in light transmission due to the hemispherical tup being much larger than the diameter of the fibres. The main conclusion drawn from impact testing was that the surface mounted RFLGs can provide an effective means for detecting damage in composites. In both cases of epoxy and polyurethane claddings the light transmission through the RFLG bundles in the top half of the composite was attenuated before the bundles in the bottom half as the load increased. A slight recovery of the attenuation was noted as the load was removed but overall this experiment demonstrated that permanent damage in terms of fibre fracture can be detected using RFLGs. Light transmission was attenuated continuously throughout the 3-point bend tests. The light transmission in the RFLGs on the top surface was attenuated almost immediately when loading commenced. All the other bundles of RFLGs began to attenuate at 50% of the

peak-load. There was no recovery of light transmission as the sample was tested to failure. The authors successfully demonstrated the ability of the RFLGs to detect the presence of damage by monitoring the transmission characteristics.

The self-sensing concept illustrated the idea of using conventional reinforcing fibres as light guides for damage detection in real-time. The successful use of reinforcing fibres for cure monitoring has been reported [118]. Generally, the fracture behaviour of E-glass fibre/epoxy composites is fibre dominated as already presented in Section 2.4.2. It has been well-established that fibre fracture can lead to stiffness degradation, ultimate strength reduction and catastrophic failure of a composite material [14, 15]. Therefore, development of a damage detection methodology that can detect *in-situ* failure of a fibre without any external sensor has substantial merit. For instance, the stiffness degradation can be directly related to the fracture of the reinforcing fibres that can be predicted by monitoring the light attenuation. In addition, the light bleeding from a composite can be used as an indication and location of the damage. E-glass fibres, therefore, can be used as reinforcing fibre light guides that can monitor, detect and locate damage in the composite.

In summary, self-sensing composites are emerging as a new class of intensity-based optical fibre sensors that can detect damage in fibre reinforced composite materials in real-time. In addition, the self-sensing fibres and composites are unique since they can provide unambiguous information throughout the life cycle of a composite materials i.e. from the processing/surface treatments of the constituents (fibres), the impregnation of the fibres with the resin system (matrix), the chemical process monitoring (fibres and matrix) and finally the *in-situ* damage detection (composite). A brief study was undertaken on the life-cycle analysis of composite materials by another researcher [119] in the Group in collaboration with the author. The research work demonstrated that it was possible to study

the effects of silane-treatment on the cross-linking kinetics. The feasibility of monitoring the impregnation process was also demonstrated.

In the next section, a brief overview of other types of optical fibre sensors is presented.

2.5.4 Other optical fibre sensors

There are many other types of optical fibre sensors, two main types of optical fibre sensors i.e. fibre Bragg gratings and extrinsic Fabry–Perot interferometric (EFPI) sensor are briefly discussed.

2.5.4.1 Fibre Bragg gratings

A fibre Bragg grating (FBG) constitutes a periodic variation of the refractive index along the core of the optical fibre. The light through the fibre grating is schematically represented in Figure 2.19.
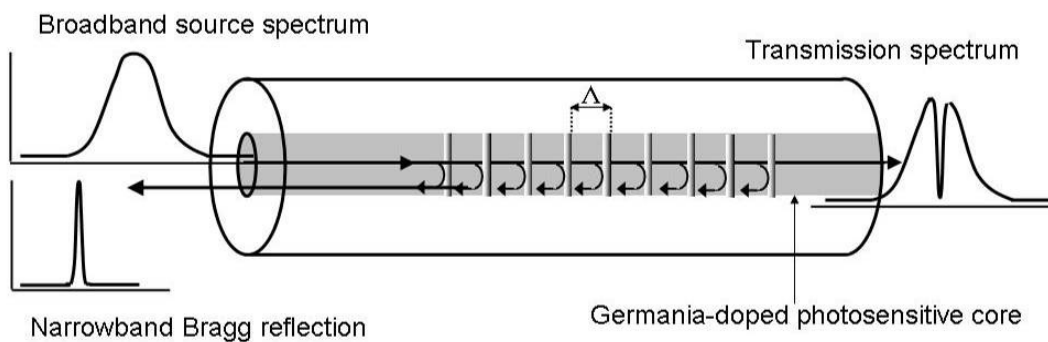
Figure 2.19 Schematic illustration of a FBG [120].

When broad-band light is coupled into the fibre grating, the light is subjected to scattering at the grating planes. The back-scattered light undergoes constructive superposition or obeys phase matching to produce a narrow-band reflection centred at λ_B. This resonance

wavelength is known as the Bragg reflection. The grating period, Λ and effective index, n_{eff}, of the core determine the Bragg reflection wavelength and can be expressed as [121]:

$$\lambda_B = 2n_{eff}\Lambda \qquad\qquad 2\text{-}15$$

When a fibre Bragg grating is subjected to parameters such as strain [122, 123], temperature [108, 123, 124] and pressure [125], the measurand-induced changes in the effective index and grating period produce a shift in the Bragg resonance wavelength. Therefore, the measurand-variations are Bragg wavelength encoded. These devices are used extensively in telecommunications [24], structural health monitoring of aerospace composites [126] and civil engineering [127, 128].

FBG can be embedded in the composite to measure strain, or they can be surface-mounted. The strain transfer from the host material to the FBGs has been researched and developed for more than a decade. Sirkis *et al*. [129] reported that the axial properties of the composite did not change, but that the transverse tensile and compressive strengths decreased by 16 and 56%, respectively. Wei *et al.* [130] developed a method to assess the strain transfer efficiency of fibre Bragg gratings in relation to the host structure. They studied the effects of various coatings on the response of the FBG. It was concluded that only 88% of the applied strain was transferred when the coating was polypropylene, compared to the epoxy and silane coatings that recorded a 99% and 91% strain-transfer, respectively. Duck *et al.* [131] investigated the mechanical load-transfer into an optical fibre due to the presence of a linear strain gradient between the sensor and the substrate. It was found that better strain transfer was obtained when the substrate was significantly stiffer with a lower strain gradient and where the FBG was located in close proximity to the substrate. A few other papers related to the effects of strain-transfer in FBG include the

work done by Botsis *et al.* [132], Barton *et al.* [133], Kai *et al.* [134], Malik *et al.* [135] and Li *et al.* [136].

Many researchers have employed FBG to measure strain, temperature and shrinkage stresses (during cross-linking) in composite materials. Interested readers may read through the references cited by Grattan and Sun [7].

2.5.4.2   Extrinsic Fabry–Perot interferometric (EFPI) sensors

An extrinsic Fabry–Perot interferometric (EFPI) sensor can be manufactured using two cleaved optical fibres housed within a precision-bore glass capillary either by fusion-welding or adhesive bonding [137]. The cleaved ends of these fibres are typically separated by a gap of few tens of micrometres. This gap between the fibres constitutes the Fabry-Perot (FP) cavity length (d). A broadband light source is coupled to one end of the fibre to illuminate the FP-cavity. An EFPI sensor measures strain through a change in the gap length 'd' as shown in Figure 2.20.
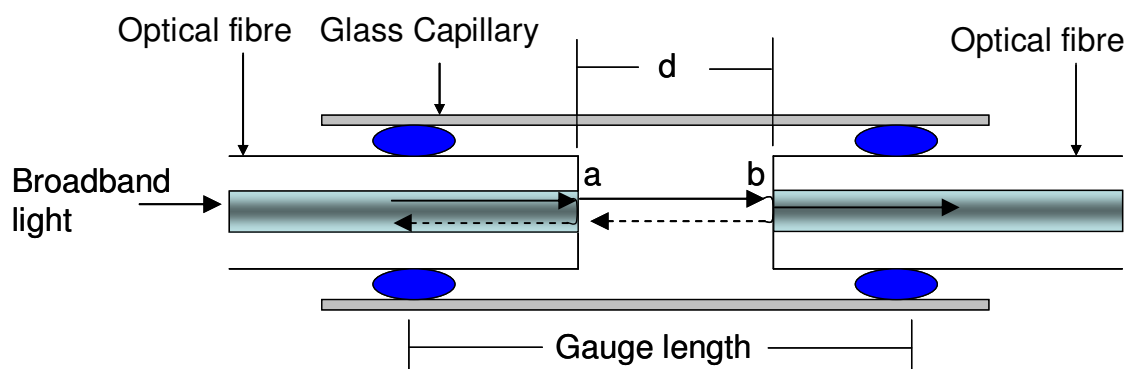
Figure 2.20 Schematic illustration of a Fabry–Perot interferometric sensor, a and b are the reflections at the cleaved fibre surfaces (the dotted-line indicates the reflected light), d is the distance between the cleaved fibres (cavity length) [137].

Figure 2.20 gives schematic illustrations of a Fabry-Perot sensor [137]. Two optical fibres in the sensor can be single mode, multimode or a combination of both. The sensitivity of

this type of sensor can be improved if metal or dielectric films are deposited on the cleaved reflector-ends [137]. The major advantages of EFPI sensors are that they are insensitive to transverse strain or temperature and have a strain-to-failure of up to 1.2% The major disadvantages are stress concentrations around these sensors [138].

In the next section, a review of acoustic emission monitoring is presented. As mentioned previously acoustic emission monitoring was used in the current study to: characterise the damage modes of FRC; trigger the high-speed camera; and to correlate the results of image analysis with the mechanical testing of self-sensing composites. Therefore, a review was carried out to discuss the acoustic emission technique and its applications for damage detection in fibre reinforced composite materials.

2.5.5   Acoustic emissions monitoring

Acoustic Emissions (AE) waves are generated due to a rapid release of energy caused by the deformation in a material or structure. Acoustic emissions have a frequency range in the region of 0.1-1 MHz and the velocity, distance and direction over which they can propagate is largely dependant upon the resultant mechanical deformation and the materials structure and composition [139-141]. Traditionally, AE sensors have been made from piezoelectric materials but recently optical fibre sensors have been used to detect AE [142, 143]. Piezoelectric transducers (PZT) are usually coupled to the specimen using silicone oil/grease. PZTs are connected to a computer-based data acquisition system through a pre-amplifier. The computer system has custom-developed software that can record and analyse the AE signals. AE has the potential to detect and locate damage and damage sites continuously. In composite materials, the generation of AE is due to one or more of the following: debonding, delamination, fibre cracking and/or matrix cracking [144-148].
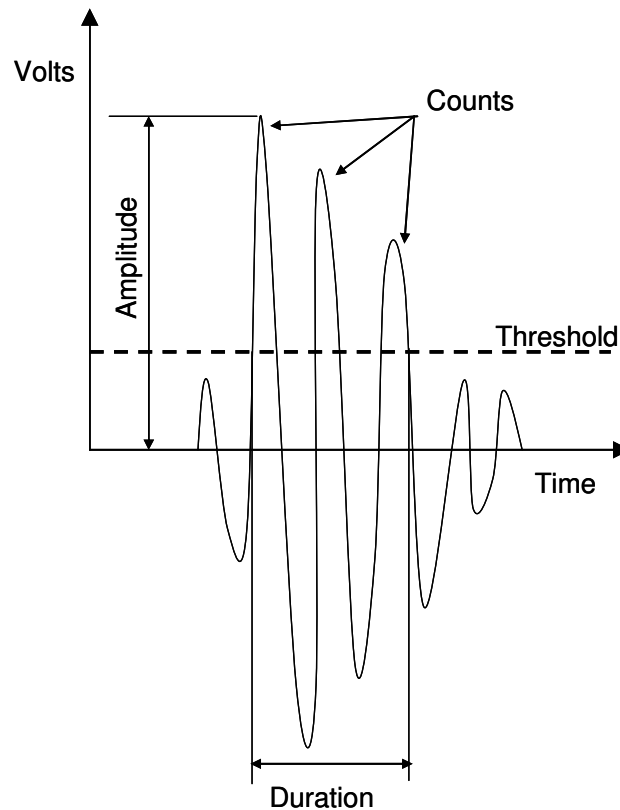
Figure 2.21 Schematic illustration of a generic an acoustic emission signature, some of the associated key-terms are also stated [149].

Table 2.5 Summary of acoustic emission terminologies [149].

Term	Definition
Amplitude	The largest peak voltage in the AE signal waveform; customarily expressed in decibels relative to 1 microvolt.
Counts	The number of times the AE signal crosses the detection threshold.
Frequency	For an oscillating signal or process, the number of signals occurring in unit time.
Average frequency	Calculated in kHz, determines an average frequency over the entire AE hit.
Duration	The time from the first threshold crossing to the end of the last threshold crossing of the AE signal from the AE threshold.
Rise time	The time from an AE signal's first threshold crossing to its peak.
Threshold	A pre-set amplitude that needs to be exceeded for data to be recorded.

One of the main advantages of AE techniques is linear location. Linear location requires two sensors to be placed in a line on the structure [143]. It is also necessary for the distance between the sensors to be recorded along with the velocity of wave propagation within the material or the structure. By using this information, it is possible to calculate a spatial source-location based on the arrival times of an AE signal at the sensors [150].

An AE event is recorded in a waveform as shown in Figure 2.21. It is the analysis of waveforms that provides information about the event that has occurred within a sample or structure. The waveform is plotted as voltage against time and it is possible to use all of the terms mentioned in Figure 2.21 and Table 2.5 to analyse and account for damage occurring in a material.

The sensitivity of an AE sensor system can be affected by the magnitude of background noise. Noise can be due to the machine that is being used to perform the test, or a poor contact between the specimen and the sensor. The amount of noise recorded can be excluded by setting a threshold value as shown in Figure 2.21. Any emissions under the threshold will not be recorded. Table 2.5 provides a list of key terminology involved in deciphering an AE waveform [149].

2.5.5.1 Acoustic emission monitoring of fibre reinforced composites

Acoustic emission has been used by several authors to study damage behaviour of fibre reinforced composite materials [139, 144, 144, 146, 151-158]. The specific damage mechanisms (fibre fracture, matrix failure, fibre/matrix debonding, delamination) produce characteristic AE signals. These can be used to identify the damage occurring in a test coupon. Additionally, AE has been employed for the mechanical testing of fibre bundles, to record fibre fractures and determine fibre strength distributions [45, 49, 61, 65, 78, 79, 159].

The strength of composites is predominantly dependent on the mechanical behaviour of the reinforcement. The determination of fibre strength requires a knowledge of the mechanical characteristics of the fibres. Fibres have a distribution of strengths that may be attributed to several factors such as; variation in fibre cross-sectional area during the process of filament manufacturing and damage during handling of the fibres and surface-flaws [1]. These factors affect the local load sharing and thus have a bearing on the strength of the composite. E-glass fibres exhibit brittle fracture behaviour and their strength can be characterised by statistical techniques such as a Weibull distribution [42, 49, 51, 53, 55, 58]. The Weibull distribution has remained the basic equation used to quantify statistical features of the tensile strength of fibres. It has been shown that the variability of the tensile property of fibres can be obtained by single-fibre testing or by the bundle tensile test (BTT) techniques [55]. Single-fibre tests are time consuming and prone to errors caused by sampling problems such as the failing of weak fibre during handling. These problems can affect the calculation of the Weibull parameters. In contrast, fibre bundles include a greater number of fibres (usually hundreds or thousands) which can be evaluated in a single test. Despite some potential problems (such as errors resulting from misalignment of the fibres within the bundle and variable tension in the filaments), such tests are faster and are used increasingly. The fibre bundle strength models are based on parallel sets of fibre, each of which has a Weibull distribution function. Acoustic emission (AE) is monitored during the BTTs in order to verify that individual filament failures are statistically independent. The large number of broken fibres and the measurement of the number of fibre breakages during the bundle test, give accurate information about the fracture strength distribution of fibres.

A number of authors have applied the BTT technique in conjunction with AE to determine the strength distribution of fibres [42, 49, 51, 53, 55, 57-61, 65]. The majority of previous

researchers provided evidence to determine the existence of a bimodal flaw population rather than the uni-modal population within a fibre bundle. Some selected papers relating to the current study are presented in the next few paragraphs.

Jihan *et al.* [78] determined the fibre strength distributions for E-glass fibre bundles that consisted of 4000 filaments. Statistical analysis of the results was carried out using Weibull strength distributions. Acoustic emission data were obtained to characterise the failure behaviour of the E-glass fibres. From AE linear location analysis, it was found that most of the AE events occurred near the mid-section of the specimen. The maximum peak-load for the bundle was 1000 (±50) N. It was reported that the Weibull distribution could not be approximated with a single straight line. This means that the fibre fracture process depends upon more than one parameter. The study provided evidence of the existence of a bi-modal flaw population rather than the uni-modal population that had been previously reported [159, 160].

R'Mili *et al.* [65] investigated the statistical failures of lubricated and un-lubricated E-glass fibres by conducting fibre bundle tensile tests along with AE monitoring. The lubricants used were petrol, Vaseline and "light-oil". These were used to reduce the friction between fibres in the bundle. In addition, the lubricant also acted as a coupling media for the AE. Gauge lengths of 30 mm, 60 mm and 100 mm were tested. The effect of relative humidity (RH) on the fracture behaviour of the fibre bundles was studied for samples equilibrated in a 30% RH environment and after immersion in water at room temperature. The Weibull distribution was used to describe the tensile strength distribution of fibres in the bundles. Two inputs were used in the Weibull distribution, the applied-strain and AE data (cumulative number of AE events). They reported that due to the lubricant, the friction between fibres was significantly reduced. Hence individual fibre failures were expected to

occur in the fibre bundle during the tensile test. The single-fibre failures were detected individually by the AE transducers. The cumulative counts of AE events and amplitude described the progress of individual fibre failures during the bundle tensile test. It was reported that lubricating the samples significantly reduced premature fibre failure. The results showed that the strength estimated for the E-glass fibre bundle at 50% of survival probability was 1.44 GPa for the samples conditioned at 30% RH (dry bundle), and 0.92 GPa for fibres bundles that were immersed in water. They suggested that this effect was due to stress corrosion in a humid environment which accelerated the growth of flaws in the fibres. They concluded that for gauge lengths higher than 30 mm, the fracture behaviour of E-glass fibres appears to be controlled by surface-flaws only.
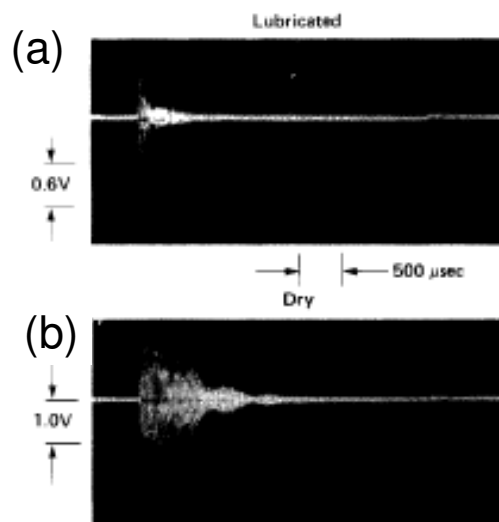
Figure 2.22 Acoustic emission waveforms of the fibre bundles: (a) Lubricated fibre bundle; and (b) Dry fibre bundle [161].

Hamstad and Moore [161] monitored the acoustic emissions emanating from single-filaments and fibre bundles in the dry and lubricated states. They used Kevlar-49® fibres under tensile loading. They found that it was comparatively difficult to distinguish between AE parameters (frequency and amplitude) as a consequence of multiple filament failures and those corresponding to single-filament fractures. They reported that the AE

parameters corresponding to multiple filament failure were governed by the relative amplitudes of the individual fractures, the time-interval and the location of the individual fibre breaks. Furthermore, they discovered that there was an AE energy overlap between the single and multiple filament fracture events. The AE waveform of the lubricated fibre bundles differed from that of dry fibre bundles as shown in Figure 2.22. With reference to Figure 2.22, the AE from the dry bundle showed a greater amplitude (1 V) when compared to the lubricated bundle (0.6 V). This difference was said to be due to the lubricant acting as a damping medium and greater friction between the dry fibres. Finally, it was concluded that during a fibre bundle test, the recorded AE events were independent of each other.

Hill and Okoroafor [49] also monitored the AE generated when tensile testing Kevlar®-49, carbon and E-glass fibres bundles. The gauge length of the fibre bundles was 70 mm and the testing was carried out at a constant cross-head displacement of 0.03 mm/minute. The as-received fibre bundles were tested dry and lubricated with silicone oil. They compared the fibre bundle strengths, the corresponding bundle strain and the elastic modulus for lubricated and dry bundles. A 10 - 20% drop in strength was reported between lubricated and dry bundles. They found that the measured Young's modulus remained constant for the lubricated and un-lubricated bundles. The load-strain tangent (LST) method was used to determine the Weibull parameters. The Weibull parameters were compared to those reported in the literature using the graphical and AE methods [51, 53, 56, 58, 59, 65]. There was a difference of approximately 3% between the Weibull parameters calculated from the LST method and those obtained by the graphical technique. It was reported that the survival probability was reduced for the dry fibre bundle tests and that the strain-to-failure of the dry bundle was 15% lower than that of the lubricated fibre bundle.

In summary, the fibre bundle test (BTT) has been used by a number of researchers [43, 49, 51, 54, 55, 59, 65, 78, 159, 162] to predict the fibre strength. Statistical methods such as the Weibull distribution are employed to predict the strength distribution of the fibres in the bundle. Acoustic emission has been applied to predict the number of filaments failing at a particular load and to predict the strength of the remaining fibres. However, there are still some reservations about detecting filament failures accurately using the acoustic emission technique and about the failure of the filaments being independent of other factors such as inter-fibre friction, the localised fractures of the fibres in the bundle and the edge-effect i.e. failure near the tensile test grips. This approach still requires more explanation and validation, for instance, in a bundle, the fibres are usually twisted and when one fibre fails, the stress distribution within the vicinity of the broken fibre and its effect on the strength of the neighbouring fibres cannot be detected by the AE technique. This might have an effect on the overall strength distribution of the fibre bundle. The possible solution might be *in-situ* detection of fibre failure followed by monitoring the effect on the neighbouring fibres.

Acoustic emission (AE) has also been used to detect damage mechanisms of composites. For fibre bundles, the prime concern is to estimate the stress distribution of the filaments within a bundle, whereas for the composite material, AE is usually employed to differentiate between different damage mechanisms occurring within a composite subjected to mechanical loading. The application of AE to identify different damage modes in fibre reinforced composite materials has been reported by many researchers [103, 139, 144, 144, 147, 151, 153, 154, 158, 163, 164]. Guild *et al.* [157] reported that composite materials gave two types of acoustic signal when subjected to mechanical loading; (i) low-level emissions which are generated by plastic deformation of the matrix material, and (ii) high-level emissions which can be associated with macroscopic events

such as fibre failure, matrix cracking, interfacial failure and fibre pull-out. However, in real composites, the results are far more complex since combined modes of failure can occur. With these materials, acoustic emission can be observed at a relatively low level of loading from the breakage of non-aligned fibres and from interfacial failure, prior to any major strength degradation. Therefore, for the identification of failure modes within FRC, more comprehensive techniques are required. In the subsequent paragraphs a brief review of damage detection using AE has been included. Researchers have employed specific methodologies to identify and relate the damage mode in composite materials to the characteristic AE signals.

Johnson *et al.* [144] performed a set of tensile tests on E-glass fibre epoxy composites with the aim of characterising AE signals to ascertain whether or not it was possible to discriminate between different types of damage modes. Four different types of composite laminates were used: three cross-ply; and one unidirectional samples. The samples were 25 mm in width and either 235 mm or 280 mm in length depending on the lay-up. Four different configurations of lay-ups including $[0, 90_2]_s$, $[90_2, 0]_s$,$[+45, -45]_s$ and $[0_4]$ were manufactured from glass fibre/epoxy prepregs. The samples were end-tabbed using aluminium 30 mm (length) x 25 mm (width). Six piezoelectric (PZT) sensors were attached using vacuum grease as a couplant and an adhesive-tape was used to hold them in place. Four PZT sensors were on one side of the specimen and the remaining two were on the opposite side. The samples were extended at 0.6 mm/s. Surface and internal matrix cracks transverse to the load direction were studied using the $[90_2, 0]_S$ and $[0, 90_2]_S$ specimens, respectively. The $[+45, -45]_S$ specimens were primarily used to study the development of delamination and matrix cracking. The $[0_4]$ specimens were used to generate AE signals corresponding to fibre breakage. They employed the six PZT transducers and these specific layup configurations to detect and characterise different

damage mechanisms in the composite specimens. For instance, they suggested that when a matrix crack was formed in one of the surface layers of the $[90_2, 0]_S$ specimen, a flexural wave was generated since the damage location was near the surface. This displacement discontinuity produced a flexural wave, which could be detected by the transducers at the same location but mounted on opposite sides of the specimen. They reported that for a flexural wave, two opposite transducers recorded the same signals but with opposite signs. If the recorded signals from the two opposite transducers are added or subtracted, an extensional or flexural wave will appear, respectively. If instead, a matrix crack was developed in the mid layer of the $[0, 90_2]_S$ specimen, there was a symmetric loading and therefore, the crack only generated an extensional wave and ideally no flexural wave. Hence, for the extensional wave, the two opposite transducers recorded the same signals but with the same sign. It was possible to conclude in which layer the matrix crack had developed by adding of subtracting the two respective waveforms. Similarly, for the other types of layups and transducer locations, the damage modes related to fibre fracture, fibre-matrix debonding were identified. Finally, they concluded that different damage modes in a composite material produce characteristic AE signatures that can be used as a tool for quantitative measurements of damage evolution.

Hugnet *et al.* [158] studied the damage modes in a glass fibre reinforced polyester using acoustic emission monitoring. The samples were prepared from E-glass fibres with polyester resin (Scott Bader, Crystic R 115 PA with Peroximon K1 hardener). The dimensions of the specimens were 100 mm (length) x 10 mm (width) x 2.5 mm (thickness) and they were manufactured by the hand lay-up technique with 12 layers per sample. Three types of samples were tensile tested to generate distinct damage modes i.e. pure resin (matrix cracking), 45º (matrix cracking and some debonding), 90º (mainly matrix cracking with some debonding) off-axis unidirectional samples. The samples were

examined using X-ray radiography and scanning electron microscopy following the tensile tests. It was reported that the pure matrix generated a burst of AE activity that could be attributed to the discontinuous micro-fracture process in the samples with an amplitude range of 55-70 dB. Tests on unidirectional samples loaded transverse to the fibres (90º off-axes) showed two ranges of AE amplitude i.e. 70% of the AE events had amplitudes 50-70 dB, and the remainder lay within the range 70-90 dB. For the 45º off-axis samples, the AE amplitude distributions were the same but the 50-70 dB events were 80% of the total recorded AE events. This was mainly due to the maximum shear stress acting on the 45º plane i.e. parallel to the fibre direction. Finally, it was concluded that at a macroscopic level, the cumulative plot of the events of each damage mechanism versus time indicates the damage initiation and progression of each failure mode.

Henrat *et al.* [165] studied damage accumulation in unidirectional, cross-ply (0º, 90º)$_{2S}$ and (90º, 0º)$_{2S}$ glass fibre reinforced plastics (GRP) subjected to monotonic uni-axial tensile tests. Damage accumulation and in-plane mechanical behaviour were monitored continuously using acoustic emission and surface-bonded tri-axial strain gauges. The laminates used in this study were made from Ciba Geigy Fibredux 913 GE-5-39 prepreg that had been cured at 150 ºC. Eight-ply unidirectional and cross-ply laminates were fabricated with a fibre volume fraction of 0.61 (±0.02). All the specimens were straight-sided coupons, 10 mm wide and 200 mm long. The stacking sequences of $[0]_8$, $[90]_8$, $[0, 90]_{2S}$ and $[90, 0]_{2S}$ were investigated. The study was based on the analysis of the cumulative numbers of events in six amplitude bands as a function of the longitudinal strain. The scale was logarithmic and the amplitude ranges in dB relative to the threshold of the transducer were: 0.69-9 dB (band 1), 10-21 dB (band 2), 22-33 dB (band 3), 34-45 dB (band 4), 46-57 dB (band 5), and all events with amplitudes greater than 57 dB (band 6). They came to the conclusion that the behaviour of unidirectional, ($[0]_S$ and $[90]_8$) and

cross-plied ([0,90]$_{2S}$ and [90,0]$_{2S}$) laminates was based on the analysis of the cumulative numbers of AE events arranged in the six amplitude bands already mentioned. It was concluded that the high-amplitude events in the 9-21 dB range had been correlated with an accelerating reduction of the longitudinal stiffness of [0]$_8$ laminates beyond 2% strain. This was attributed to an increase in fibre breakage. The amplitude distribution recorded at 0.75% strain range was attributed to the onset of transverse cracking. The greater emission rates of high-amplitude events in the [90, 0]$_{2S}$ laminates were interpreted as the effect of outer ply cracking.

Jimenez *et al.* [166] studied the acoustic emission behaviour of glass/thermoplastic composite materials subjected to tensile loading. The samples were prepared from unidirectional E-glass/polypropylene preformed tape. The dimensions of the samples were 200 mm (length) x 25 mm (width) x 1.8 mm (thickness) with the following fibre orientations i.e. 0º, 90º, 0-90º, ±45º. It was reported that 90% of the AE activities for E-glass fibre reinforced composite materials were concentrated in the frequency range 10–550 kHz. It was further concluded that the 100 kHz signal was due to fibre/matrix debonding. The occurrences between 200 and 300 kHz were attributed to fibre slippage and fibre pull-out. The two higher frequencies of 420 kHz and 520 kHz appeared in all the tests (except those at 90º) were associated with fibre fracture.

Barré *et al.* [151] investigated the damage mechanisms of four short-glass-fibre-reinforced polypropylenes (PP) in tensile, tensile fatigue and crack propagation (double cantilever beam) tests. The specimens were 150 mm (length) x 15 mm (width) and were cut from a 2.5 mm thick sheet. The tensile and fatigue tests were performed on an Instron tensile test machine. Acoustic emission was used to identify the different damage mechanisms during the tests which were later confirmed by imaging the fractured samples by a scanning

electron microscope (SEM). Different damage mechanisms were identified by the AE amplitude; for instance, matrix cracking (40-55 dB), interfacial fracture (60-65 dB), fibre pull-out (65-85 dB) and fibre fracture (85-95 dB). The comparatively low values for fibre fracture may be attributed to the fact the composites were short-fibre composites and therefore, had a lower amplitude of AE signal during fracture. They concluded that the acoustic emission monitoring and scanning electron microscopy can be used to investigate different damage mechanism in the short-fibre reinforced plastics.

Bohse *et al.* [154] discussed the acoustic emission (AE) characteristics of single-fibre composites (glass/epoxy, carbon/epoxy, glass/polycarbonate) and unidirectional reinforced multi-fibre composites (glass/polypropylene). The specimens containing single fibres measured 55 mm (length) x 20 mm (width) x 3 mm (thickness). They were subjected to tensile loading. The specimens containing multiple fibres were 120 mm (length) x 20 mm (width) x 4 mm (thickness) and were subjected to double cantilever beam (DCB) tests. The single-fibre tests provided the characteristic AE signals from the epoxy cracking and fragmentation of the fibres. These characteristic signals were used to identify the corresponding failure modes in the composites containing multiple fibres. It was reported that the epoxy-matrix cracking created lower-band frequencies than the glass-fibre breakage, with a ratio of nearly 1:3. Different failure modes i.e. matrix cracking, fibre breakage and fibre/matrix debonding or fibre pull-out were differentiated from their total power at defined frequency intervals. The mechanical energy-release rates were correlated to the AE energy-release rates for the failure modes of the composites. They concluded that the power spectrum analysis assisted in the selection and the characterisation of the AE signal to distinguish between different failure-mechanisms in the composite materials.

Bhat *et al.* [153] used AE to characterise the fatigue damage progression in unidirectional E-glass fibre composite materials. The acquired AE data were analysed using pattern recognition techniques to distinguish between different failures mechanisms namely; matrix cracking, fibre debonding and fibre fracture. It was found that the rate of AE activity from the data acquired had three distinct stages of damage before complete fracture. A brisk and short period of high AE activity was followed by a relatively silent and prolonged period. Before final failure of the specimen, a steep rise in the emission rate was recorded. With the help of visual examination during the test, the three stages of AE activity presented were related primarily to matrix cracking, interfacial debonding and gross fibre fracture.

To summarise, acoustic emission has emerged as a damage detection technique for fibre reinforced composite materials to detect, characterise and differentiate different damage mechanisms (fibre fracture, matrix failure, fibre/matrix debonding, delamination) within fibre reinforced composite materials. It has been demonstrated that different AE parameters, such as the AE amplitude and frequency content of an AE signal, correspond to a particular fracture mechanism in the composite material subjected to mechanical loading. These failure mechanisms may be either matrix cracking, fibre fracture, delamination and fibre matrix debonding or a combination of two or more of the aforementioned. They can be differentiated either individually or as a combination of the four damage modes already mentioned. However, detailed analysis is required to predict accurately and differentiate distinct damage modes when a composite test coupon is subjected to mechanical loading. The fracture behaviour of composite materials can be detected with more confidence if the fracture mechanism can be monitored *in-situ.* Embedded optical fibre sensors are the ideal candidate for this application; however their use could alter the stress/strain behaviour of the material. These issues can be addressed, if

the reinforcing fibres are used to detect damage *in-situ*. Therefore, there is substantial merit in developing techniques for *in-situ* monitoring and damage characterisation of composite materials.

There are many other techniques that can be used to detect and characterise damage in the composite materials. A brief description and their advantages and disadvantages are presented in Table 2.6.

Table 2.6 A summary of other established damage detection techniques for composite materials.

Techniques	Description	Advantages	Limitations	References
Laser-shearography	Non-contact detection by imaging the surface of specimen before and after deformation.	Non-contact. Quick ($1m^2$/minute)	Relatively complex technique; the interpretation of results require extensive processing.	[167]
Electrical resistance	The fracture or delamination in carbon fibre composite will cause a decrease in the electrical conductivity in the damaged region leading to a resistance or voltage change.	*In-situ* damage detection is possible.	The fibre must be conductors therefore, can only be applied to carbon fibres.	[101, 168-170]
Optical fibre heat emission	Delamination or damage in the composite materials can be detected and located by coupling laser into the already embedded optical fibres. When the composite is fractured the embedded optical fibres are also fractured. The transmitted laser-light energy was converted into thermal energy. That can be detected using a infrared heat emission cameras.	A considerable advantage of this method is the ability to make use of optical fibres that have already been attached or embedded into a structure for strain or temperature measurements.	The degree of change in temperature i.e. 10 °C to 16 °C is a limitation of this detection method.	[171]
Ultrasonic C-scan	Ultrasonic pulse-waves with a frequency ranging from 1 MHz to 1.5 GHz are launched into materials to detect internal flaws or to characterise materials.	It is possible to detect delamination and debonding as well as volumetric defects including voids within the structure.	High attenuation caused by absorption in porous resin and scattering by the fibres are main disadvantages, additionally water coupling is required.	[172, 173]

Techniques	Description	Advantages	Limitations	References
Thermography / Infra-red imaging	Heat is injected into the structure using heat lamps or hot air guns and is reflected by the structure. When damage occurs or a defect is detected the thermal output from the structure is altered. This change can be monitored using Infra-red cameras.	No coupling is required, it can be performed *in-situ*, and can cover large areas.	The disadvantages are that there is a limit to the thickness of the structure being monitored, it is a much better method for monitoring glass fibre composites than carbon composites and it is perceived as an expensive option.	[174, 175]
X-ray Radiography	X-rays are used to image the structure on a photographic film.	This technique can detect voids and porosity within structures.	Penetrant dye is required to be injected and access is required on both sides of the structure.	[30, 176]

2.6 Overall Summary of the Literature

The literature review has covered common and well-established methods that are employed routinely to detect damage in composite materials. It is evident that there are specialised and developmental methods that will become more commonly used in the near future. At the present time, it is appropriate to claim that self-sensing composites are a specialised method of damage detection. The advantages of self-sensing fibres over other damage detection methods include: (i) the ability to deploy the fibres into composite structures; this allows monitoring of the internal structure as well as the external surface [7, 36]; (ii) the self-sensing fibres are immune to electro-magnetic interference [8-10, 99]; (iii) they do not require a coupling agent (such as water for ultrasonic C-scans or silicone for acoustic emission) [139, 158, 177]; (iv) they can provide information over the life cycle of the composite such as fibre surface treatment, impregnation, curing of the matrix, damage detection and during the structural service life of the composite material [118]; and (v) the light transmission characteristics can be related directly to the failure of the composite material i.e. the fractured fibres will not transmit light [178].

It is evident from the literature that individual methods are more than capable of accurately detecting damage in composites. Complications arise when the need to record multiple forms of damage is required with only a single available method, for example the detection of impact damage whilst recording changes in strain, detecting fibre fracture, debonding and matrix failure by acoustic emission monitoring, etc. At the present time, for multiple parameters to be recorded, multiple sensors are required. Development of current methods or further research into the ability of a single sensor to record multiple parameters would increase the accuracy and efficiency of detecting damage in composite materials.

3 Experimental

This chapter presents details of the materials, techniques and test methods that were developed and employed in this study. Three resin systems and four different types of fibres were used. Three resin systems were selected to study the effects of the ultimate failure strains of the resins on the fracture behaviour of E-glass composites. The fracture strain of the resin systems EPO-TEK$^®$-305, EPO-TEK$^®$-310M and EPO-TEK$^®$-314 were 9.2%, 2.2% and 1.1%, respectively.

Four fibre types were used: (i) as-received E-glass fibres; (ii) silane-treated E-glass fibres; (iii) as-received custom-made small-diameter optical fibres (SDOF); and (iv) heat-treated small-diameter optical fibres. These fibres were selected because: (i) the E-glass fibres are used extensively in industrial applications; and (ii) it was necessary to develop a technique to study the fracture of the fibre in real-time. The SDOF were used as their diameters were similar to that of the E-glass fibres.

3.1 Materials

3.1.1 Resins

Three different resin systems, supplied by Promatech Ltd UK, were used in this study. These were EPO-TEK$^®$-305, EPO-TEK$^®$-310M and EPO-TEK$^®$-314. The details of the curing schedule, stoichiometric (epoxy:amine) ratios and refractive indices for these resin systems are summarised in Table 3.1.

Table 3.1 Summary of the resin systems used in this study along with the stoichiometric ratios and the curing schedules.

	Mixing ratio (epoxy:amine)	Cure schedule	Refractive index (measured at 589.6 nm and 20 °C)
EPO-TEK®-305	10:2.8	23 ℃ for 24 hours	1.476
EPO-TEK®-310M	10:5.5	25 ℃ for 24 hours	1.497
EPO-TEK®-314	100:6	120 ℃ for 3 hours	1.496

3.1.2 Fibres

(i) E-glass Fibres: The E-glass fibres used in this study were supplied by PPG Industries (UK) Ltd. These continuous, water-sized E-glass fibre bundles contained approximately 2500 filaments with an average individual fibre diameter of 15 (±3) μm. The refractive index of the E-glass preform was measured on an Abbe-refractometer and was found to be 1.56 at 589.6 nm and 20 ℃.

(ii) Small-diameter optical fibre (SDOF): In addition to E-glass fibres, custom-made small-diameter optical fibres with diameters of 12 (±2) µm were used to demonstrate the concept of *in-situ* damage detection using the reinforcing fibres. The small-diameter optical fibres were supplied by Aomolin Ltd, China. The composition of SDOF was proprietary information; however the supplier indicated that it is similar to F_2-glass. The small-diameter optical fibre bundle consisted of approximately 2800 individual filaments.

The E-glass and small-diameter optical fibres were used in the as-received state. However, as discussed in Section 4.1.1, it was necessary to remove the binder on the small-diameter

optical fibres. This was achieved by subjecting them to a pyrolysis or burn-off regime and their properties were studied.

3.2 Sample Preparation

3.2.1 Neat resins

The mechanical properties of the resin systems used in this study were determined using cast samples. The procedure for producing the cast neat-resin samples is described in the following sections.

3.2.1.1 Fabrication of the silicone mould

Two dog-bone samples were machined from a polytetrafluoroethylene (PTFE) sheet of 4 mm thickness. The dimensions of the PTFE dog-bone specimen are shown in Figure 3.1. The edges were polished using 1200 grit abrasive-paper (P1200 MetPrep, UK). The dog-bone templates were secured on a glass plate and a rectangular moat was constructed from wooden strips. A two-part silicone resin (Silax-3120 from Replication Technologies Limited, UK) was mixed thoroughly using a resin to hardener ratio of 10:5.5. The uncured resin system was dispensed to fill the moat with the PTFE templates ensuring that they were completely covered. The resin was cured at ambient temperature for 24 hours.
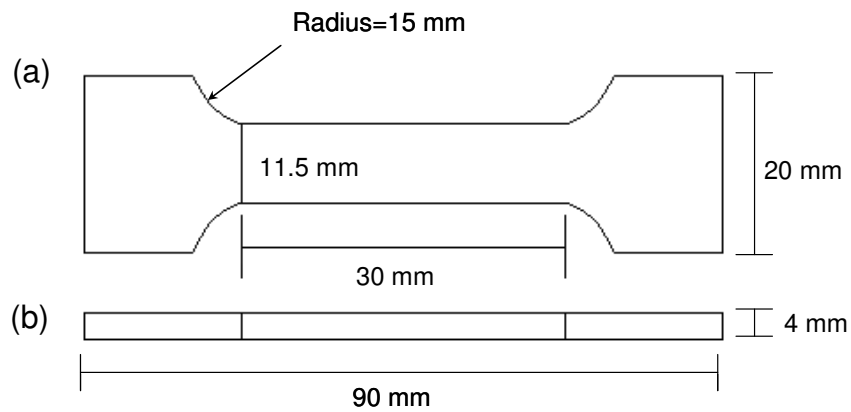
Figure 3.1 Dimensions of the dog-bone templates: (a) Front; and (b) Side views.

A schematic illustration of the mould assembly with the PTFE template along with the relative dimensions of the various components is presented in Figure 3.2.
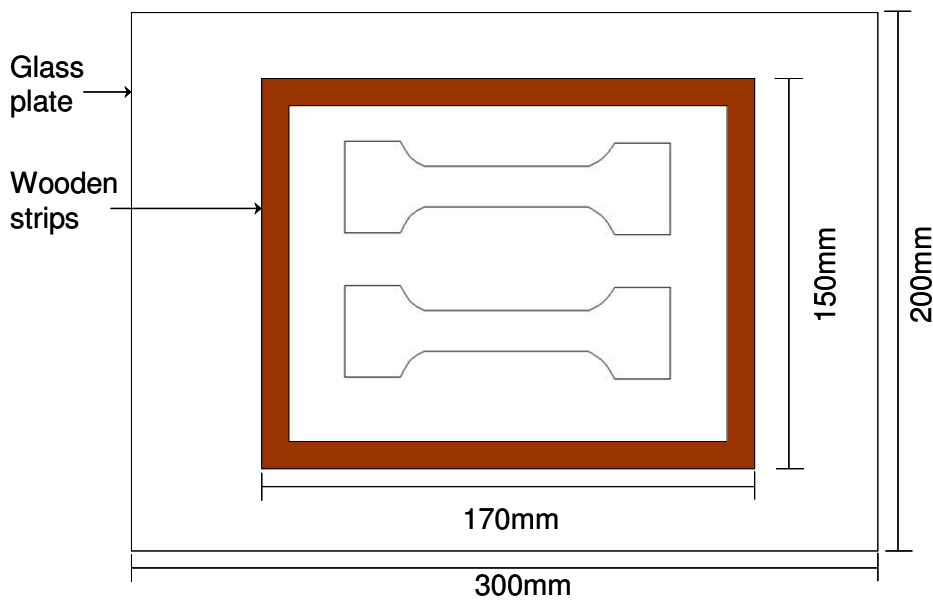
Figure 3.2 Schematic illustration of the assembly used for fabricating the mould for casting the neat-resins samples.

After the silicone resin was cured (cross-linked), the PTFE inserts were removed and the mould was trimmed to remove any "flash" and debris prior to use. The surface of the mould was cleaned with lint-free tissue (Fisher Scientific, UK) and iso-propanol.
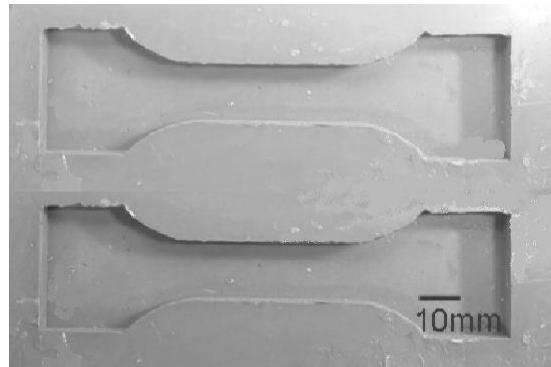
Figure 3.3 Photograph of the silicone mould that was used to cast the neat resins.

3.2.1.2 Fabrication of neat-resin dog-bone specimen

The required masses of the resin and the hardener were mixed thoroughly in an aluminium container and degassed in a vacuum chamber at -15 mm of Hg for 20 minutes. After degassing, 10 grams of un-cured resin system, was poured into the silicone mould. The EPO-TEK®-305 and EPO-TEK®-310M resin systems were then left to cure for 24 hours at room temperature. However, in the case of EPO-TEK®-314, the mould was moved to an air-circulating oven (Memmert, Germany) to cure it at 120 ℃ for 3 hours. The processing (cure) schedule for the resin systems are summarised in Table 3.1. After processing, the samples were stored in desiccators until required.

3.2.1.3 End-tabs for the neat-resin samples

In order to avoid crushing of the samples between the grips of the Instron tensile testing machine, aluminium end-tabs with dimensions of 25 mm x 20 mm x 1 mm were used for the EPO-TEK®-305, EPO-TEK®-310M and EPO-TEK®-314 samples. The end-tabs were attached to the resin samples using Scotch-Weld 9323 adhesive (3M, UK).

The EPO-TEK®-310M neat-resin specimens were too fragile to be gripped between the jaws of the Instron tensile test machine. This cross-linked resin had a failure strength of

0.24 MPa. A different methodology was adopted to address this issue. Two, 4 mm diameter holes were drilled through the centre of each end-tab after the adhesive resin had cured. 160 mm length of wire was looped through the hole. These wires were held between the grips of the Instron tensile test machine and the specimen was loaded in a similar way to the other neat-resin samples.

3.2.1.4 Surface-bonded electrical resistance strain gauges

Electrical resistance strain gauges (FLA-6-11 from Techni-measure, UK) were bonded to the surface of test specimens using an adhesive (M-Bond 200, Vishay Measurements, UK). The strain gauges were aligned by first marking the centre point on the gauge length of the specimen. The strain gauges were temporarily bonded to M-line cellophane tape (Vishay Measurements, UK). The purpose of using M-line cellophane tape was to secure the strain gauges for handling and for ensuring correct alignment with the pre-marked mid-points on the specimens. This procedure also helped to secure the electric contact base at a distance of approximately 5 mm from the strain gauge. The procedure adopted for the bonding of the strain gauges is explained in detail in the following paragraphs.

Each sample was attached to a glass plate using a strip of masking tape that was placed over the end-tabs. The mid-point of each sample was measured out and marked on either side of the sample. Tweezers were used to remove the strain gauge and electrical contact from their casing and these were placed on the glass plate. M-line cellophane tape (Vishay Measurements, UK) was used to cover the electric contacts and the strain gauge. To ensure that there were no air bubbles, medical gauze was used to apply pressure and to wipe the surface as the tape was lowered from the strain gauge end. The strain gauge and electrical contact were removed from the glass plate with the end of the gauge initially being peeled off at a 45° angle. The tape was placed on the sample with the midpoint of the strain gauge

aligned with the previously marked points on the samples. A thin layer of M-bond catalyst (Vishay Measurements, UK) was applied on the electrical contact and strain gauge. When the catalyst had dried, two drops of M-Bond adhesive were placed on the surface of the resin below the strain gauge. The tape was lowered at 45° and the M-line cellophane tape was pressed gently to ensure an even covering of M-Bond over the surface of the sample.

Immediately after the strain gauge and electrical contact had been lowered into place, a Teflon sheet, a rubber block and an aluminium block (~50 grams) were placed on top of the gauge and electrical contact with pressure being applied for 2 minutes. After the pressure had been applied the tape was left on for 5 minutes. Finally, the tape was removed at an angle of 180° to the strain gauge to leave the electric contact points ready for soldering.

The surface of the contacts and strain gauge wires were cleaned with M-Line resin solvent (Vishay Measurements, UK). The strain gauge wires were formed in a zigzag shape to allow the contacts and strain gauge to move apart during testing without breaking the circuit. One metre long pieces of strain gauge wire were soldered to the electrical contacts. The wires were then soldered to the other half of the electrical contact. The strain gauges were connected to a strain gauge amplifier (DMM4, Cambridge Electronic Systems, UK). The resistance of the strain gauge was then recorded, to ensure the soldering had connected the strain gauge to the contacts, the displayed resistance needed to be 120 Ω, +/- 1 Ω. Figure 3.4 is a schematic illustration of the neat-resin sample with attached end-tabs and electrical strain gauge.
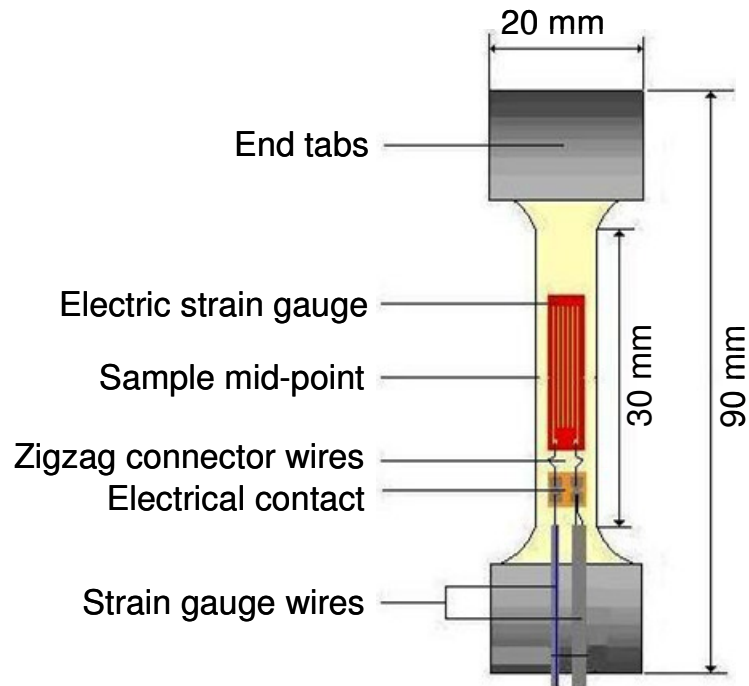
Figure 3.4 Schematic illustration of a neat-resin sample with its associated dimensions.

3.2.2 Fibre bundle

The mechanical properties of the two types of fibres were determined by tensile testing. Custom-made small-diameter optical fibres and E-glass fibres were tensile tested on an Instron (model-5566) tensile test machine. The procedure for producing the fibre bundle samples is described in the following sections.

3.2.2.1 De-binding of the small-diameter optical fibres

SEM inspection of the small-diameter optical fibres revealed that they had a high binder content. A series of experiments were undertaken to establish the pyrolysis temperature for the small-diameter optical fibres. The pyrolysis experiments were carried out in a muffle furnace (PyroTherm Furnaces, UK) for 4 hours at 400 ℃, 500 ℃ and 600 ℃ each, and for 4.5 hours at 450 ℃.

3.2.2.2 Preparation of the fibre bundle for tensile testing

A schematic illustration of the fibre bundle test specimen with a gauge length of 100 mm is shown in Figure 3.5. As mentioned previously, the E-glass and small-diameter optical fibre bundle contained approximately 2400 and 2800 filaments, respectively.

Since the fibre bundles were used as light guides, it was necessary to attach connectors or terminators at the end of the fibre bundle. Sub-miniature adapters (SMA) Type-A supplied by Thorlabs UK (ID: 11275A) were used as connectors. The procedures that were developed to attach end-connectors to the fibre bundle are described in Section 3.2.2.4. Preliminary tensile tests on the E-glass fibre light-guides indicated that when the conventional end-tabs were used, there was some damage to the fibres due to the grips of the tensile test machine. Hence modified end-tabs were designed and developed. Details of the modified end-tab design are presented in Section 3.2.2.3. End-tabs were attached to the fibre bundles at the first step of sample preparation.
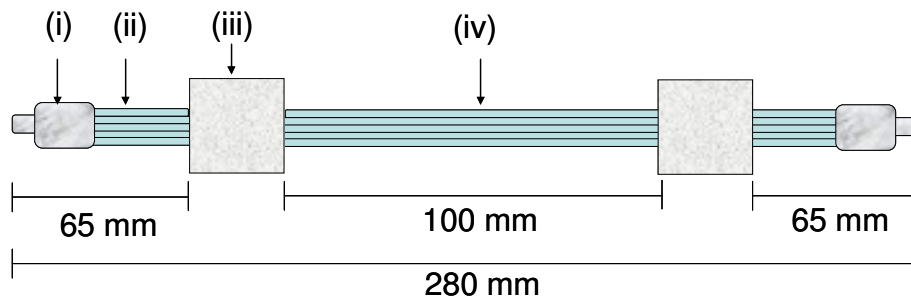
Figure 3.5 Schematic illustration of a fibre bundle sample with SMA connectors and end-tabs: (i) SMA connector; (ii) Un-impregnated section of the fibre bundle; (iii) End-tab; and (iv) Section of the fibre bundle subjected to mechanical loading.

3.2.2.3 End-tabs for the fibre bundles

Two end-tab designs were used in this study. Firstly, conventional (rectangular) and sand-blasted end-tabs were used for neat-resin and composite test specimens. Custom-designed

mild-steel end-tabs were used for tensile testing the fibre bundles to protect the fibres when being gripped in the jaws of the mechanical testing machine. A schematic illustration of the end-tab design is presented in Figure 3.6 where a rectangular slot was cut out for housing the fibres. This recess helped to avoid crushing of the fibres between the grips.

Different end-tabbing procedures were used for the E-glass and SDOF. In the case of the E-glass fibre bundles, they were initially coated with a low refractive index resin EPO-TEK®-310M before bonding to the end-tabs. This was necessary because the structural adhesive for bonding the end-tabs (Scotch-Weld 9323 adhesive, 3M, UK) had a refractive index that was significantly higher than that of E-glass. Hence significant attenuation was observed within the end-tab region. In order to minimise the light transmission losses, the region was impregnated with EPO-TEK®-310M. The refractive index of EPO-TEK®-310M was 1.497. Once the low-index resin was cured using the processing schedules given in Table 3.1, it was over-coated with the structural adhesive Scotch-Weld 9323 adhesive (3M, UK).

The end-tabbing was carried out as follows:

The end-tabbing was carried out by securing the end-tabs on a metal plate (50 x 50 cm) covered with PTFE self-adhesive sheet (Aerovac, UK). The gauge length, i.e. 100 mm, was marked on the plate. Two parallel sections of double-sided adhesive tape were attached on top of the plate at a distance equal to the gauge length. The end-tabs were then secured in the correct alignment on each of the parallel section of the adhesive tape. The purpose of the adhesive tape was to secure the end-tabs and restrict any movement during the bonding of the specimens.

Approximately 1 gram of the structural adhesive (Scotch-Weld 9323) was spread over the end-tab channel. The appropriate section of the small-diameter optical fibre bundle (see

Figure 3.7), was placed on the adhesive. For the E-glass fibre bundle a different procedure was adopted to prepare the section of fibre bundle that was bonded to the end-tabs as discussed in Section 3.2.2.5. Due care and attention was given to ensure that the tension in the individual filaments was similar; this could not be guaranteed given the number of filaments in the bundles (2500 ± 200 and 2800 ± 200 for E-glass and small-diameter bundles, respectively). A small amount of adhesive (1 gram) was applied on top of the fibre bundle section before covering it with the top end-tab. A metal plate was placed on the end-tab assembly with a dead-weight (2 kg) to ensure good contact between the top and bottom end-tabs. This assembly was then left to cure for 24 hours at room temperature.
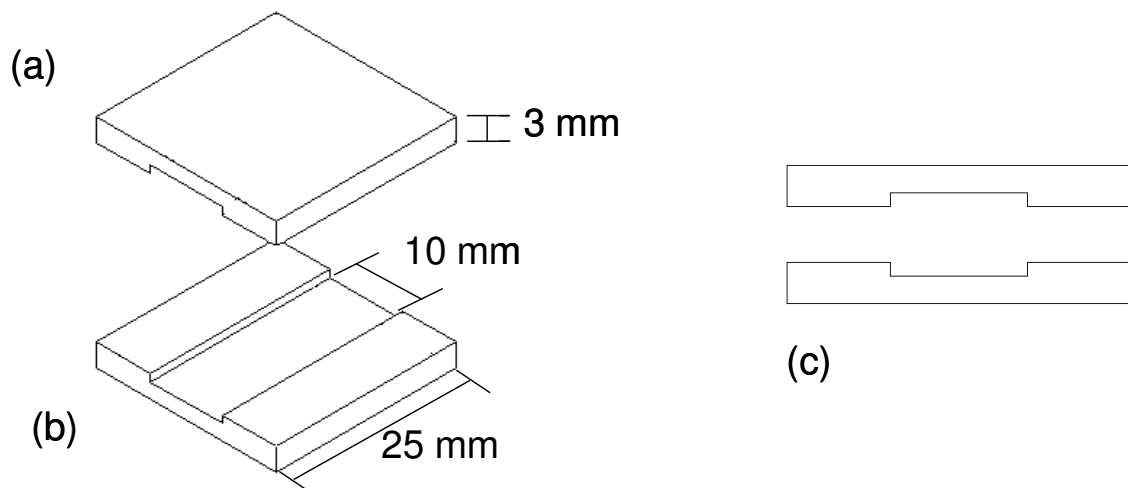
Figure 3.6 A schematic illustration of the end-tab assembly: (a) Top end-tab; (b) Bottom end-tabs; and (c) Side-view.

3.2.2.4 Fibre termination (connectors)

With reference to the E-glass and small-diameter optical fibres (SDOF) bundles, the transmitted light intensity was monitored during various operations. For example, during (i) the etching of the SDOF to reduce the thickness of the cladding, (ii) mechanical testing and (iii) high-speed photography during mechanical loading. Hence it was necessary to

attach connectors to the ends of the fibre bundle; the procedure for this is discussed in Section 3.2.2.5.

3.2.2.5   Attaching SMA connectors to the fibre bundle

The standard SMA connectors were supplied with a bore diameter of 1.2 mm; in the current study they were drilled to 1.4 mm to accommodate the as-received fibre bundles. Prior to potting the fibre bundles in the connectors, they were immersed in distilled water in an ultrasonic cleaning bath for 20 minutes. They were then dried in an air-circulating oven (Memmert, Germany) at 80 ºC for 2 hours. The SMA connectors were stored in a desiccators until required.

The required length of the E-glass or SDOF was cut using a fresh portion of a razor blade. The fibre bundle was potted in the SMA connector using low refractive index resins EPO-TEK®-314 (Promatech, UK) and Opti-tec 5007 (Intertronics, UK) for the E-glass fibres and small-diameter optical fibres, respectively. Due to the different properties of the resin and the fibres, different procedures were developed for impregnating, and/or sealing the section of fibre bundle within the SMA connector. These are explained in the following paragraphs.

Preparation of E-glass fibre bundle: Prior to potting the E-glass fibre bundle in the SMA connector it was necessary to "seal" a section of the fibre bundle; this was done to ensure that the resin used for potting the fibre bundle in the SMA connector did not seep into the gauge length region of the fibre bundle. RTV-3140 silicone resin (Dow Corning, UK) was used to seal the sections of the fibre bundle. Figure 3.7 presents a schematic illustration of the manufacturing sequence for attaching SMA connectors and end-tabs to the fibre bundle. With reference to Figure 3.7, the sample preparation began with cutting a section of fibre bundle approximately 30 cm in length. The location of the end-tabs was noted and

the fibre bundle was sealed at four different locations, using RTV-3140 silicone resin (Dow Corning, UK). The sealant was cured at ambient temperature for 24 hours. The next step was to impregnate the section of fibre bundle under the end-tabs with low refractive index resin EPO-TEK®-310M. The resin was cured at room temperature for 24 hours. This fibre bundle, with sections of cured resin (at the end-tab locations), was then bonded to the end-tabs using structural adhesive Scotch-Weld 9323 (3M, UK) and left to cure for 24 hours. The fibre bundle was then sealed again in a similar manner behind the SMA connectors. When this sealant was cured, the ends of the fibres were 'secured' using a drop of acetone and threaded into the SMA connector. The length of the fibre outside the SMA connector was then impregnated and cured using EPO-TEK®-314 resin system. The properties of this resin system are summarised in Table 3.2. The excess fibres were trimmed using a diamond wheel cutter (Dremel, UK) leaving only 1-1.5mm of fibre section. The fibre bundle assembly with the SMA connectors and end-tabs were transferred to an automatic polishing unit to polish the SMA connectors.

Preparation of small-diameter optical fibre bundles: The preparation of the SDOF bundle for tensile testing was relatively simple in comparison to the E-glass fibre bundles. This was mainly due to the following two reasons: (i) these fibres had a cladding therefore, the light transmission was unaffected by the application of the end-tab adhesive; and (ii) there was no need to use a low-refractive index resin for potting the SDOF in SMA connectors. Therefore, a resin system with a high-viscosity Opti-tec 5007 (Intertronics, UK), was employed, and this circumvented the requirement to seal the fibres at the SMA connectors.
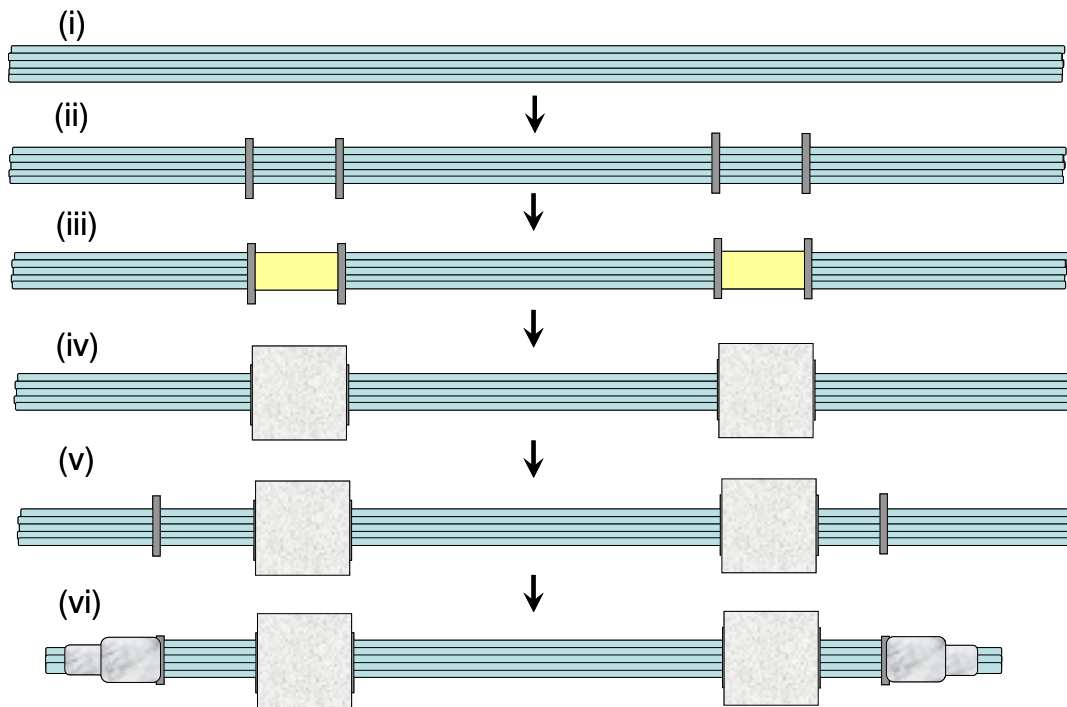
Figure 3.7 Diagram illustrating the procedure for attaching the SMA connectors and end-tabs to the E-glass fibre bundle: (i) A section of E-glass fibre bundle; (ii) E-glass fibres were sealed at four different sections with respect to the end-tabs location using RTV-3140 silicone resin; (iii) EPO-TEK®-310M resin was used to impregnate the fibre section between the two sealed regions; (iv) End-tabs were bonded to the fibre bundles; (v) The E-glass fibres were sealed at two different sections with respect to the SMA location using RTV-3140 silicone resin; and (vi) SMA connectors were attached and excess fibres were trimmed, the sample was transferred for polishing.

Table 3.2 Properties of the resin system used in this study.

Resin	Refractive index	Glass transition temperature (^{o}C)	Hardness	Cure schedule
EPO-TEK®-314	1.496	> 100	80 (Shore D)	120 ℃ for 3 hours
Opti-tec-5007	1.55	105	85 (Shore D)	25 ℃ for 24 hours

The preparation of the SDOF bundle commenced by securing the fibre bundle within end-tabs, as described in Section 3.2.2.3. This adhesive was left to cure at ambient temperature for 24 hours. The ends of the fibres were threaded into the SMA connector in a similar manner to that of the E-glass fibre bundle and impregnated and cured (25 ºC for 24 hours) using an Opti-tec 5007 (Intertronics, UK) resin system. The fibre bundle assembly with the SMA connectors and end-tabs were transferred to the automatic polishing unit.

3.2.2.6 Polishing the fibres in the SMA connectors

The fibre bundles with the SMA connectors were secured on an adapter plate (specifically designed for SMA connectors). The assembly was attached to an automatic optical fibre polisher (APC-8000, Senko, UK). The optimum polishing sequence for the E-glass and SDOF bundles were obtained by trial-and-error. The optimum polishing sequences for the E-glass and SDOF are summarised in Table 3.3.

Table 3.3 Polishing sequence for the SDOF and E-glass fibre bundles.

Grinding and polishing steps	Grinding/ polishing film type	Plate (under the grinding/ polishing film)	Force (grams)		Duration (seconds)		Speed (rpm)
			SDOF	E-glass	SDOF	E-glass	
Rough grinding	Metal plate	---------	200	200	30	30	120
Rough polish	LFD200-5S (3 µm)	Glass	150	200	60	120	180
Fine polish	LFD300-5S (0.5 µm)	Glass	150	200	90	180	180
Finishing	LFOS01-5N	Glass	180	200	120	240	180

3.2.2.7 Inspection of the polished fibre bundles

The polished fibre bundles were secured to an SMA polishing disc (D50-SMA, Thorlabs, UK) and inspected under a binocular optical microscope (Z30C, Leica Germany). Images of the polished specimen were taken using the CCD camera (Photron, UK).

3.2.2.8 Silane-treatment of fibre bundles

The as-received water-sized E-glass fibres were silane-treated to increase their compatibility with the epoxy matrix. The mechanical properties of silane-treated fibres were studied in a similar manner to that of the as-received E-glass fibres. The silane-treated E-glass fibres were also used to manufacture composites.

The coupling agents used were prepared from a 1% solution of 3-glycidoxypropyltrimethoxysilane (GPS) from Aldrich, UK using a mixture of ethanol and distilled water (4:1) and the pH was adjusted to 4 using acetic acid. The specimens were prepared in a similar manner to that described in Section 3.2.2.5. The gauge length of the sample was then immersed in the silane solution that was contained in a PTFE trough. The specimens were bonded to the edges of the trough using adhesive tape at the end-tabs. The exposed fibre portion of the connected but untreated fibre bundle was immersed in this solution for one hour at room temperature. The solution was then drained and the fibre bundle was dried at room temperature for two hours. Subsequently, the silane-treated fibre bundle was dried in an air-circulating oven at 100 ºC for three hours. The silane-treatment was carried out by Dr Liwei Wang who was the post-doctoral researcher on this project and was responsible for carrying out the *in-situ* cure monitoring studies [118].

3.2.3 Production of self-sensing composites

A detailed discussion on the design requirements for the self-sensing composite is presented in Section 4.1.6. A number of production techniques were explored to enable the manufacture of void-free self-sensing composites. The techniques investigated included (i) open-mould lamination (ii) autoclave-based processing of impregnated fibre bundles, and (iii) a resin-injection method. The first two techniques did not yield void-free composites but the resin-injection technique did and it was optimised and adopted in this study.

3.2.3.1 Resin-injection method

The most effective technique for fabricating void-free composite specimens was found by repeated trials, where incremental improvements were made each time. As a result, the method used involved the reinforcing fibres being sandwiched between two glass plates. The glass plates were sealed along the three edges and resin was injected into the mould. The resin system was then cured in an air-circulating oven.

A description of the step-by-step procedure for preparation of self-sensing composites by the resin-injection method is presented below:

Preparation of the glass mould: Two glass plates were custom-cut by a local supplier (Artic Glass and Glazing, UK). The top plate was 300 mm in length and the bottom plate was 150 mm in length; both plates were 30 mm wide and 6 mm thick, as shown in Figure 3.8(i). The edges of the plates were rounded after cutting to the required dimensions by the supplier. Firstly, a rectangular mould was formed using self-adhesive PTFE release-film (Aerovac, UK) on the longer glass plate. Two sections of PTFE release film with dimensions of 150 x 5 mm were cut using a scalpel blade. These were then attached to the face of the glass plates as shown in Figure 3.8(ii). An identical mould was formed with

similar dimensions on the shorter (top) glass plate. The thickness of the PTFE film was 0.4 mm. Therefore, when the two glass plates were joined together the dimensions of the cavity were 150 mm (length), 20 mm (width) and 0.8 mm (depth). After manufacturing of mould a release agent, Frekote® 700-NC (Loctite®, UK), was applied to the glass plates in a fume cupboard. This allowed easy removal of the composite after processing. The plates were then left to dry for 2 hours. The glass plates with mould were then stored in a desicator until required.

Production of composites: A section of the E-glass fibre bundle approximately 350 mm in length was cut from the bobbin (creel) using a razor blade. The longer glass plate was secured on a metal plate of 50 x 50 cm which was covered with self-adhesive PTFE sheet (Aerovac, UK) as illustrated in Figure 3.9(i). The fibres were secured in position on the bottom plate using small bull-dog clips on both sides. This enabled the fibres to be kept in tension and restricted any further movement of the fibre bundle. A thin layer (≈ 0.1mm) of the RTV-3140 silicone resin (Dow Corning, UK) was then applied on the PTFE spacers that were attached to the bottom glass plate. A needle (part of a syringe) was also secured to the bottom glass plate, before the top glass plate was positioned and aligned with the lower glass plate as shown in Figure 3.9(ii). The glass plates were clamped in place and sealed along three edges using the silicone sealant; the top of the mould was not sealed. The sealant was then left to cure for 24 hours at ambient temperature. After the sealant had cured, the entire assembly was placed vertically and secured using a laboratory retort stand. Five grams of the EPO-TEK® 314 resin system per sample was mixed thoroughly and then degassed in a vacuum chamber at (at -15 mm of Hg for 20 minutes). The resin was injected gradually via a syringe (Thorlabs, UK) until the mould was filled completely. A semi-automated syringe-pump (Alladin-220, World Precision Instruments, USA) was used to drive the syringe assembly. The mould assembly was left in a vertical position for

30 minutes allowing the fibres to be impregnated. More resin was added (if required) before removing the syringe. After the syringe was removed, the entry point of the needle located outside the mould was sealed with silicone sealant. The assembly was placed in an air-circulating oven (Memmert, Germany) and the resin system was cured at 120 °C for 3 hours. After cooling to room temperature, the composite was removed from the mould and the needle was detached. The dimensions of the rectangular composite specimens were 150 mm (length) x 20 mm (width) x 0.8 mm (thickness). The gauge length of the composite was similar to that of the fibre bundle (100 mm). As the fabricated composite specimen was wider than the width of the reinforcing fibres, it was necessary to polish the excess resin along the length of the specimen as illustrated in Figure 3.10. The excess resin was removed by polishing with a 2500 grit abrasive-paper (P2500 MetPrep, UK). The total length of the sample was 280 mm including the un-impregnated fibre section and the attached SMA connectors; this is shown in Figure 3.11.

End-tabbing of the composites: The end-tabbing method for the fibre bundles was explained in Section 3.2.2.3. A similar method was adopted here but the section of the composite under the end-tabs was abraded using 800 grit abrasive-paper (P800 MetPrep, UK). The composite specimen was then bonded to the end-tabs using structural adhesive Scotch-Weld 9323 (3M, UK) and left to cure for 24 hours. After this step the SMA connectors were attached as explained in Section 3.2.2.5.

Top view

Side view

6 mm

300 mm

30 mm

6 mm

150 mm

30 mm

(i) Glass plates with dimensions

Isometric view

Top view

5 mm

0.4 mm

75 mm

150 mm

Side view

5 mm

0.4 mm

20 mm

PTFE Spacers

(ii) PTFE spacers attached to the glass plates

Side view

Isometric view
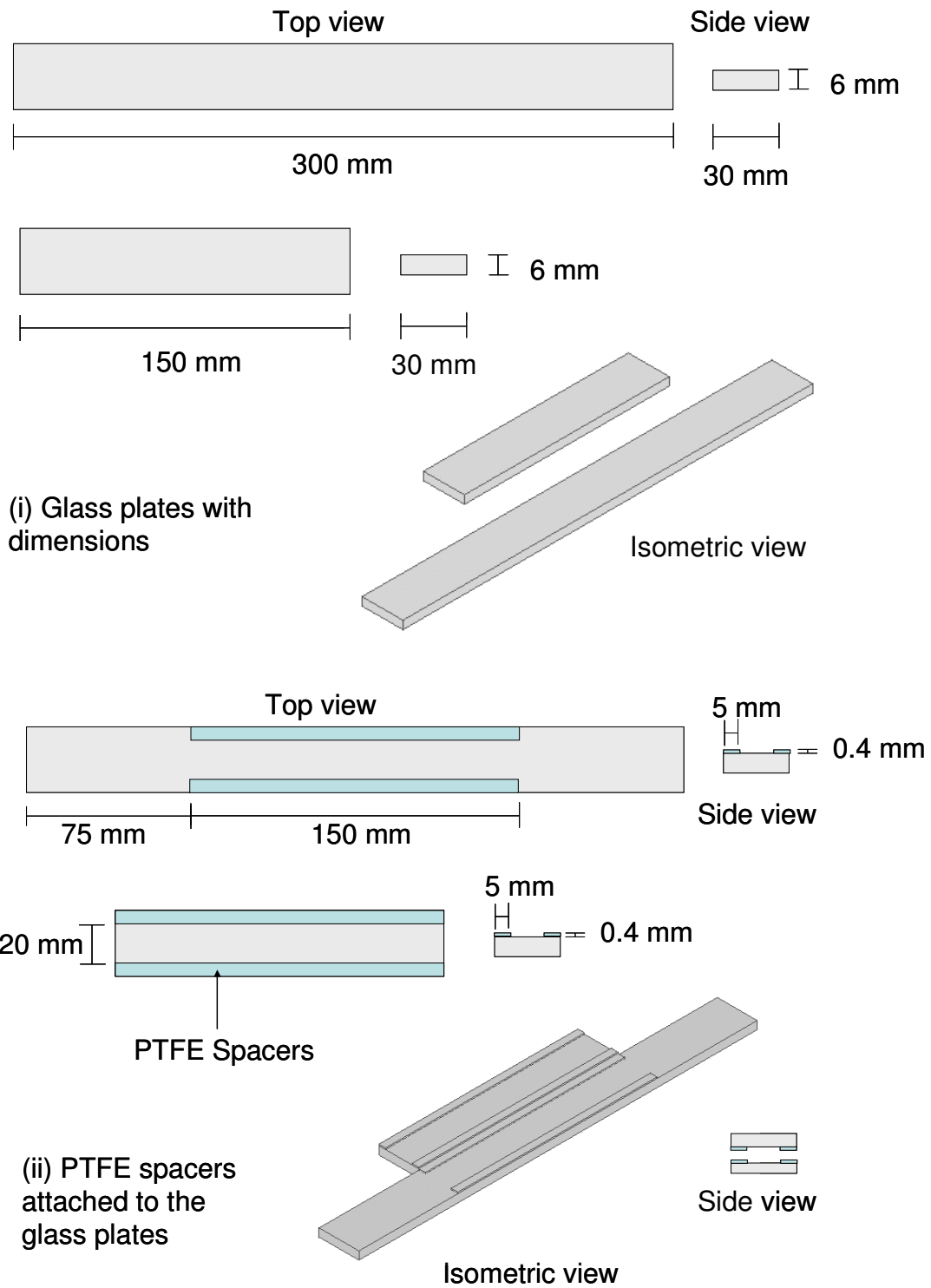
Figure 3.8 Preparation of the mould for the production of self-sensing composites: (i) Glass plates; and (ii) PTFE mould bonded to the glass plates.

Top view   Side view

Fibres secured   Syringe needle
in place   attachment

Magnified view

Isometric view

(i) Fibres secured in
the mould

Top view   *   Side view

*

*   *
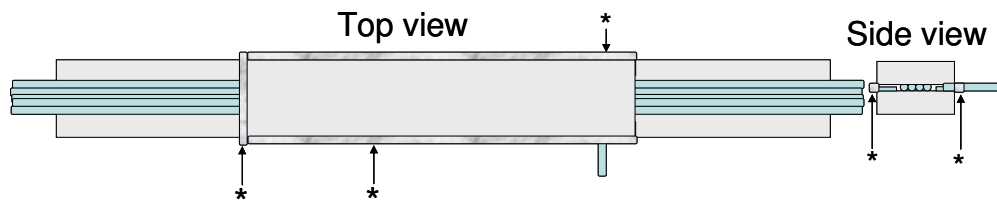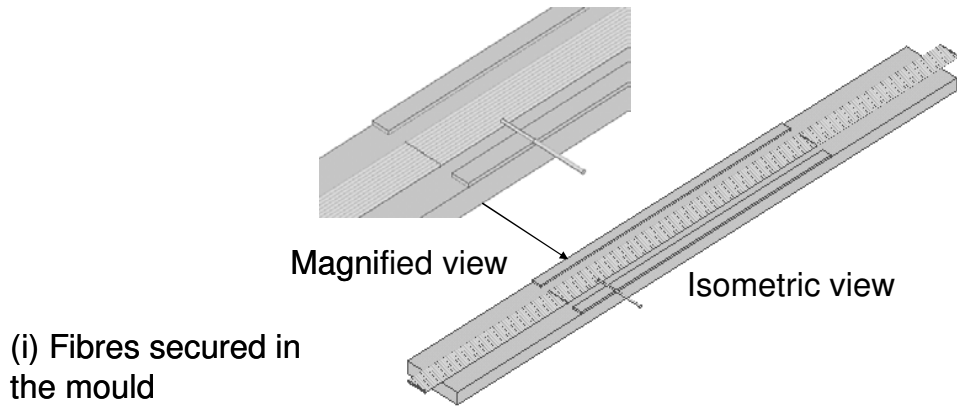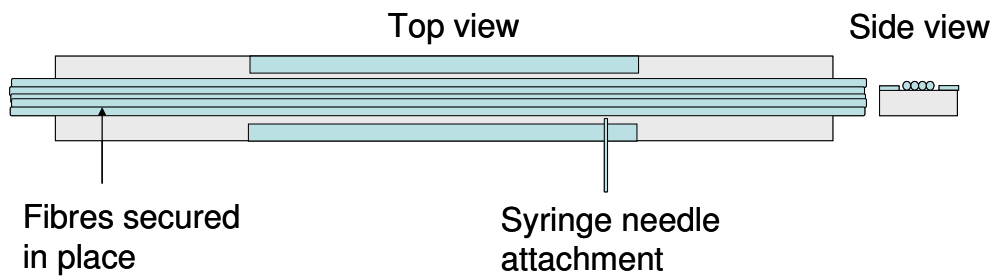
*Mould is sealed along the three edges of the
plate

(ii) Mould sealed
and resin injected

Isometric view
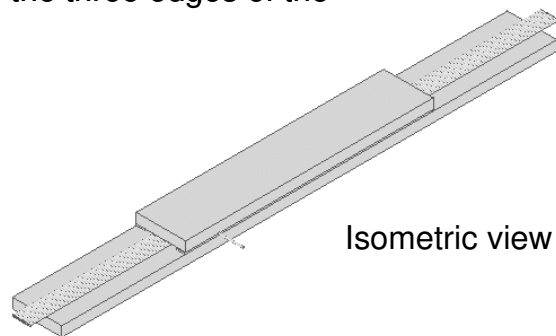
Figure 3.9 Production of self-sensing composites: (i) Fibres secured in the mould and the

needle is attached; and (ii) The mould was sealed with RTV-sealant.
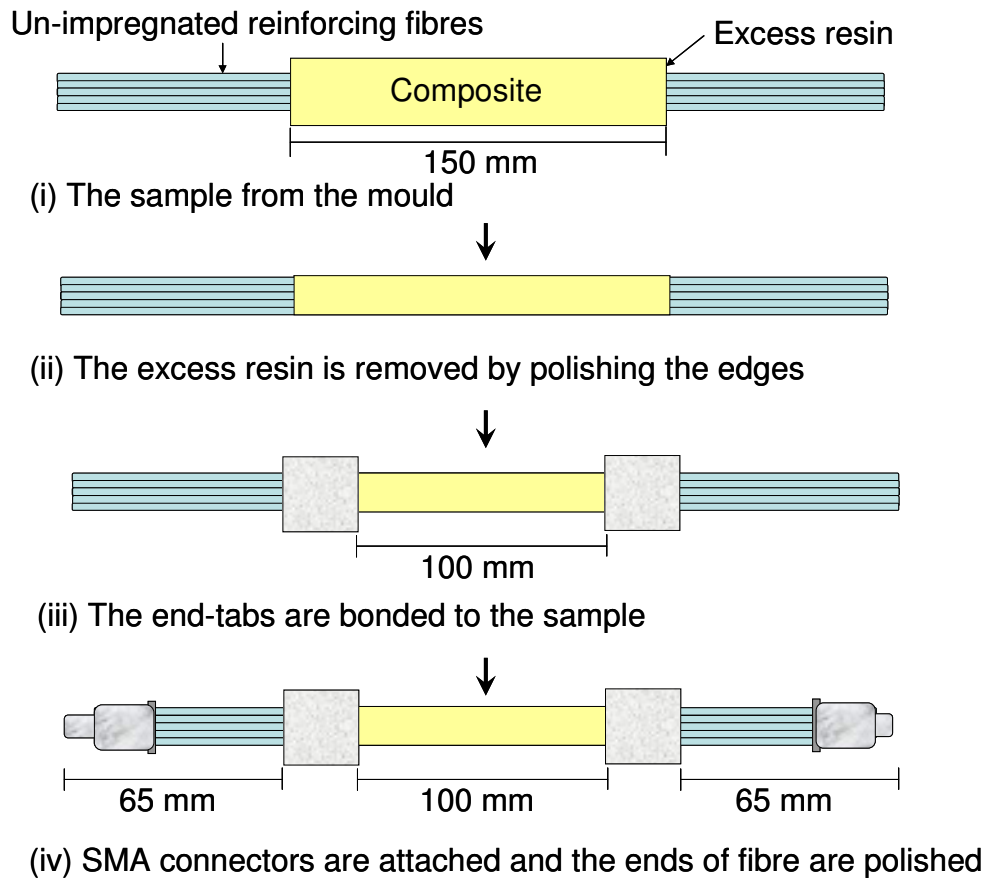
Figure 3.10 Flow-diagram for the attachment of SMA connectors and end-tabbing the self-sensing composites: (i) As-manufactured specimen; (ii) The excess resin is removed; (iii) The specimen is end-tabbed; and (iv) SMA connectors are attached, and the sample is now ready for tensile testing.

Termination of the un-impregnated section of the fibre bundle: With reference to Figure 3.10, the self-sensing composites had un-impregnated reinforcing fibres protruding from the composite. These were required to facilitate bending and directing the fibres from the jaws of the mechanical test machine. SMA connectors were attached to these ends in a similar manner to that used for the fibre bundle as described in Section 3.2.2.5. The composite with the SMA connectors and end-tabs were transferred to an automatic polishing unit and the SMA connectors were polished as detailed in Section 3.2.2.6. A schematic illustration with dimensions and a photograph of an end-tabbed composite

sample with a pair of SMA connectors are presented in Figure 3.11 and Figure 3.12, respectively.
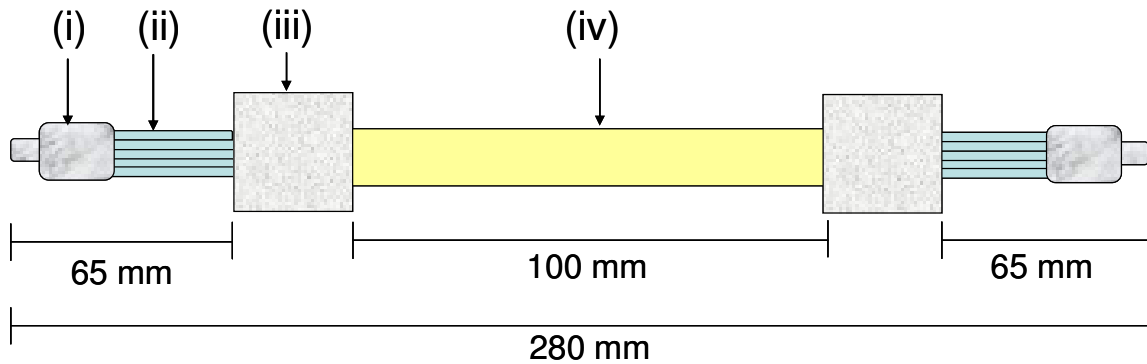
Figure 3.11 Schematic illustration of a composite sample with SMA connectors and end-tabs: (i) SMA connector; (ii) Un-impregnated section of the E-glass fibre bundle; (iii) End-tab; and (iv) Void-free composite.
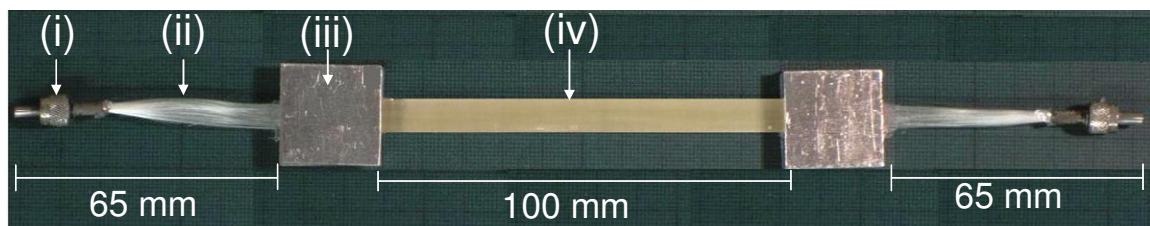
Figure 3.12 Photograph of an E-glass composite sample with SMA connectors and end-tabs: (i) SMA connector; (ii) Un-impregnated section of the E-glass fibre bundle; (iii) End-tab; and (iv) Void-free composite.

3.3 Equipment and Instrumentation

3.3.1 Tensile testing

Tensile testing was performed using an Instron model-5566 mechanical test machine. The time, extension and load were recorded using a data acquisition system and proprietary software. The machine was instrumented with a 10 kN load-cell. The Instron model-5566 has a load accuracy of +/-0.5% of the indicated load. It is worth mentioning that before testing each batch of specimens the load-cell was calibrated using a 20 N standard load.

All the tests were carried out at a cross-head speed of 1 mm/minute at 20 ℃ in a temperature regulated laboratory (1 ± ℃).

3.3.1.1   Tensile testing of neat-resin samples

The neat-resin samples were always placed into the upper tensile machine grip first and then the lower one. The grips were tightened and then the load-cell was adjusted to read between 0 and 1 N. This was necessary to remove any initial load before the start of the test. The extension was also reset to zero. The tensile test samples were tested to failure.

3.3.1.2   Tensile testing of fibre bundles

The method to setup the tensile test for the fibre samples was the same as that used for the neat-resin samples. The outer surface of the end-tabs was roughened using 800 grit abrasive-paper and the sample was clamped in the upper grip and then the lower one. The major difference in this instance was monitoring the changes in transmitted light intensity during tensile loading. A test fixture was designed and manufactured to facilitate the monitoring of the light intensity as described in Section 3.3.1.4. This fixture accommodated the attachment platforms for the high-speed camera and the light source. A schematic illustration of the experimental set-up for a self-sensing tensile test specimen is shown in Figure 3.13. The test specimen was clamped between the grips of the Instron machine and the SMA connectors for the light source and high-speed camera were attached to their respective attachments on the test fixture as illustrated in Figure 3.14. Two piezoelectric transducers were also attached to the specimen to monitor acoustic emission signals during tensile loading. These were held in place using a laboratory retort stand. A high-speed camera was used to image the fibre bundle at the stationery end; therefore, there was no physical movement of the SMA connector attached to the fibre

bundle at that location. The load, time and extension data were recorded. The tensile test was terminated when there was no further increase in the applied load.
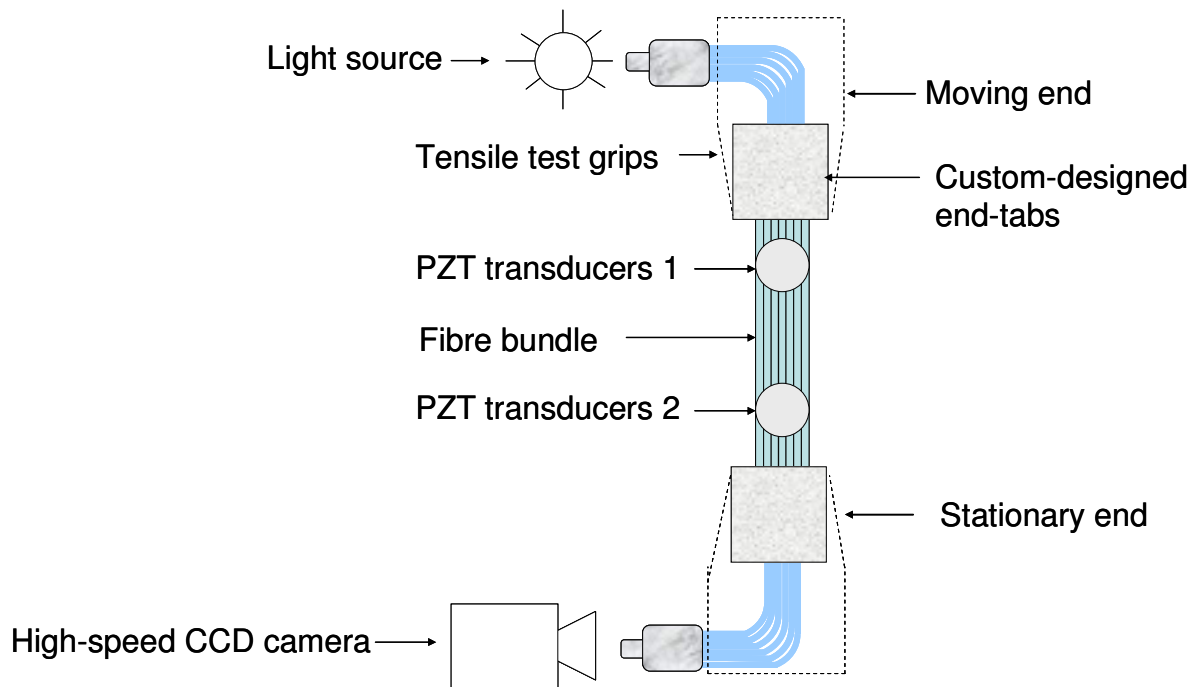
Figure 3.13 Schematic illustration of the experimental setup for *in-situ* tensile testing of fibre bundles.

3.3.1.3 Tensile testing of self-sensing composites

The tensile testing procedures for the self-sensing composite samples were exactly the same as that of the fibre bundle samples (Section 3.3.1.2). The samples were loaded into the tensile test machine and the top and bottom SMA connectors were attached to the light source and the high-speed camera attachments respectively. The test was carried out until the composite sample fractured and the applied load returned to zero.

3.3.1.4 Experimental setup for *in-situ* monitoring during tensile loading

The experimental setup for *in-situ* monitoring of the self-sensing composites during tensile loading is explained as follows.

Figure 3.14 shows a schematic illustration of the tensile test setup and the associated fixtures. A rig was designed, manufactured and attached to the Instron (model-5566) tensile test machine as shown in Figure 3.14a. This rig hosts the attachment for the SMA connectors (camera-end and light source end) and a platform to secure the laser light source. With reference to Figure 3.14, the SMA female adaptors were mounted at position 'b' for the camera-end. This ensured that there was no movement at the camera-end of the SMA connector. For safety reasons, the laser source was mounted on a platform at position 'c'. The acoustic emission piezoelectric transducers were positioned and secured in place using a laboratory retort stand as illustrated in Figure 3.14d. Two PZT transducers were attached to the specimen at positions 'e' and 'f' as shown in Figure 3.14e. The other key components of the tensile test setup are indicated in the figure caption. A photograph of the fixture and magnified views of the different components are also shown in Figure 3.15. One of the major advantages for this detachable rig was that it could be removed after the tests were completed so that other users could use the machine at their convenience.
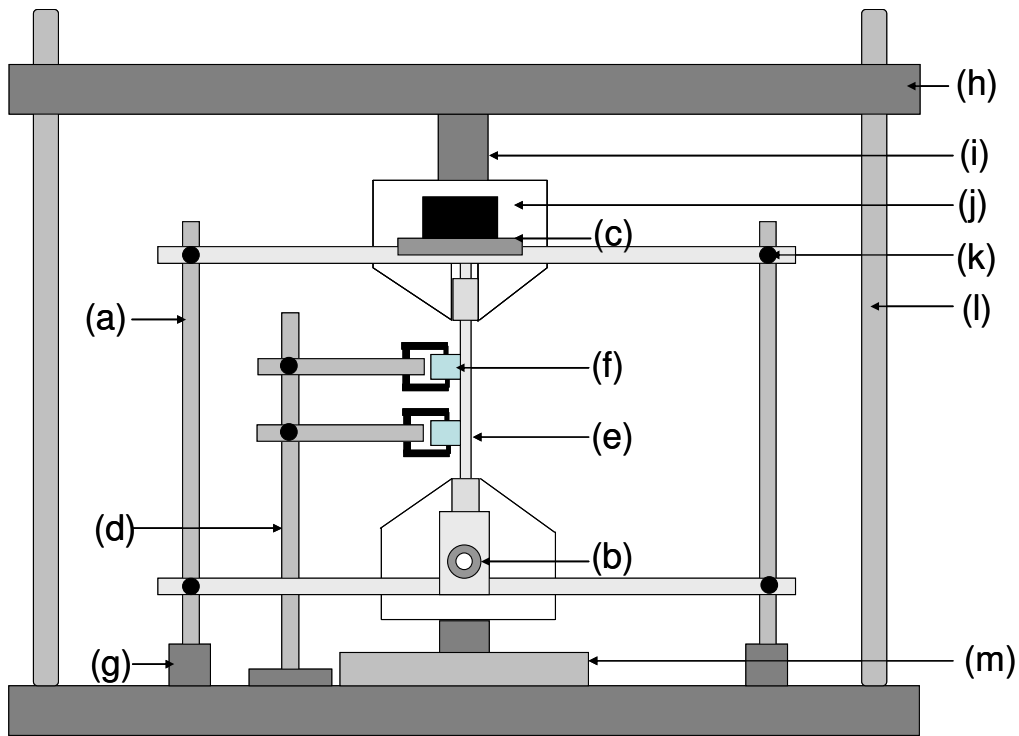
Figure 3.14 Schematic illustration for the tensile test experimental setup: (a) Tensile test rig; (b) Attachment for the SMA connector (camera-end); (c) Platform for the light source; (d) Laboratory retort stand for holding the piezoelectric transducers; (e) Tensile test specimen; (f) PZT transducer held in place using the metal stand; (g) Detachable base for the tensile testing fixture; (h) Moving end of the Instron tensile test machine; (i) Load-cell; (j) Laser light source (not visible); (k) Height adjustment mechanism for the tensile test fixture; (l) Instron machine columns; and (m) Base of the Instron machine (stationary end).
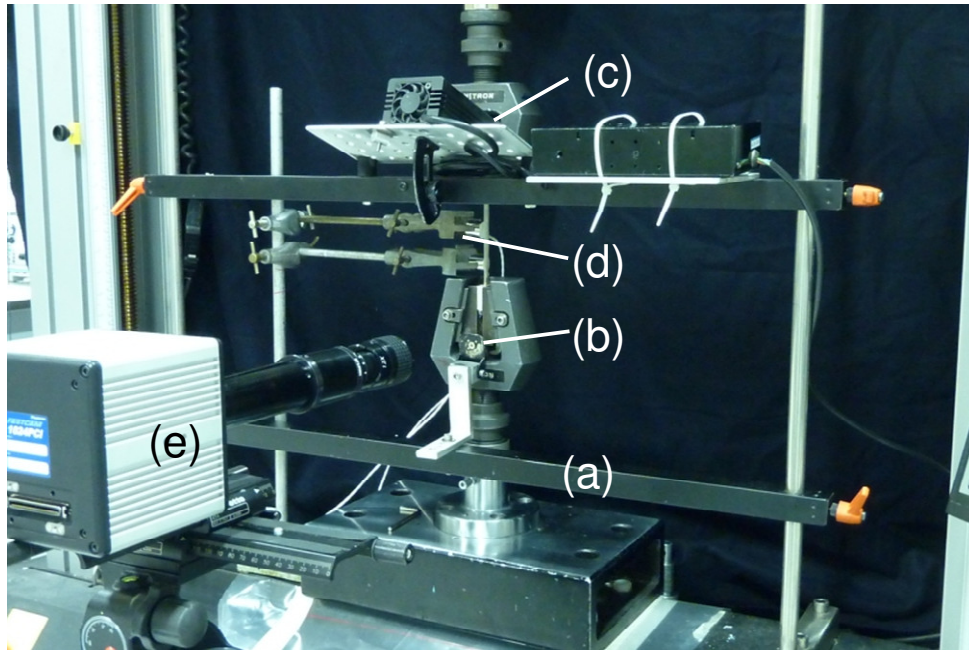
Figure 3.15(i) Photograph of the tensile test setup: (a) Tensile test fixture; (b) Attachment for the SMA connector (camera-end); (c) Attachment for the laser-light source; (d) PZT transducers secured in place using a laboratory retort stand; and (e) High-speed camera.

Magnified view of item (c)   Magnified view of item (b)
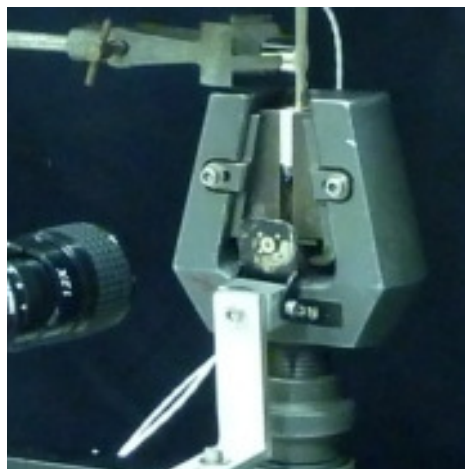
Figure 3.15(ii) Magnified view of selected key items.

3.3.2 Electrical resistance strain gauges

A Cambridge Electronic Systems DMM4 electric strain gauge amplifier was used to record changes in strain during mechanical loading. The strain gauge had the ability to operate up to + / - 20 000 micro-strain.

During the tensile test, the strain was recorded using two methods. In the first method at a set load, the value was recorded manually by reading it off the strain gauge amplifier display. In the second approach, the strain was also recorded via the acoustic emission interrogation system. This was achieved by inputting the strain signals into the AE system's (Physical Acoustics, UK) parametric channel.

3.4 Acoustic Emission Monitoring

Two conventional piezoelectric acoustic emission transducers were used during the tensile testing of the neat resin, fibre bundles and the self-sensing composites. The AE transducers used in the study were two identical narrowband R15 sensors supplied by the Physical Acoustics Corporation. The transducers were attached to the tensile test specimens using silicon gel (494-118, RS, UK). A laboratory retort stand with a clamp was used to take the weight of the transducers and secure them during the tests.
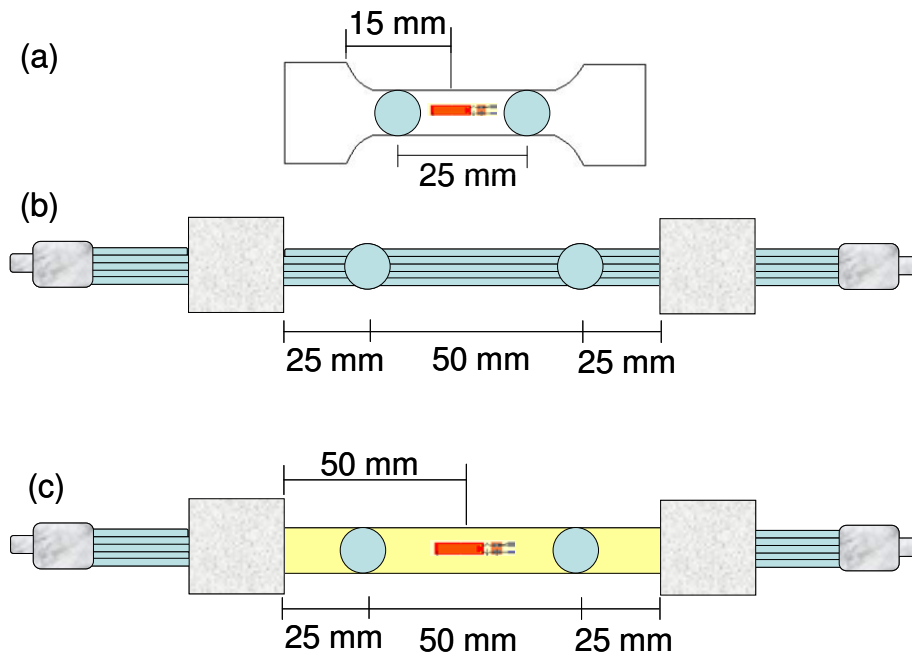
Figure 3.16 Schematic illustration indicating the experimental setup and the relative positions of the piezoelectric transducers and strain gauges for: (a) Neat resins; (b) Fibre bundles; and (c) Composite material.

Figure 3.16 'a', 'b' and 'c' show schematic illustrations indicating the relative positions of the piezoelectric transducer (and strain gauges) on the three types of test specimens used in this study.

The piezoelectric transducer were connected to a pre-amplifier (model, 2/4/6) and integrated to a data acquisition unit (PCI-2, Physical Acoustics, UK). Prior to tensile testing, the response of the piezoelectric transducer was assessed by performing a pencil lead-break. This simple test involved fracturing a 0.2 mm pencil lead (2B) at approximately 5 mm on the lower end-tab. The amplitude of this signal was recorded. A threshold setting of 40 dB was used for all the tensile tests. A photograph of the experimental setup involving a small-diameter optical fibre bundle tensile test specimen is shown in Figure 3.17; the key components are indicated.
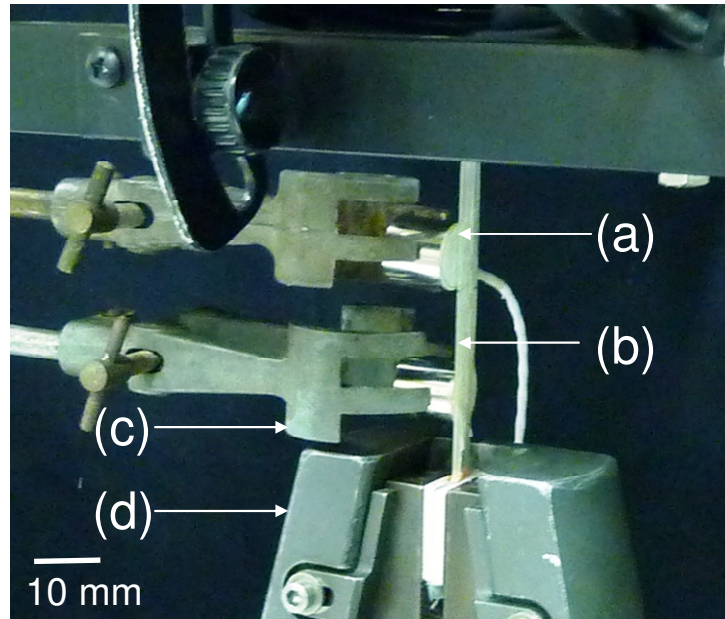
Figure 3.17 Photograph indicating the acoustic emission transducers coupled to the test specimen: (a) PZT transducers; (b) Tensile test specimen; (c) Clamps for the PZT transducers; and (d) Instron grips.

3.5   High-speed Charge-coupled Device Camera

A detailed study was undertaken prior to selecting and purchasing a FastCAM 1024 PCI (Photron, UK) high-speed charge-coupled device camera. The selection criteria that were used to rank the different cameras are presented in Table 3.4. A further discussion on this topic is presented in Section 4.1.6.4.

Table 3.4 Selection criteria for the high-speed camera.

Frame rate	60~250 frames per second
Colour/Monochrome	Monochrome
Size of sample to be viewed	1.4~2.0 mm diameter fibre bundle
Resolution	1024 x 1024 pixels
Recording time	150 seconds
Adaptors	C-mount adaptors

In the current study, the high-speed camera was used to image the ends of the polished SMA connectors during tensile loading of the test specimens. Hence, it was necessary to develop protocols to synchronise the various items of equipment such as the mechanical test machine, the acoustic emission transducers and the high-speed camera.

3.6   Synchronisation of Equipment

With reference to Table 3.4, a limitation was the recording time available on the high-speed camera. In addition, in order to keep the volume of data to a manageable limit, it was necessary to synchronise the high-speed camera to the fracture of the reinforcing fibre light guides.

In the current study, the initial signal from the acoustic emission sensor was used to trigger the high-speed camera. In other words, when the acoustic emission transducer detected an acoustic event during the tensile loading of the test specimens, this signal was used to activate the recording of the high-speed camera. This was achieved using the transistor-transistor logic (TTL) input of the high-speed camera. The TTL refers to the specific condition for electronic circuits i.e. when the defined 'AND' situation is met, the transistor switch either closes or opens the circuit. For the TTL input of the high-speed CCD camera whenever there was a current of 5 mA and the electric signal had a duration of 5 milli-seconds, the TTL conditions were met and the high-speed camera was triggered. These conditions were met by the acoustic emission alarm output signal that is explained as follows.

The acoustic emission system was a two channel system supplied by Physical Acoustics UK. It had an alarm output that had a "driving" current of 5 mA. This option provides an output whenever there is an AE event and the electric signal could last up to 50 milli-

seconds. After testing the signal on a conventional voltmeter, the alarm output was connected to the TTL input of the high-speed camera. The two integrated systems worked in the following sequence: The PZT sensors were attached to the tensile test specimen. The tensile test machine and the AE system were started simultaneously. When the first AE hit was detected by the PZT transducers, the alarm output generated an electric signal. This electric signal then triggered the high-speed camera through the TTL input switch and the recording was commenced.

With reference to the mechanical test machine, the in-built data acquisition card on the Instron (model-5566) was used to log the time, load and position of the cross-head during tensile loading. The load and the strain data from the Instron's data acquisition card were transferred to the data acquisition system on the piezoelectric acoustic emission system. The AE system provided the option for two parametric inputs; this was used to record input (±10 V) voltage through the parametric channels. The output voltage from the Instron data acquisition card was used as an input to the AE parametric channels. In this way, the load and extension were recorded with AE events. Figure 3.18 shows a schematic illustration of the mechanical testing and associated equipment for conducting the tensile tests.

| Tensile test machine Model 5566, (Instron Inc. UK) | AE data acquisition system (Physical Acoustics Limited, UK) | High-speed camera FastCAM 1024 PCI, (Photron, UK) |
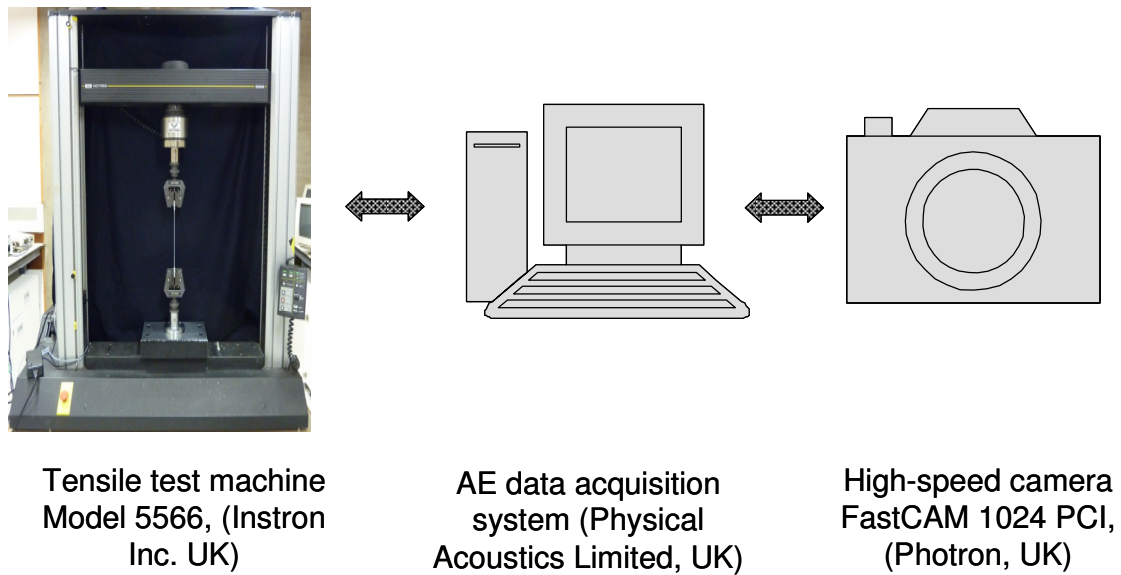
Figure 3.18 Schematic illustration of the integration and synchronisation of the mechanical test machine with the high-speed camera and the AE data acquisition system.

3.7 Image Analysis

Image analysis was a key component of the current work as it was necessary to record and to extract information from images of polished SMA connectors during tensile loading. As described in Section 3.2.1.3, significant time and effort was dedicated to obtain optical-quality polished end-faces of the fibre that were potted in the SMA connectors. It was also necessary to develop the methodologies: (i) to secure the polished SMA connector to be held steady at the same time; and (ii) to enable coupling of light to one end of the test-specimen whilst the other end was imaged using the high-speed camera.

The aim was to track the change in light intensity of the individual fibre then to relate it with other sources of information, namely acoustic emission and mechanical loading. The images taken by the high-speed camera ranged from 7000-8000 per test. Hence performing the image analysis manually was nearly impossible in view of the fact that for every batch, normally more than 10 individual samples were tested and analysed. Therefore, software

routines were investigated to enable image processing and analysis. In the first instance, custom-made small-diameter optical fibres were used to develop the image analysis routines. The following software packages were analysed to establish their suitability for analysing the images that were captured by the high-speed camera during the tensile loading of the test specimens; (i) National Instruments Vision Assistant 8.0, (ii) SExtractor astronomical software, and (iii) Matlab 8.0.

The key attributes and capabilities of each of the software packages are presented below.

3.7.1 National instruments vision assistant

The National Instruments Vision Assistant is an image analysis package that is primarily used for analysing images on an assembly line. A software routine was developed that could identify each fibre with the given template and then analyse the fibre for any light attenuation for all of the images. The software is capable of generating analysis files for each image. The routines provide reliable results but the requirement for analysing each of the resulting files is tedious and requires different software such as Matlab or a programming language such as C++, etc.

3.7.2 SExtractor astronomical analysis software

SExtractor is a program that builds a catalogue of objects from an astronomical image. It can identify different objects with high contrast and then report their properties such as orientation, light intensity, etc. This software is used by astronomers to study the relative position of galaxies and stars. The only limitation is that it can only accept images in 'Flexible Image Transport System' (FITS) format. This is the file format used in astronomy. Therefore, the conversion of all the files into this particular format was mandatory. This conversion is tedious and can cause a loss of information. Therefore, this

image analysis software was found to be inappropriate for the current project and was rejected.

3.7.3   Matlab image analysis tool box

Matlab was used successfully for the current work to analyse the images taken by the high-speed camera and to relate them to other sources of information. A macro was developed that read the first image and identified each fibre as an individual entity; the centroidal position of each fibre was specified using x-axis and y-axis coordinates. For the remainder of the images obtained during tensile loading, the light intensity of each fibre was calculated using the same coordinate positions.

3.8   Effect of Sealant on Light transmission Characteristics of E-glass Fibres

With reference to the fabrication of self-sensing fibre bundles and composites (Section 3.2.3), RTV-3140 silicone sealant (Dow Corning, UK) was used to seal the fibres at different stages of fabrication. This silicone sealant was selected because its refractive index (1.43) is lower than that of the E-glass fibres. The effect of the sealant on the light transmission characteristics of the fibre bundles was studied. Samples were prepared from water-sized E-glass fibres as per the procedure described in Section 3.2.2.4. The length of the fibre bundle was fixed at 100 mm.
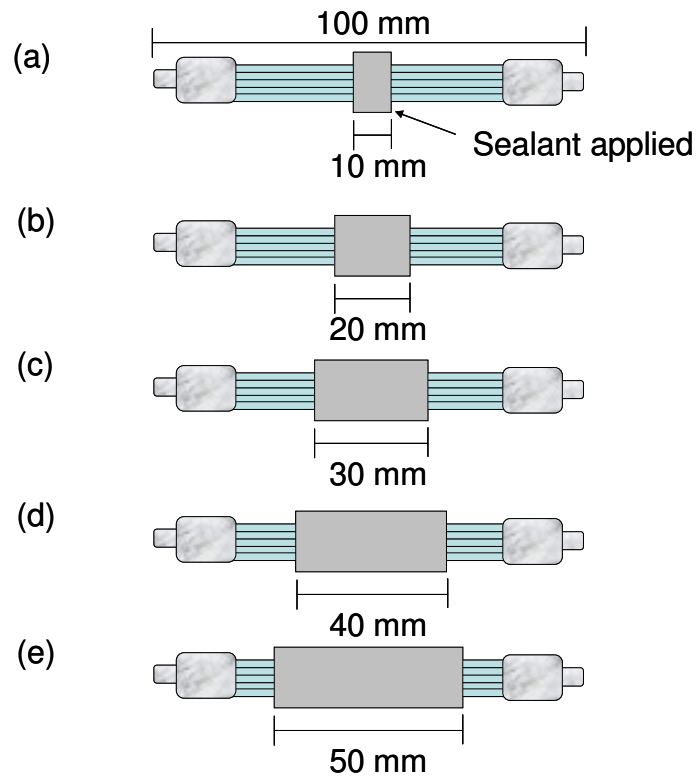
Figure 3.19 Schematic illustration of the experiment that was carried out to investigate the effect of the sealant on light transmission: (a-e) The area of the section of E-glass fibres that was impregnated with the silicone resin is indicated in (a-e).

Figure 3.19 (a-e) gives a schematic illustration of the sample preparation methodology. With reference to Figure 3.19 (a-e), sealant was initially applied on a 10 mm length of the fibre section and left to cure for 24 hours at room temperature. A white-light source (Intralux-4000, Warner Instruments, USA) was attached to one of the SMA connectors and the transmitted light was measured via the other SMA connector using a photosensitive detector (PM100, Thorlabs, UK) before and after the sealant was applied. In the next set of experiments, the sealant application length was increased in steps of 10 mm until a total of 50 mm of fibres were coated with the sealant as shown in the Figure 3.19 (a-e). Light transmission was measured at each step using the photosensitive detector.

3.9   Fibre Volume Fraction

The fibre volume fraction for composite samples was determined by imaging the cross-section of the composite under a microscope and then analysing the recorded images. The composites were manufactured in a similar manner to that described in Section 3.2.3. However, in this instance the SMA connectors or end-tabs were not attached. The samples were then cut using a diamond wheel cutter (Dremel, UK) to approximately 20 mm long sections. The specimens were mounted in the resin mounting containers supplied by Struers, UK (Flexi-form rubber cups, Cat No: 40300086). The specimens were held vertically in the epoxy resin Epofix (Struers, UK) using the holding clips supplied by MetPrep, UK (Cat No: 113043). The required masses of the Epofix resin and the hardener (stoichiometric ratio 25:3) were mixed thoroughly in an aluminium container and degassed in a vacuum chamber at -15 mm of Hg for 20 minutes. The mixed and degassed resin was then dispensed gently into the sample mounting cups. The resin was cured for 24 hours at ambient temperature. The samples were removed from the mounting cups and polished on an automatic polisher using the following sequence:

i.   grinding using 1200 grit abrasive-paper for 3 minutes;

ii.   grinding using 2400 grit abrasive-paper for 5 minutes;

iii.   polishing with a 6 µm diamond powder suspension for 20 minutes;

iv.   polishing with a 3 µm diamond powder suspension for 25 minutes; and

v.   polishing with a 1 µm diamond powder suspension for 35 minutes.

An optical microscope with a CCD camera (Leica, Germany) was used to take images at 20X magnification. The micrographs were analysed using KS 4.0 software. The analysis involved background correction, selecting optimal threshold and then calculating the fibre

volume fraction. The high contrast between fibres and matrix helped to subtract the background and identify each fibre. The area fraction of the fibres was calculated to measure the fibre volume fraction of the composite.

4 Results and Discussion

This results and discussion chapter is divided into four sections. Firstly, the quality of the test specimens and their assessment is discussed. Secondly, the results obtained during mechanical testing and acoustic emission monitoring of neat resins are presented. The third and fourth sections present the results and discussion of the fibre bundles and self-sensing composites, respectively. They include the mechanical testing, acoustic emission monitoring and the image analysis of the images captured by the high-speed camera.

4.1 Quality of the Samples and Assessment Procedures

This section consists of five main headings. Firstly, the light transmission characteristics of the as-received E-glass fibres and small-diameter optical fibres (SDOF) are discussed. Secondly, the development of optimum procedures for coupling light into the E-glass and SDOF during mechanical loading is presented. Thirdly, the effects of different parameters on light transmission through E-glass fibres and the development of optimum polishing procedures for the E-glass fibre bundles are discussed. Finally, a discussion on the quality of the self-sensing composites and fibre volume fraction is presented.

4.1.1 As-received fibres

4.1.1.1 E-glass fibres

Representative SEM micrographs of the as-received E-glass fibres are presented in Figure 4.1 (a-d). With reference to the Figure 4.1 (a-d), it can be seen that the surface of the as-received E-glass fibres are relatively free from surface contamination and debris. As mentioned in Chapter 3 these fibres were custom-drawn by PPG Industries (UK) without

the use of a conventional binding agent. Water was used as the processing aid. A few "surface" blemishes were observed on the surfaces of the as-received E-glass fibres, but these were not a frequent occurrence. The as-supplied water-sized E-glass fibres were mounted on a stand as shown in Figure 4.2a and it was kept covered when not in use. Due care and attention was given to ensure that the fibres were not damaged during extraction of the fibre bundle from the creel and during subsequent handling. The water-sized fibres were necessary for the following reasons:
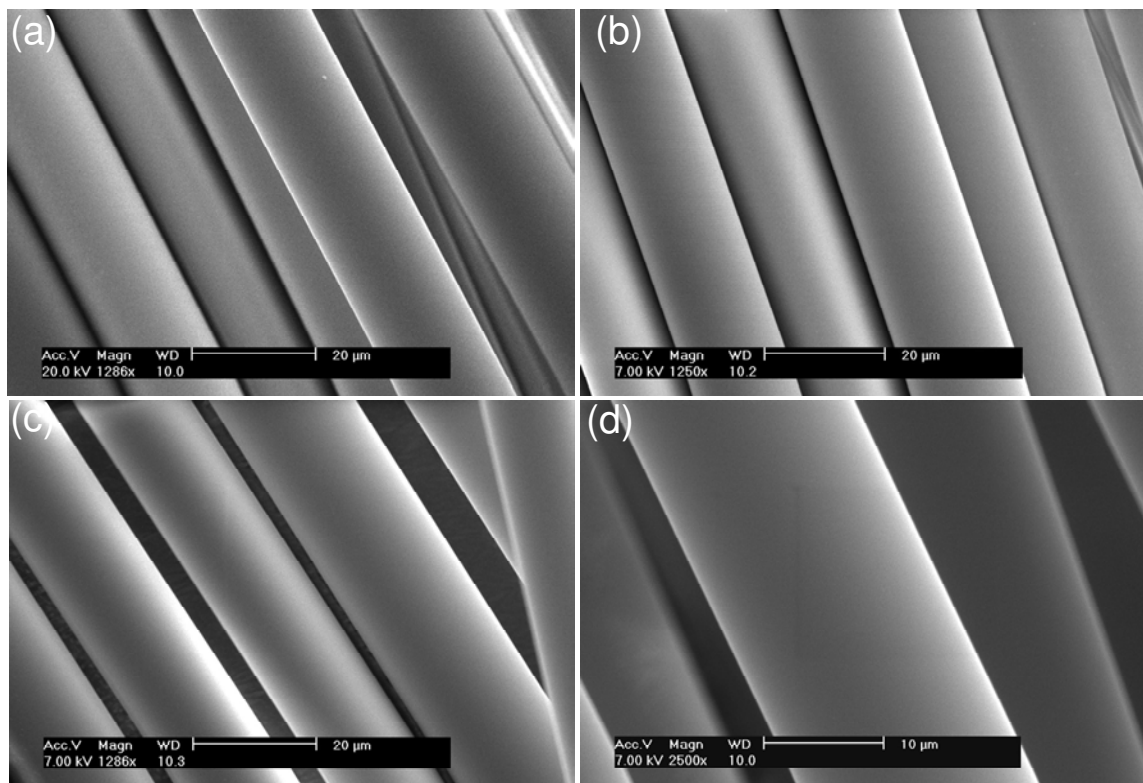
Figure 4.1 (a-c) SEM images of as-received E-glass fibres for different samples; and (d) Magnified view of (c).

The binder system on conventional E-glass fibres is proprietary information. However it may consist of lubricants, processing aids, anti-static agents and coupling agents. The 'clean' E-glass fibres were required for a parallel part of the project. This part was related to cure monitoring using evanescent wave spectroscopy (carried out by Dr Liwei Wang). Therefore, the as-received water-sized E-glass fibres were also used in the current study.

114
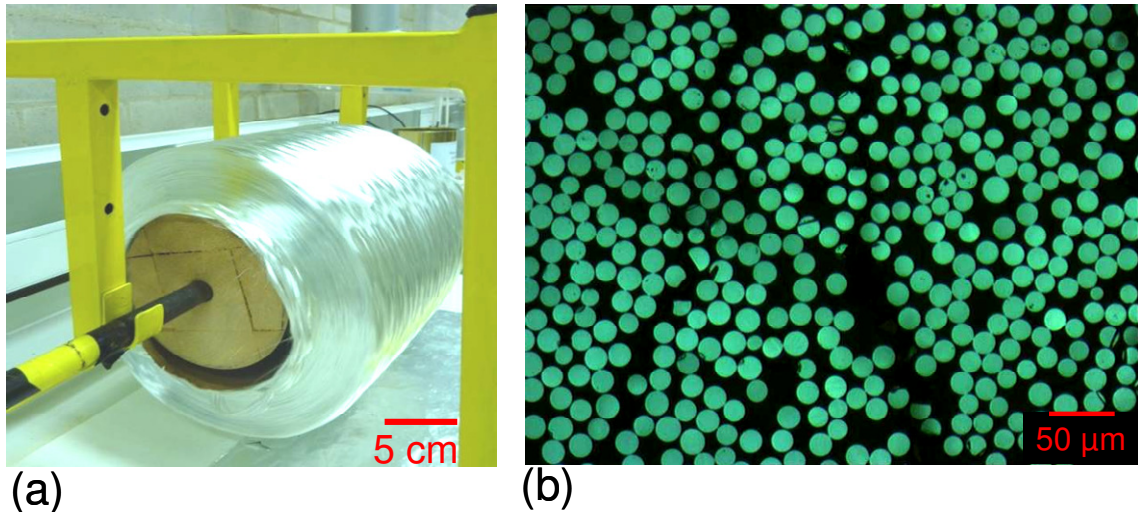
Figure 4.2 (a) Photograph of the as-received E-glass fibre creel mounted on a stand; and (b) Example of a polished transverse section of an as-received E-glass fibre bundle.

Since the self-sensing composite concept developed in the current study relied on the fracture of individual filaments, the following section presents a discussion on issues that could complicate the analysis of results presented in Sections 4.3 and 4.5 (acoustic emission monitoring and image analysis of fibre bundles and composites, respectively).

(i) Fibre diameter variation: With reference to Figure 4.2b it can be observed that the diameters of the fibres were in the range 12-17 µm. Since a large volume of cross-sectional images were taken to assess the quality of the composite specimens, a random sample of these images were analysed in terms of the fibre diameters. In the case of the E-glass fibre bundle, this diameter variation was investigated by other researchers in the Author's group [179]. Table 4.1 presents a summary of the distribution of fibre diameter. With reference to Table 4.1, the term "frame" refers to the micrograph, from which the distribution in the fibre diameter was determined. At a magnification of 20x, there were approximately 120 fibres per frame. This brief study indicated that the diameter of the water-sized fibres were in the range of 12-17 µm with majority of fibres (85%) being in the range 12-16 µm. The

average found for the five samples analysed was 15.8 µm with a standard deviation of 1.7 [179].

Table 4.1 Diameter distribution of the as-received E-glass fibres.

Frame	Total number of fibres in the frame	Diameter range of E-glass fibres		
		12 µm	15 µm	17 µm
1	60	28	26	6
2	57	20	28	9
3	89	31	46	12
4	110	55	40	15
5	59	31	21	7

(ii) Broken fibres: A point to note here is that the focus of the study was to detect fibre damage and also to interpret the fracture of these fibres. Therefore, a simple experiment was designed to estimate the number of broken fibres in a section of the as-received E-glass fibres. This was carried out by illuminating a cleaved (using a razor blade) section of the as-received E-glass bundle. A white-light source was used to illuminate the cleaved-end of the bundle that was secured in a heat-shrink tubing. The numbers of broken fibres were counted manually; light-bleeding from the location of the fractured sites was readily apparent. The length of the bundle was 28 cm; this was the length of the tensile test specimen. Table 4.2 shows a summary of the estimated number of fractured fibres in the E-glass bundle. With reference to the Table 4.2 , the number of broken fibres depends on the handling procedures both during removal from the fibre creel and during the sample preparation. As mentioned previously, the water-sized fibre bundle consisted of approximately 2400 individual filaments. The approximate number of fractured fibres is in

the range 2-5%. This could have an effect, when the mechanical properties of the fibre bundles are evaluated. Due care and attention was given to protect the fibres during the multi-stage specimen preparation process, however, the fracture of a few individual filaments during sample preparation cannot be ruled-out completely. The analysis presented in Sections 4.3 and 4.4 is based on detecting the number of intact fibres at the start of mechanical loading. Secondly, since all the fibre bundles underwent the same procedural steps, it can be assumed that the number of fractured filaments in each bundle was similar. Therefore, the effects of fibre fracture (during sample preparation) can be assumed to be negligible [180].

Table 4.2 Summary of the estimated number of fractured fibres in a sample of as-received E-glass fibres bundles.

Bundle number	Number of fractured fibres
1	52
2	60
3	76
4	49
5	55
6	73
7	82
8	65
9	56
10	63

4.1.1.2   Small-diameter optical fibres

As mentioned previously, the custom-made small-diameter optical fibres (SDOF) were used to develop the methodology and the software routines to analyse the images captured by the high-speed camera. Typical SEM micrographs for the as-received SDOF are shown in Figure 4.3(a-d).
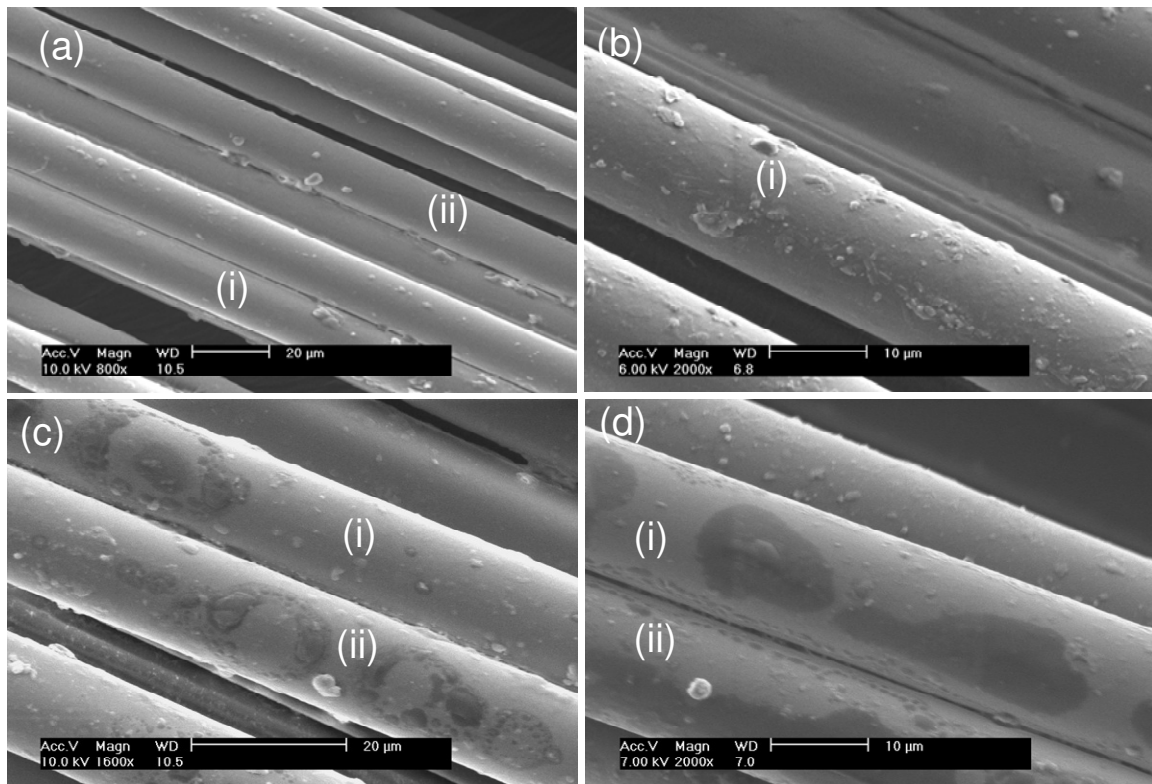
Figure 4.3 (a-d) SEM micrographs showing the surface of the as-received SDOF [181].

In contrast to the as-received E-glass fibres, the surface of the SDOF is seen to be covered in a coating of uneven consistency as shown in Figure 4.3 (a-d). After prolonged discussion with the supplier and an in-house investigation [183], it was established that the coating was predominately organic in nature.

In Figure 4.3 (a-d) three common types of features were observed to be present on the as-received SDOF.

i. Irregular shaped surface debris; see Figure 4.3a: features marked (i) and (ii) where a magnified view is presented in Figure 4.3b (feature marked (i)). From here on the coding for the surface features on the individual fibres will be included in the figure number.

ii. "Blisters"; see Figure 4.3c (i) and (ii) a high magnification image is presented in Figure 4.3d (i). These blisters may be due to the entrapment and over coating of large debris or the evaporation of the solvent used in the coating process along with the delamination of the coating.

iii. Large particles (>1 µm diameter); (see Figure 4.3c (ii) and d (ii)) It is speculated that these particles may have been present in the coating-bath used by the supplier of the SDOF.

It is probable that the surface features that are apparent in Figure 4.3 (a-d) originated from the coating process of the optical fibres; the optical fibres were coated with processing aids and an unspecified "binder" immediately after they were drawn from the melt. A series of burn-off experiments were carried out at 400 ℃, 450 ℃, 500 ℃ and 600 ℃ to establish the optimum temperature to pyrolyse the organic coating on the SDOF.

Figure 4.4 to Figure 4.5 show representative SEM micrographs of the SDOF that were heat-treated at 400 ℃, 450 ℃, and 600 ℃ respectively. A summary of the pyrolysis temperatures investigated in this study is given in Table 4.3 along with the number of samples tested.
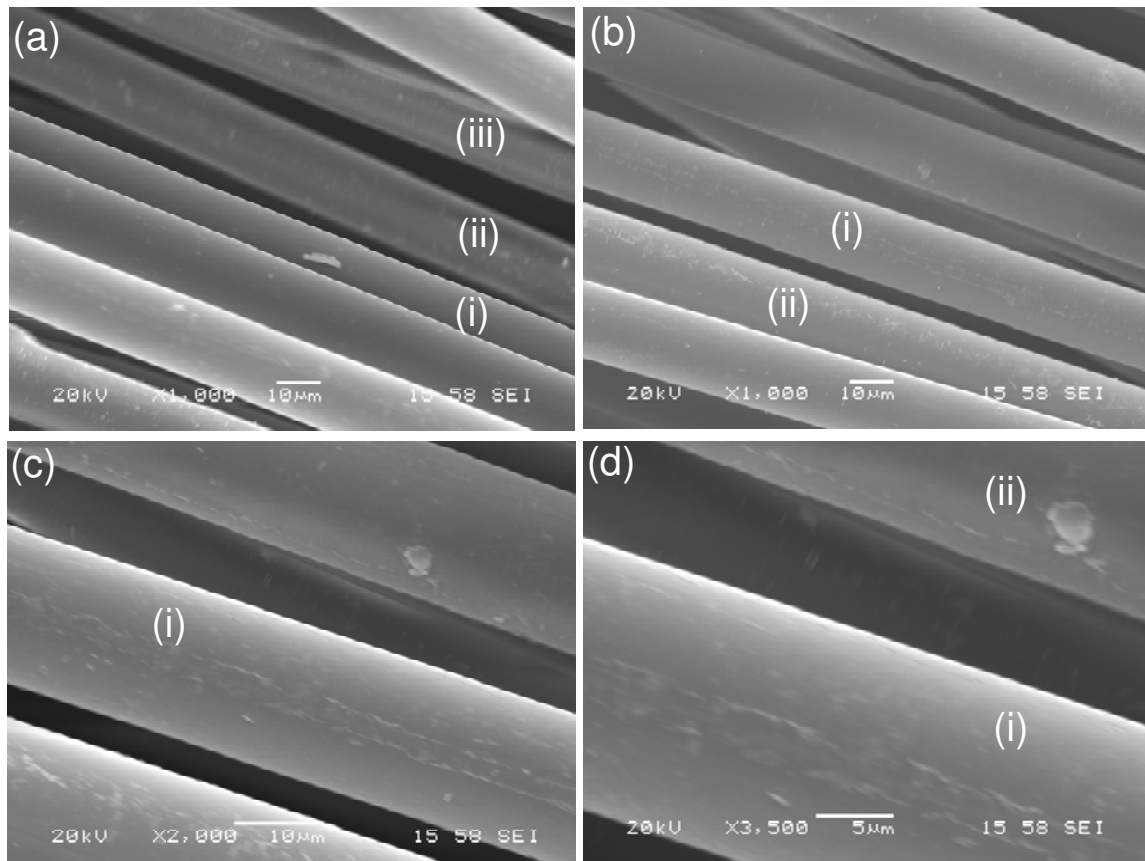
Figure 4.4 SEM micrographs showing the surface of the SDOF after subjecting them to 400 ºC for 4 hours.

On inspecting Figure 4.4 (a-d), it is clear that pyrolysis at 400 ºC for 4 hours was insufficient to oxidise the coating. With reference to Figure 4.4a, at a magnification of 1000X, the surface of the SDOF seems free from surface contamination when compared with Figure 4.3; this is also seen in Figure 4.4b(i and ii), however sporadic surface debris was observed. With reference to Figure 4.4b(ii), longitudinal "streaks" were observed on some of the fibres, (see Figure 4.3b(i)). Higher magnification images are given in Figure 4.4c(i) and Figure 4.4d(i). The origins of these streaks are not known but it was possible that the coating material had accumulated within interstitial spaces in the fibre bundle. The origin of the relatively larger debris seen in Figure 4.4d(i) is unknown; this was not a prominent feature.

Table 4.3 Summary of the pyrolysis temperatures used to oxidise the organic coating on the SDOF.

Pyrolysis temperature (ºC)	Pyrolysis time (hours)	Number of fibre bundles tested	Comments
400	4	3	Debris was still present, although larger particles were reduced in size.
400	6	3	
400	8	3	
450	4	3	Debris/streaks were present but comparatively less than the fibres heated at 400 ºC.
450	6	9	The fibres surfaces were more "shiny", cleaner and not as brittle as those heated above 450 °C.
500	4	6	As above but the fibres were significantly more brittle than those heated at 450 °C for 6 hours.
500	6	3	The post-heated fibres were brittle and some of the fibres fused together.
600	4	3	The fibres were fused to each other and were very brittle and fragile.

With reference to Table 4.3, the fibres that were subjected to a temperature in excess of 450 ºC exhibited the following characteristics:

i. Although the bulk of the surface debris was oxidised, some globular surface contamination was apparent.

ii. The fibres became progressively more brittle as the temperature was increased from 400 ºC.

iii. Above 600 ℃, the fibres were observed to fuse together as shown in Figure 4.5 (a-d) (i).

Figure 4.6 (a-d) illustrate the general surface appearance of the SDOF that were heat-treated at 450 ℃ for six hours. The images presented in Figure 4.6 (a-b) were taken at a magnification of 1000X and the fibres look relatively clean in comparison to the fibres heat-treated at 400 ℃. Images obtained at 2000X magnification show some particles retained on the surface as illustrated in Figure 4.6c. A magnified image of the fibre (i) in Figure 4.6c(i) is shown in Figure 4.6d(i). With reference to Figure 4.6d(i), the size of particles is lower than 1 µm in diameter. These particles were present in some of the samples and this may be partially oxidised contamination on the fibres. An attempt was made to remove all this debris by heating the fibres at 600 ℃ but these particles remained to a smaller extent in these samples as shown in Figure 4.5d. Additionally, at 600 ℃ the fibres start to deform and fuse to each other. This is shown in Figure 4.5 (a-d)(i). Therefore, considering all these factors and after many repeat experiments, it was decided that the fibres heated at 450 ℃ for six hours would be used for subsequent experiments.
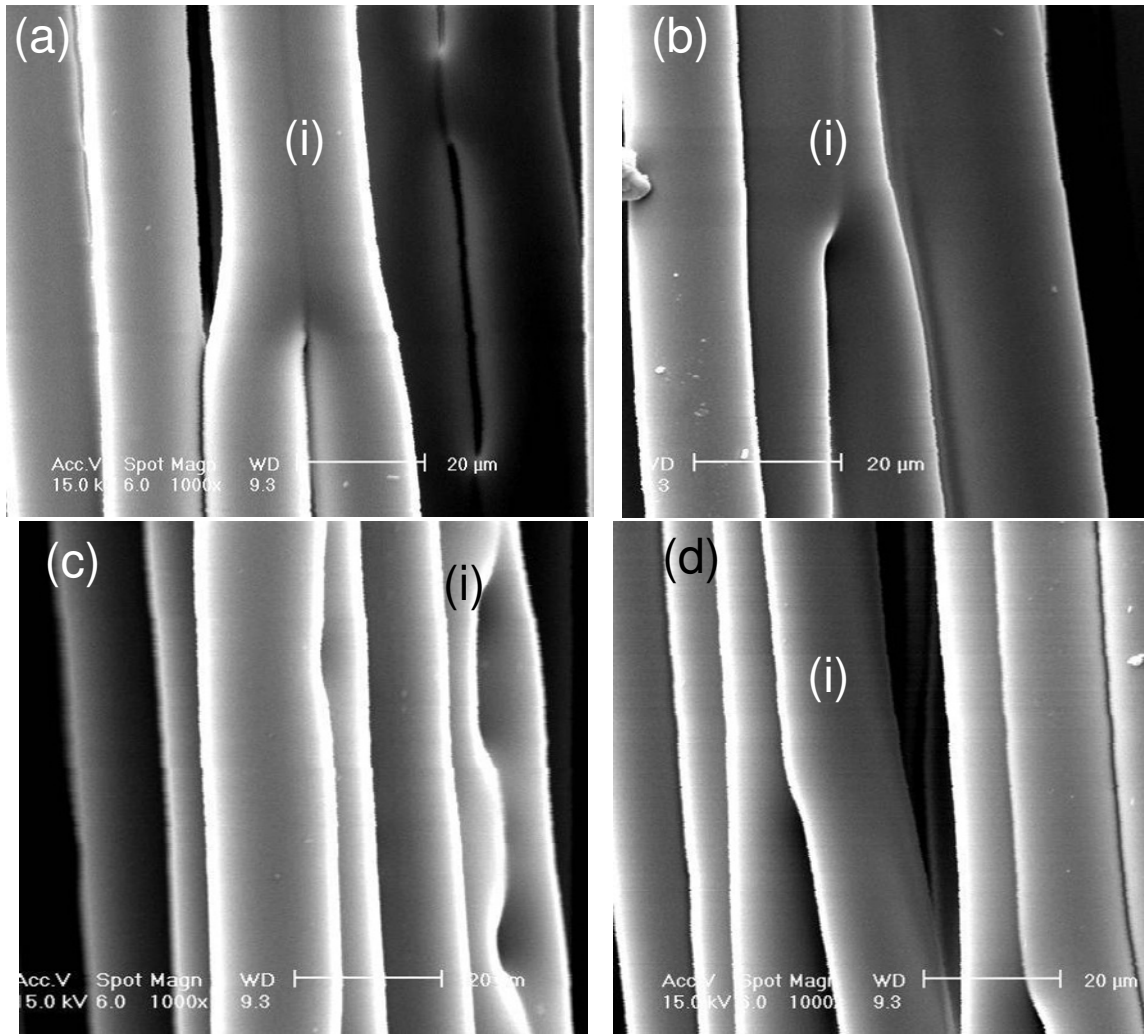
Figure 4.5 SEM micrographs showing the surface of the SDOF after subjecting them to
600 ℃ for 4 hours.
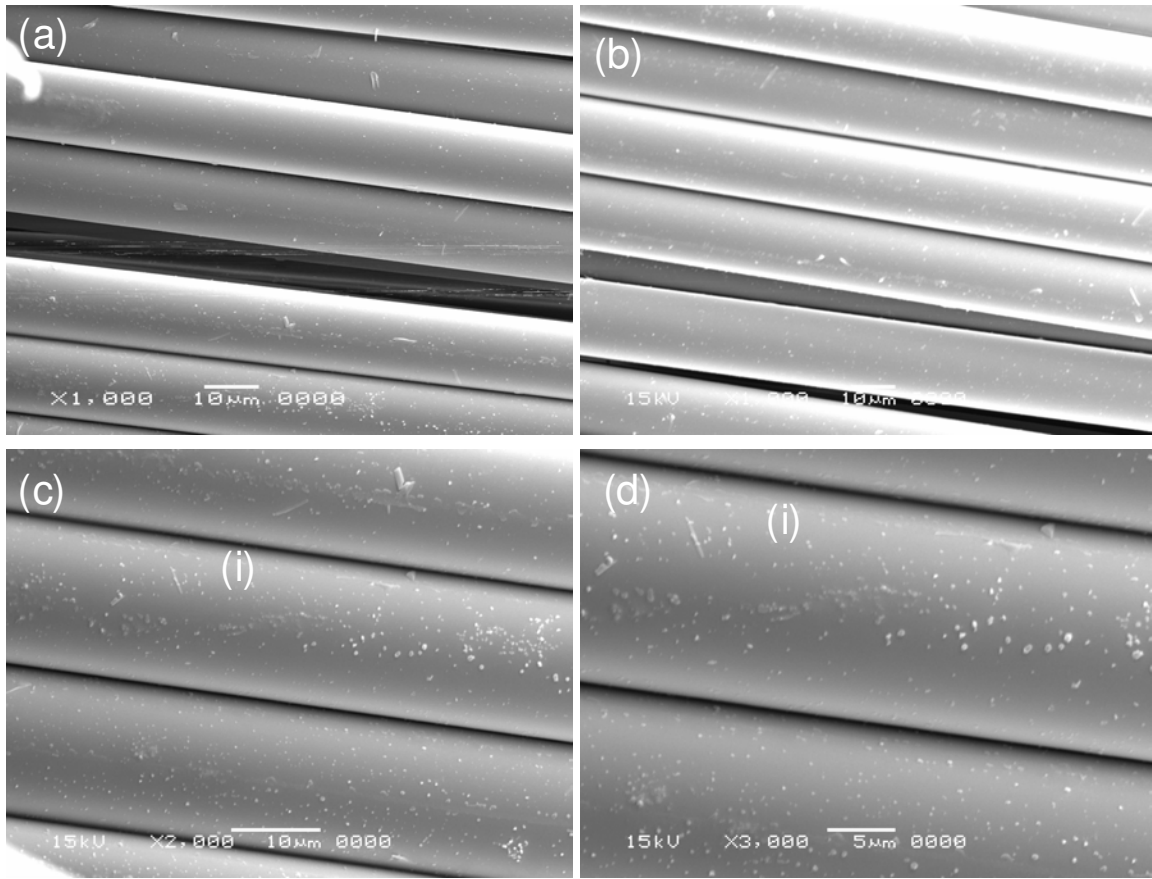
Figure 4.6 SEM micrographs showing the surface of the SDOF after subjecting them to 450 ºC for 6 hours.
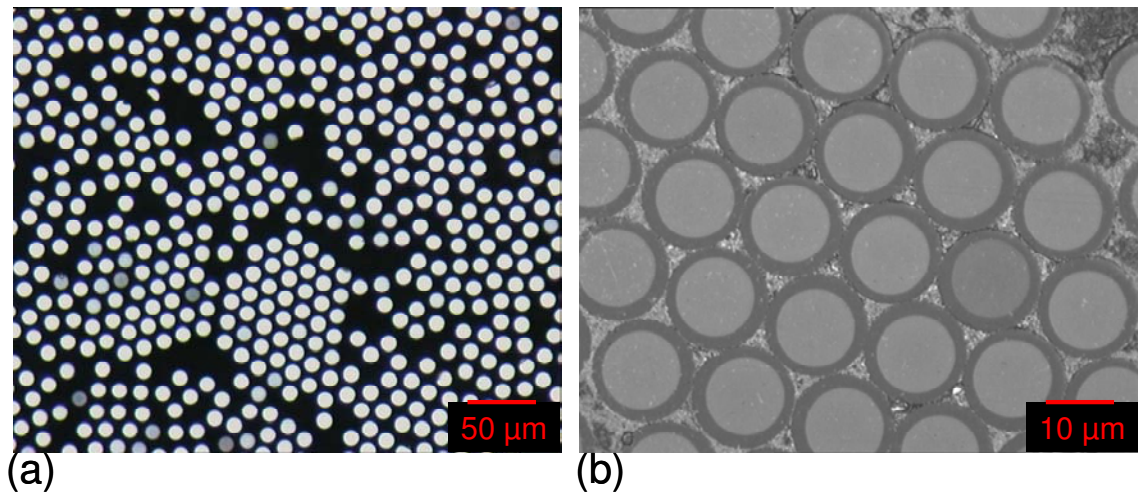
Figure 4.7 Micrograph of small-diameter optical fibres: (a) With light transmission; and (b) Without light transmission (image captured in reflection), magnified view of SDOF showing the cladding around the fibres.

Micrographs of a potted and polished SDOF bundle can be seen in Figure 4.7 (a and b). On comparing the images with that for the E-glass fibres (see Figure 4.2b); the following conclusions can be made:

i. The diameters of the E-glass fibres were in the range of 12-17 µm with an average of 15 µm and a standard deviation of 3. On the other hand, the diameter range for the SDOF is 12 with a standard deviation of 1.

ii. With reference to Figure 4.7b, it is apparent that the thickness of the cladding is not uniform. This has been investigated by one of the researchers in the Group [181]. It was reported that the cladding thickness varies between 1.2 µm and 2.2 µm.

4.1.1.3 Conclusions on the as-received fibres

The conclusions drawn from the investigation on the as-received fibres are summarised as follows:

i. The E-glass fibres were supplied as "water-sized" where the "size" or coating that is normally applied to the E-glass was not used. This was necessary as a part of the project (investigated by the post-doctoral fellow) was to investigate the effect of coupling agents on the cross-linking kinetics using evanescent wave spectroscopy.

ii. The as-received E-glass fibres were relatively free from the surface contaminations as inferred by the SEM analysis. This was not the case for the SDOF where significant surface contaminations were observed. Hence it was necessary to subject the SDOF bundles to a temperature regime to oxidise the coating. The optimum conditions were found to be heating the SDOF bundles in air at 450 ℃ for 6 hours. The E-glass fibres were used in the as-received state unless where specified.

iii. The diameter variation in the E-glass and SDOF were found to be ±3 µm and ±1 µm respectively.

iv. In the case of the SDOF, the thickness of the cladding was found to be between 1.2 µm and 2.2 µm.

v. The effect of the variations in the diameter of the E-glass and the thickness of the cladding were not investigated in detail in this study. However, this did not detract from the aim of this study, namely, to develop a technique to study the fracture of individual filaments.

4.1.2 Connectors

A primary requisite for the current research project was to enable the efficient coupling of light into and out of the ends of the fibre bundles. A number of techniques were investigated to achieve efficient coupling of light into fibre bundles. For instance, a short section (2 cm) of heat-shrunk tubing was used to secure the fibres prior to cleaving with a

fresh portion of a razor blade. The degree of repeatability of this method was poor in terms of positioning the fibre bundles within the connectors of the light source and detector.

With reference to Figure 4.2b and Figure 4.7 (a and b), polishing the potted fibre ends was found to produce "optical-quality" fibre end-faces. Therefore, the decision was made to develop the technique to pot and polish the ends of the fibre bundles, this was necessary for analysing the images captured by the high-speed camera.

Examples of connections that are used in the telecommunications industry include fixed connection (FC) connectors, straight terminus (ST) and lucent connector (LC) [22]. However, these connectors are generally meant for single and multi-mode optical fibres whose outer diameter is 125 µm. On the other hand, the diameter of the as-received E-glass fibre bundle was 1.4 mm; therefore, irrespective of the type of connector, it was necessary to select the one where the diameter of the inner bore could be drilled out to accommodate the E-glass and SDOF bundles.

Table 4.4 Attributes of the fibres types used in the study.

	As-received E-glass	SDOF
Average diameter (µm)	15±3	12±1
Number of filaments	2400±100	2800±100

With regard to the various connector designs mentioned above, the sub-miniature adopter type-A (SMA) was found to be most appropriate in terms of drilling out the inner bore. A 1.4 mm drill was used to increase the bore of the SMA connector. The edges were de-burred using a fine file.

In the case of the SDOF, these were supplied in 1m lengths as large bundles. It was established that approximately 3 grams of the SDOF was equivalent to 30 cm of a single E-glass fibre bundle. A summary of the relevant data for the two fibre types used in the study are presented in Table 4.4.

The E-glass and SDOF fibres were potted in the drilled-out SMA connectors using the procedures explained in Section 3.2.2.6. The benefits of using the SMA connectors were as follows:

i. This method was repeatable where the fibre bundles with approximately the same dimensions could be prepared in a reproducible manner.

ii. The SMA connectors enabled the ends of the fibre bundles to be formed into a circular cross-section. This assisted with coupling the light into the fibre bundle using conventional light sources. Moreover, it was easy to image the other end of the fibre bundle using the high-speed camera.

iii. It offered adequate protection to the fibre ends and minimised the damage caused by handling and loading the samples for tensile testing.

iv. As the fibre ends were potted in the SMA connectors, using an epoxy resin system, they could be polished easily using an automatic polisher.

4.1.3   Optimisation of the procedure for polishing the SMA connectors

A key aspect of the project was to study the fracture of individual E-glass fibres in real-time. Therefore, it was necessary to develop a technique to attach connectors to the E-glass fibre bundles. In order to optimise the coupling of light in and out of the connections, it was necessary to develop the optimum polishing procedures.

The ends of the fibre bundles (already potted in the SMA connectors) were polished as described in Section 3.2.2.6. The potting resin used was EPO-TEK®-314 (see Table 3.2 for details of this resin system). The refractive index of this resin (1.496) was lower than that of E-glass (1.56) to minimise the attenuation of light in the connector region. The other factor that influenced the selection of this resin as the potting medium was because of its relative hardness after the cross-linking. Thus, it was suitable for polishing on the automatic polisher. This was in contrast to the other resin system EPO-TEK®-310M and EPO-TEK®-305 that proved to be difficult to polish.
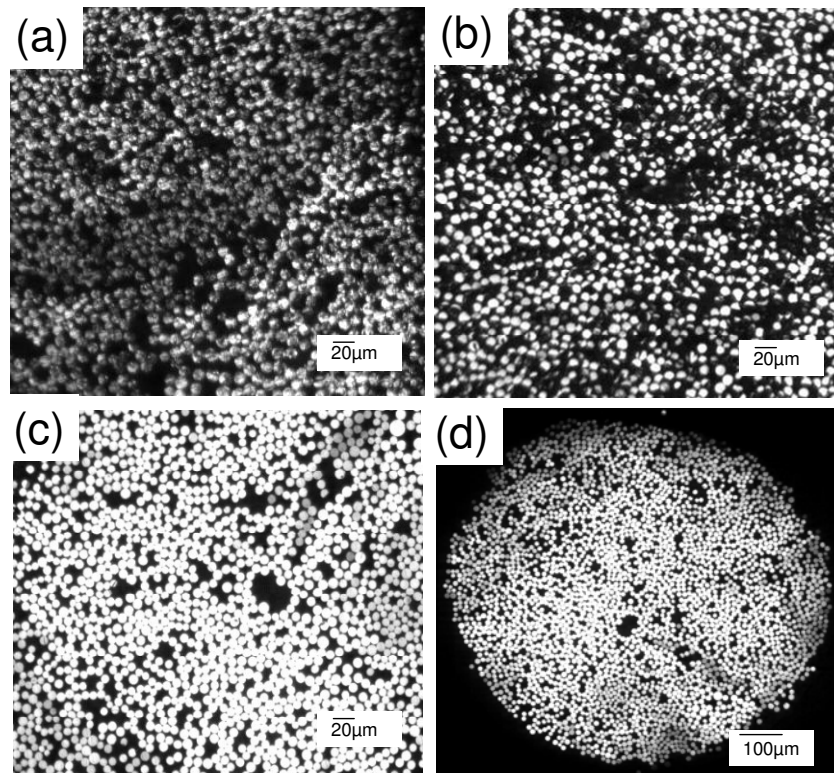
Figure 4.8 Optical micrographs of E-glass fibres after different stages in polishing: (a) Initial grinding using a metal plate; (b) After polishing with a 3 µm diamond-doped polishing film; (c) After polishing with a 0.5 µm diamond-doped polishing film; and (d) Final image quality of a SMA with a potted E-glass fibre bundle.

Figure 4.8 (a-d) presents the observed improvement in the quality of the potted E-glass fibre bundles in the SMA connectors, during different stages of polishing. With reference

to Figure 4.8a, this represents the first stage of the polishing sequence where the SMA connector with E-glass fibre bundle was ground on a metal plate. The next stage of polishing was carried out using a 3 µm diamond-doped polishing film where the sample was polished for 2 minutes. The connectors were cleaned thoroughly in an ultrasonic bath for 2 minutes. The final polishing sequence involved the use of a 0.5 µm diamond-doped polishing film; the operation was carried out for 4 minutes. The net effect of the polishing can be seen in Figure 4.8d where a near-optical quality is observed.

4.1.4 Parameters affecting the light transmission

The effects of different parameters on the light transmission characteristics of the E-glass fibre bundles were investigated. Fibre bundles were prepared as described in Section 3.2.2 with three different lengths; 50 mm, 150 mm and 250 mm. These fibre bundles were not end-tabbed. However, SMA connectors were attached to facilitate the light coupling and transmission through the fibre bundles. A white-light source (Intralux-4000, Warner Instruments, USA) and a 200 mW green laser emitting at 532 nm (Shanghai Dream Laser Technology Co. Ltd., China) was used to transmit light through the E-glass fibres. The light was detected using a photosensitive detector PM100 (Thorlabs, UK). After measuring the light intensity for the uncoated specimens, the same fibre bundles were coated with the low refractive index resin EPO-TEK®-314; the transmitted light intensity was measured again.

4.1.4.1 Effect of bundle length on light transmission

The light transmission characteristics of E-glass fibre bundles of different lengths were investigated. Figure 4.9 (a and b) present a summary of the light transmission through as-received E-glass fibres as a function of sample length, using a white-light source and the green laser, respectively. It was found that the transmitted light intensity decreased with an

increase in the length of the sample. On comparing the data, the decrease in light intensity was 85% when the length of the sample was increased from 8 to 15 cm. A further decrease of more than 80% was observed when the sample length was increased from 15 to 25 cm. The percentage decrease in the light intensity was almost the same for both types of light source. This was most likely due to the attenuation caused by the absorption or scattering of the transmitted light within the fibres. Absorption losses in the glass can be due to the intrinsic structure of the material or the impurity-based absorption (see Section 2.3.2 for details). Intrinsic absorption is caused by interaction of the propagating light with the components of the glass [21, 23]. Pure silica has a low absorption window between 800 and 1700 nm. It has been reported that the E-glass fibres have least absorption at a wavelength of around 532 nm [10]. It is also evident by comparing Figure 4.9a and b, where the transmitted light intensity was significantly higher when a green laser (emitting at 532 nm) was used. Another factor that may contribute to the light attenuation was due to scattering. The scattering losses results from density and composition variations. In almost all types of glass, the scattering centres are primarily impurities such as oxides and transition metal ions, with sizes typically smaller than the wavelength of light. This is classified as Rayleigh scattering [21]. Mie-scattering occurs when the relative dimensions of the random compositional in homogeneities are comparable to the wavelength of the propagating light [21]. Examples of factors that can give rise to Mie-scattering include irregular dimensions and geometric symmetry within the optical fibre core and cladding, localised strain fields, voids and the refractive-index-variations along the length of the fibre. It was difficult to differentiate whether the light attenuation that occurred (due to increase in length of test specimen) was due to absorption or scattering or combination of both types. However, it is evident that the length of the fibres has a detrimental effect on the light transmission characteristics of E-glass fibres.

The other types of losses associated with light transmission in the fibres are extrinsic losses that may be due to macro-bending and micro-bending (see Section 2.3). The losses due to macro-bending are less dominant in the present case since the samples were kept straight to minimize this effect (see Figure 2.4 for macro-bending). However, the effects of micro-bending of the fibres could increase with the increasing length of fibre since the 'water-sized' fibre bundles were supplied with inherent twists. The twists were produced during the manufacture of the E-glass fibres. Practically, it was difficult to completely eliminate these twists; however they were removed as much as possible during the fabrication of tensile test specimens. In other words, the twists within the gauge length of the tensile test specimens were removed manually. Due care and attention was taken that the fibres were not fractured during this manipulation.

Coating the fibre bundle with a low-refractive index resin also causes a reduction in the transmitted light intensity. However, this effect was not as dominant as the increase in length of the fibre bundle. In the next section, the effect of coating the fibres on light transmission is investigated.
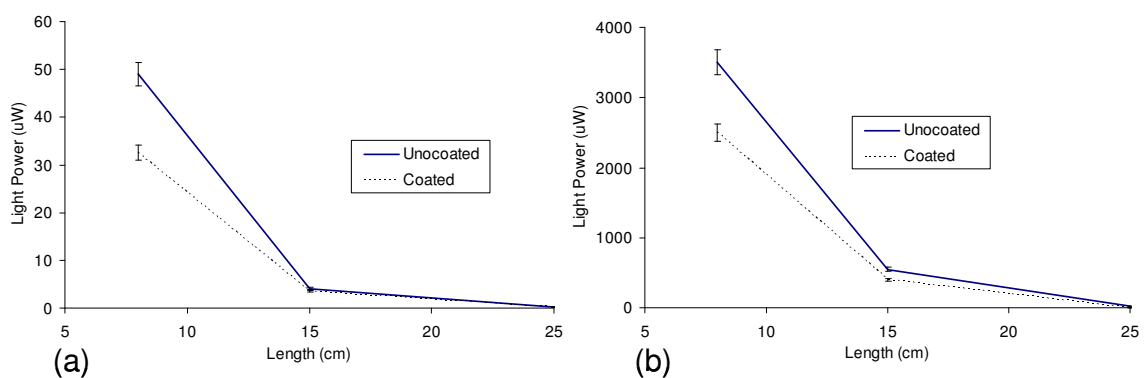
Figure 4.9 Graphs showing the light transmission through the as-received (uncoated) E-glass fibres as a function of specimen length: (a) Light transmission using a white-light source; and (b) Light transmission using a green laser.

4.1.4.2 Effect of coating the fibre bundle

The effect of coating the fibre bundle with a low refractive index resin was studied. The transmitted light intensity for the fibre bundles was measured before and after coating with EPO-TEK®-314. Three different lengths of fibre bundle were investigated: 8 cm, 15 cm and 25 cm. It was found that the transmitted light intensity decreased by 30%. Figure 4.9 (a and b) show the effect of coating the fibre bundles on the transmitted light intensity for the white-light source and the green laser respectively. The change in light intensity was due to the difference between the refractive index (RI) of the EPO-TEK®-314 resin (RI = 1.496) and the air (RI ≈ 1). Due to the change in the outer medium of the fibre (cladding), the light guiding properties of the fibres were changed and therefore, the transmitted light intensity was reduced. According to Equation 2.4, the light acceptance is a function of the numerical aperture (NA), where NA is defined as:

From Equations 2.2 and 2.3:

$$NA = \sin\theta_{max} \qquad\qquad 4\text{-}1$$

and

$$\sin\theta_{max} = (n_1^2 - n_2^2)^{1/2} \qquad\qquad 4\text{-}2$$

where the notations were defined previously.

The refractive indices of the E-glass fibre, EPO-TEK®-314 resin system and air were 1.56, 1.496 and 1, respectively. By substituting the numerical values of refractive indices, the NA was found to be 1.19 in the case of air acting as the cladding, whereas in the case of EPO-TEK®-314 as the cladding the NA was found to be 0.44. It can be observed that the

133

NA was reduced significantly (60%) due to a change of the cladding from air to epoxy resin. Hence the light transmission through fibres was also reduced and that can be observed from the graphs shown in Figure 4.9 (a-b).

In summary, the major light attenuations in the fibres were intrinsic losses. The increase in length of the E-glass fibre causes a significant increase in the attenuation due to absorption and scattering of the light in the fibres. The effect of a change in the refractive index of the outer medium was another contributor to the light attenuation but to a lesser extent than the length. It has been reported [117] that the cladding should not have any significant absorption at the wavelength of light so that the evanescent field can decay to a lower value. However, this effect was not considered in this study since the matrix of the E-glass composite material acted as a cladding to enable total internal reflection. Therefore, the length of the specimen was more critical than the selection of cladding. The length of the specimen in this study was fixed at 28 cm for E-glass. In the case of SDOF, the length of the fibre bundle was not an issue as a silica cladding was present. This will be discussed in more detail in Section 4.1.6.2.

4.1.4.3 Effect of sealant on light transmission

The refractive index of silicone sealant RTV-3140 (Dow Corning, UK) used for sealing the fibres was 1.43. This was necessary to stop the potting resin from impregnating the fibres outside the connector region. The effects of the silicone sealant on light transmission through the E-glass fibre bundle were investigated. Samples were manufactured as described in Section 3.8. The sealant was applied on the 10 mm length of the fibre section and left to cure for 24 hours at room temperature. The length of the sealant that was applied on the fibre-bundle was increased in sections of 10 mm until a total of 50 mm of fibre bundle was coated with the sealant as shown in the Figure 3.19. Figure 4.10 shows

the effects of a sealant covered length on light transmission. It was found that the sealant significantly affects the light transmission if it covers more than 10 mm of the fibre bundle. However, in the case of self-sensing fibres and composites, the length of fibre bundle coated with sealant was always less than 5 mm. Therefore, it can be concluded that there was no significant change in light transmission due to the application of silicone sealant for the current work.
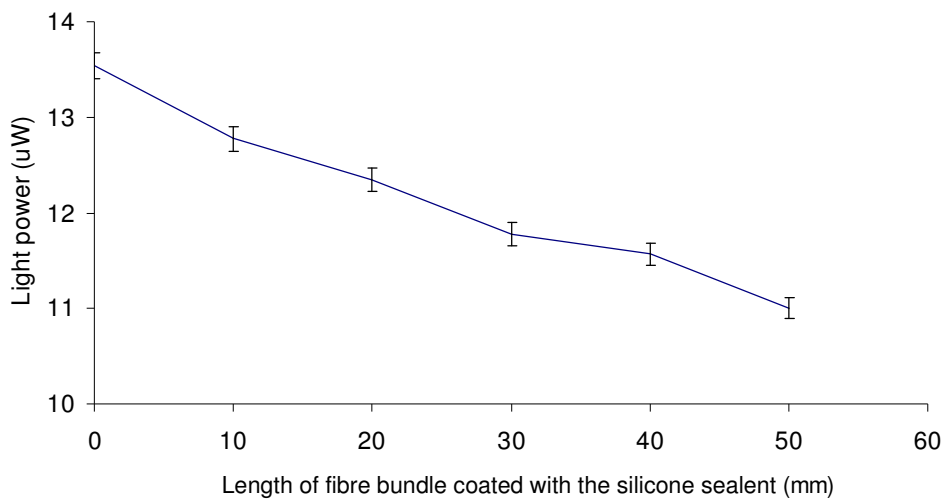
Figure 4.10 Graph showing the effects of silicone sealant on light transmission through the E-glass fibres.

4.1.5 Sample quality

4.1.5.1 Fibre bundles

Although it was relatively simple to manufacture the fibre bundles for tensile testing, the following issues are highlighted.

i. The number of intact or un-fractured fibres: This topic was introduced in Section 4.1.1, in the case of E-glass fibre bundles, the number of filaments in water-sized bundles were 2800±100. Significant care and attention was taken to ensure that the fibre bundle was supported from the moment it was cut from the creel through to the

potting, curing, end-tabbing and mechanical testing stages. In the case of SDOF, these fibres were supplied in 1 m bundles and hence it was necessary to extract the required length. In terms of ease of handling, the as-received fibres were found to be robust (no fibres were observed to fracture during handling). As shown in the previous sections, these fibres had a relatively thick cladding.

ii. The E-glass fibre bundles were un-sized and supplied with inherent twists. The presence of twists in the fibre bundle can increase inter-fibre friction, introduce surface-flaws through abrasion, and length variations of fibres in the bundle. These issues can affect the strength distribution and cause variable tension in the fibres. In order to reduce these effects, the fibres in the bundle were very gently spread manually, without damaging the fibres. The fibres were spread out on a metal plate (50 x 50 cm) covered with an adhesive-backed PTFE sheet. They were then clamped using small clips as detailed in Section 3.2.2. This was done to ensure that the tension in the filaments remained the same as far as possible. Although the twists were removed as far as practically possible, they could not be removed completely. In the case of SDOF, the magnitude of twists was much lower than for the E-glass fibre bundles. However, in the case of SDOF bundles, it was relatively easy to spread the fibres and make them parallel before fabricating the tensile test specimens.

4.1.5.2 Self-sensing composites

4.1.5.3 Manufacturing of self-sensing composites

The manufacturing of self-sensing composite commenced with an open-mould fabrication technique. The manufactured samples were used to develop the test rig, integrate different equipment, to commission the high-speed camera and the acoustic emission system. In

addition, fibre testing was carried out to develop software macros for the image analysis routines.

At the same time, different avenues for manufacturing good quality composites were explored. Figure 4.11 shows images of self-sensing composites manufactured from the open-mould fabrication process. On inspecting Figure 4.11, the extensive presence of voids, dimensional inconsistency, and misaligned fibres is apparent. The magnified views of three different sections clearly show the excessive number of voids and regions with no fibres or resin, and the misalignment of the fibres within the composite. This sample was one of the better samples that were produced using the open-mould process. The other main problem with this technique was the inconsistency between samples. These samples were manufactured using the low stiffness EPO-TEK$^{®}$-310M resin system. This resin system was cross-linked at room temperature, and the ultimate failure strength of this resin system was 0.24 MPa. Therefore, it cannot be used to manufacture composites of high strength and stiffness. After many trials, the open-mould fabrication method was abandoned and a resin-injection technique was developed.
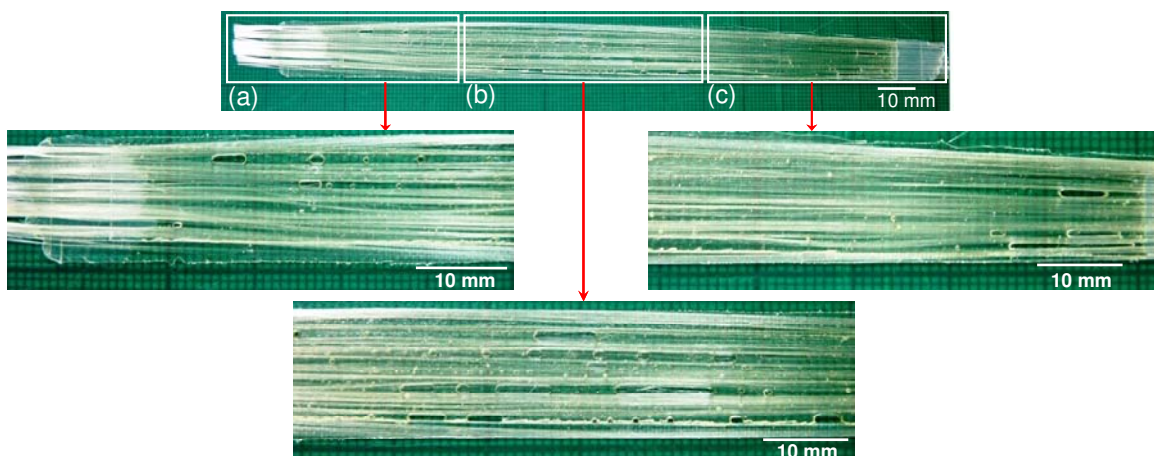
Figure 4.11 Self-sensing composite manufactured from EPO-TEK$^{®}$-310M resin using the open-mould fabrication process with magnified views of sections 'a', 'b' and 'c'.
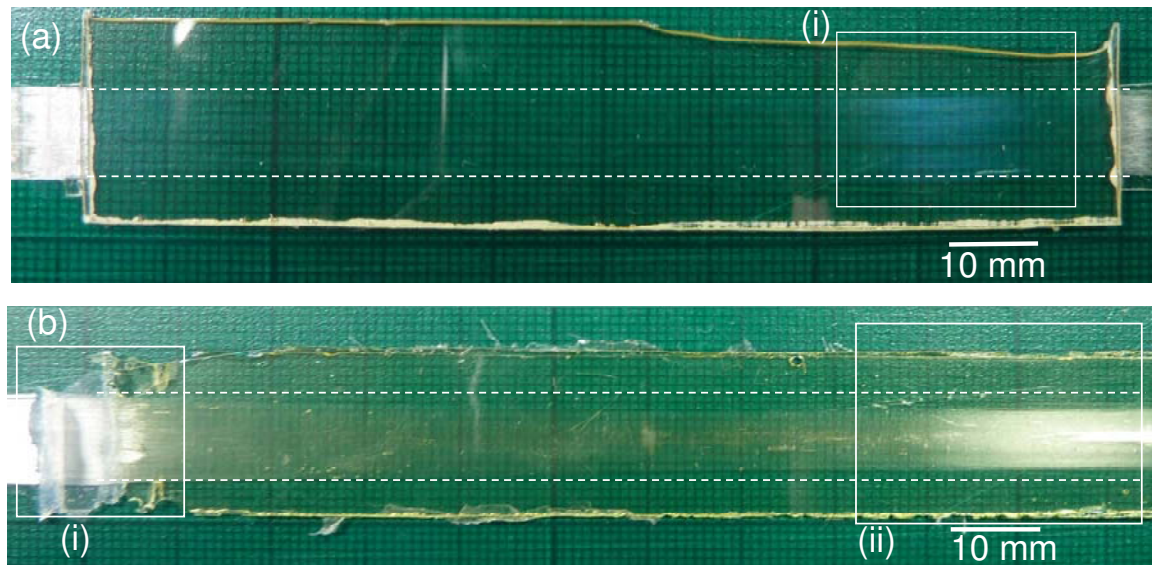
Figure 4.12 (a-b) Representative photographs of two self-sensing composite samples manufactured by the resin-injection technique; the dotted-line is the perimeter of the composite, the region outside the perimeter represents the cured neat resin.

The resin-injection technique addressed and overcame most of the issues stated above. It was possible to control the tension in the fibres using the bull-dog clips at the end of the glass plates as discussed in Section 3.2.3. The fibres were first separated and spread gently to remove the twists to make them parallel. This resulted in an increase in the width of the fibre tow, which assisted in the impregnation of the fibres [182]. The EPO-TEK®-314 resin was injected gradually, and the impregnation was monitored visually by inspecting the impregnated fibres through the glass plate. The process was halted whenever necessary to allow the fibres to impregnate properly without causing the formation of voids and air-pockets. Additionally, after injecting the resin, the mould was left in a vertical position for 60 minutes to ensure that resin could flow between fibres to expel any trapped air. The top and bottom glass plate provided a glass quality surface finish for the self-sensing composites specimens.

138

The main advantages of this technique are as follows:

i. It provided a 'good' surface finish and uniform thickness. The measured thickness of the specimens manufactured from this technique was found to be 0.75 ± 0.01 mm. Figure 4.12 show images of the self-sensing composites manufactured from the resin-injection technique. With regard to Figure 4.12 (a and b), the quality of the composite is obvious in terms of the surface finish and the absence of voids. The area highlighted by the white box was the reflection from the fibres due to the illumination used, this does not represent an under impregnated region.

ii. It was comparatively easy to control and align the fibres within the mould in a consistent manner. Figure 4.13(a-d) show cross-sectional views of the composite after polishing; the circular fibre-ends indicate the degree of alignment attained by this manufacturing method.

iii. The requirement for an un-impregnated section of fibre bundle at both ends of the composite was achieved successfully in a repeatable manner.

iv. It allowed the use of the high-stiffness resin (EPO-TEK®-314) for manufacturing the composites. In the case of the open-mould fabrication process, this resin system could not be used since the shrinkage during cross-linking was high. Additionally, with the open-mould process, it was not possible to manufacture samples where the fibres were highly aligned.

v. Different types of fibres can be used to manufacture good quality composites with negligible void contents.
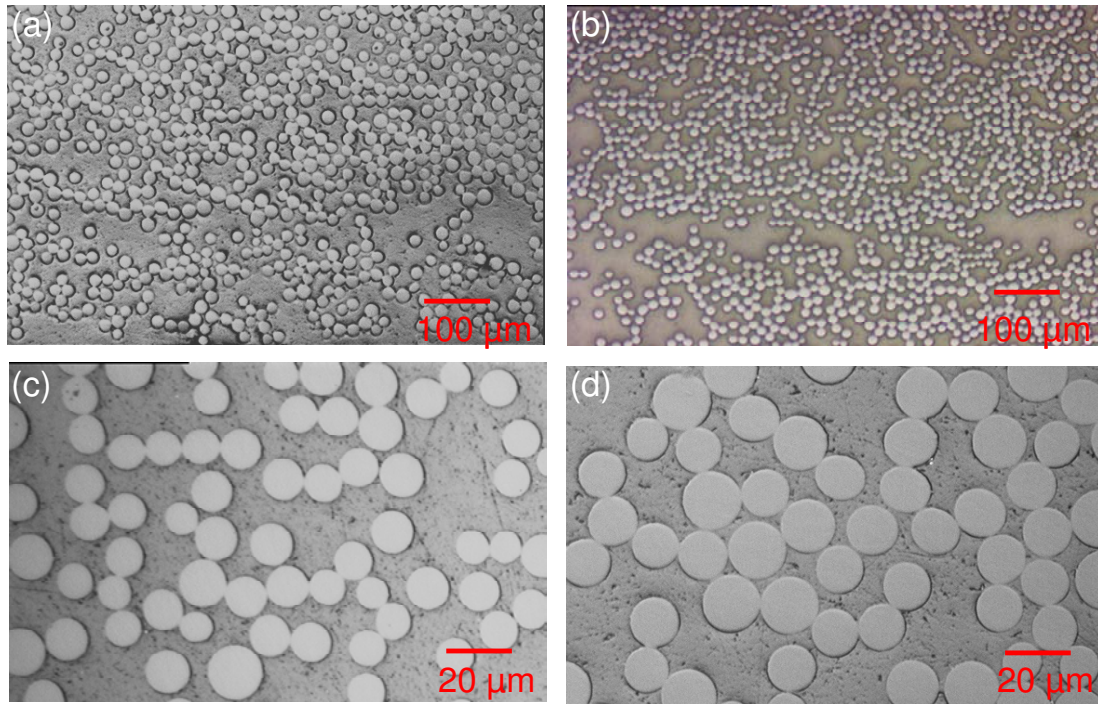
Figure 4.13 Typical cross-sectional views of composites manufactured from resin-injection technique: (a-b) At 5X magnification; and (c-d) At 20X magnification.

The disadvantages of this technique are as follows:

i. The sealing of the mould around the glass plate was critical since there was a possibility of resin leakage during cross-linking at elevated temperatures. This issue was addressed and a procedure was developed that requires the sealant to be applied in three sequential steps and after each step the sealant was cured for 24 hours. Firstly, the sealant was applied to the fibres, and between the top and bottom glass plate, secondly around the joint of the top and bottom glass plate and finally near the injector needles.

ii. This process is time consuming and requires moulds to be prepared separately for each sample.

Despite these limitations, this technique proved to be the best for the fabrication of the self-sensing composites and it was successfully applied to manufacture, test and analysis more than 100 test coupons during this research programme.

4.1.5.4   Fibre volume fraction

The fibre volume fraction (FVF) was determined using an image analysis technique [16]. The samples were prepared as described in Section 3.9. The micrographs of the composite samples were analysed using KS™ 4.0 software. This involved background correction, selecting an optimal threshold and then calculating the fibre volume fraction. The high contrast between fibres and matrix helped to subtract the background and identify each fibre. The sources of error in these calculations were low but may include an element of over estimation due to the presence of fibres touching. This can be rectified by increasing the threshold of luminance. However, this may cause a reduction in the areas of the fibres themselves. Therefore, different iterations were performed before calculating the FVF for each image.

Figure 4.14 (a-d) shows typical micrographs of composites made from the E-glass fibres and the small-diameter optical fibres used in this study. It was found that there were negligible voids present in the composites made using the resin-injection technique. More than 20 different sections of composite samples were analysed using optical microscopy and no observable voids were found in any of the samples. This may be attributed to the fact that the: (i) the resin was de-gassed before injecting it into the mould; and (ii) the mould was properly sealed, therefore, entrapped air was able to escape through the unsealed top edge of the glass plates as shown in Figure 3.9. Figure 4.15 shows the average values for the fibre volume fraction of the self-sensing composites manufactured using different types of fibres with their respective standard deviations.
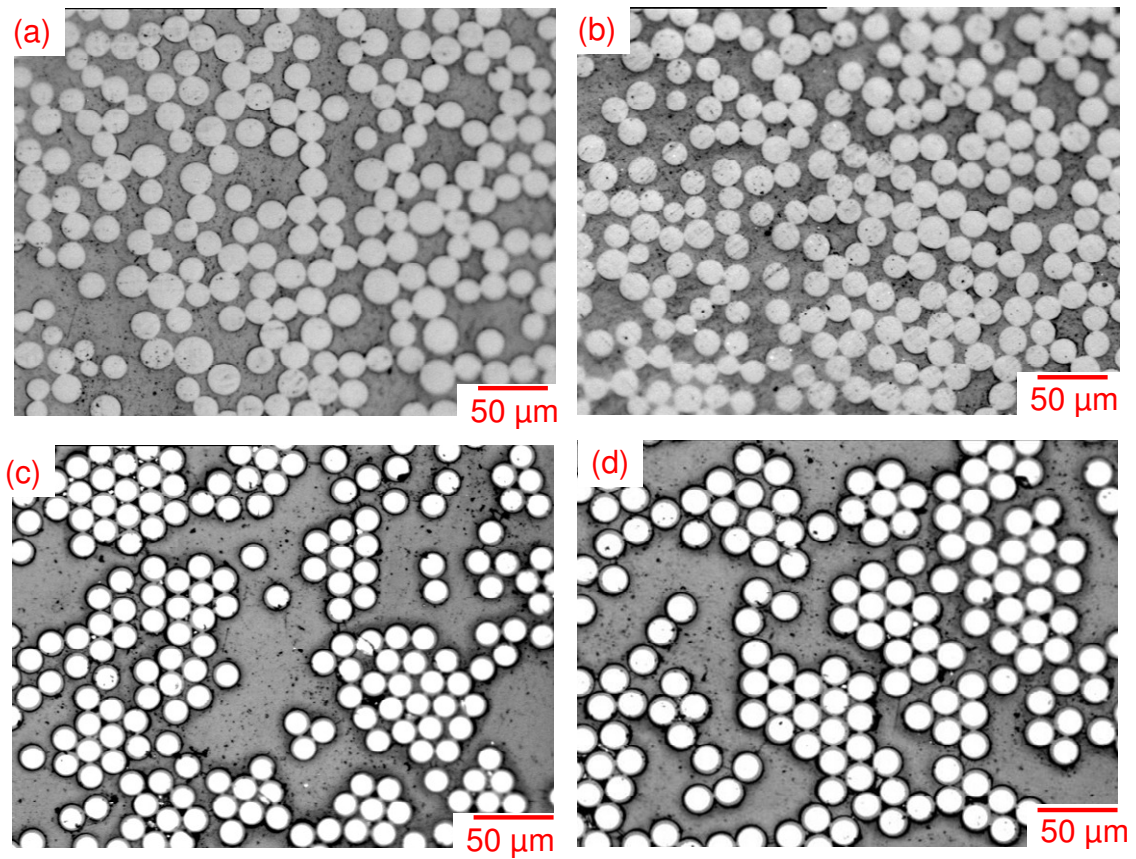
Figure 4.14 Typical micrographs of cross-sections of self-sensing composites manufactured from: (a) As-received E-glass fibres; (b) Silane-treated E-glass fibres; (c) As-received SDOF; and (d) Heat-treated SDOF.
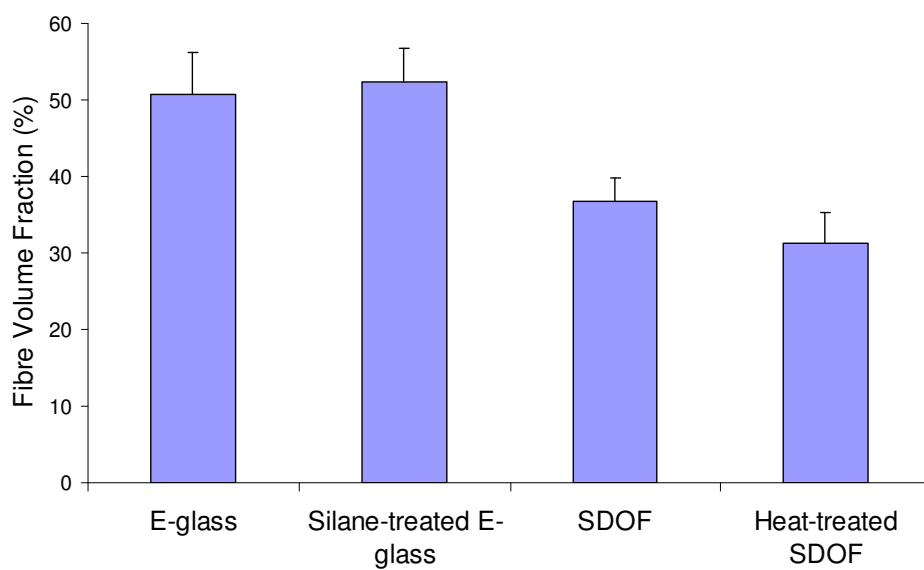
Figure 4.15 Fibre volume fraction of the self-sensing composites.

With reference to Figure 4.15, the FVF of the composite manufactured from the as-received E-glass and the silane-treated E-glass are similar. However, in the case of SDOF composites, the fraction of the FVF was lower than the E-glass composites. This was due to the fact that the average diameter of SDOF was 12 µm in comparison to the average diameter of 15 µm of the E-glass fibres. Secondly, the area fraction of SDOF was lower compared to the area-fraction of E-glass fibres in the composite. Therefore, the FVF of E-glass composites was higher than SDOF composites.

4.1.6   Design criteria for the self-sensing composites

4.1.6.1   Light transmission

The light transmission through the core of an optical fibre is attained by total internal reflection. This was discussed in detail in Section 2.3. The light can only be transmitted if the refractive index (RI) of the outer medium (cladding) is lower than the core of the optical fibre [23]. The RI of the E-glass fibres and SDOF are 1.56 and 1.62 respectively. The refractive index of the cladding of SDOF was 1.51. In the case of E-glass fibres, the matrix of the composite was also acting as the cladding around the fibres. The refractive index of the EPO-TEK®-314 resin system used in this work was 1.496 (see Section 3.1 for details). The thickness of the cladding can affect the light transmission through fibres [21]. The thickness of cladding should be able to decay the evanescent loss to a lower value (see Section 2.3). The penetration depth can be calculated using Equation 2-6:

$$d_p = \frac{\lambda}{2\pi n_1 \left(\sin^2 \theta - \sin^2 \theta_c\right)^{1/2}} \qquad \text{4-3}$$

where the notations have been defined previously.

The penetration depth of the evanescent field was calculated by considering an incidence angle greater than the critical angle (n_1=1.56, n_2=1.496, θ=75° and θ_c=73.53°) and is found to be 3.9 µm. Therefore, the thickness of cladding has to be greater than 3.9 µm. The resin-injection technique was developed to manufacture void-free composites. The absence of voids ensured that the thickness of the epoxy matrix (acting as cladding around the fibres) was always greater than 3.9 µm for each fibre. However, the possibility of fibre-to-fibre contact could cause light-coupling and/or evanescent losses. It was not possible to accurately quantify these losses and issues. Therefore, the losses associated with evanescent losses were not considered any further. The other losses associated with light transmission have been discussed already in Section 4.1.4.

4.1.6.2 Dimensions

The length of the composite test specimens was selected on the basis of light transmission capabilities of the E-glass fibres. With reference to Section 4.1.4, the transmitted light intensity was significantly reduced when the length of the fibre bundle was increased to more than 200 mm. After a significant number of trials, the gauge length of the self-sensing test specimen was fixed at 100 mm, whereas the total length of the sample was 280 mm; the remaining 180 mm was allocated for end-tabs (50 mm), SMA connectors (50 mm) and the un-impregnated section (80 mm) of the fibre bundle. This un-impregnated section was required to enable the fibres at the bottom of the Instron-jaws to be taken out to facilitate the coupling of light into the fibres and imaging at the other end (see Figure 3.11).

4.1.6.3 Critical fibre volume fraction

Manufacturing composites with a high fibre volume fraction and the ability to couple light into and out of the composite was a mandatory objective for *in-situ* damage detection.

Initially, the samples manufactured from open-mould fabrication exhibited a low fibre volume fraction of ~10% and a high void content (>15%). Different manufacturing methodologies were explored to increase the fibre volume fraction and the overall quality of the composite. The main constraint was to seal the fibres effectively at the end-tabs to leave an un-impregnated section of the fibre bundle (see Section 3.2.3). With the open-mould process, it was not possible to seal the fibres effectively and the seepage of resin was worsened when more fibres were added to increase the fibre volume fraction. Therefore, in order to solve the problem, the resin-injection technique was developed. The critical fibre volume fraction is the percentage of fibres in a composite below which the fibres were not able to reinforce the matrix (see Section 2.4.1). The critical fibre volume fraction was calculated using the method described in Section 2.4.1. The average ultimate failure stress of the matrix and the fibres will be reported in Section 4.3. To determine the critical fibre volume fraction, the ultimate stresses of the fibres are plotted against the ultimate failure stress of composites. The intersection point of the two plots defines the critical fibre volume fraction as shown in Figure 4.16. Alternatively, it can be calculated using the equations given in Section 2.4.1. To calculate, the critical fibre volume fraction the fibre stress at the onset of matrix cracking is calculated using the relation:

$$\sigma_{1u} = f\sigma_{fmu} + (1 - f)\sigma_{mu} \qquad\qquad 4\text{-}4$$

where σ_{fmu} is the fibre stress at the onset of matrix cracking ($\varepsilon_1 = \varepsilon_{mu}$).

The critical fibre volume fraction can then be calculated using Equation 2-12:

$$f' = \frac{\sigma_{mu}}{\sigma_{fu} - \sigma_{fmu} + \sigma_{mu}} \qquad\qquad 4\text{-}5$$

where the terms have been defined previously.

Table 4.5 shows the magnitude of the different parameters used to calculate the critical fibre volume fraction. The critical fibre volume fraction was approximately 4.3% for the E-glass composites and 3.25 % for the SDOF composite. This is the percentage of fibres in the composites above which the fibres will reinforce the matrix. Although this value was very low, it predominantly depends upon the ultimate tensile strength of the matrix. Since the matrix exhibited an ultimate tensile strength of 27 MPa, a lower percentage of fibres can reinforce the matrix.

Table 4.5 Summary of the magnitude of different parameters used for calculating the critical fibre volume fractions.

	E-glass fibres	SDOF composite
σ_{mu} (MPa)	27	27
σ_{fu} (MPa)	940	1050
σ_{fmu} (MPa)	278	285
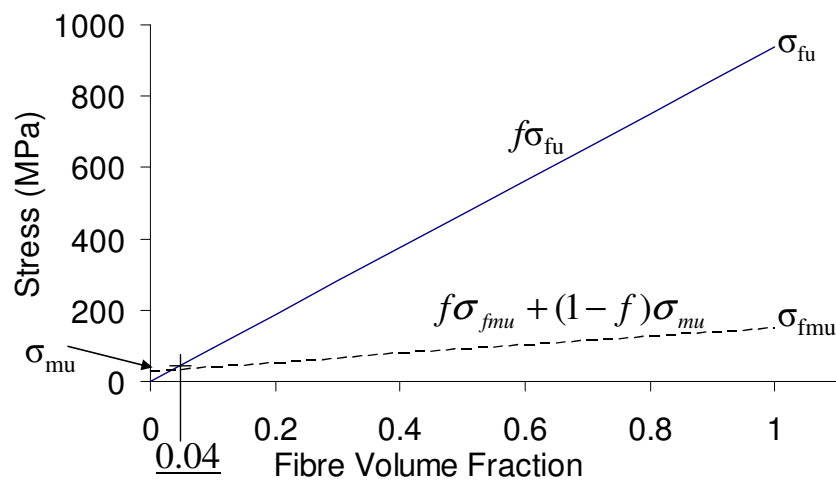
Figure 4.16 Graph showing an estimation of critical fibre volume fraction for E-glass using the graphical-method.

146

4.1.6.4 Selection of light source and high-speed camera

The E-glass fibres transmit maximum light at a wavelength of approximately 532 nm [11, 117]. Therefore, a green laser source of 200 mW (Shanghai Dream Laser Technology Co. Ltd., China) with an output wavelength of 532 nm was chosen for this study. A white-light source (Intralux-4000, Warner Instruments, USA) was used for the small-diameter optical fibre bundles.

With reference to Section 3.5, a high-speed charge coupled device was used to capture images of the fibre bundles during tensile testing. The basic requirements for the high-speed camera are presented in Table 3.6. A brief discussion regarding these requirements is presented below:

Charge coupled device (CCD) sensor: CCD cameras are used to record images as digital signals. Although there are other means of capturing images such as photographic film, the CCD camera was identified as the most suitable means of capturing sequential images during tensile testing of the self-sensing fibre bundles and composites. The key factors associated with the decision were as follows:

    i.   User specifiable speed for capturing the images.

    ii.   Variable focal length via the 12X microscopic lens.

    iii.   Ability to capture sequential images that could be stored and post-processed.

Mode of operation of Photron PCI-1024 high-speed CCD cameras: An image is projected through a lens onto the photoactive region that is made of an array of capacitors. The proportional light intensity of the image causes each capacitor to accumulate a proportional electric charge at that location. Once the array has been exposed to the image,

a control circuit causes each capacitor to transfer its contents to its neighbour. The last capacitor in the array releases its charge into a charge amplifier, which converts the charge into a voltage. By repeating this process, the controlling circuit converts the entire contents of the array in the semiconductor to a sequence of voltages, which it samples, digitises and stores in its memory [183].

Image capturing speed and memory to record images: The high-speed photography requires large and extremely efficient digital random access memory (RAM) that can store the images captured by the camera [183]. The RAM should be capable of digitally storing thousands of images during a short recording sequence. For instance, 8000-10000 images might be captured for a footage of only 120 seconds. The RAM capacity affects the capabilities of the camera since it restricts the maximum recording time available to record the images. It also controls the image capture speed. The image capture speed defines the number of images to be recorded per second. For example, if the high-speed camera captures images at 60 frames per second (fps) then for 120 seconds it will record 7,200 frames and if the high-speed camera records at 250 fps then the number of images will be 30,000 frames for the same sequence of 120 seconds.

The RAM was one of the most costly elements for the high-speed camera. Therefore, a reasonable balance was required to select the appropriate memory and the image capture speed. After the assessment of different available camera systems a frame rate of 60 fps and a recording time of 120 seconds was finally selected; it required 4 GB of RAM.

Resolution: The resolution of an image defines the number of pixels used to build an image on the CCD sensor. A very high-resolution image requires a large memory to store it. The resolution was also constrained due to the available RAM of the high-speed camera. On the other hand, analysis of the images with a low resolution may effect the information

associated with each image. After some preliminary image analysis an appropriate resolution of one mega pixel was selected.

Table 4.6 Specifications of the high-speed camera used in this study.

Manufacturer	Photron, UK
Frame rate	60-100,000 frames per second
Triggering	TTL 5Vp-p, switch closure
Sensor	CCD monochrome sensor with 17μm pixel size.
Resolution	One Megapixel
Lens Mount	Interchangeable F-mount and C-mount standard
Camera Control	PCI bus in a Windows PC
Saved Image Formats	AVI, JPEG, PNG, TIFF, FTIF, BMP, RAW, RAWW

Lens-attachment: The diameter of the fibre bundle potted in the SMA connector was 1.4 mm. A lens attachment was required to magnify and focus the fibre-bundle-end on the CCD sensor of the high-speed camera. A microscopic lens attachment (12X Zoom Extender, Navitar, UK) was employed for this purpose.

After a careful review of all the requirements and the budget available for the purchase of the high-speed camera, a FastCAM-1024-PCI from Photron UK was finally selected. This model provided a reasonable balance between all of the above mandatory requirements. In addition it has an external digital trigger, which assisted in effective time synchronisation with the AE system. The specifications of this model are summarised in Table 4.6.
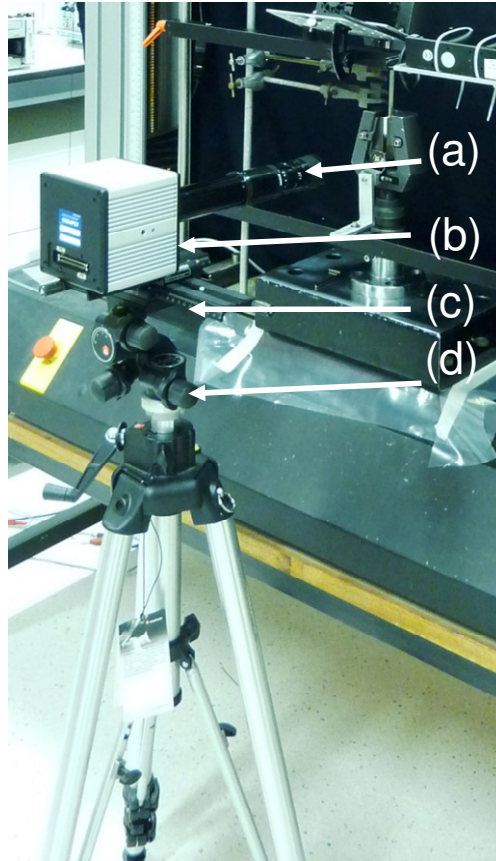
Figure 4.17 High-speed camera setup: (a) Lens attachment; (b) High-speed camera; (c) Positioning plates; and (d) Tripod stand.

Additional accessories: The high-speed camera was mounted on a tripod stand (Nikon, UK) for focusing the fibre-bundle end. Additionally two horizontal positioning plates were attached to the tripod stand to assist the fine focusing requirements for imaging. Figure 4.17 shows an image of the high speed camera, the positioning plates and the lens attachment.

4.1.7 Conclusions on the quality of samples and assessment procedures

The conclusions drawn from Section 4.1 are summarised as follows:

Fibre surface: The surface appearance of the as-received E-glass and SDOF were characterised using SEM and optical microscopy. The E-glass fibre surfaces were 'clean' and they were used without any further treatment. However, these fibres were silane-

treated for some experiments; this is discussed in Section 3.2.2.8. On the other hand, the surface of the SDOF was found to be contaminated with a significant volume of debris. It was necessary to subject the SDOF to a heat-treatment to oxidise the binder/coating. The optimum heat-treatment conditions were found to be 450 °C for 6 hours.

Fibre diameter: A brief study was undertaken to determine the variation in the fibre diameter for the E-glass and SDOF. The diameter range for the E-glass and SDOF was found to be 15±3 µm and 12±1 µm, respectively.

Fibre fracture: A simple test was conducted to estimate the number of broken filaments in a bundle. This was carried out by illuminating one end of a fibre bundle in a dark room and detecting visually the number of broken fibres as inferred by light bleeding from the fractured fibres. Ten bundles were evaluated. The number of fractured filaments in the E-glass bundles was estimated to be 2-5%.

Polishing: Appropriate techniques were designed and developed to enable the fibre bundle, to be potted and polished in the SMA connectors. The quality of polishing was adequate to image each filament by the high-speed camera.

End-tabbing: A new end-tab design was used to enable the fibre bundles and the composites to be tested in tension without damaging the fibres in the gripped region in the jaws of the Instron tensile test machine.

Manufacturing of void-free composites: A resin-injection system was developed to manufacture void-free composites. The average fibre volume fraction for the E-glass and SDOF were found to be 47% and 42%, respectively.

High-speed camera system: A detailed study was undertaken to identify an imaging system that could capture the fracture of the individual filaments in the E-glass and SDOF bundles

and composites. The imaging system that was selected after an exhaustive study was a PCI-1024 manufactured by Photron UK.

Synchronisation: Appropriate hardware and software routines were developed to synchronise the AE data acquisition system, tensile test machine and high-speed camera. The first AE hit detected via a pair of piezoelectric transducers during tensile testing was used to trigger the high-speed camera and to record the applied-load and strain as parametric inputs.

4.2 Mechanical Testing of Neat Resins

Mechanical testing was performed to obtain the data on Young's modulus, strain-to-failure and tensile strength of the neat resin samples. Three resin systems, EPO-TEK[®]-305, EPO-TEK[®]-310M and EPO-TEK[®]-314 were investigated in this study. The neat resin samples were fabricated as described in Section 3.2.1.2. Conventional electrical resistance strain gauges were surface-bounded to the neat resin samples as described in Section 3.2.1.4. Acoustic emission (AE) monitoring was employed to record the AE signal produced during tensile loading of test specimens. Eight to ten test specimens were tested for each type of resin.

4.2.1 Tensile test results of the neat resins

The tensile test results of the neat resins are summarised in Table 4.7. The EPO-TEK[®]-305 and EPO-TEK[®]-310M samples were ductile with a Young's modulus of 8.6 MPa and 3.4 MPa respectively. On the other hand, the EPO-TEK[®]-314 samples were stiffer with a higher Young's modulus of 1047.9 MPa. Representative stress versus strain plots of the three neat resins are presented in Figure 4.18 (a-c). The epoxy resin system EPO-TEK[®]-305 exhibited the highest strain-to-failure of approximately 9%. The fracture of EPO-TEK[®]-305 was gradual with multiple visible cracks that propagated in the vicinity of the centre of the gauge length. In the case of EPO-TEK[®]-305, the secant moduli were calculated [184, 185] at strains of 0.8%, 7.1% and 9.7% as shown in Figure 4.19. The calculated secant moduli are summarised in Table 4.8.

The failure of EPO-TEK[®]-310M was gradual with a strain-to-failure of approximately 3%. However, no visible cracking was observed as in the case of the EPO-TEK[®]-305 resin system. The epoxy resin EPO-TEK[®]-314 was the stiffest resin investigated with a strain-

to-failure of 1%. These test coupons fractured catastrophically accompanied by the emission of projectile fragments. The stress-strain plot was linear with a well-defined failure-point that indicates the brittle nature of the resin as shown in Figure 4.18c.

Table 4.7 A summary of the average mechanical properties of the neat-resin samples ([*]the stress-strain curve was highly non-linear. Therefore, the section modulus at 0.8% strain is reported).

.

Resin type	Number of samples tested	Elastic modulus (MPa)		Ultimate tensile strength (MPa)		Strain-to-failure (%)	
		Average	S.D.	Average	S.D.	Average	S.D.
EPO-TEK®-305	6	94.4[*]	1.1	6.7	1.4	9.2	0.4
EPO-TEK®-310M	6	3.48	0.6	0.2	0.04	2.2	0.2
EPO-TEK®-314	6	1047.9	22.5	27.2	2.1	1.1	0.6

Table 4.8 A summary of the secant modulus for the EPO-TEK®-305.

Strain (%)	Secant modulus (MPa)
0.8	94.4
7.1	32.1
9.7	25.2
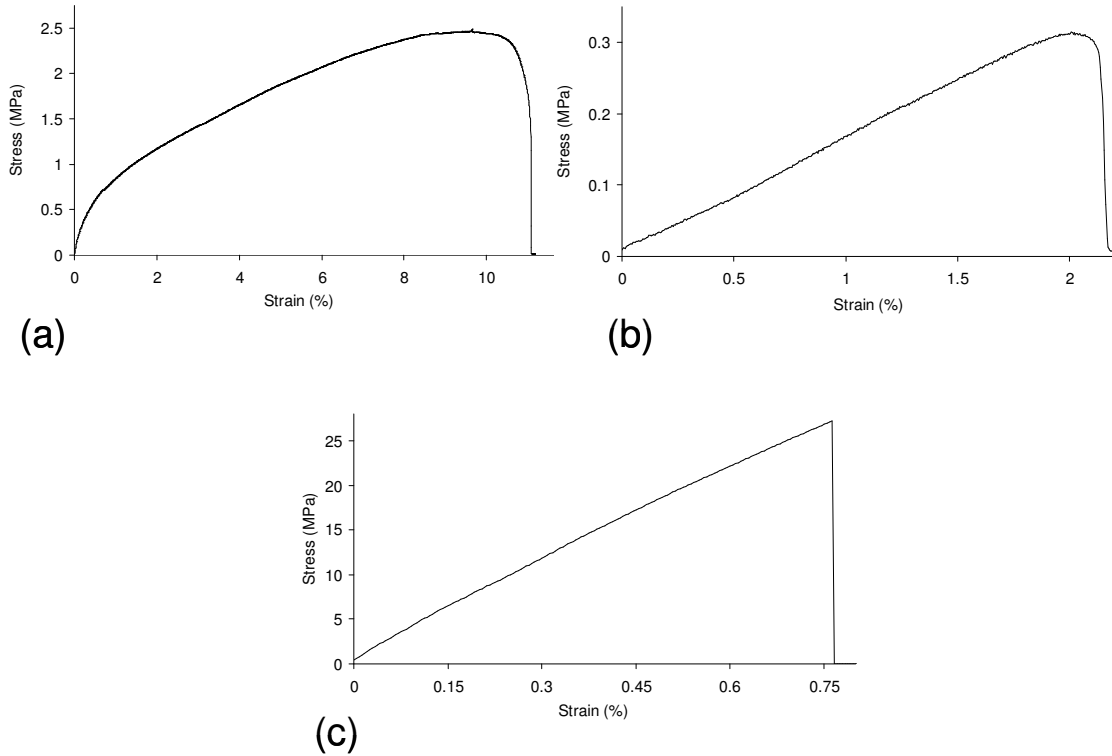
Figure 4.18 Graphs showing typical stress versus strain plots for: (a) EPO-TEK®-305; (b) EPO-TEK®-310M; and (c) EPO-TEK®-314 neat resins.
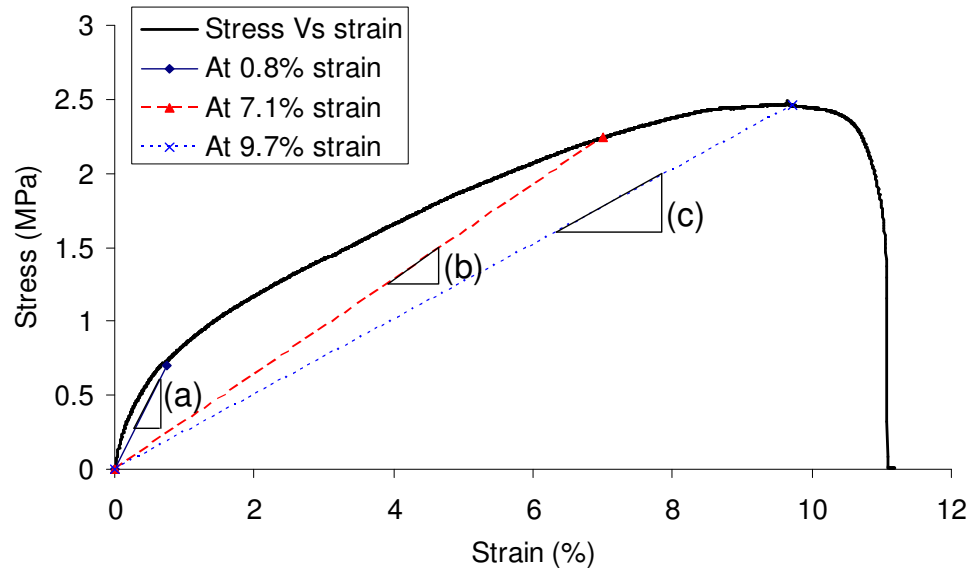
Figure 4.19 Representative graph for the illustration of secant moduli calculations in the case of the EPO-TEK®-305 resin system; the slope of the line connecting the origin and the stress/strain plot at: (a) 0.8% strain; (b) 7.1% strain; (c) 9.7% strain.

The mechanical properties reported by the manufacturer for the three resin systems were given as the "storage modulus", however, no further details were provided. The storage modulus is generally obtained from dynamic mechanical thermal analysis (DMTA) and the following properties have to be cited: (i) test frequency; (ii) temperature; (iii) the geometry of the test fixture; and (iv) the mode of load application. As this information was not reported by the manufacturer, it is not possible to compare and discuss the data obtained in the current study where the data were generated via tensile tests.
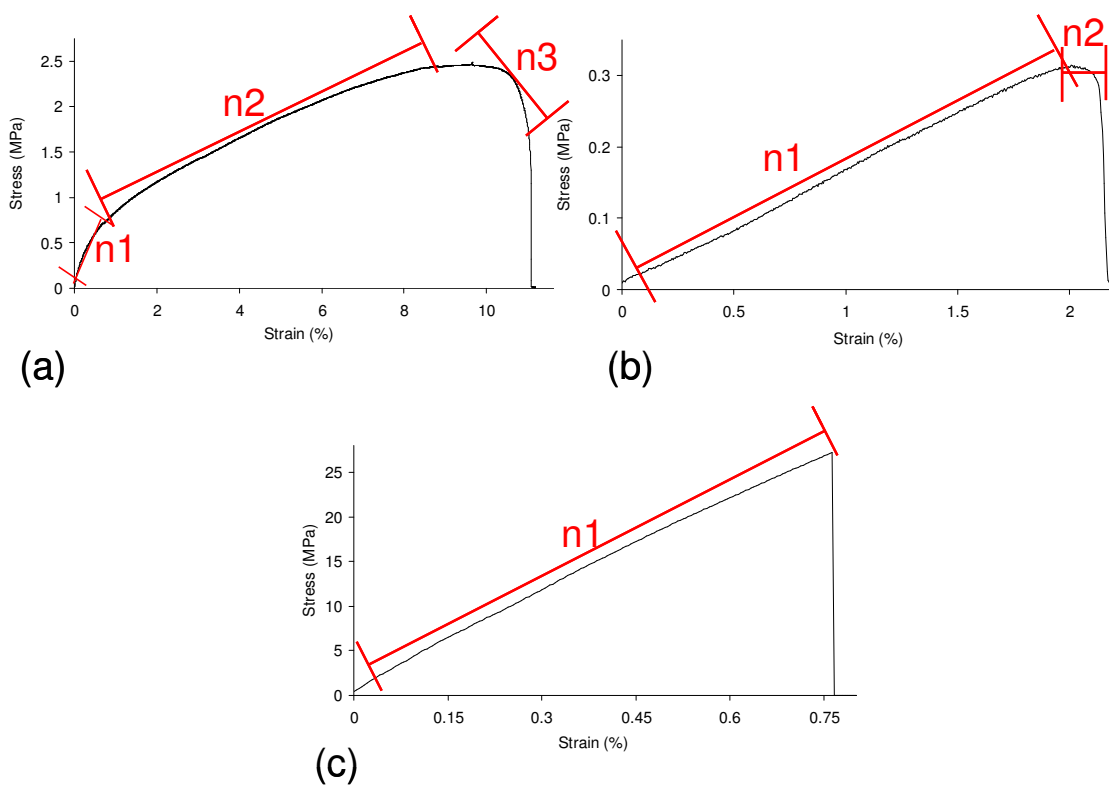
Figure 4.20 Graphs showing regions of stress versus strain plots of: (a) EPO-TEK®-305; (b) EPO-TEK®-310M; and (c) EPO-TEK®-314 resin.

The different regions of stress versus strain plots for the three resin systems are shown in Figure 4.20 (a-c). With reference to Figure 4.20a, the stress versus strain plot of EPO-TEK®-305 exhibited three regions. The region labelled 'n_1' may be regarded as the elastic region where the stress was directly proportional to strain. This section was small as

compared to the other two sections of the stress versus strain plot. The EPO-TEK®-305 resin was ductile; the hardness of this resin system was only 19 on the Shore-D scale, as compared to EPO-TEK®-314 that exhibited a hardness of 80 on the same scale.

Table 4.9 Summary of published data related to the mechanical testing of neat resins.

Reference	Materials	Failure strength (MPa)	Failure strain (%)
Groot *et al.* [155]	Araldite (epoxy)	70	1.2
[186-188]	Polymethyl methacrylate (PMMA)	65	10
	Polystyrene	56.6	2.4
	Polycarbonate	62	8
Bohse *et al.* [154]	Polypropylene (Notched samples)	35	
Barré *et al.* [151]	Polypropylene with 0.5 mm short-fibres	37.7	0.9
Huguet *et al.* [158]	Polyester	70	7.5
The mechanical properties of resin used in the current work	EPO-TEK®-305	6.7	9.2
	EPO-TEK®-310M	0.2	2.2
	EPO-TEK®-314	27.2	1.1

The tensile testing of EPO-TEK®-305 exhibited non-linear stress-strain plots. The behaviour of tensile test specimens can be regarded as highly non-linear in the second region labelled 'n_2' on the stress versus strain plot, i.e. between 1-9% of the applied strain. The transition from regions n_2 to n_3 may be due to yielding prior to failure. It was visually observed that at this point, a crack was initiated that propagated perpendicular to the

longitudinal axis of the test coupon. As the applied stress was further increased, the crack propagated in the vicinity of the centre of the gauge length until the complete fracture of the test coupon. Representative images of fractured specimens of the EPO-TEK®-305 resin are shown in Figure 4.21a.

The EPO-TEK®-310M resin demonstrated a slightly different behaviour; the stress versus strain plot was linear as shown in Figure 4.20b. The deformation in this section was elastic. The elastic modulus was calculated by the slope of region n_1 on the stress versus strain plot. In the case of EPO-TEK®-310M, the yield point is poorly defined (region n_2), however the test specimen fractured catastrophically. The EPO-TEK®-314 resin system was brittle in nature, with a linear stress versus strain plot and a defined failure point as indicated in Figure 4.20c. The elastic modulus was calculated using the slope of the section highlighted by line 'n_1'. The mechanical properties of the EPO-TEK® resins are summarised in Table 4.7.

The published data related to the mechanical properties of neat resins are summarised in Table 4.9. With reference to Table 4.9, the ultimate failure strength of the neat resins range between 35-70 MPa. Groot *et al.* tested epoxy samples with a cross-sectional area of 75 mm^2. The gauge length was 100 mm. The cross-sectional area of the neat resins used in this study was ~55 mm^2. Table 4.9 shows the ultimate failure strength of three thermoplastics i.e. PMMA, polystyrene and polycarbonate. These resins were selected since their failure strains are within the same range of the resin systems used in this study. It can be observed that the failure strength of the EPO-TEK® resin system was comparatively lower. The choice of the resin systems used in this study was influenced by the optical properties of the commercially available resins. The resin systems used in this study were low-refractive index materials. The physical properties of the EPO-TEK® resin

systems were different. For example, the viscosity of the EPO-TEK®-305 resin was the lowest and it was fairly easy to impregnate the fibres. The pot-life for this resin was 20 minutes; therefore, it was unsuitable for the resin-injection technique. On the other hand, the pot-life of the EPO-TEK®-310M was 2 hours but the viscosity was too high to impregnate the fibres using the resin-injection technique. In addition, EPO-TEK®-310M was flexible with low stiffness. Considering all these factors, EPO-TEK®-314 was finally selected for the manufacturing of self-sensing composites. Its' stiffness was the highest among the three resin systems investigated. It has a pot-life of 96 hours. Additionally, with this resin system the fibres could be impregnated more easily using the resin-injection technique. The fracture behaviour of the neat-resin test specimens will be discussed with the acoustic emission results.

4.2.2   Acoustic emission monitoring and evaluation

Acoustic emission (AE) is a well-established technique which is capable of detecting different damage types in fibre reinforced composites [61, 79, 141, 151, 153, 155-157, 159, 161]. The experimental procedures for the AE experiments were described in Section 3.4. The analysis of the acoustic signal is presented in this section to identify the characteristic damage modes occurring in the test coupons.

An example of typical settings used for the AE system is summarised in Table 4.10. The values cited in Table 4.10 were selected after consulting the literature [58, 151, 154, 155, 158, 161, 165] and the manual for the AE monitoring system. The threshold was selected by loading the samples in the Instron grips and then performing a "dry" test to establish the background noise. Noise in the system was due to the tensile test machine, grips and other electrical equipment [65]. Pencil lead break tests were performed on the end-tabs and the acoustic signal emanating from the fracture of a 0.5 mm diameter (2HB) pencil-lead was

used to set the threshold. After a number of trials, thresholds of 25 dB and 40 dB were finally selected for the neat resins and composites respectively. A lower threshold for neat resins was required due to the attenuation of the acoustic wave in the neat resins [151, 158, 165].

Table 4.10 Transducers and typical settings used for the AE experiments.

Sampling rate	2 MHz
Preamplifier gain	40 dB
Threshold detection	25 dB, 40dB
Coupling	Silicon grease
Peak definition time	50 micro-seconds
Hit definition time	100 micro-seconds
Hit lock time	300 micro-seconds
AE sensor	R15, Micro-80

4.2.3 Acoustic emission monitoring of the neat resins

AE testing was performed using two surface-mounted Micro-80 piezoelectric transducers (PZT) supplied by Physical Acoustics, UK. The experimental details for the AE setup were described in Section 3.4.

In conventional AE testing, the acoustic wave produced by a source is converted to a voltage signal by a piezoelectric (PZT) transducer. The amplitude of the AE-signal (AES) is the highest peak voltage attained by an AE waveform. The voltage signals recorded by the PZT transducer were expressed on a decibel (dB) scale (1 dB = 1µV [149]). The maximum amplitude of the AES recorded during tensile testing of neat-resin samples was

60 dB. The peak frequencies produced by matrix cracking ranged between 30–180 kHz. Table 4.11 presents a summary of the amplitudes of the AES and number of hits produced during mechanical testing of the neat-resin samples.

Table 4.11 Summary of acoustic emission results of the neat-resin samples.

Sample type	Number of samples	Number of hits		Amplitude (dB)		Peak frequency (kHz)	
		Average	S.D.	Average	S.D.	Average	S.D.
EPO-TEK®-305	6	191	74	39.4	2.6	118.6	82.1
EPO-TEK®-310M	6	26	25	22.4	4.73	214.4	85.6
EPO-TEK®-314	6	238	179	36.9	2.2	94.7	28.1
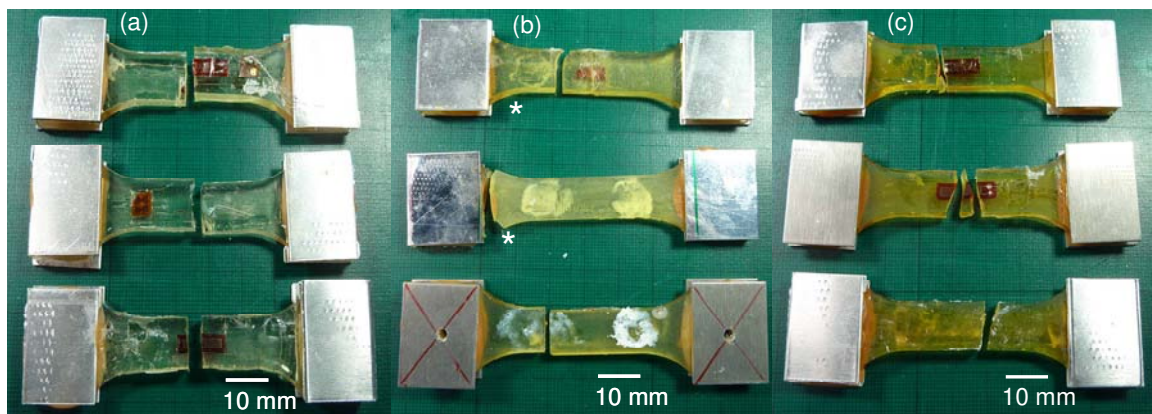
Figure 4.21 Images showing typical fractured samples for: (a) EPO-TEK®-305; (b) EPO-TEK®-310M; and (c) EPO-TEK®314 resin.

Figure 4.22 (a-f) shows the AE results for the three different resins used in this study. With reference to Figure 4.22a, the number of AE hits recorded during the tensile testing of EPO-TEK®-305 neat-resin coupons varies between 150 and 330 for the majority (83%) of the tested-samples. The average number of hits per sample was found to be 200 ± 70. In

the case of EPO-TEK®-305, Figure 4.22b shows that the amplitude of the AE signals were in the range of 35 to 45 dB.
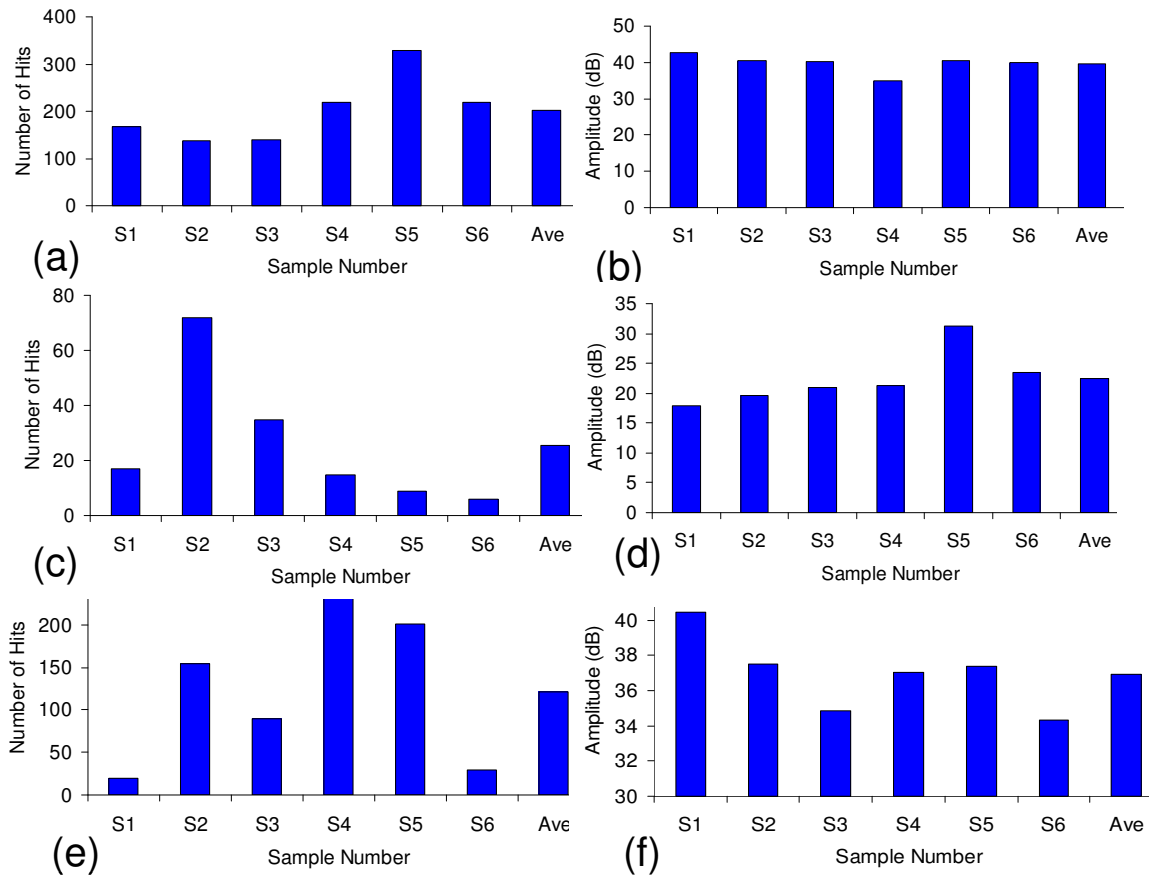
Figure 4.22 Plots of AE hits and amplitude for: (a-b) EPO-TEK®-305; (c-d) EPO-TEK®-310M; and (e-f) EPO-TEK®314 resin systems.

In Figure 4.22c, it can be observed that the variability in the number of AE hits recorded for the EPO-TEK®-310M resin system was more compared to EPO-TEK®-305. However the AE amplitude, varied over a narrow range (36 to 42 dB) for the majority of test coupons. The behaviour of the amplitude variation with respect to EPO-TEK®-305 and EPO-TEK®-310M was similar. With reference to Figure 4.22e, the EPO-TEK®-314 resin showed a higher variability in the number of hits when compared to the other two resins. The maximum amplitudes of the acoustic emission signal (AES) of 41 dB, 37 dB and 23

dB were obtained for EPO-TEK®-305, EPO-TEK®-314 and EPO-TEK®-310M resins respectively.

On comparing the graphs in Figure 4.22 (a-f), it can be observed that the variability in the number of hits was relatively low in the case of the resin type which produced a higher average amplitude of acoustic emission.

The number of AE hits recorded could have been affected by the location of the PZT transducer, fracture location, material properties, attenuation of AE waves and the threshold setting of the AE signal [151, 158, 165]. The location of the PZT transducer was fixed as discussed in Section 3.4; however the number of AE hits detected by the transducer were influenced strongly by the location and propagation of the fracture. For example, the variability in the location of cracking was more in the case of EPO-TEK®-310M and EPO-TEK®-314 resin systems, hence there was variability in the number of hits detected. In the case of EPO-TEK®-305, all the test coupons fractured in the vicinity of the centre of gauge length. Therefore, the variability in the number of hits was significantly lower than the other two resin types. Figure 4.21 shows images of fractured test specimens for the EPO-TEK® resins. With reference to Figure 4.21, all the test coupons of the EPO-TEK®-305 resin system fractured in the vicinity of the centre of gauge length, whereas the damage-location was different for the other two resin systems.

4.2.4   Analysis of the acoustic emission signals of the neat resins

The number of AE hits, amplitude and frequency are the most widely adopted parameters for describing damage in composite materials [151, 158, 165]. Different damage modes in a composite generate their characteristic frequencies and amplitudes during mechanical loading [47, 48, 125, 139, 144-148, 158, 177, 189-191]. In this section, an analysis of AE signals (recorded during the tensile testing of neat-resin samples) is presented.

The extent of damage in a test coupon can be assessed by plotting the cumulative number of AE hits against time. The cumulative number of AE hits was calculated by the successive addition of AE hits recorded from each AE signal detected as the test progressed. The change in slope of the cumulative AE hit plot against time is indicative of the evolution of damage in the test coupon [45, 65, 79].
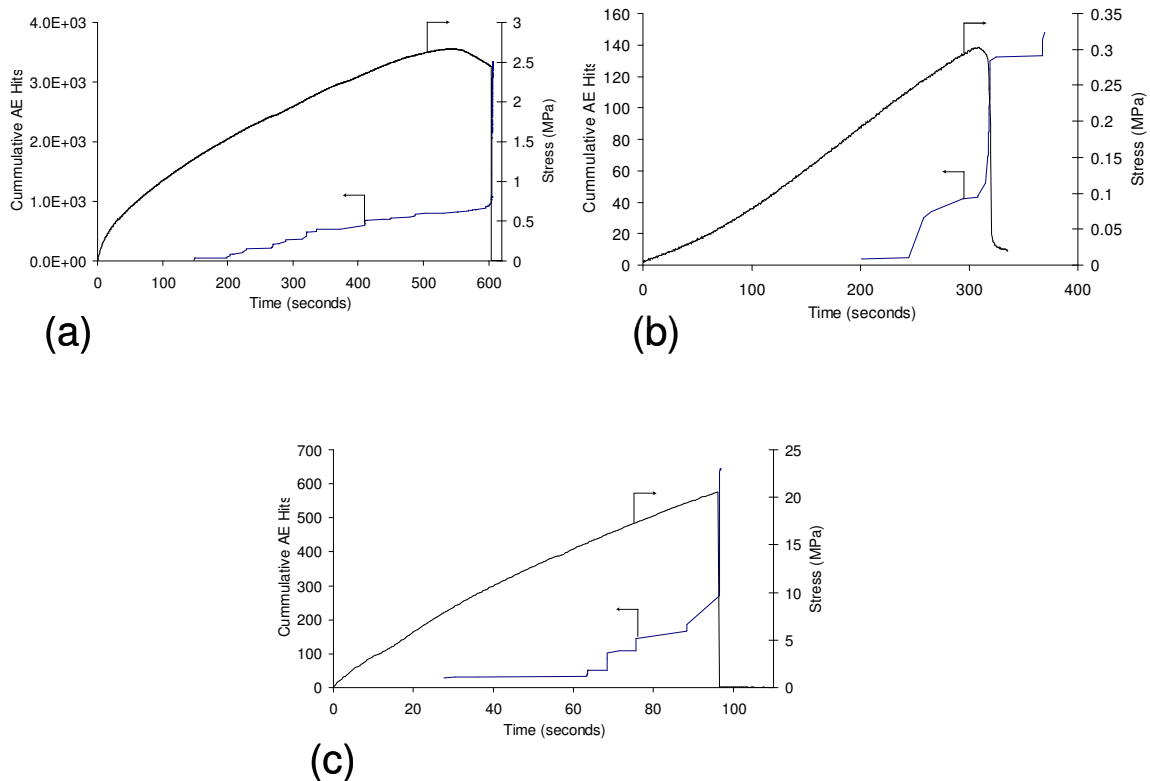
Figure 4.23 Graphs showing representative cumulative AE hits and load as a function of time for: (a) EPO-TEK®-305; (b) EPO-TEK®-310M; and (c) EPO-TEK®314 resin.

Figure 4.23 (a-c) shows the representative plots of cumulative AE hits and calculated stress versus time for the three resin systems. Figure 4.23a shows that there was a gradual increase in the cumulative hits with a series of step-rises occurring over short durations. This was representative of the behaviour of the EPO-TEK®-305 resin system. The EPO-TEK®-305 fractured with a visible crack propagating in the vicinity of the centre of the coupon as shown in Figure 4.25. On the contrary, the increase in AE hits for EPO-TEK®-310M resin was abrupt with sudden change of slope as shown in Figure 4.23b.

Figure 4.23c shows a representative plot of cumulative hits versus time of the EPO-TEK®-314 neat-resin system. A gradual increase in the cumulative AE hits with a series of steps-rises was observed. The EPO-TEK®-314 specimens generated audible cracking during the tensile testing. As previously mentioned, EPO-TEK®-314 exhibited catastrophic failure due to the hardness and brittle nature of the resin system. The hardness of this resin system was 80 on a shore-D scale. Its modulus was more than 110 times the other two EPO-TEK® resins. However, there was no significant difference in the magnitude of amplitude of the AES generated by the EPO-TEK®-314 resin system.
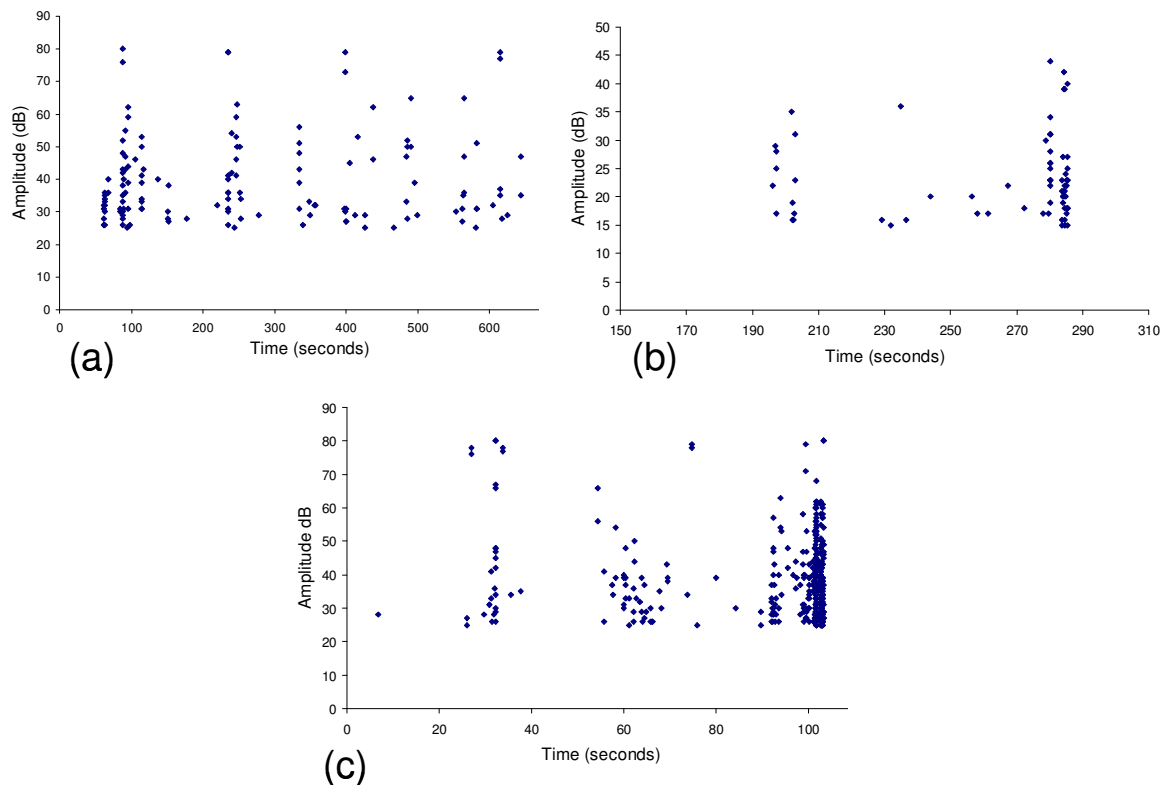
Figure 4.24 Graphs showing amplitude of the AES as a function of time for: (a) EPO-TEK®-305; (b) EPO-TEK®-310M; and (c) EPO-TEK®314 neat-resin samples.

Figure 4.24 (a-c) shows representative graphs of the amplitude of the AE signal as a function of time for the three resin systems. By comparing the plot of EPO-TEK®-305 with the other two resins, it can be observed that with the resin system with a comparatively

high ultimate strain (<8%) i.e. EPO-TEK®-305, intermittent AE hits were produced during the loading phase, however the majority of AE hits were observed at the onset of failure. Whereas in the case of EPO-TEK®-310M and EPO-TEK®-314, the majority of high-amplitude AE hits were observed prior to catastrophic failure. EPO-TEK®-310M and EPO-TEK®-314 exhibited brittle fractures with ultimate strains of 2% and 1%, respectively.
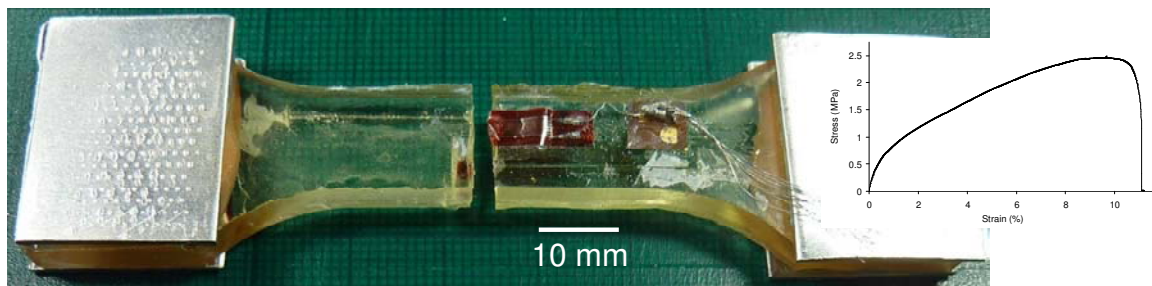
Figure 4.25 A representative image of a fractured EPO-TEK®-305 neat-resin specimen, the insert shows the corresponding stress-strain data.
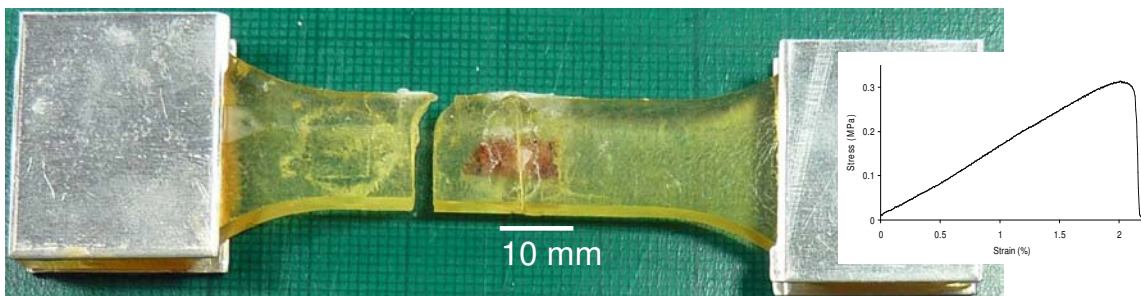
Figure 4.26 A representative image of a fractured EPO-TEK®-310M neat-resin specimen, the insert shows the corresponding stress-strain data.
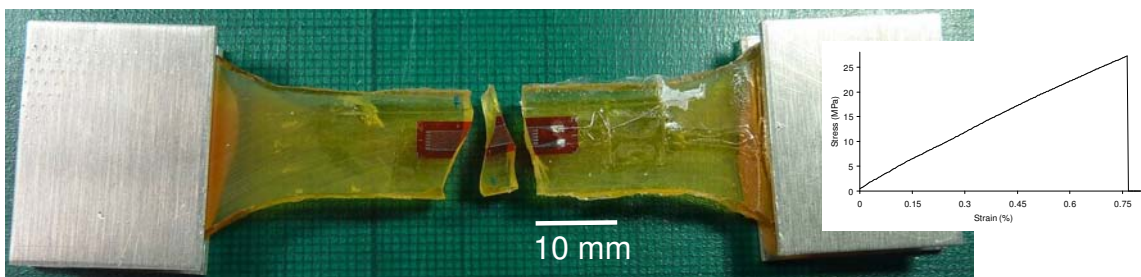
Figure 4.27 A representative image of a fractured EPO-TEK®-314 neat-resin specimen, the insert shows the corresponding stress-strain data.

Figure 4.25 shows a typical fractured test specimen of the EPO-TEK®-305 resin system. The observations during the tensile test were as follows: In all of the samples-tested (6 samples) a predominant crack developed at approximately 7-8.5% of the strain-range. The crack propagated perpendicular to the longitudinal axis of the test coupon, until the coupon fractured. The stress/strain plot shown in the insert in Figure 4.25 was non-linear but for all the samples, a single predominant crack was initiated (approximately ot the centre of the gauge length of test coupons) that propagated to failure.

Figure 4.26 shows a typical fractured test specimen of EPO-TEK®-310M; the stress/strain curve is shown as an insert in the fractured image. The stress/strain behaviour of EPO-TEK®-310M was linear for all the tested-samples (6-samples); the peak-load was poorly defined, a crack was initiated at approximately 2% of strain that propagated in the transverse direction and the sample then fractured catastrophically (in comparison to the EPO-TEK®-305 test coupons). However, an interesting observation was noticed towards the end of crack propagation, a few samples (60%) yielded just before failure (see Figure 4.26).

In the case of EPO-TEK®-314, Figure 4.27 shows a photograph of a fractured test specimen and the stress/strain plot as an insert. Unlike the other two resin systems, the EPO-TEK®-314 test specimens exhibited linear-elastic stress/strain plots. There was no evidence of yielding in the test specimens, and for the majority of the cases the samples fractured by fragmenting in the damage location.

Although the same casting methods were used to produce neat-resin test specimens, the specimens that exhibited a failure strain greater than 2% (EPO-TEK®-305) were practically easier to cast. However, in the case of EPO-TEK®-314, it was comparatively difficult to ensure the same quality of the edges. The EPO-TEK®-314 samples were

polished carefully by using 2500 abrasive-paper to remove any flashings. However, due to the brittle nature of the resin system, a few surface-flaws might have initiated.

Table 4.12 A summary of AE characteristics of polymers reported by various authors.

Source	Materials	Test type/ Condition	Amplitude (dB) or Frequency (kHz)	Average number of hits
Groot *et al.* [155]	Araldite (epoxy)	Tensile	90-150 kHz	>120
Bohse *et al.* [154]	Poly-propylene	Tensile Notched samples	40-80 dB	>100
Barré *et al.* [151]	Polypropylene with 0.5 mm short fibres	Tensile	40-60 dB	<80
Huguet *et al.* [158]	Polyester	Tensile	55-70 dB	100-180
Haselbach *et al.* [192]	Epoxy L-20 (Rutapoxl®)	Tensile	30-60 dB	-----

The published data relating to the acoustic emission results of neat resins are presented in Table 4.12. The amplitude of the AES of three EPO-TEK® resins was 30-70 dB. This was within the same general range as reported by Barré *et al.* [151] and Haselbach *et al.* [192]. They reported that the amplitude of the AES of polypropylene (PP) and epoxy L-20 (Rutapoxl®) was 30-60 dB. Barré *et al.* found that the number of AE hits were 80 per test specimen. The material of the test specimen was 40% short-glass fibres and 60% PP. The length of the short-fibres was less than the critical length; therefore, the failure mode

during tensile loading was mainly matrix cracking. Similarly, Haselbach *et al.* reported that neat-resin specimens of epoxy L-20 produced amplitude of the AES, 30-60 dB. This amplitude range was reported to be generated by the matrix cracking [87, 144, 153, 154, 156, 157, 165]. Although Barré *et al.* tested PP whereas Haselbach *et al.* tested a different epoxy resin system, the amplitude of the AES corresponding to the matrix cracking was approximately the same. It has been reported by several authors that different failure modes of fibre reinforced composite materials generate their characteristic frequencies and amplitudes (see Section 2.5.5). Although during mechanical testing of composite test coupons, it is relatively difficult to identify exactly the specific amplitude of the AES and frequencies generated by the damage mechanisms in the composite materials. However few researchers [151, 154, 155, 165] tested specimens that can only generate one type of failure in the test coupon, for instance, fibre/matrix debonding and matrix fracture can be generated by changing the orientation of the fibres in the composite specimen or by testing neat-resin samples. The rationale of the neat resin acoustic emission testing was to determine the specific amplitude of the AE signal corresponding to the matrix failure and this was successfully achieved. This magnitude of the amplitude of the AES (30-60 dB) was observed in the acoustic emission monitoring of self-sensing composites. This amplitude was generated particularly at the strain-to-failure of the matrix (1%), although the composite test coupon fractured at a strain greater than 1%. This will be discussed in more detail in the acoustic emission monitoring of composite test specimen in Section 4.5.4.

4.3 Mechanical Testing of the Fibre Bundles

Conventional E-glass fibres (PPG Ltd., UK) and custom-made small-diameter optical fibres (SDOF) were used in this study. The E-glass fibres were silane-treated and the SDOF were heat-treated to pyrolyse the binder. The attributes of these fibres were discussed in Section 4.1.1. Fibre bundles from as-received and treated E-glass and SDOF bundles were prepared and tensile tested according to the procedures described in Section 3.3.1.2. The results obtained from the tensile test, acoustic emission monitoring and image analysis are presented in the next sections.

4.3.1 Tensile test results of the fibre bundles

This section describes the tensile test results for different fibre types. The end-tabs, as shown in Figure 3.6, were designed to avoid crushing of the fibres between the grips of the tensile test machine. Slippage of the test specimen within the end-tab was not observed for the fibre bundles.

Figure 4.28 (a-d) shows representative graphs for the load versus extension for the four types of fibre. The load versus extension plots did not show an abrupt increase after the peak-load was attained. This indicates non-catastrophic failure of the fibre bundles. This may be attributed to the following factors: (i) the tension of the fibres within the bundle was variable and therefore, they were not loaded evenly [58, 180]; (ii) the fibres in the bundle were not perfectly aligned parallel to each other; and (iii) there was a strength distribution of the fibres. All these factors could have resulted in an uneven load distribution between individual fibres of the bundle, and therefore, the bundle fractured non-catastrophically.
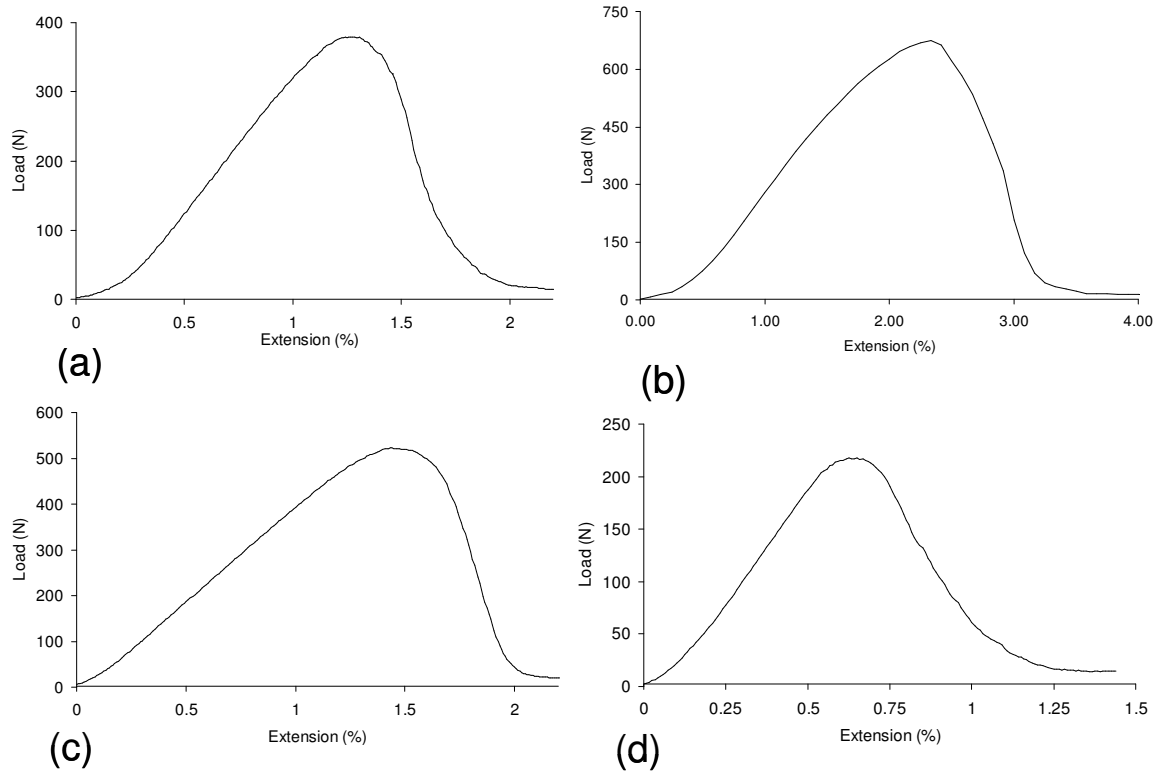
Figure 4.28 Graphs showing load as a function of extension for: (a) As-received E-glass fibre bundle; (b) Silane-treated E-glass fibre bundle; (c) As-received SDOF bundle; and (d) Heat-treated SDOF bundle.

As-received fibre bundles: Figure 4.28a shows the peak-load for the E-glass fibre bundle is approximately 400 N with a maximum extension of ~2%. A similar graph for the as-received SDOF bundle shows a peak-load of ~550 N with maximum extension of 2% as shown in Figure 4.28c. However, these values differ significantly when the fibres were silane-treated and heat-treated in the case of E-glass fibres and SDOF, respectively. Table 4.13 presents a summary of average mechanical properties of the fibre bundles. It can be observed from Table 4.13, that the average peak-load of the as-received SDOF was higher than the as-received E-glass bundles. As already mentioned, the E-glass fibres were un-sized and exhibited a variation in the peak-load due to surface-flaws and inter-fibre friction during tensile loading [61, 193]. It was observed that 70% of the samples fractured at around 550±50 N and the rest fractured at around 390±50 N. However, in the case of the

as-received SDOF, all the samples fractured at 550±50 N. The conclusion here is that the average peak-load of the as-received SDOF was higher than the as-received E-glass fibres.

Table 4.13 A compilation of the average mechanical properties of the fibre bundles used in this study.

Fibre bundle type	Number of samples	Maximum load at failure (N)		Extension at maximum load (%)	
		Average	S.D.	Average	S.D.
As-received E-glass	7	500.1	55.1	1.8	0.34
Silane-treated E-glass	6	601.2	57.2	2.1	0.25
Small-diameter optical	6	544.6	30.9	1.4	0.05
Small-diameter optical (heat-treated)	6	216.4	18.2	0.7	0.10

Silane-treated E-glass fibre bundle: The overall aim of the current study was to investigate and cross-correlate the influence of surface treatments and processing conditions on the fracture behaviour of unidirectional glass fibre reinforced composites. The as-received E-glass fibre bundles were silane-treated as described in Section 3.2.2.8.

The basic function of fibre surface treatments is to improve the fibre surface compatibility with the matrix and to create a strong bonding at the fibre matrix interface [13, 15]. These conditions are necessary for effective load-transfer from the matrix to the fibres. Coupling agents are molecules which have one end compatible with the silane structure of the glass and the other end compatible with the matrix. They can be thought of as bridges connecting the reinforcement and the matrix [15].

Figure 4.28b shows the tensile test results for silane-treated E-glass fibre bundles. The average peak-load was observed to increase, when the E-glass fibres were silane-treated. This may be because: (i) the silane-treatment of the E-glass partially 'bonded' the glass fibre filaments and this could have rendered a degree of protection to the fibres from abrasion damage; (ii) it is speculated that since the silane-treatment of these fibres resulted in the partial 'bonding' there may have been load-transfer between the fibres during tensile loading. This is not possible in the case of the as-received fibre bundle, as when each filament fractures, it ceases to carry any load [49, 180]; and (iii) it has been reported [45, 61] previously that a coating can improve the mechanical properties of reinforcing fibres. The speculation here is that the coating reduces the significance of surface-flaws. This may account for the fact that the average peak-load increased by 15% when compared to the as-received E-glass fibre bundle.

Heat-treated SDOF: Figure 4.28d shows the load versus extension plot of a heat-treated SDOF bundle. The binder on the SDOF bundle was removed by pyrolysis at 450 ºC for 6 hours. The average peak-load of a heat-treated SDOF bundle was approximately 220 N. This is lower than 40% when compared with the as-received SDOF bundle. The average peak-load of the as-received SDOF and heat-treated SDOF were 544.6 N and 216.4 N, respectively. The decrease in peak-load may be attributed to the heat treatment of fibres, where the fibres become fragile and brittle (see Section 4.1.1). Feih *et al.* [193] discussed the effects of burning of glass fibres and heating time on the tensile strength and failure mechanisms. It was reported that the heat-treatment of E-glass fibre bundles causes a 30% decrease in the ultimate strength. The chemical composition remained almost unchanged [193]. It was found that the heat-treated fibre bundles showed a larger scatter in strength than the un-heated fibres, which suggested an increase in the flaw-sizes [45, 50]. This increase in magnitude and dimensions of the flaw-size was supposed [193] to be caused by

the heat-treatment of the fibre bundles. Similar effects were noticed during the tensile testing of the heat-treated SDOF bundles. The peak-load of the heat-treated SDOF bundle was decreased by 40% and a greater variation in the peak-load was observed from sample-to-sample. However, the removal of binder from the as-received SDOF resulted in comparatively better mechanical properties of the composites manufactured from heat-treated SDOF.

Table 4.14 Selected published data related to the mechanical properties of E-glass fibre bundles.

Reference	Approximate number of filaments	Gauge length (mm)	Fibre bundle clamping method	Ultimate failure strength (MPa)	Failure strain (%)	Manufacturer
R'Mili *et al.* [65]	2000	100	Fibres were glued into metal tubes	850	2.1	Vetrotex Ltd.
Hill *et al.* [49]	600	70	Aluminium end-tabs	970	1.9	Fibreglass Ltd.
Okoroafor *et al.* [50]	600	70	Aluminium end-tabs	1250	2.3	Not reported.
Results obtained in this study						
As-received E-glass	2400	100	Aluminium end-tabs with slot (see Figure 3.6)	982	1.8	PPG Ltd. UK.
Silane-treated E-glass	2400	100		1123	2.1	
SDOF	2800	100		1088	1.4	Aomolin Ltd. China
SDOF (heat-treated)	2800	100		520	0.7	

Table 4.14 lists a selection of the published data, including the current work related to the tensile testing of E-glass fibre bundles. The ultimate peak-load of the fibres used in this study varies between 500-600 N for E-glass, with an average extension-to-failure of 1.8-2.2 %. Comparing the data obtained in this current study with the published data, it can be concluded that the peak load and extension-to-failure of the E-glass fibres was within the same general range, it is difficult to compare the data generated by the different researcher cited in Table 4.14 for the following reasons:

(i) Fibre-diameter: It was demonstrated in Section 4.1.1, that the E-glass fibres have a diameter distribution of ±3 µm, whereas the variation in SDOF was found to be ±1 µm. This diameter variation will influence the stress the individual fibres can carry. The effects of variation in the fibre diameter on the tensile properties of fibre bundles were not discussed by the researchers cited in Table 4.14. In general, they have tended to use mean diameters for calculating the ultimate fibre strength [43, 65, 159, 180]. Variations in the diameters can cause a change in the local load-sharing and the transfer of load between the surviving fibres [65]. Therefore, the effects of diameter variation are likely to be more critical in a composite than a fibre bundle [45, 65].

(ii) End-tabs and method of loading: The different clamping techniques used may also account for the observed variation in the strength of the fibre bundles cited in Table 4.14. In this current study, the fibres were impregnated within the end-tabbed region to facilitate the light transmission as described in Section 3.2.2. Therefore, the load was transferred from the end-tabs to the impregnated section of the fibre bundle, and then to the filaments in the bundle. By contrast, the fibres used by R'Mili [65] were bonded directly to the metal tubes or aluminium end-tabs [45] by other researchers. For example, Hill *et al.* used aluminium end-tabs with a gauge length of 160 mm, whereas R'Mili *et al.* used metal

tubes to bond the 100 mm fibre bundles; the filaments could be squeezed and damaged between the metal-tubes when the test specimens were clamped between the jaws of a tensile test machine. In addition, due to the metal tubes, it was also possible that the inherent twists in the bundle may contribute to the lower peak-load of the bundles tested by R'Mili. A custom-designed end-tab (see Figure 3.6) was used in this current study to avoid the crushing and squeezing of fibres. Therefore, the strength of un-sized E-glass bundle was higher than that reported by R'Mili. A comparative increase in the strength of silane-treated E-glass bundles was observed and this could have been due to the better load-transfer as discussed previously.

(iii) Fibre supplier: The fibres cited in Table 4.14 were supplied by different manufacturers. Therefore, it is reasonable to expect a variation in their properties.

(iv) Strain-rate sensitivity: It is well-known that glass fibres are strain rate-sensitive [194, 195]. R'Mili *et al.* tested fibre bundles at 2 µm/second, whereas Hill *et al.* tested bundles at 0.03 mm/minute. Not all the researchers cited in Table 4.14 and in Section 2.5.5 reported the rate of loading during tensile testing of the fibre bundles. Therefore, it is reasonable to accept a variation in the mechanical properties.

In conclusion, a characteristic feature of all four types of fibre was the non-catastrophic failure of the fibre bundle. The average peak-load of E-glass fibre bundles was increased when they were silane-treated. On the other hand, the peak-load was decreased when the SDOF bundles were heat-treated. The results obtained in this study were similar when compared with published data.

In the next section the acoustic emission data relating to the tensile testing of the fibre bundles are presented.

4.3.2   Acoustic emission monitoring of the fibre bundles

Acoustic emission monitoring of the fibre bundles was carried out according to the procedures described in Section 3.4. The fibre bundle test specimens were prepared from as-received E-glass fibre, silane-treated E-glass fibre bundles, as-received small-diameter optical fibres (SDOF) and heat-treated small-diameter optical fibres.
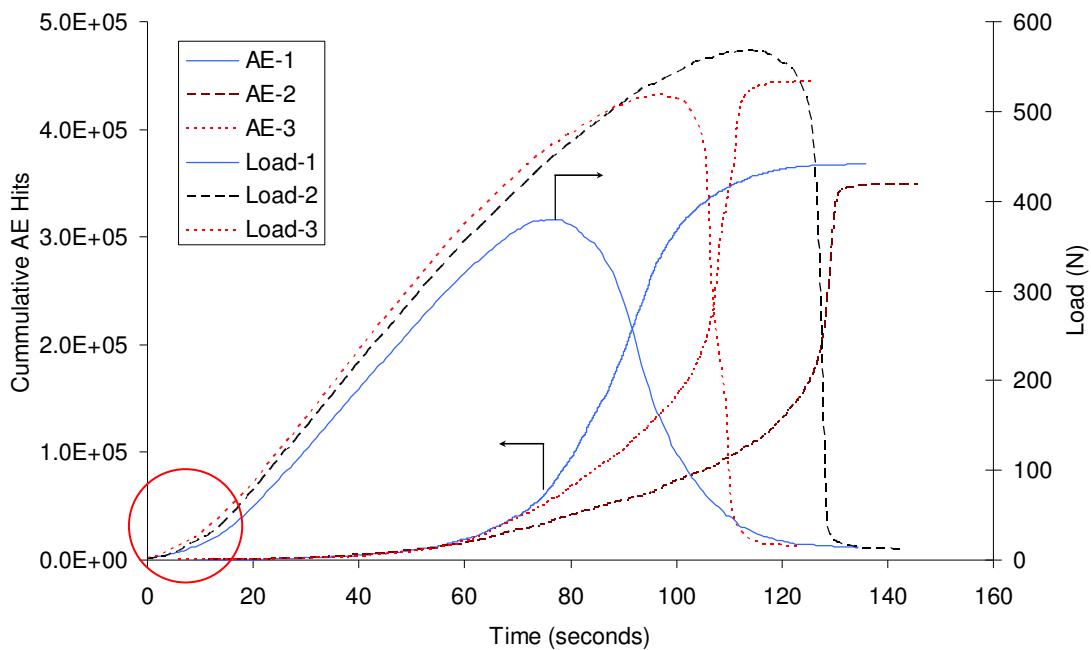
Figure 4.29 Graph showing plots of cumulative AE hits and the applied load as a function of time for three different specimens of as-received E-glass fibre bundles.

Figure 4.29 and Figure 4.30 show representative graphs of cumulative AE hits and applied load as a function of time for three test specimens of the as-received E-glass fibre bundles and SDOF. With reference to Figure 4.29 and Figure 4.30, an initial lag was observed between 0-15 seconds of loading the sample, as highlighted by a red circle on the load versus time graphs. This lag was the due to the tensile test machine compliance [65].

Table 4.15 Calculated slopes of the plots of load versus time and cumulative AE hits versus time for three samples of as-received fibre bundles.

	As-received E-glass bundle		As-received SDOF bundle	
	Load/time (N/second)	Cumulative AE hits/time (hits/second)	Load/time (N/second)	Cumulative AE hits/time (hits/second)
Sample-1	5.8	11370.9	6.6	6012.2
Sample-2	6.5	16092.1	6.8	7406.9
Sample-3	6.7	14162.8	7.0	6571.2

As discussed previously, the notable increase in the cumulative number of AE hits is indicative of damage occurring in the test specimens. In the case of fibre bundles, this increase in the AE hit plot is normally observed at the onset of fracture. The cumulative AE plot kept on increasing even after the peak-load [55, 65, 180] due to the strength distribution of the fibres in the bundle. The E-glass fibre bundles exhibited a variation in the peak-load (between different samples) due to the twists, inter-fibre friction and surface-flaws. During the manufacturing of test samples, the twists present in the E-glass bundle were minimised by gently separating the fibres on a metal plate (see Section 3.2.2). However, the twists could not be removed completely. These effects can cause the fibre bundle to fracture at lower peak-loads [45, 65, 78, 159]. It was reported that the increase in the magnitude of surface-flaws in E-glass fibre bundles, increases the variation of peak-load from sample to sample [61, 193]. During this study, it was observed that 30% of samples fractured at 390±50 N and the rest fractured at 550±50 N. Although the methodology of sample preparation and the test procedures were the same, the observed variability in the peak-load could be due to the twists, inter-fibre friction and localised fibre-failure of the E-glass bundles [61, 193] as mentioned earlier. However, in the case of

the as-received SDOF, all the test specimens exhibited the least variation in the peak-load and fractured around 550±50 N.

Table 4.15 shows the calculated slopes of the two types of as-received bundles for the linear part of the load versus time plot (i.e. before peak-load). The slopes of the cumulative AE hits plot were calculated for the corresponding values of hits between 90-100 seconds for the SDOF and 80-110 in the case of E-glass fibre bundles. By comparing the calculated slopes of the as-received E-glass bundles, it can be observed that the cumulative AE hits of samples-2 and 3 increased at a slightly higher rate in comparison to sample-1. This was due to the difference in the rate of decrease of the load/time plot (after the peak-load) of the test specimen. The rate of decrease in load (after the peak-load was attained) of sample-1 was 13.5 N/second, whereas it was 176.8 N/second and 70.6 N/second for samples-2 and 3 respectively. By comparing the slopes of plots of AE hits with the rate of decrease in load; it can be observed that they were changing in direct proportion to each other. For instance, the slope of sample-2 was the highest (16092.1 hits/second) and the rate of decrease of the load was also the highest i.e. 176.8 N/second. The following factors may have contributed to the variation in the rate of the decrease of load/time plot (after the peak-load was attained) between sample-1 and other two samples: the interaction of fibres in the bundle; localised fibre failure; meandering fibres; twists and surface-flaws. In the case of samples-2 and 3, it is speculated that the majority of the fibres were fractured before the peak-load; however the fibre bundle resisted the applied load due to the twists and adhesion between fibres of the bundle. Therefore, it can be inferred that the cumulative hits plots were predominantly dependent upon the failure behaviour of the fibres in the bundle.
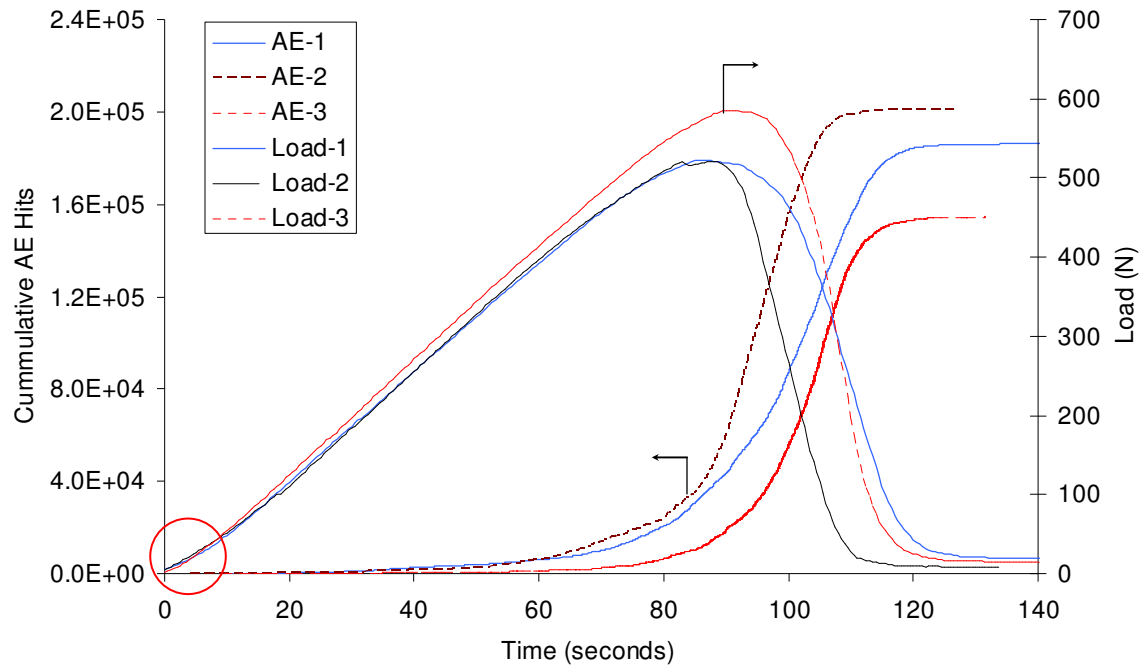
Figure 4.30 Graph showing traces of cumulative AE hits and the applied load as a function of time for three different specimens of as-received SDOF bundles.

In the case of the SDOF bundles, the plot of cumulative AE hits was influenced by the load/time plot and the rate of decrease in the load (after the peak-load was attained). Figure 4.30 shows the graphs of load and cumulative AE hits as a function of time for the three test specimens of as-received SDOF bundles. The slope of cumulative AE hits increased significantly after ~80 seconds (i.e. at the onset of failure of the fibre bundle). This increase in AE hits at the onset of failure was observed for all the SDOF bundles. The peak-load of all the as-received SDOF bundles (6 samples) only varied ±50 N. Therefore, the variation in the calculated slope of cumulative AE plots was also negligible as shown in Table 4.15.

Table 4.16 A comparison of the acoustic emission parameters of the fibre bundles.

Fibre bundle type	Number of samples	Number of hits		Amplitude (dB)		Peak frequency (kHz)		Average frequency (kHz)	
		Average	S.D.	Average	S.D.	Average	S.D.	Average	S.D.
As-received E-glass	7	6591	1086.1	59.7	5.1	54.5	11.8	67.1	12.2
Silane-treated E-glass	6	18914	3688.7	51.5	1.5	48.6	3.3	74.7	11.1
As-received SDOF	6	4452	652.9	60.4	2.9	130.8	10.3	90.4	5.7
SDOF (heat-treated)	6	6830	1704.3	58.1	2.9	89.6	14.5	112.8	28.2

The acoustic emission results of the four fibre types are summarised in Table 4.16. With reference to Table 4.16, the average number of hits recorded for the as-received E-glass fibres were 6591 with a standard deviation (SD) of 1086.1. This number of hits is ~30% greater than for the as-received SDOF. The average number of AE hits recorded for the as-received SDOF test coupons was 4452 with a SD of 652.9. The E-glass fibre bundles usually exhibit a broom-like appearance after fracture. This is caused by inter-fibre friction [45, 65, 78, 159, 193]. Figure 4.31 shows a representative image of a fractured E-glass fibre bundle.

Figure 4.31 A representative photograph of a fractured as-received E-glass fibre bundle specimen.

The friction between the fibres in a bundle may cause localised failure of fibres [49, 51, 65, 159, 180]. It was possible that the fibres were fracturing at isolated locations due to the inter-fibre friction or random flaws. These effects were more dominant in the un-sized bundles when compared to the 'sized' fibre bundles [159, 193]. The localised failure of fibres in the bundle produced a lower amplitude (40-60 dB) hits at strains that are lower than the failure-strain of the fibre bundle. This will be discussed in detail in Section 4.3.3. R'Mili *et al.* [65] found that the inter-fibre friction in the fibre bundle becomes more dominant as the gauge length of the bundle was increased. Although the comparative effects of inter-fibre friction were not obvious from the experiments done in this study (the gauge length was fixed at 100 mm), however the effects of inter-fibre friction were noticed when the E-glass bundles were silane-treated.

In the case of the silane-treated E-glass fibre bundles, the recorded number of hits was almost three times that of the E-glass fibre bundle as shown in Table 4.16. It was observed that the fibres were partially 'bonded' as a consequence of the silane-treatment process; and comparatively greater adhesion between the filaments was obvious. As described in Section 3.2.2, the silane-treatment involved a series of steps through which the fibres were exposed to a mixture of the silane ethanol and distilled water solution and subjected to heat-treatment (drying). Although the relative contribution of the silane treatment towards the degradation of individual fibres was not known from the experiments conducted, its

influence during the tensile testing appeared as an increase in the number of hits detected at low strain levels when compared with that of the as-received bundles. With reference to the mechanical tests, the onset of AE hits also occurred earlier in the case of the silane-treated E-glass fibre bundles.

Figure 4.32 A representative image of a fractured silane-treated E-glass fibre bundle specimen.

A representative image of fractured silane-treated E-glass bundle is shown in Figure 4.32. Comparing the image presented in Figure 4.32 with that of an as-received E-glass fibre bundle (Figure 4.31), the absence of broom-like failure is obvious.

There is one additional factor to be considered; to compare the number of AE hits recorded for different specimens of the same fibre type, the number of unbroken fibres should be considered. The number of unbroken fibres in a bundle will vary from sample to sample before the tensile test. For example, the fibres in a bundle can fracture before testing due to the manual handing, fibre-to-fibre contact and specimen manufacturing procedures. In addition, a few fibres can fracture during the loading of the specimen on the Instron machine. It was reported that 5-10% of the total number of fibres can fracture before the tensile-tests [58, 180]. The author's estimate of broken fibres was less than 5% as previously discussed in Section 4.1.1. Considering the fact that every specimen was subjected to the same set of procedures from manufacturing to the loading in the Instron grips, the effects of initial broken fibres on the AE data were considered similar and therefore, can be assumed to be insignificant.
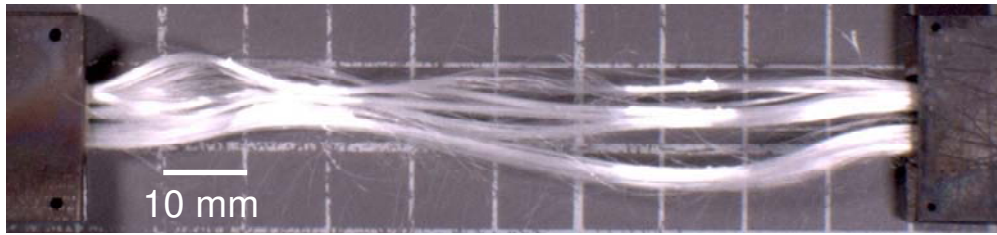
Figure 4.33 Representative image of a fractured as-received SDOF bundle specimen.

The average amplitude of the AES was 59.7 dB with a SD of 5.1 dB for the as-received E-glass and 51.5 with SD of 1.5 for the silane-treated E-glass bundle. The peak frequency of the AE hits exhibited an average of 54.5 kHz and 48.6 kHz for the as-received and silane-treated fibre bundles, respectively. The average amplitude of the AES for the E-glass fibre bundle was reported to be approximately 70-90 dB [65, 78, 79, 159].

With reference to Table 4.16, the average number of AE hits recorded for the as-received SDOF was 4452 with a SD of 652.9. The average amplitude of the AES was 60.4 dB with a SD of 2.9. The average peak frequency and average frequency were found to be 130.8 kHz and 90.4 kHz, respectively. These fibres were supplied with a coating and an organic binder (see Section 4.1.1.1). Although, the effects of the organic-binder on the monitored AE signal were not evaluated by these experiments, however when the binder was pyrolysed, a greater number of AE hits were recorded for the heat-treated SDOF. The coating is likely to cause a reduction in the inter-fibre friction and thus fewer AE hits were produced during tensile testing. It is possible that the presence of the organic-binder improved the mechanical coherence and therefore, the amplitude of the AES was also increased.

Figure 4.34 Representative image of a fractured heat-treated SDOF bundle specimen.

In the case of the heat-treated SDOF, the standard deviation of the AE results was comparatively greater than the other fibre types. This may be attributed to the pyrolysis of the binder and a change in the material surfaces (see Section 4.1.1.2). The ultimate peak-load of the heat-treated SDOF was around 60% of the peak-load of the as-received SDOF. In the case of the heat-treated SDOF, the average numbers of AE hits were 15% greater than for the as-received SDOF. The most likely cause of this increase was due to the increase in the friction between filaments as a consequence of the heat treatment. The heat-treated SDOF produced a greater number of lower AE amplitude hits, this is in accord with the work done by previous researchers [65, 78, 79, 159]. They reported that the low amplitude hits were generally due to the inter-fibre friction. Representative images of fractured test specimens for the as-received and heat-treated SDOF are shown in Figure 4.33 and Figure 4.34, respectively.

In the next section an analysis of the AE data is presented. The AE data were correlated to the mechanical test results of the fibre bundles.

4.3.3   Analysis of the acoustic emission data for the fibre bundle

As mentioned previously, a change in the slope of the cumulative AE hits is indicative of the evolution of damage occurring in a test coupon. In the case of tensile testing of fibre bundles, the plots of cumulative AE hits against time show a gradual increase in the slope before the peak-load; at the onset of failure, the slope increases rapidly to a maximum and then gradually tends towards zero by the time most of the fibres in the bundle are fractured. Similar graphs were reported for AE monitoring of E-glass fibre bundles subjected to tensile testing by various authors [45, 65, 78, 78, 159].

Figure 4.35 Graphs showing the cumulative AE hits and load as a function of time for: (a) As-received E-glass fibre bundle; (b) Silane-treated E-glass fibre bundle; (c) As-received SDOF bundle; and (d) Heat-treated SDOF bundle.

A similar trend was observed for the four types of fibre used in this study. Figure 4.35 (a-d) show representative graphs of the load and cumulative hits as a function of time for the four fibre types. It was established in Section 3.6 that the AE system was synchronised with the tensile test machine and the high-speed camera. Therefore, the AE results can be cross-correlated to the tensile test parameters and the image analysis data. The slope of AE hits started to increase significantly when the test coupons reached 90 – 95% of their peak-loads. A deviation from this behaviour was observed in the case of the silane-treated E-glass fibre bundle, as shown in Figure 4.35b. The silane-treated E-glass bundle showed a gradual increase in the slope of the cumulative AE hits from the onset of the AE hits. The adhesion between the silane-treated fibres was higher when compared to the un-treated fibres. The increased adhesion between the fibres was likely to have caused additional AE

hits (see Table 4.16) and localised failure of fibres. It was observed that the AE activity continued to occur even after the peak-load of the four types of fibre bundles.

As previously discussed in Section 4.1.1, the E-glass fibres in a bundle have a distribution of diameters. The varying diameters affect the stress in the individual fibres and their failure load. Additionally, the fibres in a bundle have a distribution of strengths due to the presence of surface-flaws of varying severity and origin. Furthermore, the fibres in a bundle were not entirely parallel. The bundles were supplied with an intrinsic twist and therefore, the length of filaments in a bundle can vary. During the preparation of fibre bundle specimens, the fibres in the bundles were separated as described in Section 3.2.2. This was done to reduce the effect of the twist in a bundle. However, it is difficult to claim that the bundles were completely free of twists. The varying lengths of filaments in a bundle can affect the magnitude of tension in the filaments when the bundles were loaded. The load applied to the fibre bundle cannot be distributed uniformly since the fibres were subjected to varying tension due to different lengths. Since all the filaments in the bundle cannot be subjected to an even load, therefore, it can be assumed that they were not under the same tension. Consequently, the fibres in a bundle exhibited a non-catastrophic behaviour after the peak load until almost all the fibres in the bundle were fractured.

The plot of amplitude of the AES as a function of time gives information about the amplitude of the AES distributions in a fibre bundle subjected to tensile loading [65]. Figure 4.36 shows representative plots of the amplitude of the AES versus time for the four types of fibre studied. To determine the distributions in the amplitude of the AES data, the frequency of occurrence (the number of data points recorded for the amplitude of the AES) was plotted against the amplitude. Figure 4.37 (a-d) shows representative plots of the frequency of occurrence (histogram) versus amplitude for the four fibre types.
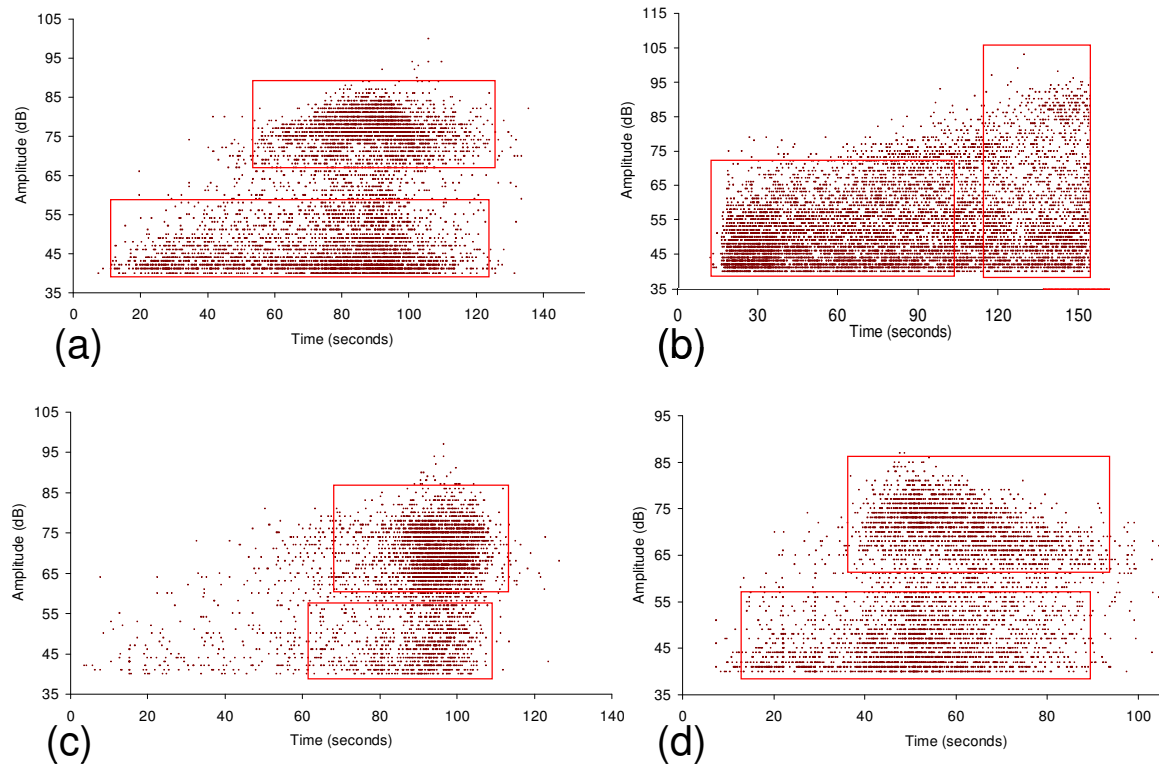
Figure 4.36 Graphs showing the amplitude of the AES as a function of time for: (a) As-received E-glass fibre bundle; (b) Silane-treated E-glass fibre bundle; (c) As-received SDOF bundle; and (d) Heat-treated SDOF bundle.

Two amplitudes of the AES distributions were observed from Figure 4.37 (a-d). The first distribution (70-90 dB) was likely to be caused by individual fibre failures whereas the second amplitude of the AES distribution (42-55 dB) was due to inter-fibre friction [65]. It was possible that the fibres were fracturing at isolated locations due to inter-fibre friction as discussed previously in Section 4.3.2. In addition, the twists in the fibre bundle caused individual fibres to fracture at more than one location. R'Mili *et al.* tested E-glass fibre bundles and found the two distributions to be 80-90 dB and 45-55 dB. The sensors were located at the tensile test machine grips and there was a possibility of damping the lower amplitude distributions. However, in this current study, the PZT transducers were attached to the fibre bundles with silicone grease (see Section 3.3). Therefore, this may explain why

the numbers of AE hits recorded during this study were greater than the ones recorded by R'Mili *et al.* for the testing of E-glass fibres.
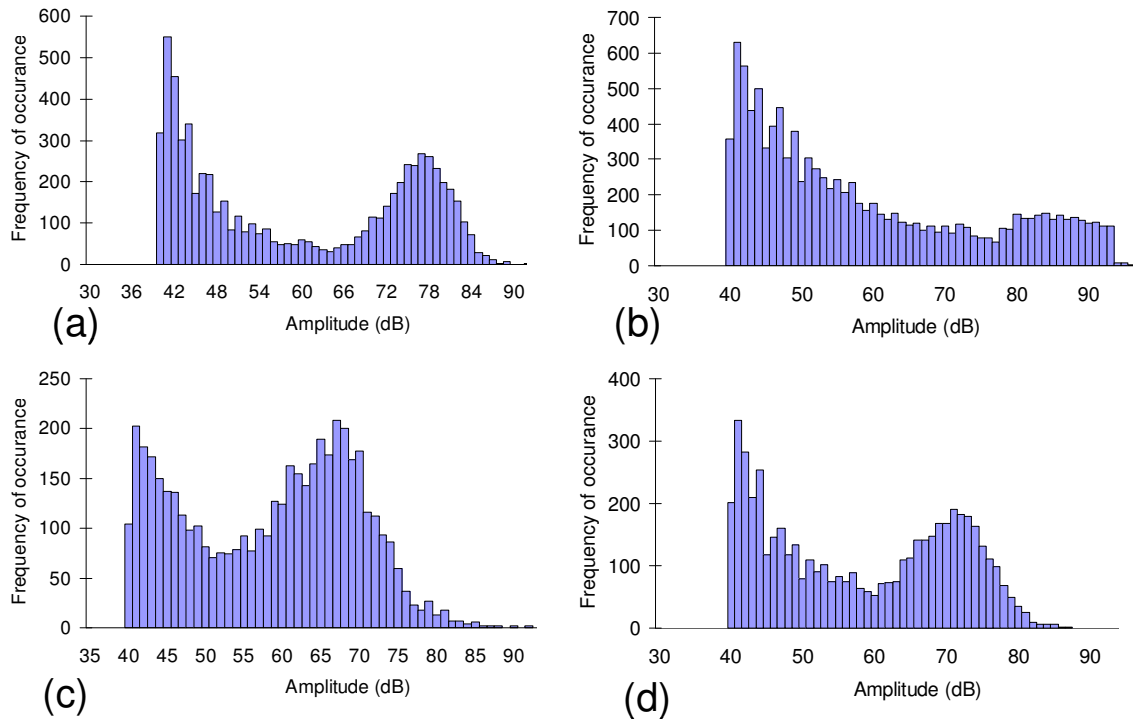
Figure 4.37 Histogram plots of the amplitude of the AES for: (a) As-received E-glass fibre bundle; (b) Silane-treated E-glass fibre bundle; (c) As-received SDOF bundle; and (d) Heat-treated SDOF bundle.

Figure 4.36 (a-d) shows two different amplitude distributions on the amplitude of the AES versus time plots highlighted by red boxes. The numbers of recorded data-points for the amplitude of the AES vary for each fibre type as shown in Figure 4.36. In the case of silane-treated E-glass fibres, the number of AE hits recorded for the higher amplitude of the AES distribution (70-90 dB) was significantly less than for the lower distribution (42-55 dB). This may be due to the fact that the fibres were 'bonded' and localised failure was more dominant. The localised failure of fibres produced greater number of lower amplitude of the AES hits as shown in Figure 4.37b. In the case of the as-received E-glass fibre bundle, comparatively more hits were produced in the lower range than for the as-

received SDOF. As discussed previously the as-received E-glass fibres exhibited greater inter-fibre friction and this may account for the increase in the number of hits recorded [45, 65, 78]. Additionally, the fibres in the E-glass bundles had relatively more twists than for the SDOF and therefore, the twisted fibres in the bundle can lead to fractures at more than one location. This could have increased the number of localised fibre failures, and hence the lower amplitude of the AES hits recorded.

In the case of the as-received SDOF, both the amplitude distributions exhibited approximately similar numbers of AE hits. The number of lower amplitude hits was lower compared to the other fibre types. The as-received SDOF had an organic binder as mentioned in Section 4.1.1. Although the relative affect of the organic binder towards the recorded AE signal was not known from the experiments conducted, its influence during the AE monitoring appeared as a decrease in the number of low amplitude hits of the AES when compared to that of the heat-treated SDOF bundles. The presence of the binder may have caused damping of the AE signal and therefore reduced the number of low-amplitude hits. The presence of the binder also increased the mechanical coherence and reduced the inter-fibre friction and hence the localised failure of fibres was reduced. A similar behaviour was observed for all the tested specimens of as-received SDOF bundles.

For the heat-treated SDOF, the number of recorded AE hits for the lower amplitude range (42-55 dB) was comparatively greater than for the as-received E-glass fibres as shown in Figure 4.37d. It was possible that the removal of binder by pyrolysis decreased the damping of the AE signal and increased the magnitude and severity of surface-flaws. The heat-treated SDOF were comparatively more brittle and fragile from visual inspection and manual handling as discussed in Section 4.1.1. The effect of the pyrolysis of SDOF on the monitored AE signal was a comparative increase in the number of lower amplitude AES

hits. Another factor is the increase in inter-fibre friction that produces additional AE hits [61]. It was difficult to quantify these effects, however a similar trend was observed for all the heat-treated SDOF bundles.
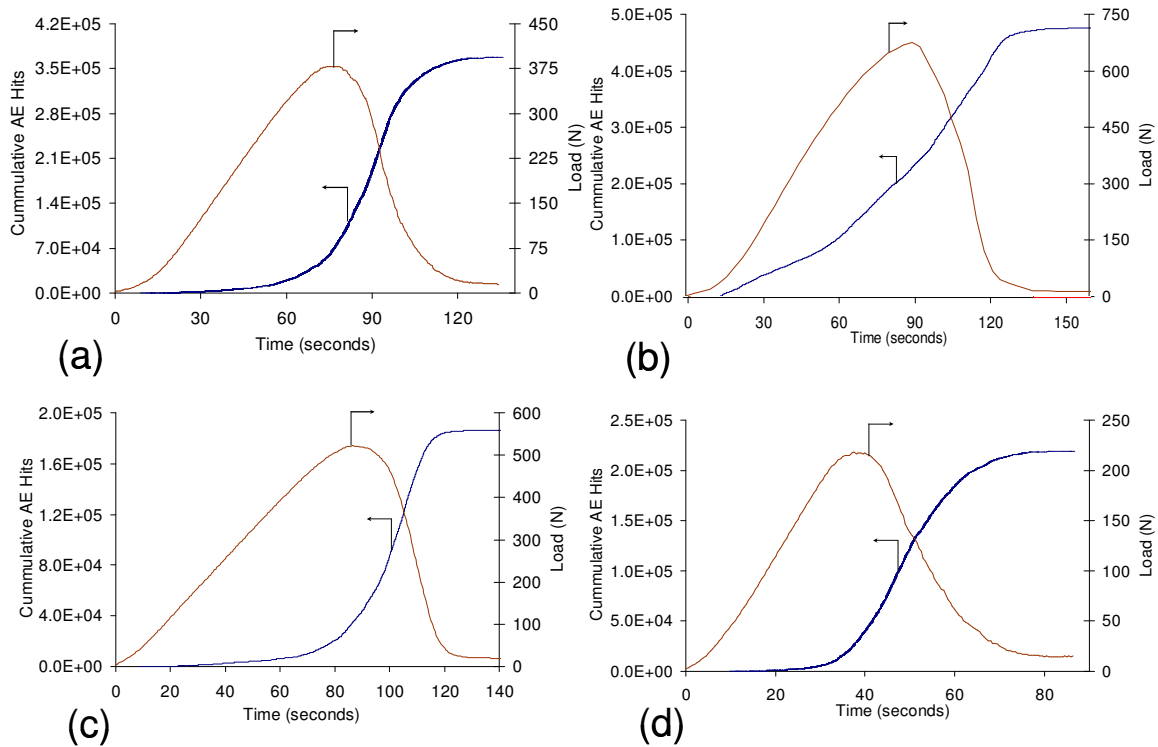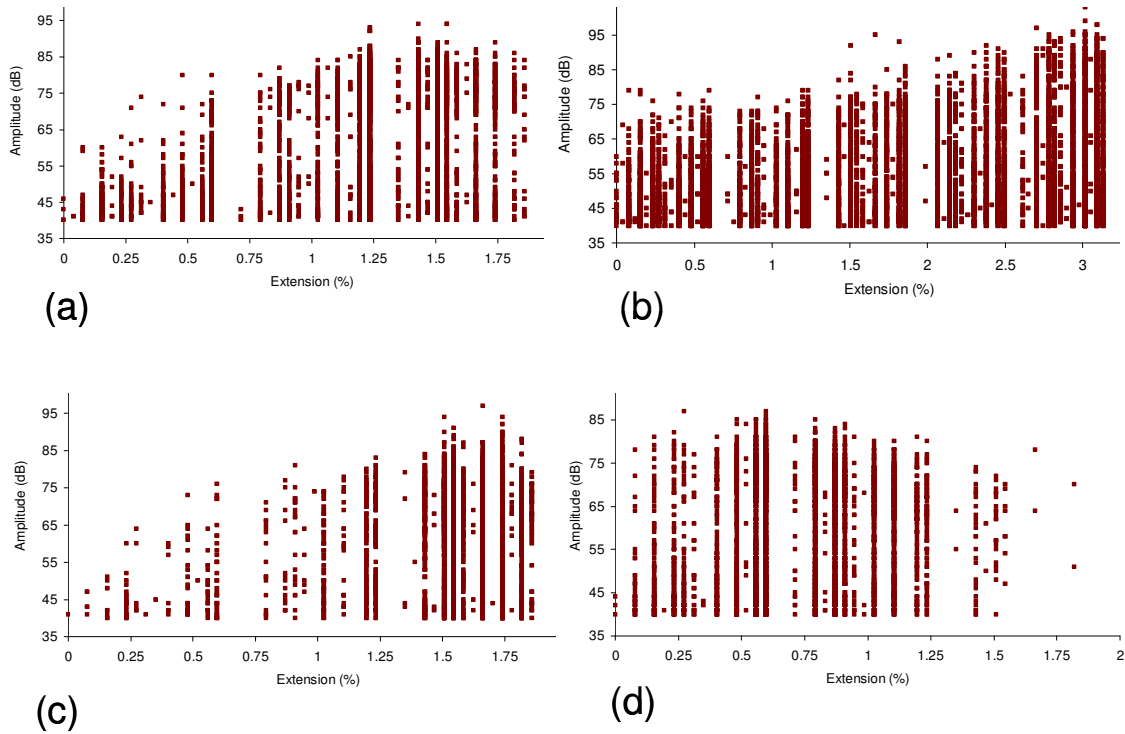

Figure 4.38 Graphs showing the amplitude of the AES as a function of extension for: (a) As-received E-glass fibre bundle; (b) Silane-treated E-glass fibre bundle; (c) As-received SDOF bundle; and (d) Heat-treated SDOF bundle.

The two distributions mentioned earlier were in agreement with the work reported by R'Mili *et al.* Hill *et al.* and Cowking *et al.* [45, 65, 159]. They found the two distributions were in the ranges of 40-60 dB and 80-95 dB. It was also reported that the amplitudes of the AES increase with applied strain. This was due to the fact that weak fibres fail at a low strain and stronger fibres at a higher applied strain. This effect is shown in Figure 4.38 (a-d). Figure 4.38 (a-d) shows representative graphs of the amplitude of the AES as a function of specimen extension for the four fibre types. From Figure 4.38 (a-d) the low amplitudes of the AES in the range 40-65 dB were recorded at extensions in between 0.5-1%.

In the case of the as-received E-glass and silane-treated bundles, the amplitudes of the AES were 65 dB up to 0.5% of extension and more than 75 dB after 2% extension, respectively. In the case of the as-received SDOF, it was 65 dB at 1% of extension. However, in the case of the heat-treated SDOF a different trend was observed; higher amplitude hits were recorded even at a lower strain as shown in Figure 4.38d. The most likely cause of this behaviour is the apparent brittleness induced in the heat-treated fibre bundles.

In conclusion, the AE monitoring of fibre bundles revealed that there were two types of failure modes occurring in the bundle: a lower amplitude of the AES related to the inter-fibre friction; and a high amplitude of the AES related to the fibre fractures. The inter-fibre friction was found to be a dominating factor in the case of un-sized and as-received (un-treated) E-glass fibre bundles. The as-received SDOF bundles exhibited a different behaviour due to the presence of the organic binder. The heat-treatment of the SDOF bundle reduced the strength of the bundle, thus causing the fibres to fail at a lower strain. The silane-treated E-glass fibres produced significantly higher number of low amplitude AES hits due to the partial adhesion of fibres. This adhesion increased the friction between fibres. Therefore, localised fibre fractures occurred at a low strain and produced low amplitudes AES hits.

In the next section, the Weibull statistical analysis was performed to provide evidence for the two types of strength distributions in the bundles and to show the variation in the ultimate peak-load of the bundles statistically.

4.3.4 Weibull strength distribution

The strength of fibres can be characterised by using the two-parameter Weibull distribution [43, 45, 49, 58, 65, 78]. It has been demonstrated earlier that the fibres in a bundle have distribution of strengths due to the presence of surface-flaws and the probabilistic nature of fibre fractures in a bundle. The Weibull distribution was used in the current study to evaluate the statistical nature of fibre failure in a bundle.

A theoretical model of a bundle of fibres consists of a set of N_o parallel fibres with statistically distributed strengths. The test coupons were loaded parallel to the direction of the fibres; the fibres fractured when the load on them exceed their ultimate tensile strength. After each fibre failure, the load was redistributed amongst the unbroken fibres. This means that after each fibre break, the stress was equally distributed on the surviving fibres assuming no interaction between the broken fibres and their neighbours.

Chi *et al*. [43] utilized the load-strain curve of fibre bundle failure in their research work, while Cowking *et al.* [159] employed both the load-strain curve and the load-events curve (using acoustic emission) to count fibre failures. They determined the Weibull parameters and obtained the Weibull modulus and bundle strength.

The probability of survival of a single fibre of normalised length 'L' under an applied strain 'ε' is described using the two-parameter Weibull distribution:

$$PF(\varepsilon) = e^{-[L(\frac{\varepsilon}{\varepsilon_o})^m]}$$

4-6

where 'ε_o' and 'm' represent the Weibull scale and shape parameters for strain, respectively. 'ε_o' represents the strain associated with a probability of failure of 63%; whereas 'm' describes the flaw distribution and describes the coefficient of variation.

At an applied strain 'ε', the number of surviving fibres in a bundle, which initially consists of N_o fibres, is given by:

$$N_S(\varepsilon) = N_o e^{-[L(\frac{\varepsilon}{\varepsilon_o})^m]}$$

4-7

This expression is related to the applied tensile load F on the fibre bundle by:

$$F(\varepsilon) = AN_o E \varepsilon e^{-[L(\frac{\varepsilon}{\varepsilon_o})^m]}$$

4-8

This expression is the load-strain relationship for a bundle of fibres under tension, where 'A' is the average cross-sectional area of a single fibre and 'E' is the Young's modulus of the fibre bundle.

The Weibull shape parameter 'm' is obtainable via two methods [159]; (i) maximum load method; and (ii) graphical method.

i.   Maximum load method:

$$m = \frac{1}{\ln[\varepsilon_{max} S_o / F_{max}]}$$

4-9

where ε_{max} is the strain at the maximum load point and S_o is the initial gradient ($dF/d\varepsilon=0$) of the load-strain curve.

ii.   Graphical methods

A plot of either ln [ln (N_o/N_s)], from Equation 4.7, or of ln[ln ($S_o\varepsilon/F$)], from Equation 4.8, against ln(ε) will give a straight line if the Weibull analysis is appropriate. The slope of the straight line is the Weibull modulus 'm'.

The Weibull scale parameter ε_o is obtainable from:

$$\varepsilon_o = \varepsilon_{max}\left(Lm\right)^{1/m}$$

4-10

The fibre strength 'σ_b' is defined as:

$$\sigma_b = \frac{F_{max}}{AN_o}$$

4-11

and the median fracture stress σ_{med} (at $N_s/N_o = 0.5$) as:

$$\sigma_{med} = \sigma_b\left(1.884m\right)^{1/m}$$

4-12

and the fibre modulus 'E' as:

$$E = \frac{S_o}{AN_o}$$

4-13

Equations 4.7 to 4.13 have been used by several authors [43, 45, 49, 51, 55, 58, 65] to determine the Weibull parameters using either the maximum load method and/or the graphical method.
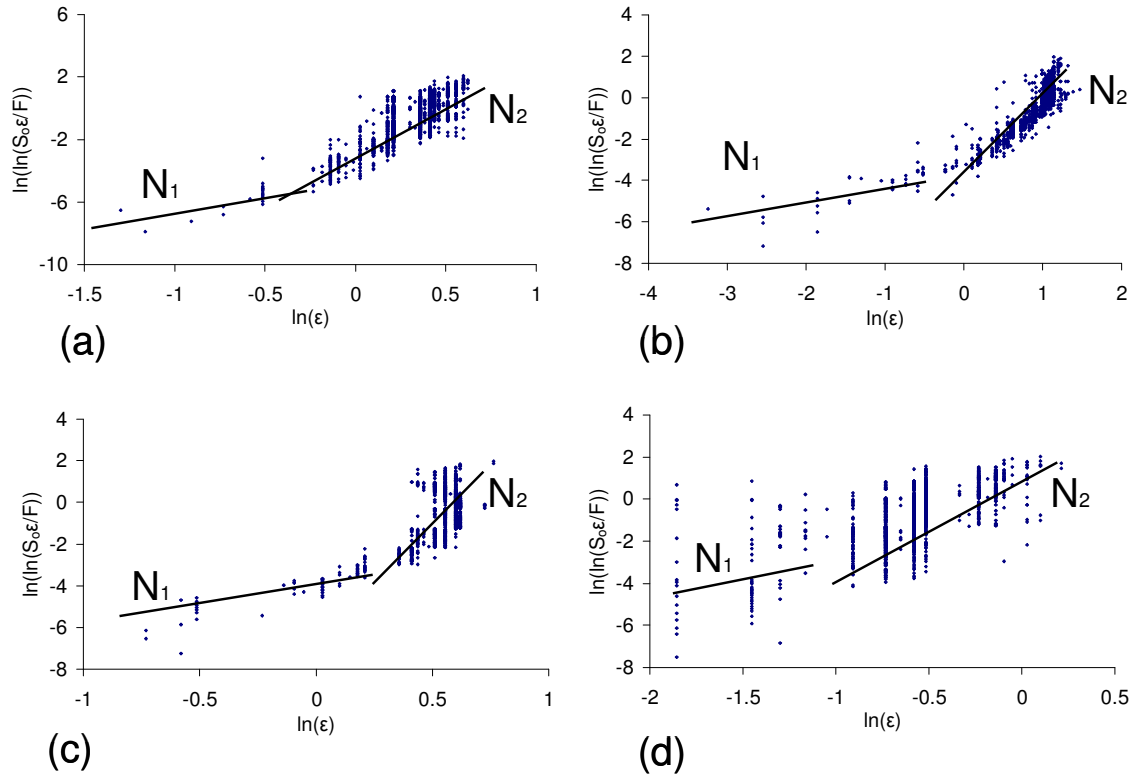
Figure 4.39 Graphs showing the plots of $\ln[\ln (S_o\varepsilon/F)]$ as a function of $\ln(\varepsilon)$ for: (a) As-received E-glass fibre bundle; (b) Silane-treated E-glass fibre bundle; (c) As-received SDOF bundle; and (d) Heat-treated SDOF bundle.

Figure 4.39 (a-d), show representative plots for the $\ln[\ln (S_o\varepsilon/F)]$ against $\ln(\varepsilon)$ for the four fibre types. With reference to Figure 4.39 (a-d), it can be argued that the datasets can be represented by two populations. This was confirmed by a T-test where it found that there were two distinct populations for each data set which were statistically independent. Therefore, it can be inferred that the flaw distribution was bimodal rather than uni-modal.

In Figure 4.39 (a-d), the lines indicated as N_1 and N_2 represent liner regression trend-lines based on the two datasets. The calculated slopes of lines N_1 and N_2 are summarised in Table 4.17. With reference to Table 4.17, the lower the value of Weibull modulus, higher is the spread in the analysed data. In the case of the as-received E-glass fibre bundle, it can be observed from Table 4.17, that the slopes of lines N_1 and N_2, are greater than that of the

silane-treated E-glass bundles. Hence, the as-received bundles exhibited lower spread in the data. Similar behaviour can be observed in the case of heat-treated SDOF bundles where the two slopes were significantly lower than the as-received SDOF bundles. It is difficult to discuss the results presented in Table 4.17 further for the following reasons. The cross-head speed used in the current study was 1 mm/minute; this is 20 times greater than that used by other research such as R'Mili [65] and Cowking [159]. The execution of tensile tests using high cross-head speed can cause simultaneous multiple fibre fractures over a short period. This can make the interpretation and analysis of the data difficult. This problem can be resolved if the individual failure events can be separated, for example via acoustic emission and using a lower cross-head speed for the tensile tests.

Table 4.17 Weibull modulus obtained using the graphical method.

	Slope of line N_1	Slope of line N_2
As-received E-glass fibres	3.3	5.78
Silane-treated E-glass fibres	0.9	3.5
As-received SDOF	2.4	7.5
Heat-treated SDOF	1.1	1.8

Table 4.18 shows the comparison of calculated Weibull modulus and scale parameters of the fibre bundles used in this study along with published data. The values shown in Table 4.18 for the two Weibull parameters were calculated using Equations 4.7 to 4.13 as per the procedures described by Chi *et al.* [43] and Hill *et al.* [49]. With reference to Table 4.18, the Weibull modulus 'm' is indicative of strength distribution; the higher the value of 'm', the lower the strength distribution. 'ε_o' is the failure-strain associated with a 0.63 probability i.e. 63% of fibres will fail at this strain in the bundle. In the case of the as-

received SDOF, the distribution of strength was minimum since the value of 'm' is the highest amongst the four data sets. On the other hand, when these fibres were heat-treated, the strength distribution becomes half of its original value. Physically the 'm' is related to the flaw distribution in the fibres and therefore, it reflects that an increase in the surface-flaws caused an increase in the failure strength distribution [58, 65].

Table 4.18 A comparison of the published data for Weibull parameters with the self-sensing fibre bundles used in this current study.

	m	$\varepsilon_{o\,(\%)}$
R'Mili *et al.* [65]	2.8	2.1
Anderson *et al.* [58]	5.3	2.5
Hill *et al.* [45]	9.4	2.4
Average Weibull parameters determined during this study		
As-received E-glass fibres	8.6	2.30
Silane-treated E-glass fibres	6.7	2.32
As-received SDOF	13.1	2.37
Heat-treated SDOF	4.7	2.37

Table 4.18 illustrates that the Weibull moduli 'm' obtained from the as-received (untreated) E-glass bundles are higher than those obtained from silane-treated bundle tests, indicating a narrow range of peak-load due to progressive fibre failure. The scale factors (ε_o) from the as-received (untreated) are smaller. These variations in the Weibull parameters are associated with inter-fibre friction. The friction induces progressive fibre failure, multiple fibre fracture in the untreated and un-sized bundles, reducing the bundle

strength [45]. The presence of friction may induce failure due to the load transfer from fractured to un-fractured adjacent fibres. This load-transfer process becomes very effective beyond the maximum load, with friction inducing rapid fracture and a rapid load drop. Clarke *et al.* showed that at small separations, every primary failure triggers failure in the neighbouring fibres. They used linear arrays of fibres embedded in a solid epoxy matrix. It was reported that the average fibre strength was reduced by 30% when compared to the strength obtained from single-fibre tests [196]. The adhesion between the fibres of the bundle was increased due to the silane-treatment. It was possible that due to increased adhesion the load transfer was comparatively more effective than for the as-received (untreated) E-glass bundles. Consequently, the untreated E-glass bundles fractured at a comparatively lower peak-load.

Due to the statistical nature of the failures modes in fibre bundles there is no consensus in the literature for the magnitude of the Weibull modulus for E-glass fibre bundles. This can be observed by comparing the values of 'm' in Table 4.18. The results obtained depend upon the test conditions and flaw distribution of the fibres in the bundle. However, it is interesting to note that the ε_o is approximately the same. Comparing the results obtained in this study with the ones cited in the literature, the Weibull modulus 'm' ranges between 4.7 to 13.1, whereas the ε_o was approximately 2.3%, that reflects the variation in the modulus 'm' and shows the consistency in the ε_o. The difficulties associated with comparing the mechanical data from different laboratories were presented in Section 4.3.1.

4.4 High-speed Photography and Image Analysis

The *in-situ* monitoring of the light transmission through conventional E-glass fibres during tensile loading was one of the prime objectives of this project. A high-speed charge-coupled device (CCD) camera was employed to monitor the light transmission through the self-sensing fibres and composites. The number of images captured by the high-speed camera ranged from 7000 to 8000 per test; therefore, software routines had to be developed to enable large-scale image processing and analysis. The light attenuation through individual filament was tracked and correlated to acoustic emission and mechanical loading. In the first instance, custom-made small-diameter optical fibres (SDOF) were used to develop the image analysis routines. Representative images taken by the high-speed camera from the potted and polished small-diameter optical fibres and E-glass fibres are shown in Figure 4.40.

(a)   (b)
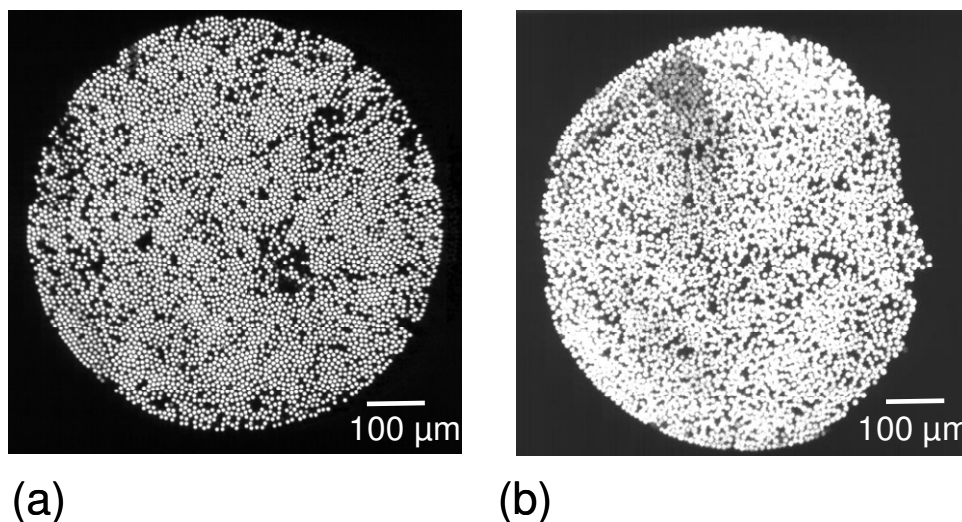
Figure 4.40 Representative images showing the potted and polished fibre bundle cross-sections for: (a) Small-diameter optical fibres; and (b) E-glass fibres.

The details of the integration and synchronisation of the various equipment were discussed in Section 3.6, with reference to the surface-mounted PZT transducers, the first AE hit

above a specified threshold was used to trigger the high-speed camera. AE monitoring was used to identify different damage modes in the fibre bundles and the self-sensing composites.

4.4.1   Image analysis

Matlab™ was used in the current study to analyse the images taken by the high-speed camera. A macro was developed to read the first image and to identify each fibre as an –

individual entity; the centroidal position of each fibre was specified using x and y-axis coordinates. The light intensity of each fibre was calculated using these coordinate positions. The coordinates for the rest of the images remained the same since the camera-end of fibre bundle was stationary (see Figure 3.13).

Figure 4.41a shows the first image that was captured at the start of the tensile test (t=0) involving the small-diameter optical fibres. Figure 4.41b represents the transposition of Figure 4.41a using the Matlab™ software. This step involved, background correction and adjustment of the luminance threshold using the software routines. Figure 4.41c is a x-y location plot after image processing in Matlab™- of the same image shown in Figure 4.41 (a and b). The quality and processing of the images presented in Figure 4.41c was found to be adequate in order to enable the fracture of reinforcing glass fibres to be studied. It was found that the Matlab™ routines were able to identify and process each individual fibre with an accuracy of 94 ±2%.
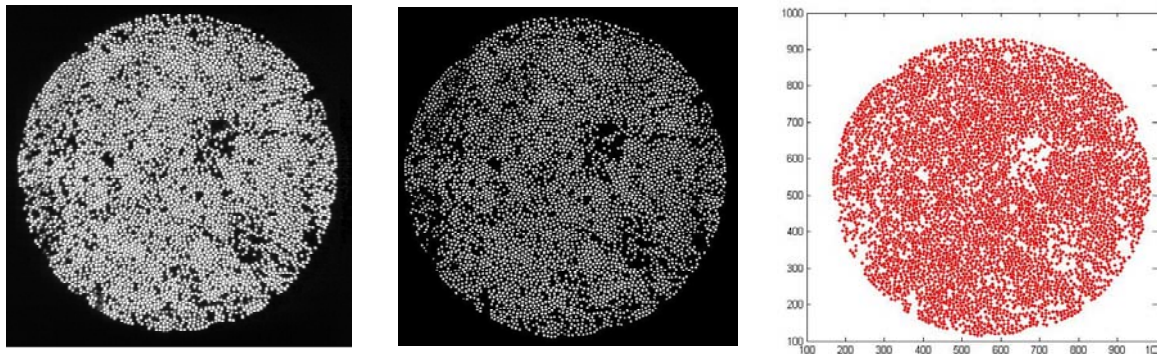
Figure 4.41 Illustration of the analysis steps involved with processing the images obtained via the high-speed camera: (a) Image from the high-speed camera at t=0 (first image); (b) Background-corrected image using Matlab™ ; and (c) X-y plot for the location of the individual fibres.

Figure 4.42 (a-c) shows a series of images, captured by the high-speed camera during tensile testing of the small-diameter optical fibre bundle. The corresponding light intensities for Figure 4.42 (a-c) are shown in Figure 4.42 (d-f), respectively, where the x- and y-axes indicate the location of each fibre and the z-axis represents the light intensity at each location.
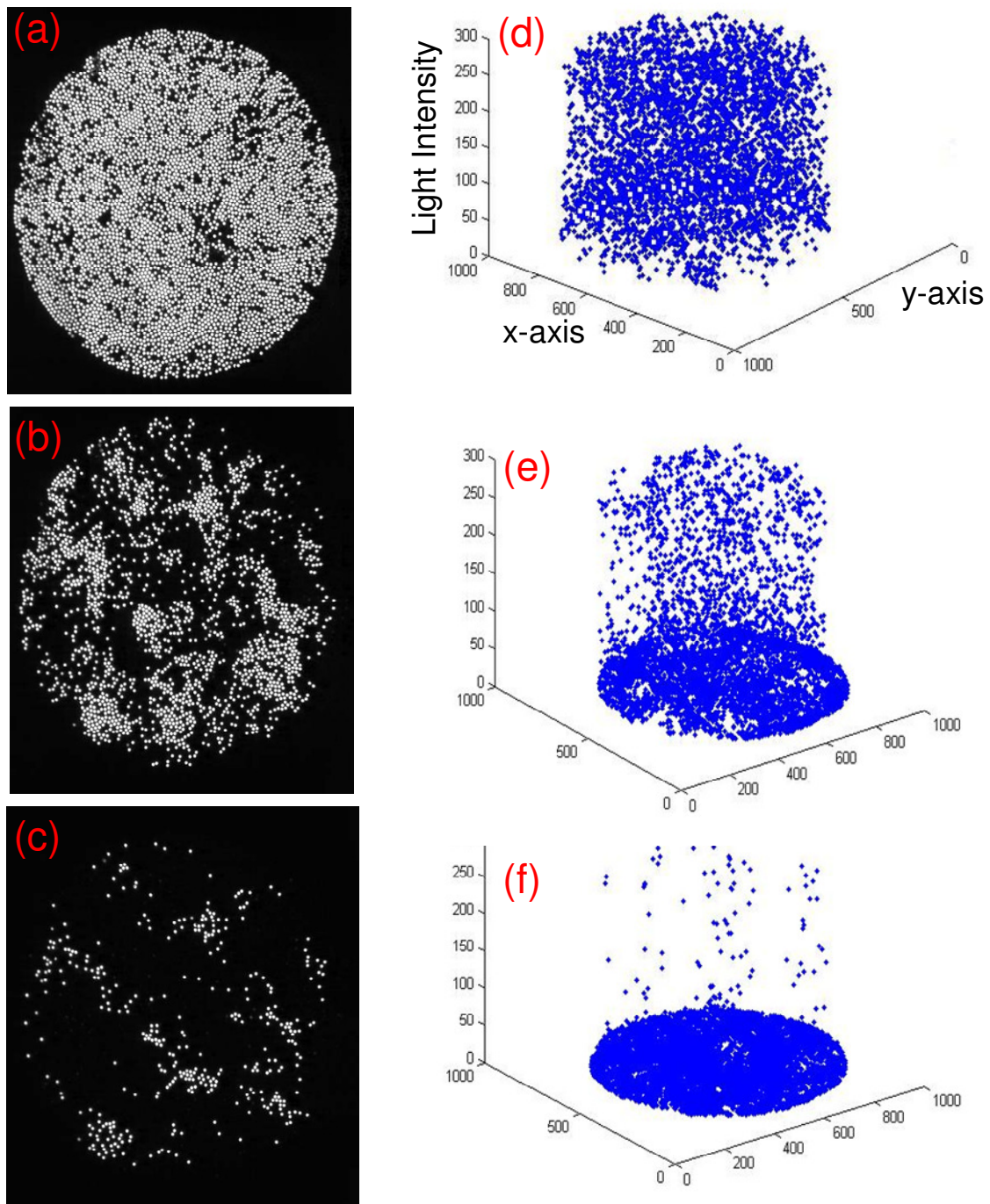
Figure 4.42 (a-c) Examples of images captured by the high-speed camera at different time intervals during tensile loading of a small-diameter optical fibre bundle: (a) After 10 seconds (600th frame); (b) After 50 seconds (3000th frame); (c) After 80 seconds (4800th frame); and (d-f) The corresponding x-y location plots and light intensities.

Fibre about to   Light attenuated   Fibre fractured
fracture
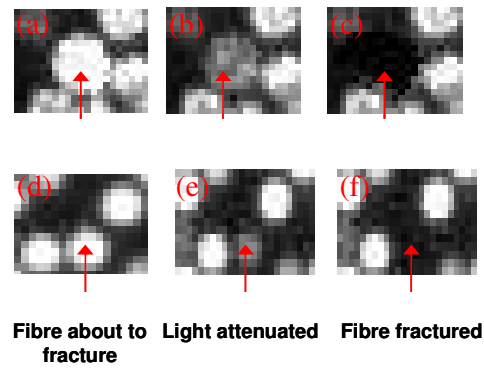
Figure 4.43 Identification of the integrity of individual fibres by monitoring the transmitted light intensity for the E-glass filaments (a-c), and SDOF (d-f): (a and d) Whilst the sample was loaded in tension; (b and e) Just prior to fracture; and (c and f) Immediately after fibre fracture.

The image analysis routines were capable of identifying and tracking the survival or fracture of each fibre in the bundle. An investigation was carried out to establish the feasibility of using the image analysis routines to detect imminent fracture of individual filaments. Figure 4.43 (a-c) and (d-f) demonstrate two typical examples of sequential images captured during the tensile testing of E-glass and small-diameter optical fibres, respectively. The images have been magnified to make clearer the light changes in the fibre just before during and after the fracture process. Figure 4.43 (a-c) shows three sequential frames, for the E-glass fibre bundle; the arrow in frames (a-c) indicate the position of a fibre before, during and after the fracture, respectively. This trend was observed for all of the fibres, where an attenuation of the transmitted light intensity was observed just prior to failure. Figure 4.43 (d-f) illustrates a similar sequence of three consecutive images for the SDOF bundle. Figure 4.43 (d-f), demonstrates that the fracture of the individual filaments in the SDOF bundle can be detected by monitoring the transmitted light intensity. From these two representative examples of E-glass and SDOF, it can be concluded that the failure of individual filaments resulted in the attenuation and ultimately complete extinguishing of the transmitted light.

4.4.1.1 Variation in the transmitted light intensity

The variation in the transmitted light intensity through the fibre bundles and the composite was normalised by considering the first image as the starting point for each data set. This means that the first captured image corresponded to the maximum transmitted light intensity for that particular test. This approach is reasonable since the strength of the fibre bundle can be assumed to be maximum before the test and that the change in transmitted light intensity was proportional to the number of surviving fibres. The transmitted light intensity was found to vary from sample-to-sample by less than 5%. From Figure 4.44 to Figure 4.47, it can be stated that the transmitted light intensity is proportional to the number of surviving fibres, i.e. the plot of the light intensity exhibited the same trend as the load versus extension graph (in the case of the fibre bundles) or the stress versus strain graph (in the case of composites). The light intensity decreased at the onset of failure as shown in Figure 4.44 and Figure 4.47, for both the fibre bundles and composites, respectively.

The decrease in light intensity was due to two reasons; a change in optical properties of the fibres and due to the fracture of the fibres. A discussion on these two reasons will be presented in Section 4.4.2.
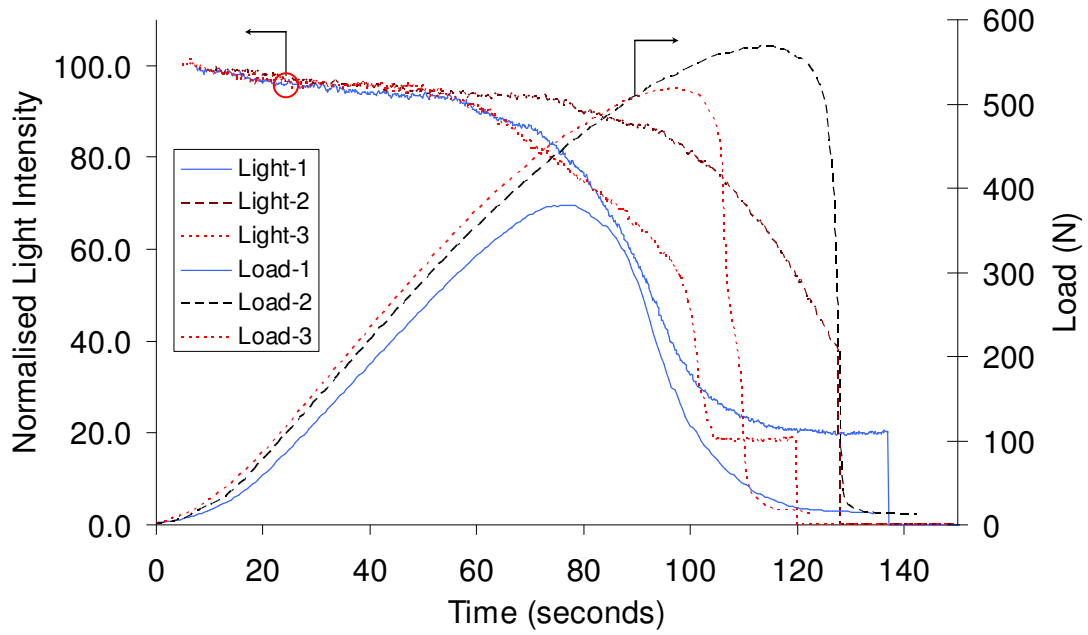
Figure 4.44 Typical graph showing the normalised transmitted light intensity and applied load as a function of time for three different samples of as-received E-glass fibre bundles.
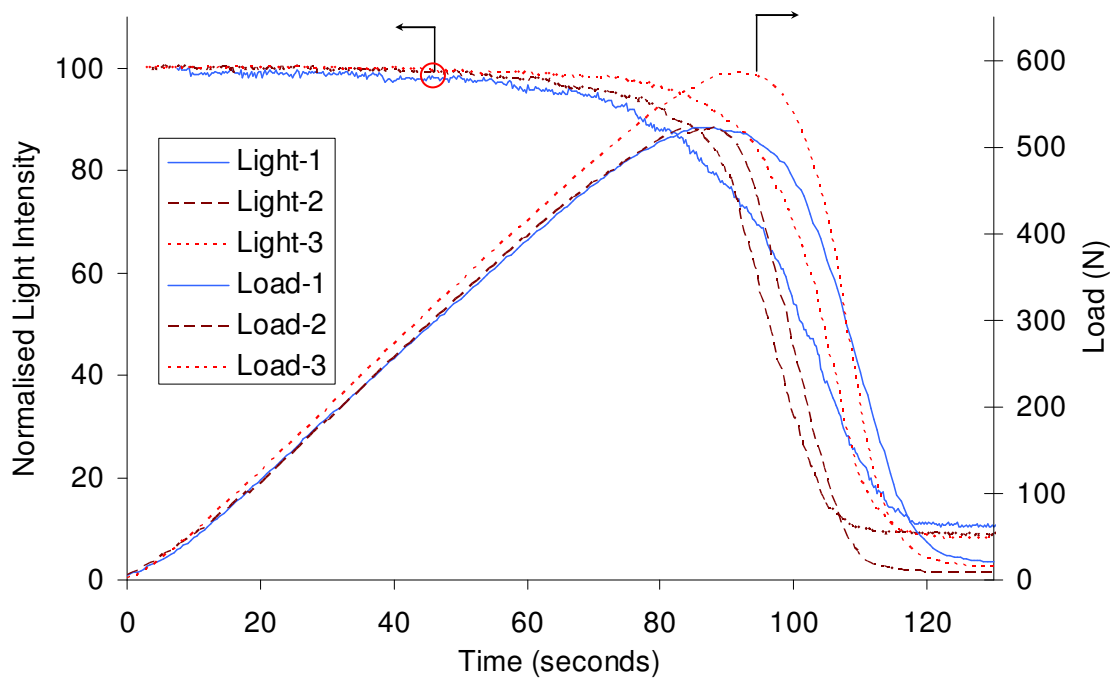
Figure 4.45 Typical graph showing the normalised transmitted light intensity and applied load as a function of time for three different samples of as-received SDOF bundles.

In the case of the E-glass fibre bundle, Figure 4.44 shows that there was a gradual decrease in the transmitted light intensity up to the peak load, however the magnitude of the decrease depends upon the failure behaviour of the fibre bundle after the peak-load. The rate of decrease in the load (after the peak-load) of sample-1 was 13.5 N/second, whereas it was 76.83 N/second and 70.65 N/second for samples-2 and 3, respectively. In the case of the E-glass fibre bundles, it was found that the net decrease in transmitted light intensity (for 75% of test specimens) was 20-25% at the peak-load; if the rate of decrease in load was 15-20%. For instance, it is 19% in the case of sample-1, however in the case of samples-2 and 3 it is 30% and 40%, respectively. It is evident from Figure 4.44 that the decrease in peak-load was rapid in the case of samples-2 and 3. It is speculated that the majority of the fibres were fractured before the peak-load; however the fibre bundle resisted the applied load due to the twists and adhesion between fibres of the bundle. On the contrary, it was also possible that the number of fractured fibres in the bundle was lower and therefore, the transmitted light intensity was reduced due to the high magnitude of the applied-strain; the fibres then fractured rapidly at the peak-load and the transmitted light intensity was finally reduced to zero. If the load versus time graph of samples-2 and 3 exhibited similar appearance as that of sample-1, the decrease in light-intensity graphs could be more gradual. This behaviour can be observed in the case of as-received SDOF bundles, as shown in Figure 4.45. By comparing the trend of the light intensity graphs of the E-glass and SDOF bundles, it can be concluded that the change in transmitted light intensity predominantly followed the trend of the load versus time graph. The image analysis routines were capable of detecting the light attenuation with respect to the mechanical behaviour of each sample. The light intensity plots followed a similar trend as that of the load versus time plot (after the peak-load). Hence, it was possible to relate the attenuation of transmitted light with the mechanical behaviour of fibre bundles.
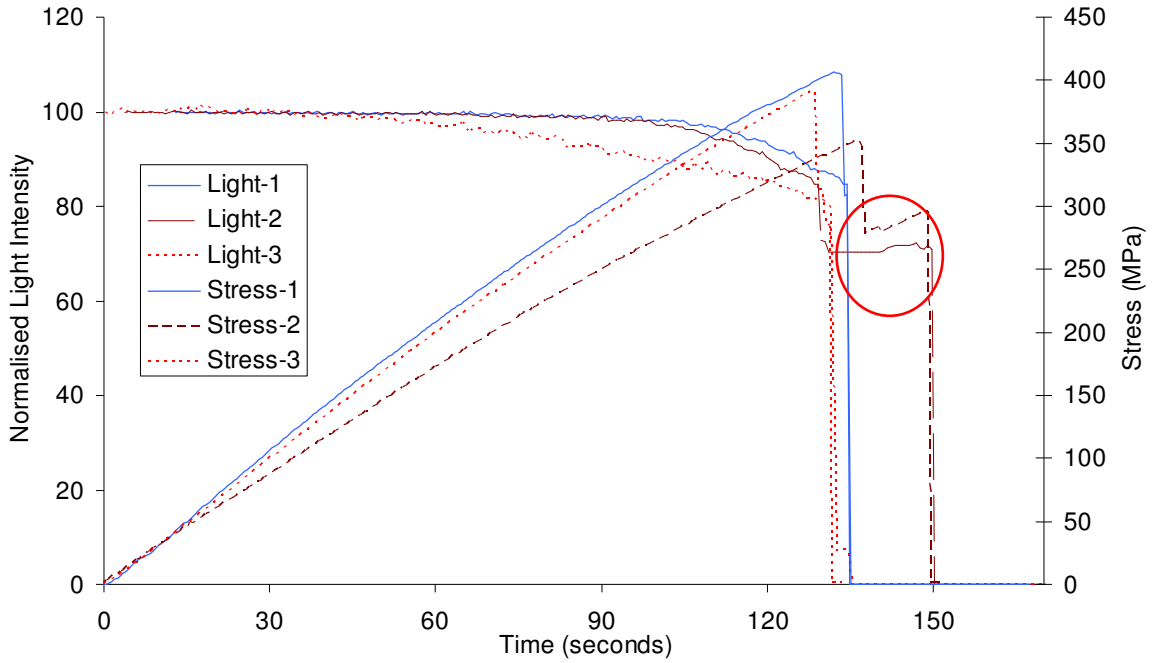
Figure 4.46 Typical graph showing the normalised transmitted light intensity and applied stress as a function of time for three samples of as-received E-glass composites.
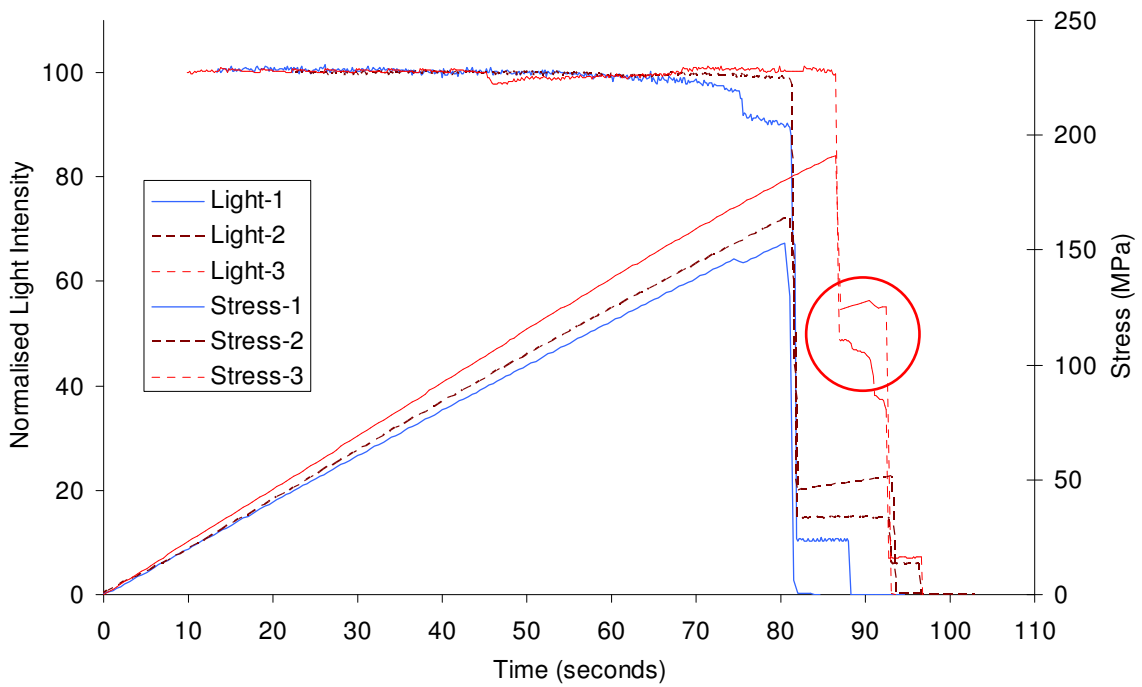
Figure 4.47 Typical graph showing the normalised transmitted light intensity and applied stress as a function of time for three test samples of the as-received SDOF composites.

In the case of self-sensing composites, Figure 4.46 and Figure 4.47 show the graphs of normalised light intensity and stress as a function of time for E-glass and SDOF composites, respectively. By comparing the plots, it is obvious that the plots of normalised light intensity were influenced by the stress versus time plots. In the case of E-glass composites, the matrix was also acting as a cladding. Therefore, it was possible that the net attenuation of light was due to the change in the optical properties of the fibre (as discussed previously) and/or matrix and due to fracturing fibres. However, in the case of the SDOF composite, the net attenuation of light was mainly due to the fibre fracture since the core of small-diameter optical fibres had a cladding on them. The difference in trends of light attenuation for E-glass and SDOF composites will be discussed in detail in Section 4.5.5.

Figure 4.46 shows a gradual decrease in the transmitted light intensity in the case of three samples of the E-glass composite. It was found that the decrease in light intensity was 15-18% at the onset of failure of the test coupon. In the case of sample-2, the test coupon exhibited failure in steps after ~130 seconds; the light intensity graphs also decreased to a minimum in steps as highlighted by red circle on Figure 4.46. In the case of as-received SDOF composites, Figure 4.47 shows the light intensity and stress as a function of time plots for three test specimens. It can be observed that the light intensity was stable until 90% of the ultimate failure stress. At the onset of failure the light intensity was decreased ~8%. Sample-3 exhibited failure in steps after ~85 seconds of loading the sample. The transmitted light intensity plot was also reduced to zero in steps as highlighted by the red circle on Figure 4.47. Hence, it can be concluded that the image analysis routines were capable of detecting damage in the self-sensing composite test coupons. The light attenuation can be related to the stress versus time plots.

In conclusion, the image analysis routines were employed to analyse thousands of images of more than 100 test specimens of fibre bundles and composite samples. It can be stated with confidence that the image analysis routines developed were able to identify and track the imminent fracture of each filament in fibre bundles and composites with an accuracy of 95±2%. This may be regarded as the most significant achievement since it is now possible for the first time to study the fracture of individual filaments in real-time.
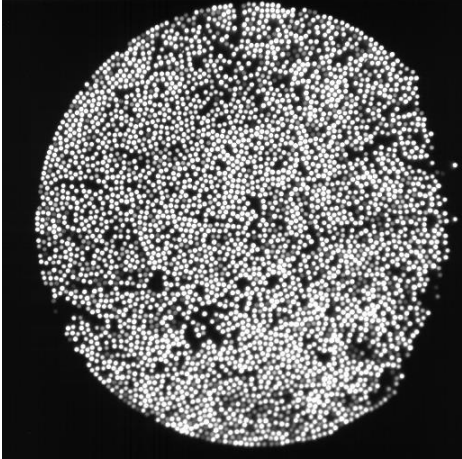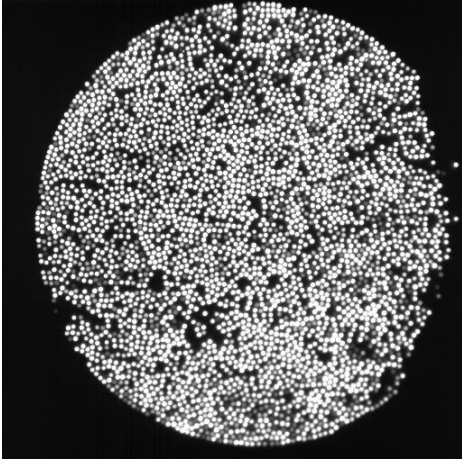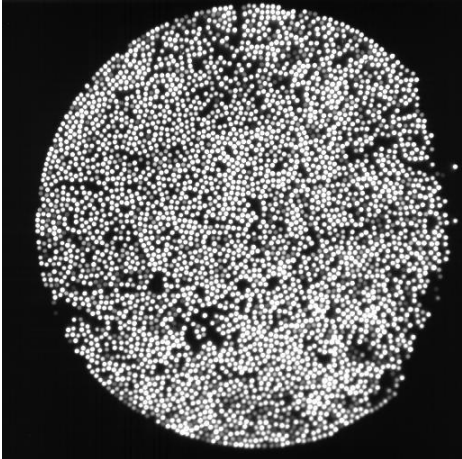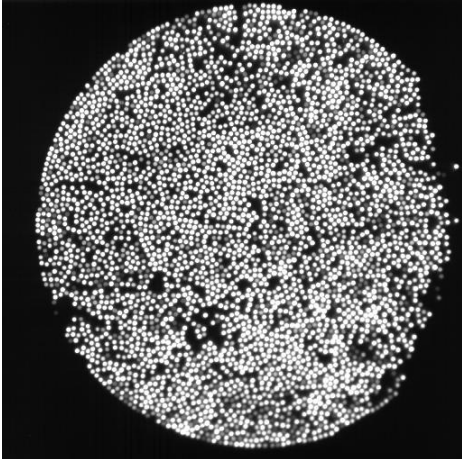
4.4.2 Image analysis of the fibre bundles

Table 4.19 presents a summary of tensile tests and *in-situ* monitoring of the light attenuation by the high-speed camera in the case of fibre bundle test specimens. With reference to Table 4.19, the numerical values are given for the data corresponding to the particular image. The abbreviations "I", "t", "L" "UT" and "UTp" corresponds to image number, time (seconds), load (Newtons), percentage of the peak-load, and percentage of peak-load after failure i.e. after the peak-load was attained, respectively.
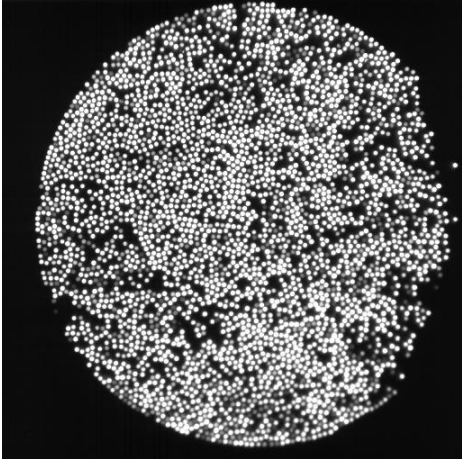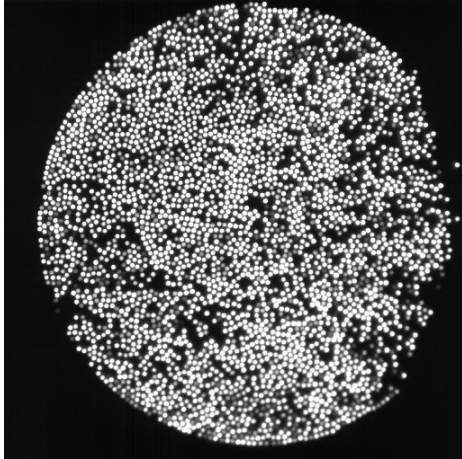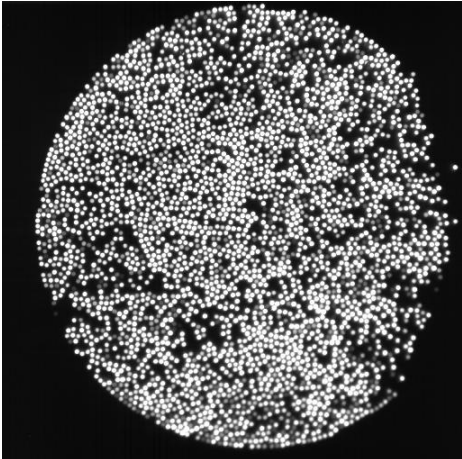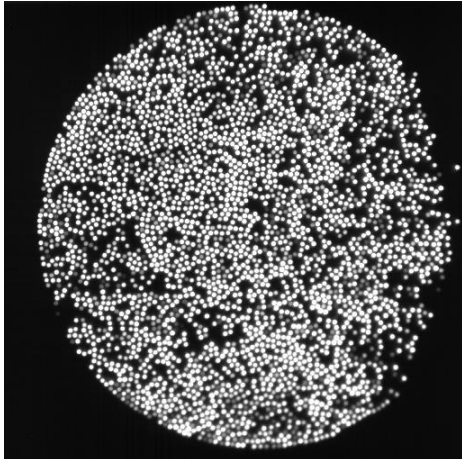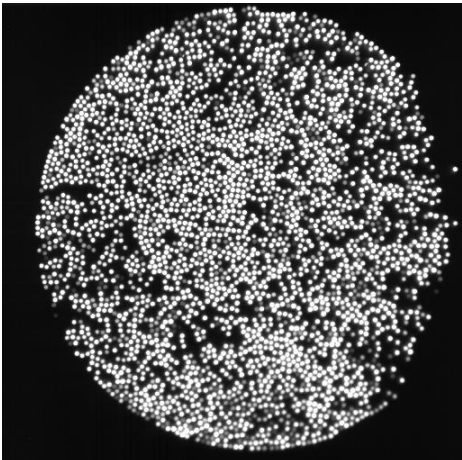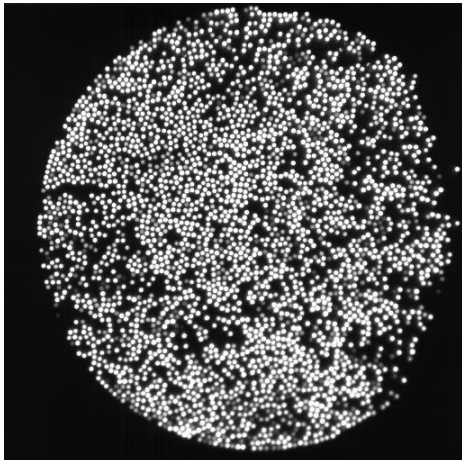
With regard to Table 4.19, the first image was captured after 3.04 seconds when the first AE hit was detected. This triggered the high-speed camera and it started recording continuously. The images taken at regular intervals of approximately 20 seconds (from continuous recording) are presented with the corresponding load in Newtons until the sample was about to reach its maximum peak-load of 584.5 N. This peak-load was used to calculate the corresponding percentage of the ultimate peak load (UT) of these images. After 86.37 seconds (5000th) image, the next frames shown were captured after every 0.34 seconds to demonstrate the light attenuation in the images before and after the failure point of the fibre bundle. The images show minimal change from the first image to the 5300th image with a corresponding ultimate peak load of 584.5 N i.e. (100%). From this point in time onwards, there was a larger, visible change in the images when the test specimen was

beyond its maximum peak-load. This means that the fibres began to fracture at a faster rate. This is shown by the images captured every 0.34 seconds. It can be clearly seen that the fractured fibres stopped transmitting light.
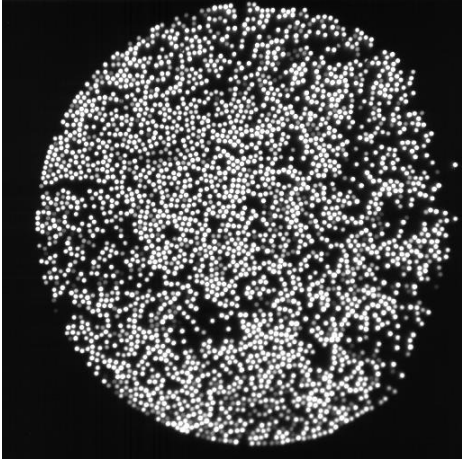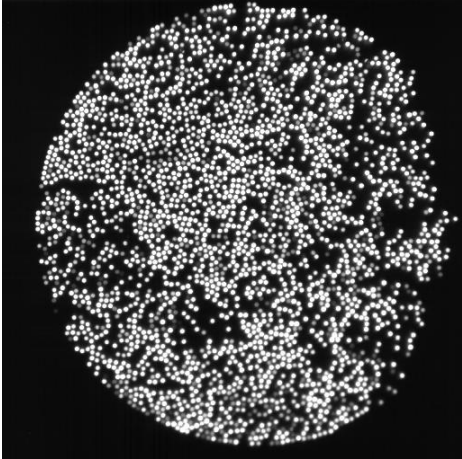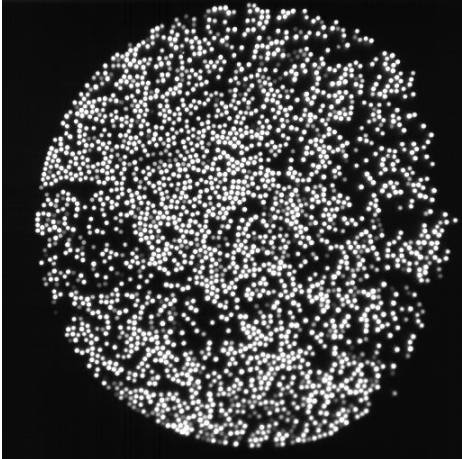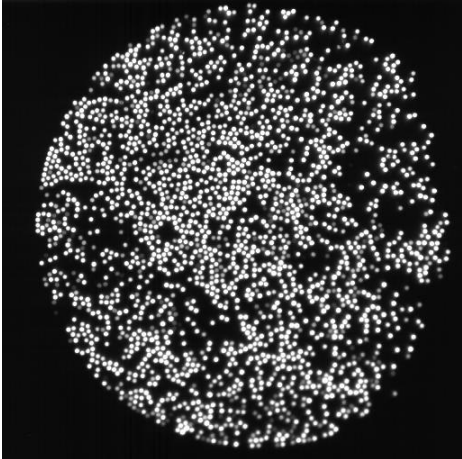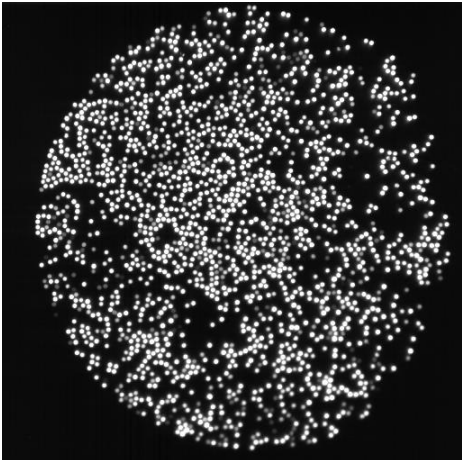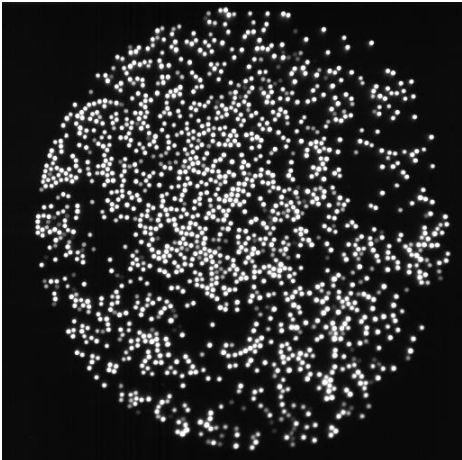
Table 4.19 Summary of tensile test and *in-situ* monitoring of light attenuation in a fibre bundle.

I =1, t =3.04, L =30.5, UT =5.26	I =1250, t =23.87, L =172.23, UT =29.66
I =2500, t =44.7, L =320.16, UT =55.17	I =3750, t =65.54, L =529.43, UT =91.28
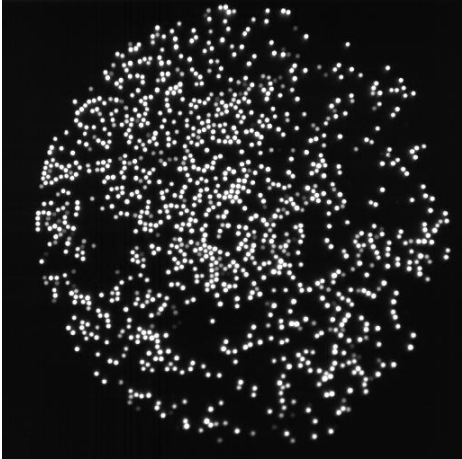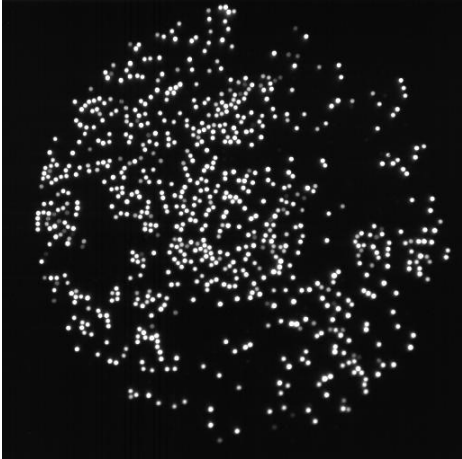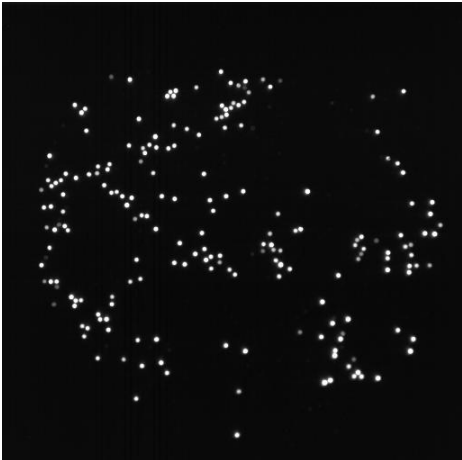
I = Image number, t = time, L = load, UT = percentage of the peak-load, and
UTp= percentage of peak-load after failure i.e. after the peak-load was attained

I =5000, t =86.37, L =576.88, UT =99.31	I =5100, t =88.04, L =578.74, UT =99.30
I =5200, t =91.38, L =583.97, UT =99.85	I =5300, t =93.05, L =584.85, UT =100
I =5400, t =93.05, L =582.99, UTp=99.68	I =5500, t =94.70, L =581.85, UTp=99.49

I = Image number, t = time, L = load, UT = percentage of the peak-load, and
UTp= percentage of peak-load after failure i.e. after the peak-load was attained

I =5600, t =96.37, L =576.42, UTp=98.56	I =5700, t=98.04, L =570.02, UTp=97.46
I =5800, t =99.70, L =542.31, UTp=92.73	I =5900, t =101.37, L =519.35, UTp=88.8
I =6000, t=103.04, L =477.30, UTp =81.61	I =6100, t=104.70, L = 451.20, UTp=77.15

I = Image number, t = time, L = load, UT = percentage of the peak-load, and
UTp= percentage of peak-load after failure i.e. after the peak-load was attained

213

I =6200, t =106.37, L =381, UTp=65.14 | I =6300, t =108.04, L = 285.97, UTp=48.9

I =6400, t =109.70, L =223.43, UTp=38.2 | I =6500, t =111.37, L =156.76, UTp=26.8

I =6600, t =113.09, L =97.50, UTp=16.67 | I =6700, t =114.76, L =66.17, UTp=11.31

I = Image number, t = time, L = load, UT = percentage of the peak-load, and
UTp= percentage of peak-load after failure i.e. after the peak-load was attained

I =6800, t =116.43, L =43.71, UTp=7.47	I =6900, t =118.10, L =32.52, UTp=5.56
I =7000, t =119.77, L =26.67, UTp=4.56	I =7500, t =128.79, L =16.37, UTp=2.8
I =8000, t =136.37, L =15.125, UTp=2.59	Last image

I = Image number, t = time, L = load, UT = percentage of the peak-load, and
UTp= percentage of peak-load after failure i.e. after the peak-load was attained
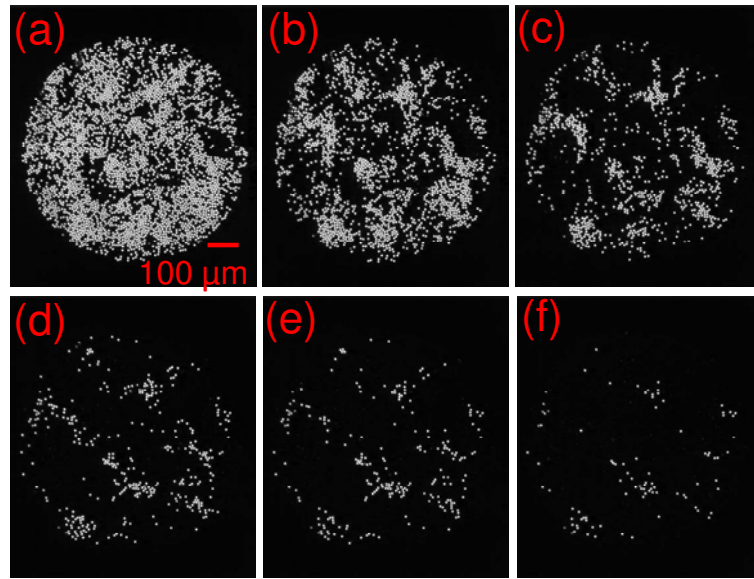
Figure 4.48 (a-f) Consecutive images of SDOF: (a) Image captured at onset of failure in the bundle; and (b-f) Images captured every 10 seconds thereafter.

As mentioned previously, the fibres in the bundle were not loaded evenly, due to twists, cross-overs and varying lengths and strength distributions. Therefore, they continued fracturing randomly after the peak-load was attained. The failures of the individual filaments in the bundle do not cause the tow failure and therefore, the bundles fail non-catastrophically. The observed non-catastrophic failure of fibre bundles has been reported by many researchers [43, 49, 51, 54, 55, 65, 78, 159, 180]. Previous researchers have employed acoustic emission monitoring to record the failure of individual filaments in the bundle but the interpretation of AE data is still an issue of ongoing research [65, 79, 87, 159, 161]. It was established previously (see Section 4.4.1) that the cut-off of the transmitted light was due to fibre-fracture. Therefore, from the 5300th image (Figure 4.48 (a-f)), it is obvious that fibres were fracturing even after the peak-load. The self-sensing fibre bundles demonstrated this effect in real-time without any additional external sensor. Once again, this may be regarded as the one of the most significant achievements; although previous researchers discussed the fracture of fibres after the peak-load, direct evidence for this is presented for the first time in this study. The image analysis routines

were capable of identifying the attenuation of transmitted light; it was found that the light was attenuated at a rate similar to the rate of decrease in load (after the peak-load). This can be observed by the normalised intensity versus time plots for the fibre bundles as shown in Figure 4.49 (a-d).
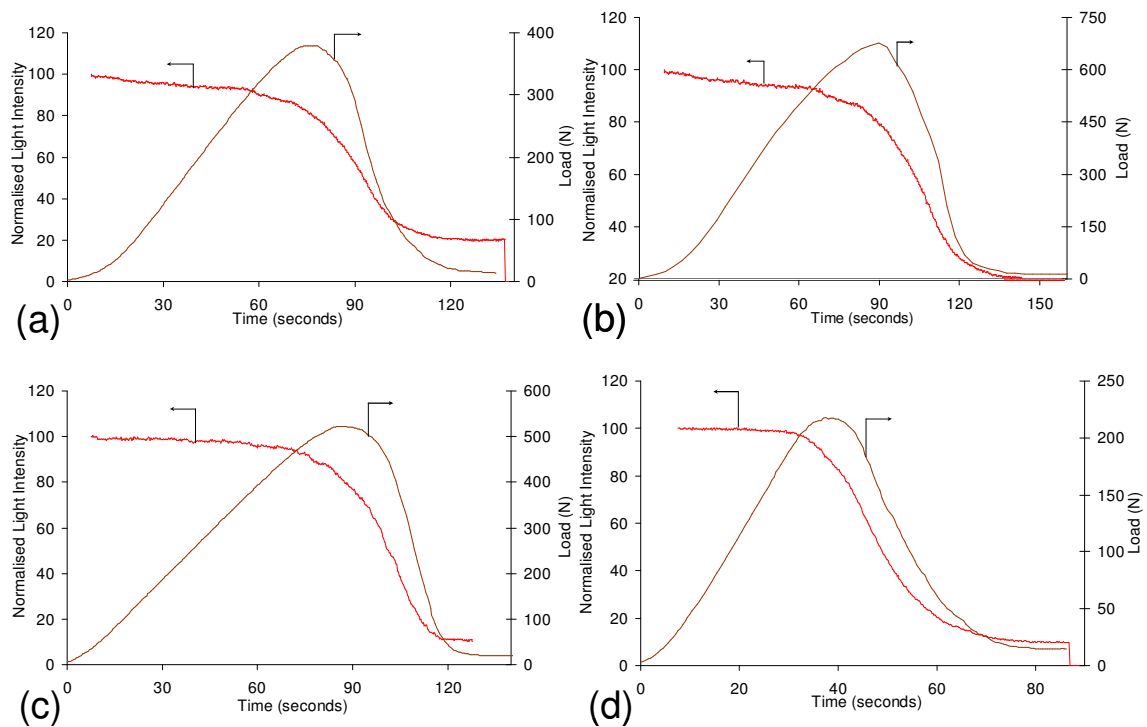
Figure 4.49 Graphs showing the normalised transmitted light intensity and applied load as a function of time for: (a) As-received E-glass fibre bundle; (b) Silane-treated E-glass fibre bundle; (c) As-received SDOF bundle; and (d) Heat-treated SDOF bundle.

Figure 4.49 (a-d) shows the relationship between the transmitted light intensity and applied load as a function of time for the as-received E-glass fibre, silane-treated E-glass fibre, as-received SDOF and the heat-treated SDOF bundles, respectively. In the majority of cases, a rapid decrease in the transmitted light intensity was observed when 90% or more of the peak-load was attained. At the peak-load of the fibre bundle, the light intensity was decreased 17% and 20% in the case of as-received E-glass and silane-treated E-glass fibre bundles, respectively. The net decrease in the light intensity of a fibre bundle (before peak-load) could be due to two reasons: change in the light guiding properties of the fibres (due

to the applied strain); and/or due to the fracturing of fibres. These effects can also occur simultaneously. Under the influence of an applied load the refractive index and/or light propagating characteristic of optical fibres can change. Kiesel [197] reported that in the case of silica, the change in light guiding properties is directly proportional to the applied load for 1-2% of applied strain. In this region (1-2% of strain) the propagation of light through an optical fibre is altered by two effects: the change in index of refraction of the optical medium and the change in length of the medium. These effects can be referred to two separate sets of material properties: the photo-elastic coefficients and mechanical coefficients. An applied strain of greater than 2%, can cause necking and local finite deformation of optical fibres, which require non-linear strain coefficients [198, 199]. Hence, it can be concluded that a strain as low as 1% can influence the light propagation through conventional optical fibres [197]. However, these effects are out of the scope of this study (the number of fibres in the bundles were 2400-2800) and therefore, are not considered in this work. At the peak-load, the percentage extension in the test-specimen was 1.26%; therefore, the light propagation is affected at this magnitude of strain. Amir and Ahamdi [79] estimated the number of fractured-fibres during the loading-phase (before peak-load was attained) of fibre bundles by the total number of AE hits produced above 60 dB. It was reported that the amplitude of the AES corresponding to the fracturing of fibres produce AE hits of $\geq$60 dB [65, 78, 151, 159, 160]. Using the same threshold (60 dB), it was estimated that ~526 AE hits were recorded from the start of the test until the peak-load was attained. Therefore, the number of fractured fibres was assumed to be 526; (i.e. 16% of the total number of fibres). This can be observed from by comparing the first and 5300th image captured by the high-speed camera as shown in Table 4.19. It can be concluded that the number of fractured fibres were predominantly reducing the transmitted light. The number of fibres in an E-glass bundle was ~2800, therefore, it was relatively

difficult to exactly quantify or differentiate between the effects of the two causes of decrease in the light intensity. However, the net effect was ~16% decrease in the transmitted light intensity.

In the case of as-received SDOF bundle, the decrease in light intensity was 15% and the number of hits recorded corresponding to the fibre fracture (where the amplitude of the AES greater than 60 dB) was ~492. Therefore, in the case of the as-received SDOF, the decrease in light intensity was mainly due to the fractured fibres. In the case of the heat-treated SDOF, the decrease in light intensity at the peak load was 12% and 282 fibres were fractured before the peak load of the bundle. The percentage extension at the peak-load was 0.62%. It was possible that the light propagation was not affected at 0.62% extension. Therefore, the net decrease in light intensity was lower as compared to the other three types of fibre bundles. Hence the decrease in overall light intensity may be attributed to the fracturing fibres in the case of heat-treated SDOF bundles.

For the four types of fibre bundles, the decrease in normalised light intensity after the peak-load occurred at a rate similar to the decrease in the "unloading" rate. The failure of the fibre bundle was non-catastrophic in nature for the reasons discussed in Section 4.3.1. The light intensity was seen to decrease rapidly due to the fractured fibres. The effect of the applied strain (after the peak load) on the light transmission was negligible as it was superimposed by the fracturing fibres. This process continued until all the fibres in the bundle were fractured.

The major findings of this section are summarised below:

i. The failure of individual filaments can be related directly to the attenuation of the transmitted light.

ii. It has been demonstrated that the complete cut-off of the transmitted light was an indication of the failure of the filament that can be detected by the image analysis routines.

iii. It has been demonstrated *in-situ* that the number of fractured fibres in a bundle before the peak-load is negligible (< 10%) when compared to the total number of fibres in the bundle.

iv. As previously mentioned in Section 4.3.2, the fibres in the bundle fractured even after the peak-load and the failure of individual filaments did not cause tow failure. The self-sensing fibres proved this effect in real-time for the first time. This may be regarded as a significant achievement since the fracturing of the fibres was monitored *in-situ* and without any external sensor or monitoring system. The fibres themselves demonstrated the fracture due to attenuation of the transmitted light.

In conclusion, the image analysis technique developed was employed successfully for the *in-situ* damage detection of self-sensing fibre bundles. It has been demonstrated conclusively that this is a unique technique that can be employed to detect fracture of individual fibres. There is no doubt that it is now possible to detect imminent fracture of individual filaments in a bundle. The self-sensing technique provided evidence that the filaments in the bundle were fracturing randomly at different times and therefore, causing a non-catastrophic failure of the fibre bundle. The use of light transmission for *in-situ* monitoring of damage in fibre bundle is reported for the first time. Although, E-glass [10] and quartz fibres [8] were employed previously to detect damage, however, they were embedded in the composite to detect damage during impact and flexural loading (see Section 2.5.7). The further development of this technique to relate the stress and strength distribution of fibres to the transmitted light intensity may reveal detailed characteristics of the fibres fracturing in a bundle.

4.5 Mechanical Testing of Self-sensing Composites

Self-sensing composites offer a unique advantage of detecting the damage in real-time. The damage in a composite test coupon was detected *in-situ* by employing the acoustic emission monitoring and high-speed photography of the RFLGs. The results of self-sensing composite materials are presented in the next sections.

Table 4.20 Classification of the self-sensing composite materials used in this study.

	Fibre type	Composite classification
1.	As-received E-glass fibre	As-received E-glass composite
2.	Silane-treated E-glass fibres	Silane-treated E-glass composite
3.	As-received small-diameter optical fibre (SDOF)	SDOF composite
4.	Heat-treated SDOF	Heat-treated SDOF composite

Four types of composites were manufactured in this study from E-glass and SDOF fibres. The E-glass fibres were silane-treated and SDOF were heat treated as discussed in Section 4.1.1. Table 4.20 shows the composites manufactured from different fibre types and treatments. From here on the composites will be classified depending on the specific type of fibres and treatment used.

4.5.1 Tensile test results of the self-sensing composites

The tensile testing was carried out at a cross-head speed of 1 mm/minute under ambient temperature. Custom designed end-tabs were used to prevent the test specimens from being damaged in the jaws of the mechanical test machine.
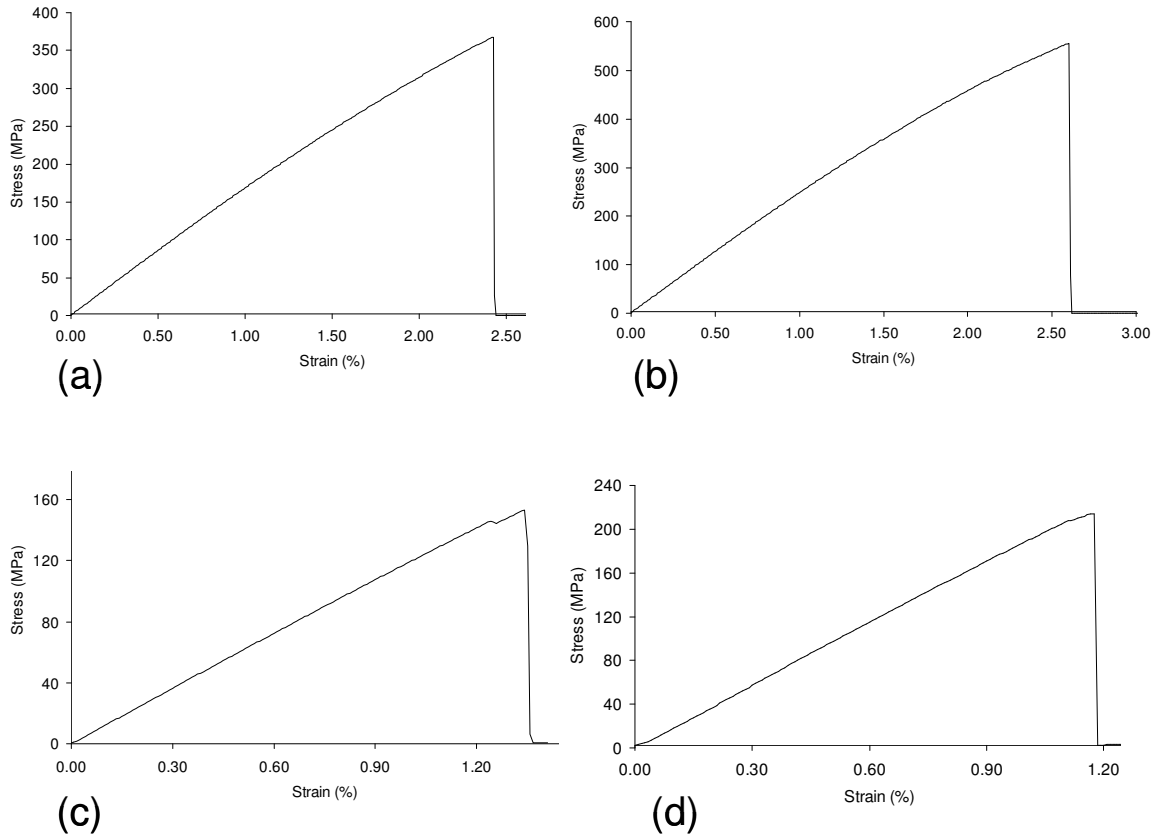
Figure 4.50 Graphs showing the stress versus strain for the composites manufactured from: (a) As-received E-glass fibres; (b) Silane-treated E-glass fibres; (c) As-received SDOF; and (d) Heat-treated SDOF.

Figure 4.50 (a-d) shows representative graphs of stress versus strain for the four types of composites investigated during this study. The composites were manufactured by using the resin-injection method as discussed in Section 3.2.3. The average mechanical properties of the composites are summarised in Table 4.21. The elastic moduli of the composites were calculated using the linear portion of the stress-strain plot. After tests on twenty individual specimens, the majority of the stress versus strain plots were found to be linear until failure. The mechanical-properties presented in Table 4.21 are average of 6 samples. The deviation in the results was 5-8%. The possible causes of the observed variations may be attributed to general experimental errors, such as, loading the sample in the jaws of the Instron machine, possible misalignment between the end-tabs and the quality of polishing

222

at the edges. Although, due care and attention was given to standardise the specimen-fabrication process, the variations associated with manual fabrication cannot be ruled out. However, it can be stated that the results of the tensile tests were in good agreement (5-8%) of each other.

Table 4.21 A comparison of the average mechanical properties of the self-sensing composites determined experimentally.

Composite type	Number of samples	Elastic modulus (GPa)		Ultimate tensile strength (MPa)		Strain at failure (%)	
		Average	S.D.	Average	S.D.	Average	S.D.
As-received E-glass fibres	7	18.2	2.03	428.1	57.34	2.4	0.31
Silane-treated E-glass fibres	6	21.8	2.85	505.3	52.57	3.1	0.3
Small-diameter optical fibres	6	13.1	1.56	186.5	27.18	1.4	0.08
Small-diameter optical fibres (heat-treated)	6	16.1	1.86	177.8	22.61	1.1	0.13

With reference to Table 4.21, the silane-treated E-glass composite exhibited better mechanical properties than the as-received E-glass composites. This can be seen by comparing the elastic moduli and ultimate tensile strength (UTS). The average UTS and strain-to-failure was ~14% greater than for the as-received E-glass composites. The most likely cause was the better surface adhesion of the silane-treated fibres with the epoxy matrix. The fibre-matrix interface was comparatively more effective and therefore, resulted in better mechanical properties [1, 15, 200, 201]. This was also evident by observing the image of a fractured test specimen of a silane-treated composite as shown in

Figure 4.56. Figure 4.56 shows extensive interfacial debonding and transverse matrix cracking in the test coupon when compared to the fractured test specimen of the as-received E-glass composite (Figure 4.55). This will be discussed in more detail with the acoustic emission results.

In the case of as-received SDOF and heat-treated SDOF composites test specimens, the average failure strengths were 186.5 MPa and 177.8 MPa, respectively. The average strains-to-failure were 1.4% and 1.1%. The strain-to-failure of the SDOF composites was less than half of the E-glass composites. Although the properties of SDOF bundles were comparable to the E-glass bundles, however the composite manufactured from the SDOF exhibited inferior mechanical properties. The most likely cause of this difference was the absence of a strong interfacial bond between the fibres and the matrix. This affects the load transfer between fibres and/or fibres and the matrix. This was also evident by comparing the acoustic emission data for these two types of composites. The relevant frequencies and amplitude of the AES of interface-failure were not recorded.

The voids in the composite have predominant effects on the mechanical properties and structural integrity of composites. It is well-established that the specific mechanical properties of composites such as tensile modulus, flexural and inter laminar shear strength (ILSS) and the ultimate strengths are degraded due to the presence of voids [202-208]. Voids are basically the discontinuities or defects that are induced during the manufacturing of the composite materials. There are several causes of void formation, with the two most common being the entrapment of gases (mostly air) during lay-up and the volatiles released from the resin system during cure [204]. Olivier *et al.* [204] investigated the effect of void content (0.3-10.3%) on the tensile modulus and strength of carbon/epoxy laminates. Their results indicate that a void content of 10% reduces the longitudinal tensile

strength by ~12%. Liu *et al.* [209] found that the tensile strength decreases by ~14% when the void content increases from 0.6 to 3.2%. Although there is no consensus in the literature regarding the quantitative effect of the void content on the mechanical properties of a composite; it is understood that the voids have detrimental effects on matrix-dominated and out-of-plane properties, such as inter-laminar shear strength, compressive strength, through-thickness tensile strength and impact toughness. The longitudinal (fibre dominated) properties of laminates are usually not significantly affected by voids unless the porosity content is relatively high [203, 204, 206, 208, 210, 211]. Therefore, it was concluded that in the case of self-sensing composites, the effects of voids can be ignored since they were negligible. The presence of voids in the self-sensing composites was discussed in Section 4.1.5.

4.5.2   Estimation of mechanical properties using the rule-of-mixture

The theoretical basis of the rule-of-mixtures has been discussed in detail in Section 2.4.1. This model assumes that the continuous fibres are well-bonded to the matrix so that under an applied load, the fibres and matrix deform together i.e. the strain in the composite is equal to the strain in the fibres and matrix. In this section, the properties of the self-sensing composites were estimated on the basis of the rule-of-mixtures. The ultimate tensile strengths (UTS) of the fibres were determined using the Weibull statistical analysis, the experimentally determined UTS of the matrix system (EPO-TEK$^{®}$-314) is 27.17 MPa, therefore, the tensile strength of the unidirectional composite can be estimated from Equation 2-10.

From Equation 2-10;

$$\sigma_1 = f\sigma_f + (1-f)\sigma_m \qquad\qquad 4\text{-}14$$

The elastic modulus of the composite can be calculated from:

$$E_1 = fE_f + (1 - f)E_m \qquad\qquad 4\text{-}15$$

where the notations have been defined previously.

Table 4.22 A comparison of the estimated mechanical properties calculated using the rule-of-mixtures versus experimentally determined properties of self-sensing composites.

Composite type	Estimated properties from the rule-of-mixtures		Experimentally determined properties from Table 4.21			
	Elastic modulus (GPa)	Ultimate tensile strength (MPa)	Elastic modulus (GPa)		Ultimate tensile strength (MPa)	
			Average	SD	Average	SD
As-received E-glass	17.9	447.3	18.2	2.1	428.1	57.3
Silane-treated E-glass fibres	18.4	542.7	21.8	2.8	505.3	52.5
Small-diameter optical fibres	15.8	419.7	13.1	1.5	186.5	27.1
SDOF (heat-treated)	12.9	199.3	16.1	1.8	177.8	22.6

Table 4.22 shows a comparison of the estimated mechanical properties (calculated using the rule-of-mixtures) with experimentally determined properties of the four types of self-sensing composites. The following observations can be made; the elastic moduli of the four types of composite agree with the rule-of-mixture's moduli within ±3 GPa. For instance, the estimated elastic moduli are 17.9 GPa, 18.4 GPa, and 12.9 GPa, and the experimentally determined moduli are; 18.2 GPa, 21.8 GPa and 16.1 GPa for the as-

received E-glass, silane-treated E-glass and heat-treated SDOF composites, respectively. However, in the case of the as-received SDOF composite, the estimated elastic modulus was lower than the experimentally determined modulus. The experimentally determined elastic modulus was 13.1 GPa, whereas the estimated modulus was 15.8 GPa. This was most likely due to the weak-adhesion between the fibres and matrix caused by the coatings, as a result the strain in the matrix was not the same as the strain in the fibres. The rule-of-mixture assumes that the fibres and matrix are perfectly bonded. Due to the weak-bond between fibres and matrix the SDOF composites exhibited a lower elastic modulus.

By contrast to the estimated elastic moduli, the experimental values of the ultimate failure strengths were lower than the estimated values from the rule-of-mixtures. The following factors may have contributed to the observed discrepancy between the estimated and experimental UTS: (i) the tensile strength of the E-glass fibres was calculated from the experimentally-obtained peak loads of the fibre bundles, assuming a constant fibre diameter of 15 µm and an average of 2800 filaments in the bundle, the possible variation in the diameter of the fibres affects the fibre cross-sectional area, as discussed previously, this was not the case with the batch of E-glass fibre used; (ii) the difference in Poisson's ratio of the fibre and matrix; (iii) the fibre strength distributions; and (iv) the presence of twists and waviness in the fibres (see Section 2.4).

The rule-of-mixtures assumes that the strain in the composite is equal to the strain in the fibres and matrix. This can only be accurate if the difference in the Poisson's ratio of the fibre and matrix is negligibly small. Since this is not practically possible, therefore, under an applied axial stress the fibres and matrix tend to deform with respect to their elastic moduli. If the bonding between fibres and matrix is strong they tend to deform together and thus keeping the Poisson's effect to minimum. By contrast, if the interfacial bond is

weak these effects may become more dominant. This may be appreciated further by comparing the estimated and experimental UTS of the as-received SDOF. The estimated UTS is 419 MPa and the experimentally determined value is 186 MPa, which is less than half of the estimated value. Assuming that the void content is negligible, this may only be explained by the difference of strain in the fibres and matrix and the absence of a strong bond between the fibres and matrix.

Due to these reasons there is variation in the estimated and experimental properties of self-sensing composites. However, the rule-of-mixtures provided a good approximation (5-12%), to predict the stiffness and corresponding strengths of the composites.

4.5.3 Acoustic emission monitoring of the self-sensing composites

Acoustic emission is a well-established technique for analysing different damage mechanisms within fibre reinforced composite materials such as fibre/matrix fracture, fibre-matrix de-bonding and de-lamination. In this section, the acoustic emission results of the self-sensing composites are presented.

The number of hits, amplitude, peak frequency and average frequency of the composites made from the four types of fibres are presented in Table 4.23. Table 4.23 shows that the average number of 14149 hits was recorded with a standard deviation (SD) of 2095 for the as-received E-glass composites. The average amplitude was 53.2 dB with a SD of 1.9. The average peak frequency was 162.7 kHz with a SD of 19.1. In the case of silane-treated E-glass composites, the average number of hits was 15076 with a SD of 2665. The average frequency was 118.1 kHz and the peak frequency was 145.5 kHz with SDs of 11.8 and 17.7, respectively. The higher numbers of hits agreed with the number of AE hits recorded for the silane-treated E-glass fibre bundle (see Table 4.16). The average amplitude for the silane-treated E-glass composite was 51.9 dB with a SD of 1.7. On comparing the AE data

recorded for the as-received (untreated) and silane-treated E-glass composites, it can be observed that the number of hits, amplitudes of the AES and frequencies were within the same general range.

Table 4.23 A comparison of the acoustic emission parameters for composite samples.

Composite type	Number of samples	Number of hits		Amplitude (dB)		Peak frequency (kHz)		Average frequency (kHz)	
		Average	S.D.	Average	S.D.	Average	S.D.	Average	S.D.
As-received E-glass fibre	7	14149	2095	53.2	1.9	162.7	19.1	105.3	12.8
Silane-treated E-glass fibres	6	15076	2665	51.9	1.7	145.5	17.7	118.1	11.8
Small-diameter optical fibre	6	5136	758	59.2	2.4	163.4	13.9	119.3	14.5
Small-diameter optical (heat-treated)	6	8871	1394	54.5	1.8	204.2	21.3	179.2	19.0

The AE results for the as-received SDOF composite material show that the average number of AE hits produced were less than for the other types of self-sensing composites investigated. This may possibly be due to the damping (due to organic-binder) of the AE signal. Table 4.23 shows an average of 5136 hits with a SD of 758 recorded for the SDOF. The amplitude of the AES was 59.2 dB with a SD of 2.4. An average peak frequency of 163.4 kHz and a SD of 13.9 were recorded for this composite type.

In the case of the heat-treated SDOF, the average number of AE hits recorded was 8871 with a SD of 1394. The amplitude was within the same range as that of the other types of composites. However, the peak frequency (204.2 kHz) was far greater than for the other types of composites. The likely cause of this deviation was the brittleness induced by the heat-treatment of the fibres, and it agreed with the AE data presented for fibre bundle testing (see Table 4.16). The average frequency of this composite type was 179.2 dB with a SD of 19.0.

In the next section, the analysis of AE data is presented. The plots of peak frequencies and amplitude versus time give information about the different modes of damage occurring in the test coupons.

4.5.4   Analysis of the acoustic emission data for the self-sensing composites

The plots of cumulative AE hits versus time were shown in Section 4.3.3 for the fibre bundles. In this section similar graphs for the composites are presented.

Figure 4.51 (a-d) shows the stress and cumulative AE hits as a function of time plots for the four types of composites. It is apparent from Figure 4.51 (a-d) that the cumulative AE hit plots are influenced by the applied stress and hence the evolution of damage in the composite. A gradual increase in the cumulative hit plots of the as-received E-glass composite was observed in the range 40 – 50% of the applied stress. Figure 4.52 shows a representative plot to illustrate the calculation of slopes in the case of E-glass composites. With reference to Figure 4.52, the data presented in Table 4.24 was derived on the basis of two regions of the AE hits plot as indicated by two straight lines and their respective slopes 'a' and 'b'. Similar calculations were made for the remaining three types of self-sensing composites. The calculated slopes of the four types of composites are summarised in Table 4.24. In the case of the E-glass composite, the slope of the AE plot was increased

6.7 times (from its initial value i.e. 413 hits/second) after 90 seconds of loading the sample. A similar trend was observed in the case of the silane-treated E-glass composite, after ~90 seconds of loading the test specimen as illustrated in Figure 4.51b. With reference to Table 4.24, the initial slopes of cumulative AE hits plot were 413 and 388 for the as–received and silane-treated E-glass composites, respectively. The slope of both the graphs changed at 90 seconds and increased by 5.2 and 6.7 times of their respective initial values. The onset of change in cumulative AE hit plots was taken to represent the point at which the damage-evolution in the composites started to increase significantly. It was found that until 90 seconds the fracture mechanism occurring in these test coupons was mainly matrix cracking. It was apparent from the amplitude of the AES and peak-frequency versus time graphs; where low peak frequency (<100 kHz) and low amplitude of the AES (<65 dB) hits were recorded as shown in Figure 4.53 (a and b) and Figure 4.54 (a and b) respectively. A discussion on these graphs is presented in the second part of this section.

In the case of as-received SDOF composite, a step change in the AE activity was observed as shown in Figure 4.51c. The slope of the AE plot representing the as-received SDOF composite increased abruptly after 64 seconds of loading the test specimen. The increase in slope was approximately 15 times of its initial value. This difference in the acoustic behaviour of the E-glass and the as–received SDOF composites was most likely due to the uneven organic-binder present on the small-diameter optical fibres. Due to the presence of the uneven organic binder the fibre-matrix interface was not effective and resulted in poor load transfer (between fibres and/or fibres and matrix). As discussed in Section 2.4.2, in the case of the weak interface and relatively high strain-to-failure of the fibre, when the applied load reaches the strain-to-failure of the fibre, the matrix is incapable of distributing load (weak-interface) and therefore, fibre-matrix debonding occurs [15, 16]. In general, the

composite specimens fail by longitudinal splitting (debonding) and fibre fractures. All the test coupons of the as-received SDOF composite fractured on exactly the same manner. Figure 4.57 shows a representative image of a fractured specimen of the as-received SDOF composite. The amplitudes of the AES and peak-frequencies related to the matrix-cracking and fibre-matrix debonding were not recorded in the case of the as-received SDOF composite as shown in Figure 4.53c and Figure 4.54c, respectively. This was due to the fact that the composite test coupons fractured at ~1.2% of strain. The strain-to-failure of the matrix (EPO-TEK®-314) was 1% and therefore, the matrix cracking and fibre fracture occurred almost simultaneously.

Table 4.24 A summary of calculated slopes for plots of cumulative hits versus time for the self-sensing composites.

Composite type	Time at onset of initial (gentle) rise in slope (seconds)	Time at the exponential (rapid) rise in slope (seconds)	Slopes (hits/second)	Calculated increase in slope
As-received E-glass	24	90	413	-----
	90	128	2772	6.71 times
Silane-treated E-glass	27	90	388	-----
	90	156	2021	5.5 times
As-received SDOF	23	64	478	-----
	64	82	7334	15 times
Heat-treated SDOF	8	60	1681	-----
	60	71	15836	9 times
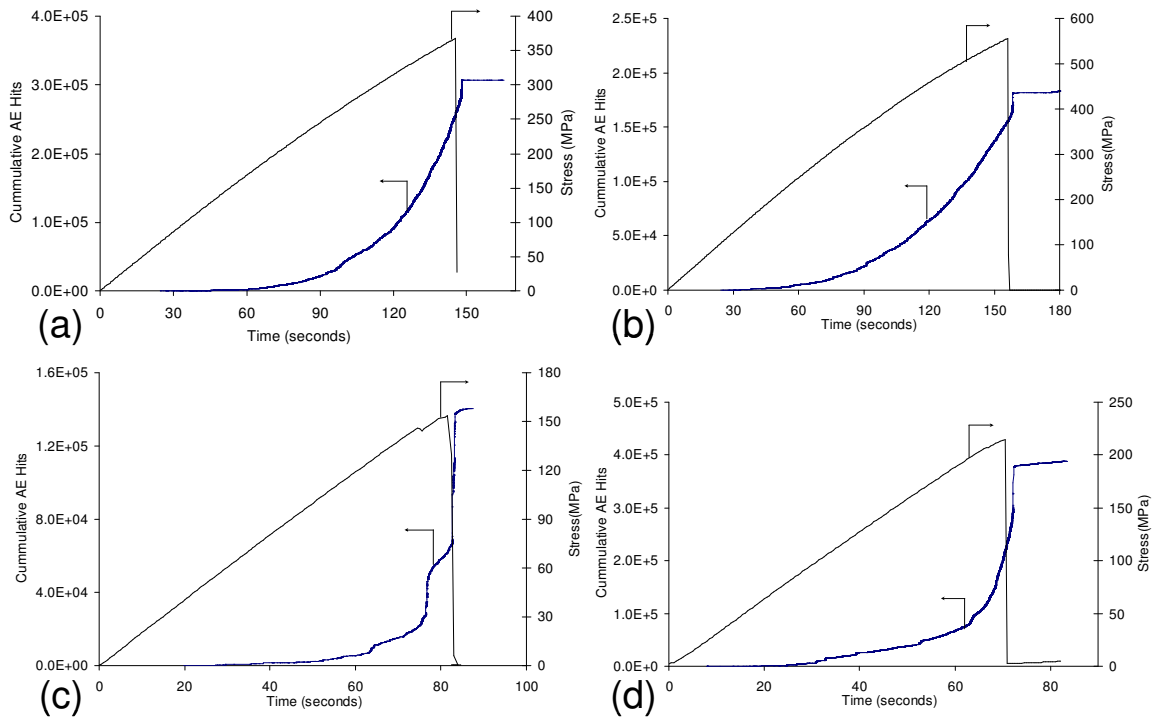
Figure 4.51 Graphs showing the cumulative AE hits and load as a function of time for composites manufactured from: (a) As-received E-glass fibres; (b) Silane-treated E-glass fibres; (c) As-received SDOF; and (d) Heat-treated SDOF.
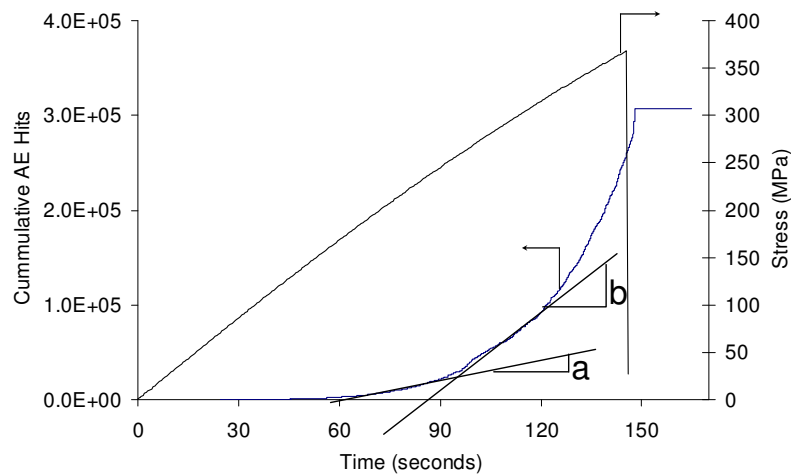
Figure 4.52 Representative graph and an illustration indicating the calculation of slopes of AE hits versus time plot in the case of the E-glass composite, 'a' and 'b' represent the slopes of lines between 30-90 seconds and 90-128 seconds on the AE hits plots, respectively. The calculated slopes of the four types of composites are summarised in Table 4.24

In the case of the heat-treated SDOF, a different trend was observed. The organic binder was removed by pyrolysis and therefore, the fibre-matrix interface was comparatively strong and effective. Hence the AE data of the heat-treated SDOF was more similar to the E-glass composites than the as-received SDOF composite. A gradual increase in the cumulative AE hits plot was observed as shown in Figure 4.51d. However, in contrast to the E-glass, an increase in the slope of the cumulative AE hits was observed at ~85% of the ultimate failure strength. This was possibly due to the lower strain-to-failure of the heat-treated SDOF composite specimen in comparison to the other types of self-sensing composites.
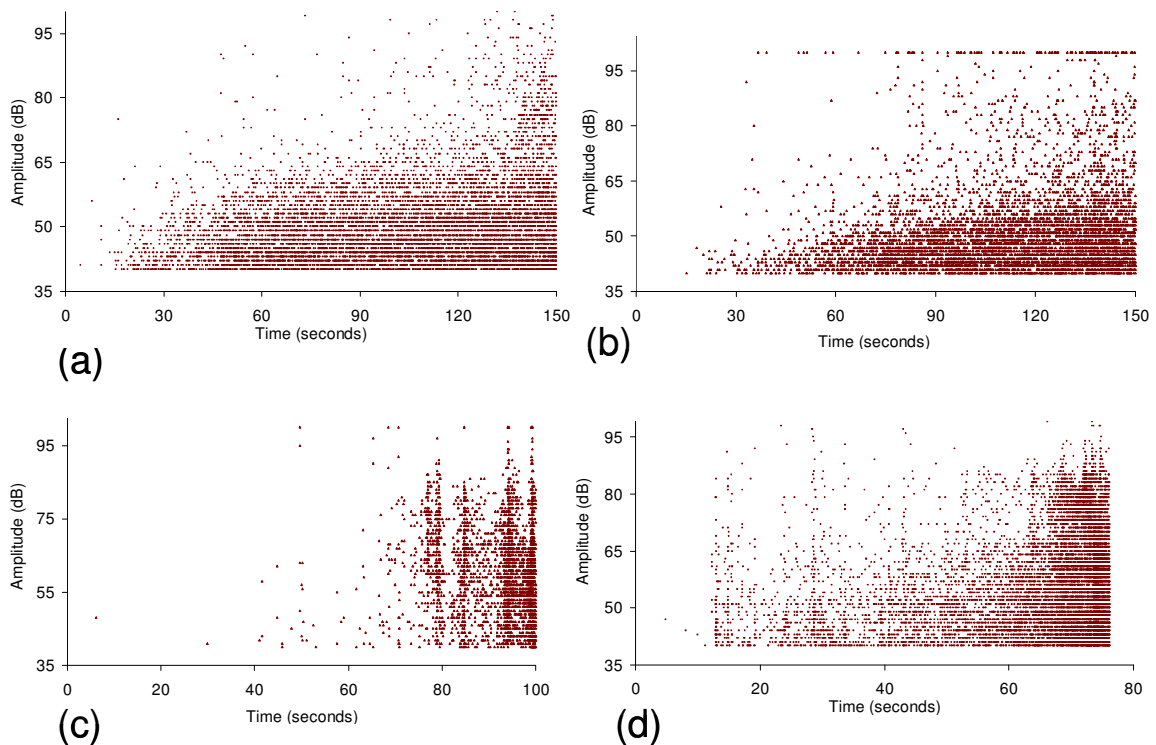
Figure 4.53 Graphs showing the amplitude of the AES as a function of time for composites manufactured from: (a) As-received E-glass fibres; (b) Silane-treated E-glass fibres; (c) As-received SDOF; and (d) Heat-treated SDOF.
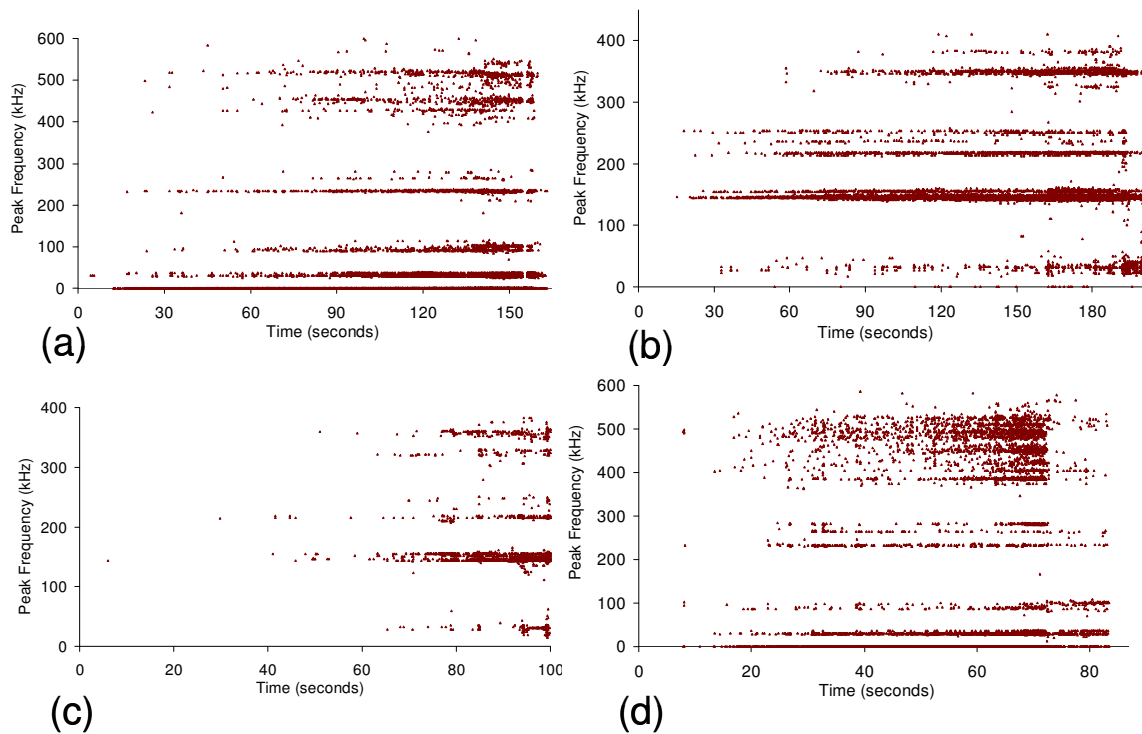
Figure 4.54 Graphs showing the peak frequency as a function of time for composites
manufactured from: (a) As-received E-glass fibres; (b) Silane-treated E-glass fibres; (c)
As-received SDOF; and (d) Heat-treated SDOF.

Table 4.25 A comparison of published data related to the peak frequency and amplitudes
of the AES of E-glass composites with the data obtained from self-sensing composites.

Damage mode	Barré *et al.* [151] Bhatt *et al.* [153] Henrat *et al.* [165]		Self-sensing composites (current work)	
	Frequency range (kHz)	Amplitude (dB)	Frequency range (kHz)	Amplitude (dB)
Matrix cracking	30-180	40-60	30-150	40-60
Fibre pull-out	180-240	60-65	150-220	55-65
De-bonding	240-310	65-85	200-300	60-80
Fibre fracture	300-500	85-95	350-550	80-100

.

As mentioned previously, the amplitude of the AES and the peak frequency distribution in an AE signal can be used to characterise the damage behaviour of composite materials [156, 157]. Table 4.25 summarises the published data of the peak-frequencies and amplitudes for different damage mechanisms in glass fibre composites along with the data obtained in this study. The amplitudes of the AES and peak frequencies recorded during the tensile testing of self-sensing composites are also presented in Table 4.25.

There is relatively little information in the literature related to the acoustic emission and mechanical properties of unidirectional E-glass composites where the strain-to-failure of the matrix is much lower than E-glass fibres. However, the relevant papers were discussed in Section 2.4.2. Table 4.25 shows that the amplitudes of the AES and the peak frequencies recorded during tensile testing of self-sensing composites are within the same general range of the published data. Henrat *et al*. and Barré *et al.* carried out tensile tests on unidirectional pre-pregs and a short fibre polypropylene (PP) E-glass composite, respectively. Whereas Bhatt *et al.* used S-glass/epoxy composites for fatigue testing. The amplitudes of the AES were recorded using PZT transducers. Although the test specimens, and test type and/or conditions were different to each other, the recorded amplitudes did not differ significantly. A similar effect was noticed during the AE monitoring of self-sensing composites. The recorded amplitudes and peak frequencies did not differ significantly for the four types of self-sensing composites; additionally these were comparable with the published data. The AE monitoring of neat resins and fibre bundles produced amplitudes of the AES corresponding to matrix cracking and fibre fracture. Similar values of amplitudes and peak frequencies related to matrix cracking and fibre fracture were recorded during the testing of self-sensing composite test specimens. However, if a specific failure mode was not generated in a test specimen (for instance,

interfacial debonding was not observed for as-received SDOF composite) the relevant amplitude of the AES and peak frequencies were not generated.

Figure 4.53 (a-d) shows the graphs of amplitudes of the AES as a function of time for the four types of the self-sensing composites. The evolution of damage in the test coupons was initiated by matrix cracking. The strain-to-failure of the matrix (1%) was lower than the fibres and therefore, the failure of the composite was matrix dominated [1, 2, 15]. It is understood that if the interface is strong and the matrix is brittle with a comparatively low strain-to-failure; transverse matrix cracking will take place when the composite specimen is loaded in tension (see Section 2.4.2). In the case of self-sensing composites, the failure of both types of E-glass composite was predominantly matrix cracking before ~90 seconds. The test coupons generated amplitudes and peak frequencies related to the matrix cracking between 0-90 seconds of loading the test coupons. This was apparent by the amplitude of the AES of 40-55 dB and peak frequency recordings of 30-180 kHz as shown in Figure 4.53 (a and b) and Figure 4.54 (a and b). Few data points related to higher amplitudes and frequencies (out of the specified data ranges) are generally ignored [155]. The stress in the sample was ~250 MPa at 90 seconds of loading the sample. The strain at this stress was between 1 to 1.35% as shown in Figure 4.50 (a and b). Hence, the matrix in the composite was approaching its failure-strain at ~90 seconds. After 90 seconds, the stress was carried by the fibre-matrix interface. As the stress was increased further, the interface failed, and therefore, the amplitudes of the AES and peak frequencies related to the fibre/matrix debonding were produced after 90 seconds of loading the sample. The failure of the fibre/matrix interface and debonding produced amplitudes of the AES of 55-75 dB and peak frequencies between 150-300 kHz (see Table 4.25). These amplitudes and peak frequencies were observed between 90-120 seconds. After the failure of the fibre-matrix interface, the stresses were entirely carried by the fibres in the test coupons. After

120 seconds the amplitudes of the AES of 80-100 dB and peak frequency distribution of above 350 kHz were mostly produced. These frequencies correspond to fibre fracture in the test coupons.
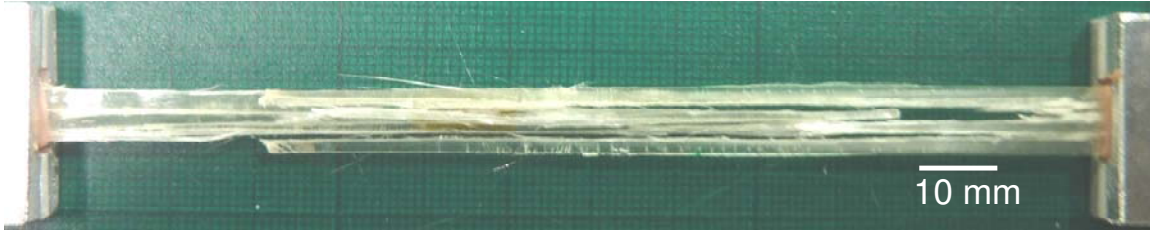
Figure 4.55 Representative image of a fractured as-received E-glass composite.

In the case of the silane-treated E-glass composite, the initial number of recorded AE hits (prior to 90 seconds after loading the sample) was comparatively less in the low amplitude of the AES range (40-65 dB) as shown in Figure 4.53b. These low range amplitude hits were more clustered towards the end of the test after approximately 90 seconds. This different trend was most likely due to an effective interface and better load transfer; hence the extensive transverse matrix cracking also occurred between 90-120 seconds. Figure 4.56 shows a representative image of a fractured specimen of the silane-treated E-glass composite. With reference to Figure 4.56, it can be observed that the composite was fractured by extensive interfacial de-bonding and transverse matrix cracking.
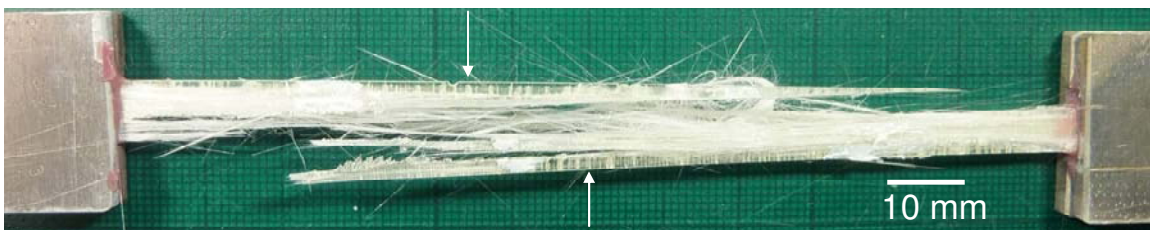
Figure 4.56 Representative image of a fractured silane-treated E-glass composite with arrows pointing towards extensive transverse failure of the epoxy matrix.

Figure 4.53 (c and d) and Figure 4.54 (c and d), show the plots of the amplitude of the AES and peak frequency as a function of time for the as-received SDOF and the heat-treated SDOF composite, respectively. Figure 4.53c shows very few AE hits before 60 seconds of loading the sample. All the amplitude ranges corresponding to different failure mechanisms in the composites (see Table 4.25) are clustered between 80-100 seconds. At ~90 seconds the stress in the composite was 145 MPa as shown in Figure 4.53c. The strain in the composite was less than 1.3% at ~145 MPa (see Figure 4.50c). Therefore, matrix cracking and the fracture of the test specimen occurred almost simultaneously. The as-received SDOF composites test coupons exhibited inferior mechanical properties when compared to the E-glass composites. The ultimate failure strength and strain-to-failure of SDOF composites was almost half of the E-glass composites. The possible causes of this behaviour may include a poor fibre/matrix bond. The interfacial debonding produces frequencies of 200-300 kHz. The number of data points corresponding to this frequency range was negligible in the case of as-received SDOF test coupons, as shown in Figure 4.54c. This means that peak frequencies corresponding to the interfacial debonding of fibres and matrix were not produced. Additionally, transverse matrix cracking was not observed and the composite fractured by longitudinal splitting (debonding) due to the reasons previously discussed. This effect was observed for almost every test coupon of the as-received SDOF. Figure 4.57 shows a representative image of a fractured test specimen of the as-received SDOF composite. Another notable feature of Figure 4.54c is a fewer number of AE hits. The most likely cause of this behaviour is the damping produced due to the presence of the binder on the as-received small-diameter optical fibres.

In contrast to the as-received SDOF, the recorded amplitude of the AES and peak frequency versus time graphs for the heat-treated SDOF exhibited similar behaviour to the E-glass composites as shown in Figure 4.53d and Figure 4.54d, respectively. However, in

this case, these frequencies and amplitudes of the AES were produced relatively earlier (30-60 seconds) when compared to the E-glass composites. As shown in Figure 4.38, the heat-treated SDOF bundles produced high amplitude hits at comparatively low-strain (>1%). Figure 4.53d and Figure 4.54d show the presence of respective amplitudes and peak frequencies related to the matrix cracking and interfacial de-bonding between 0-60 seconds. After 60 seconds a higher amplitude of the AES (70-95 dB) was recorded before failure; this range was related to the fibre failure. The heat-treated SDOF composite exhibited matrix cracking and interfacial de-bonding as shown by the representative image of a fractured test specimen in Figure 4.58.

Figure 4.57 Representative image of a fractured as-received SDOF composite.

Figure 4.58 Representative image of a fractured heat-treated SDOF composite with an arrow highlighting the region of partial interfacial debonding.

In conclusion, the AE monitoring of self-sensing composites showed the specific damage modes associated with the fibre reinforced composite materials. The E-glass composite exhibited matrix dominated failure, i.e. due to the low strain-to-failure of the matrix; it fails first. The matrix cracking was followed by interfacial debonding. Transverse matrix cracking was also observed visually during the tensile tests. Finally the composite specimen fractured catastrophically due to the facture of the fibres. The high amplitude

(75-80 dB) and high frequency (~500 kHz) hits at the end of the test confirmed that the fibres were fracturing at that time. This was also confirmed by the image analysis routines where the majority of the fibres were transmitting light just prior to the failure of the composite specimen. This will be discussed in more detail in Section 4.5.5. The presence of the uneven coating on the as-received SDOF resulted in a relatively weak fibre/matrix bonding and poor load-transfer. Therefore, the specific amplitudes of the AES and frequencies of interfacial debonding were not produced. From visual observations it was confirmed that the SDOF composite did not develop transverse matrix cracks and failed by longitudinal splitting (debonding). The removal of the binder by pyrolysis resulted in a better interfacial bond and therefore, the failure of the heat-treated SDOF was comparatively more similar to the failure of both types of E-glass composites. Finally, it was possible to relate the fracture behaviour of the four types of composites to the recorded AE amplitudes and frequencies. The recorded amplitudes and frequencies agreed with the published data.

In the next section, image analysis of self-sensing composite test specimens is presented. The details of image analysis routines are already discussed in Section 4.4.1.
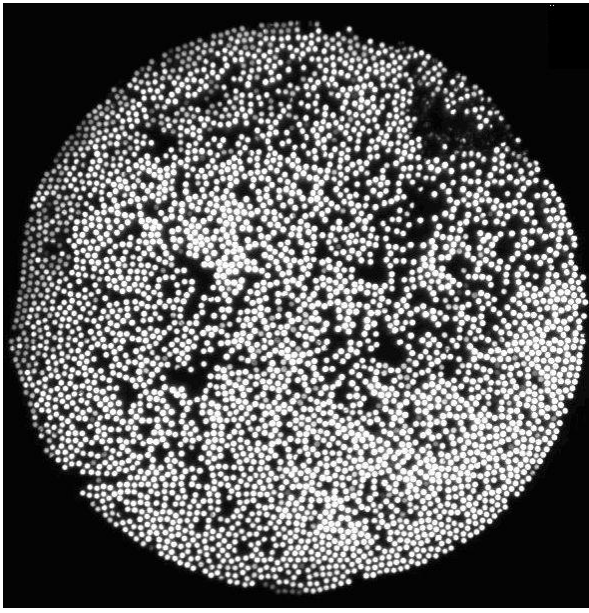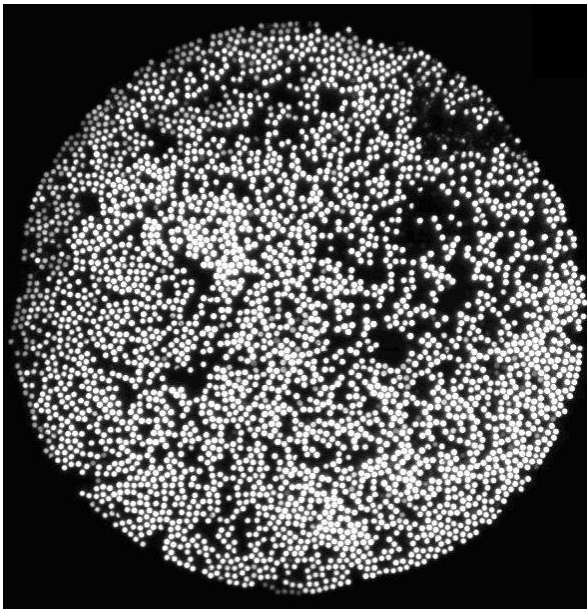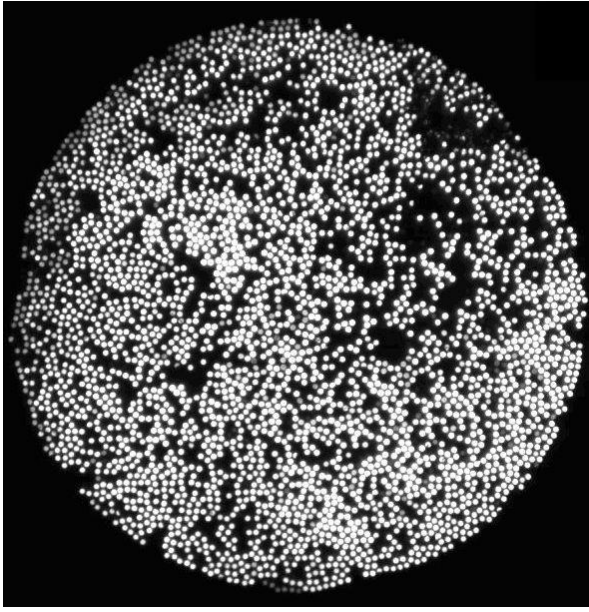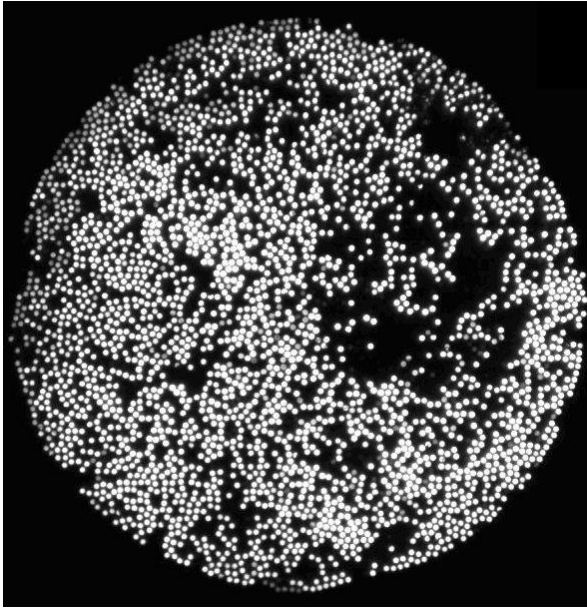
4.5.5 Image analysis of self-sensing composites

Table 4.26 presents a summary of tensile test and *in-situ* monitoring of light attenuation by the high-speed camera in the case of a self-sensing composite test specimen. With reference to Table 4.26, the numerical values are mentioned for the data corresponding to the particular image. The abbreviation "I", "t", "L" and "UT" corresponds to image number, time (seconds), load (Newtons) and percentage of the ultimate tensile strength (UTS). The first image was captured after 28.40 seconds when the first AE hit was detected. This triggered the high-speed camera and it commenced recording continuously.

The images taken at 1%, 2.7%, 10%, 76% and 98% of the ultimate tensile strength (UTS) are shown in Table 4.26.

Table 4.26 Summary of tensile test and *in-situ* monitoring of light attenuation in the case of self-sensing composites.

I =1, t =28.40, L =30.5, UT =1	I =583, t =38.12, UT =2.7
I =2187, t =64.85, UT =10	I =2365, t =67.8065, UT =76

| I =2406, t =68.495, UT =98 | Image captured just prior to failure |

100 μm
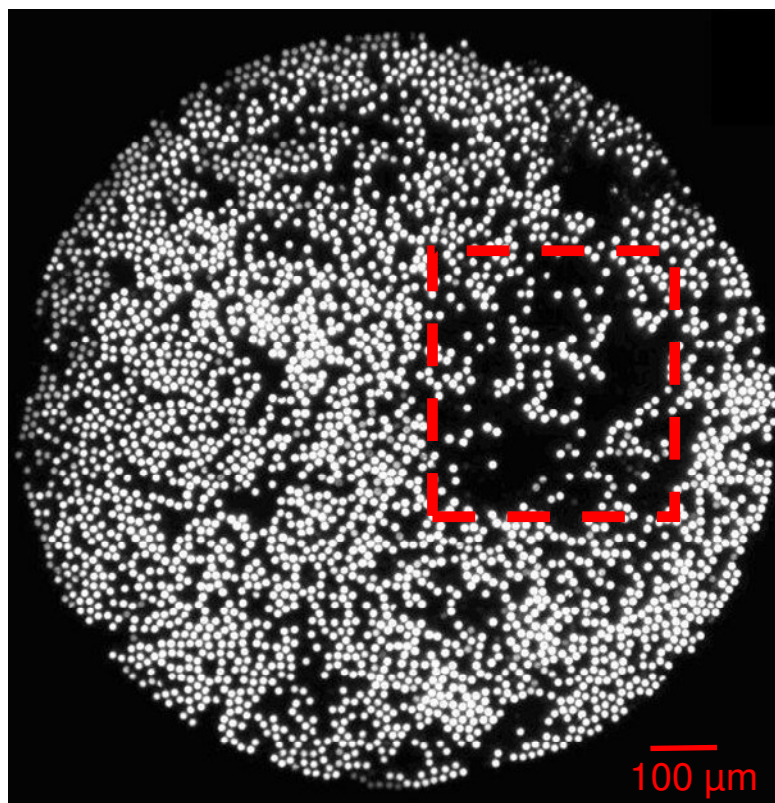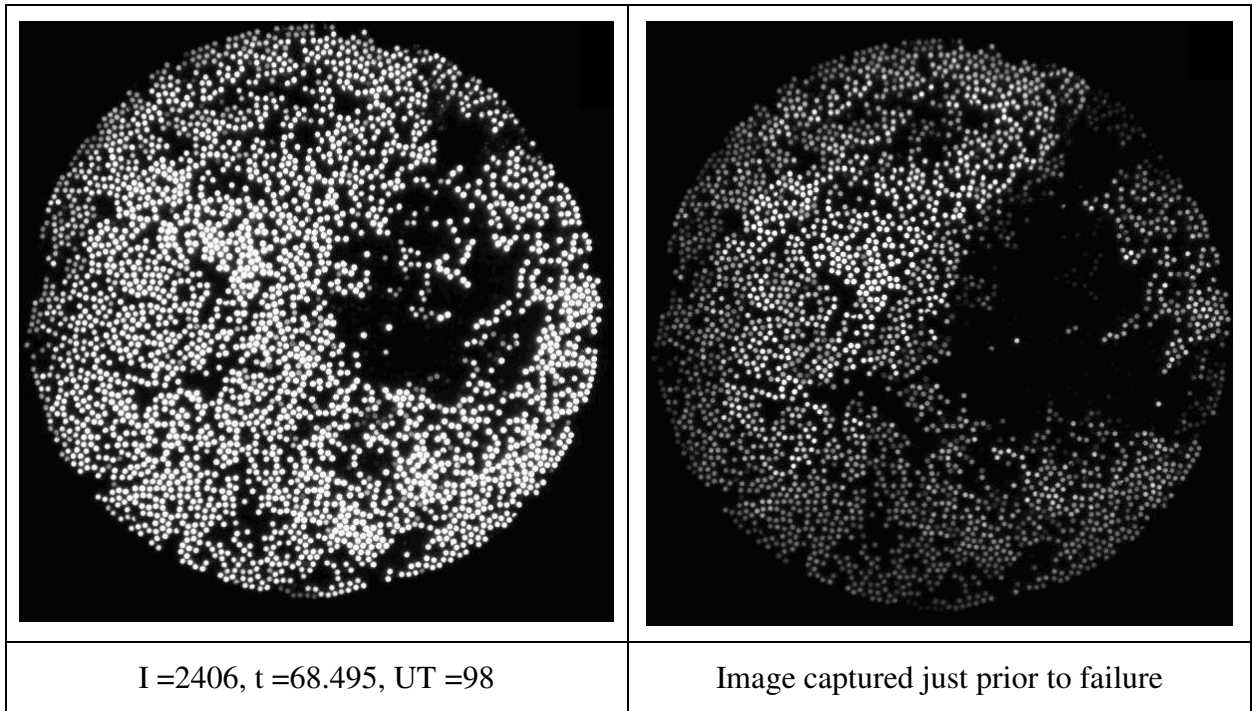
Figure 4.59 Image of a self-sensing composite captured after 68 seconds of loading the sample, the failure of weak fibres is obvious; the enclosed area represents the case where 7-8 % of the fibres stopped transmitting light due to fibre-fracture.

The images show almost no change from the first image to the one captured at 76% of UTS. At this magnitude of stress 7-8% of the fibres were fractured and stopped transmitting light, as shown in the 2365th image. This image was captured 67.8 seconds after loading the sample. The last image was captured just before the complete cut-off of the transmitted light and failure of the sample. It was evident that the light was significantly attenuated. By comparing the images presented in Table 4.19 and Table 4.26, it was observed that most of the fibres in the composite test specimen were transmitting light (i.e. they were surviving) until the composite specimen completely fractured. Approximately 7-8% of the total fibres in the composite specimen were fractured before the onset of catastrophic failure as shown in Figure 4.59. The applied stress was then distributed between the surviving fibres. The composite test specimen was fractured after 15 seconds of experiencing 76% of the UTS (76 % UTS was achieved at 67.8 seconds of loading the sample). It is noteworthy, that the effect of the varying tension and strength distribution of the fibres in the bundle was superimposed by the presence of the matrix, which helped to redistribute the applied load. The weak fibres fractured earlier than the other fibres resulting in the onset of failure as discussed in Section 2.4 where load-sharing was discussed. The stress originally carried by the weak fibres was redistributed to the neighbouring fibres and therefore, due to a stress concentration, 'singlet' failure was followed by 'doublets' and 'triplets' until complete fracture [16]. There are certain points to be mentioned here: (i) failure of the composite was initiated by the fracture of weak fibres in the composite; (ii) in the case of the composite specimen, the failure of the weaker fibres may cause the neighbouring fibres to fail; (iii) the composite strength was dependent upon the fracture of the weak fibres, since if they fail then they will cause the neighbouring but strong fibres to fracture, due to the imposed stress concentration; and (iv) the weak fibres fracturing earlier predict the onset of damage in a composite test coupon.
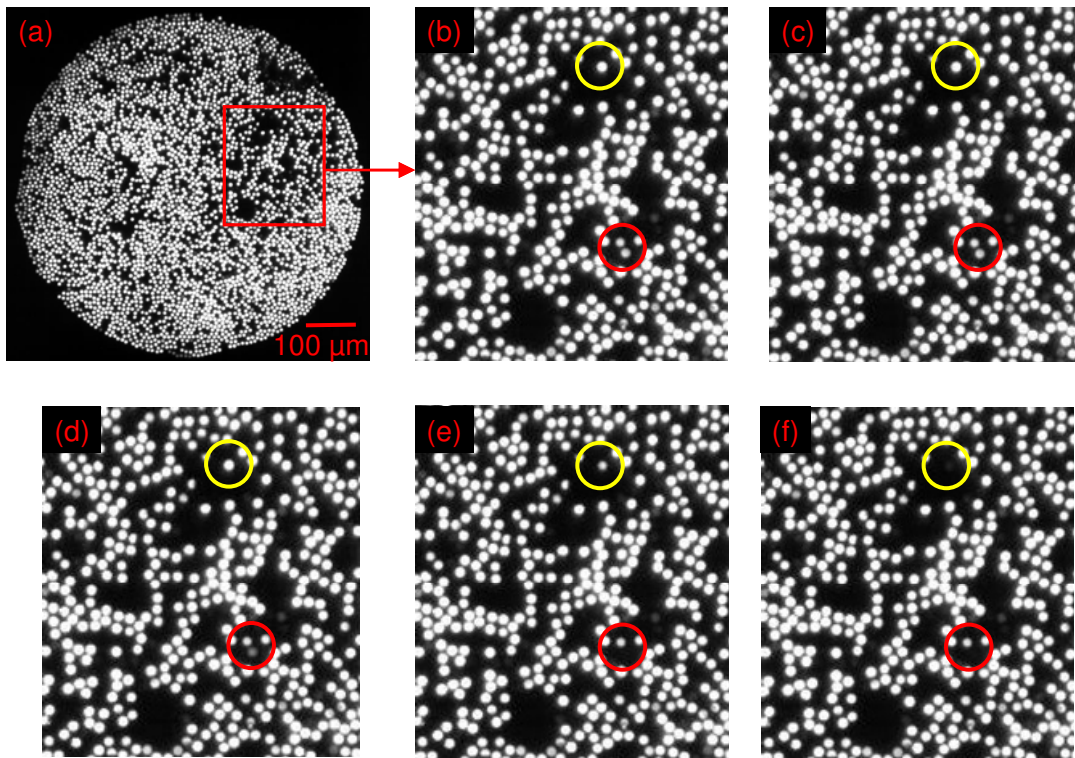
Figure 4.60 Demonstration of the sequential fibre failure in the SDOF self-sensing composite: (a) Image captured by the high-speed camera with a highlighted section where fibres fractured sequentially; (b) Magnified view of the section with two fibres highlighted with red and yellow circles that are about to fracture; (c) Image captured after 16.67 milli-seconds showing the attenuated light in the fibre inscribed in the red circle; (d) The fibre in the red-circle is about to fracture; (e) The fibre within the red circle was fractured while the light was attenuated for the fibre in the yellow-circle i.e. it is about to fracture; and (f) Both the fibres were fractured and thus stopped transmitting light.

This study has demonstrated conclusively that the imminent fracture of individual filaments in a composite test specimen can be detected. Figure 4.60 shows the possibility of detecting progressive fibre failure in a composite test specimen. With reference to Figure 4.60, the image labelled 'a' is the potted and polished view of the self-sensing composite specimen, captured by the high-speed camera. Magnified views of a section of image 'a' are shown in images b-f. The images b-f are the consecutive frames captured by the high-speed camera at 16.67 milli-seconds intervals. These consecutive images were selected to demonstrate the phenomenon of sequential fibre failure. The red circle in

Figure 4.60 (b-f) shows that one of the fibres was fractured during the tensile testing. The fibre in the red circle (Figure 4.60c) was about to fracture and the light was attenuated as illustrated in Figure 4.60d. The fibre was then fractured and ceased to transmit light, as shown in Figure 4.60e. At exactly the same time, another fibre, highlighted by the yellow circle, shared the load of the fractured fibre and light was attenuated as shown in the same figure, (Figure 4.60e). This fibre was then fractured and stopped transmitting light, as illustrated in Figure 4.60f.

In this representative example of sequential fibre failure, it has been demonstrated that it is possible to detect the imminent fibre fracture caused by the fracture of neighbouring fibres. The example presented in the preceding section could be more accurate if the fibre bundles were coherent and therefore, the fracture of the fibre highlighted by the red circle could be related to the fracture of the fibre in the yellow circle. In addition, if the high-speed camera can be operated at more than 60 frames per second it may be possible to record more stages before the fracture of a fibre (in this study the high-speed camera captured the images at 60 frames per second, therefore, only one stage was recorded before the fracture of an individual filament). However, this example provides an idea of how the self-sensing concept could be used to predict and demonstrate sequential fibre failure and the onset of damage in fibre reinforced composite materials.

In the future, this technique can be further developed to study the fracture sequence of individual filaments (i.e. progressive fibre failure) in fibre bundles or a composite, if coherent fibre bundles are used. The coherent bundles have equal length of fibres and all the fibres are parallel with negligible twists or cross-over. Therefore, the composite manufactured from coherent fibre bundles have identical ends with respect to spatial

location of the fibres. When coherent bundles become available, it can be demonstrated conclusively that as one fibre fractures it causes the neighbouring fibre to fracture.

In the next paragraphs, the overall change in transmitted light intensity during the tensile test is reported. The image analysis routines were capable of analysing 7000-8000 images captured per test. The high-speed camera was synchronised with the AE system and the Instron, therefore, the normalised light intensity can be plotted with the applied stress on the same time axis.
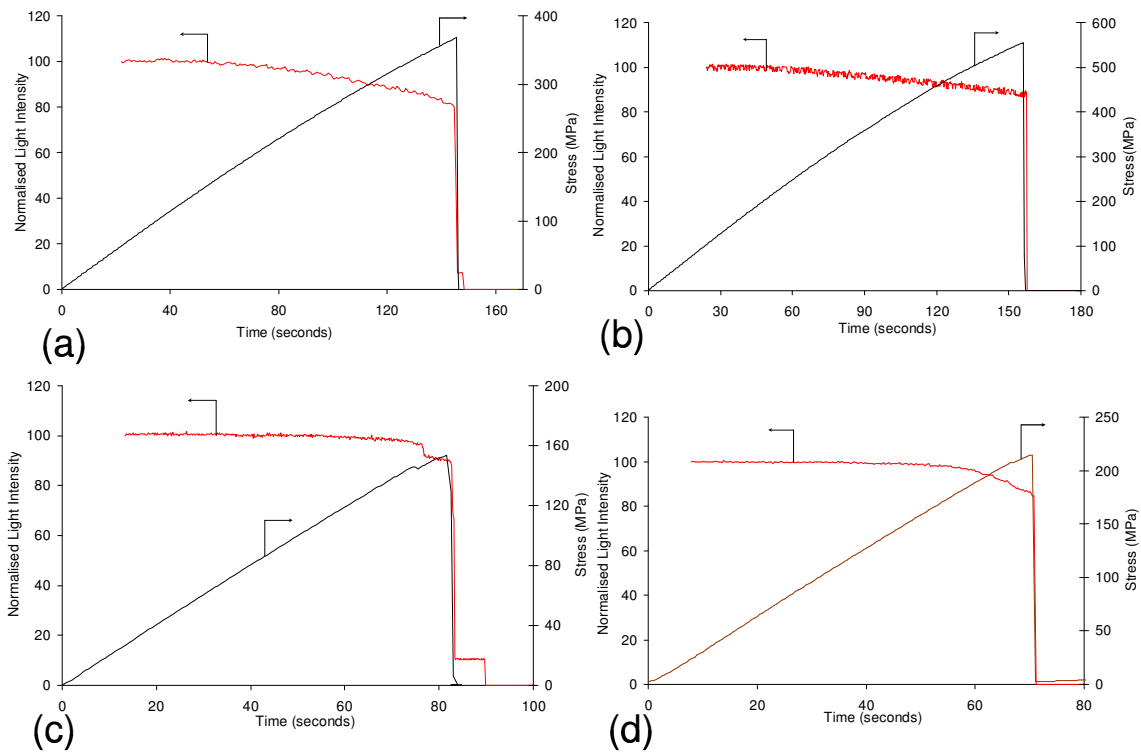
Figure 4.61 Graphs showing the normalised transmitted light intensity and applied stress as a function of time for composites manufactured from: (a) As-received E-glass fibres; (b) Silane-treated E-glass fibres; (c) As-received SDOF; and (d) Heat-treated SDOF.

Figure 4.61 (a-d) show the representative graphs of transmitted light intensity and applied stress as a function of time for the as-received E-glass composite, silane-treated E-glass composite, as-received SDOF and heat-treated SDOF composites, respectively. The catastrophic failure of a composite test specimen as inferred from the plot of stress versus

247

time was reflected in the plot of light transmission. The change in transmitted light intensity was due to the reasons discussed in Section 4.4.1. In the case of both types of E-glass composites, there was a gradual decrease in the transmitted light intensity until the catastrophic failure of the test coupons. Just prior to fracture, the net decrease in transmitted light intensity was ~17% and 20% in the case of E-glass and silane-treated E-glass composite specimens, respectively. The strain-to-failures of as-received E-glass and silane-treated E-glass composites were 2.4% and 3.1%, respectively. However, the average strain-to-failure of the matrix (EPO-TEK®-314) was 1% (see Section 4.2.1). At this magnitude of strain, the matrix in the composite was fractured and this was confirmed by the corresponding AE amplitudes and frequencies (see Section 4.5.4). This magnitude of strain (1%) was achieved after 58 seconds of loading the sample. Considering all these factors, the possible causes of the net decrease in the light intensity before the catastrophic failure of a composite test coupon, may be attributed to: (i) the E-glass fibres used in this study were un-sized and the matrix was also acting as a cladding for the total internal reflection, therefore, it was possible that under the applied stress the optical properties of the matrix were changed and transmitted light was attenuated; (ii) due to matrix cracking, transverse cracks were developed, this can effect the light transmission through the fibres; (iii) additionally, the light transmission may be affected due to the micro-bending losses (see Section 2.3.3.2); it was reported that when the core-cladding interface was not smooth it could attenuate the transmitted light [21, 26]; and (iv) the possible relative movement of the fibres and the epoxy matrix (debonding) can affect the core-cladding interface. The combined affect of all these factors reduced the light intensity to ~20% until the specimen fractured at its ultimate failure stress. These effects were not noticed in the case of the SDOF composites since the core of the fibres had a cladding on it.

In the case of both types of SDOF composites, the light intensity remained stable until 90% of the ultimate failure stress. In the case of as-received SDOF and heat-treated SDOF composites, a decrease of 8% and 10% was observed just prior to failure, respectively. However, the change was more abrupt for the as-received SDOF composite as shown in Figure 4.61c. This change was due to abrupt failure of the test coupon. The as-received SDOF composite had a comparatively weak fibre-matrix interface. This affected the fracturing of test coupons and they failed by longitudinal splitting along fibre edges. This was also evident from the cumulative AE hits plot (see Figure 4.51c) where the slope of cumulative AE hits increases gradually for the E-glass composites and heat-treated SDOF composite, whereas for the as-received SDOF composites, the change in the slope was abrupt. The transverse matrix cracks were not observed in the case of SDOF composites and therefore, the transmitted light was not affected by the behaviour of the matrix. In the case of the SDOF composites, the attenuation of the transmitted light (before the peak load) was mainly due to the fibres fractured before the failure of test coupons.

The difference in trends of the transmitted light intensity between E-glass and SDOF may be attributed to; (i) better light transmission characteristics of the SDOF as compared to the E-glass fibres; (ii) the failure of E-glass composites was mainly due to fibre fracture and interfacial de-bonding, whereas, for the SDOF composites the matrix failure and fibre fracture occurred almost simultaneously as discussed in Section 4.5.4; and (iii) the fibres were transmitting light comparatively longer until the sample fractured. Therefore, the net decrease in transmitted light at the onset of failure was 10% lower in the case of SDOF composites.

The use of reinforcing fibres as light guides was reported by Hayes *et al.* [8] Kister *et al.* [10] and other researchers [9, 20, 100, 117]. Hayes *et al.* employed quartz fibres that were

embedded in a composite panel of a 16-ply carbon fibre pre-pegs composite system. Similarly, Kister *et al.* used conventional E-glass fibres that were coated with epoxy polyurethane and a sol-gel to act as a cladding material. The coated E-glass fibres were embedded, in the composite to detect damage during mechanical loading. Both the mentioned research groups although using reinforcing fibres to detect damage in the composite but the concern remained that the reinforcing fibres were treated or embedded specifically in a composite with a sensing panel.

In the current work, the reinforcing fibres were used without any external medium, the as-received fibres were used to manufacture composites and all the fibres in the composites reflected the state of damage in the test coupon. In contrast to the work done by Hayes *et al.* here the whole composite acted as a sensor, and there was no need to process or apply any coating on the embedded fibres but instead the fibres were used as sensors themselves.

In conclusion, it has been demonstrated that the damage modes in self-sensing composites can be related to the attenuation of transmitted light. The image analysis routines showed that the light intensity was reduced due to a change in the cladding (matrix) in the case of E-glass composites before the catastrophic failure. However, in the case of SDOF composites, the decrease in light intensity was mainly due to the facture of weaker fibres before the ultimate failure of the composite specimen. This study demonstrated conclusively, that the developed technology of self-sensing composites can be used to detect damage in composites test coupons in real-time. The imminent fracture of individual filaments can be tracked using a high-speed camera and subsequent image analysis.

5 Conclusions

5.1 Conventional E-glass Fibres as Sensors

This study has demonstrated that conventional E-glass fibres can be used as light guides. Therefore, it was possible to use E-glass fibres as intensity-based sensors to detect the fracture of individual fibres during tensile loading. The light attenuation characteristic of E-glass fibres was determined experimentally. It was found that provided the length of the test specimen was kept below 30 cm, adequate light transmission could be achieved to enable the high-speed camera to detect each fibre in the bundle or composite.

5.2 Integration and Synchronisation of Equipment

Appropriate hardware and software routines were developed to enable the following items of equipment to be linked and synchronised: (i) high-speed CCD camera; (ii) piezo-electric acoustic emission data acquisition system; and (iii) the tensile test machine. The detection of the first acoustic event due to the fracture of a glass fibre in the test specimen was used to trigger the high-speed camera. The applied load was recorded by the AE system as a parametric input from the tensile test machine. This arrangement was necessary to study and cross-correlate the attenuation of light and AE data as a function of applied load. The CCD camera was selected on the basis of the specification required to enable real-time imaging of the ends of the fibre bundle.

5.3 Manufacturing of Void-free Composites

The development of the resin-injection technique was also one of the major achievements in this work. It was demonstrated that the resin-injection technique can produce void-free composites, with a good surface finish and uniform thickness. Due to the resin-injection

technique, it was relatively easy to leave an un-impregnated section of fibres at the ends of composite test-coupon. This un-impregnated section was required to couple light into and out of the fibres. The rule-of-mixtures was used to compare the experimental and estimated mechanical properties of self-sensing composites; they agreed to within ±12%.

5.4 Application of Acoustic Emission Monitoring

The acoustic emission technique was deployed successfully to identify characteristic AE signals produced during tensile testing of neat resins, fibre bundles and composites test specimens. For example, the amplitude of the AES corresponding to matrix failure (neat resin) was 60-70 dB. The amplitude of the AES for the failure of fibres in a bundle and a composite were 70-90 dB and 80-100 dB, respectively. The AE monitoring of fibre bundles revealed that there were two types of failures occurring in the bundle, a lower amplitude of the AES (42-55 dB) relating to inter-fibre friction and a high amplitude of the AES (70-90 dB) relating to fibre fractures. This behaviour was also confirmed by Weibull statistical analysis. Weibull statistical analysis of the fibre bundles demonstrated that the Weibull distribution was bi-modal. The Weibull constants, 'm' and 'ε_o', obtained in the current study were 8.6 and 2.3, respectively. The data were calculated using the maximum load method as discussed in Section 4.3.4. They correlate well with published data. In the case of the self-sensing composites, it was possible to relate the damage modes occurring in the four types of composites to the recorded AE amplitudes and frequencies (see Table 4.25). The amplitude of the AES and frequencies were in good agreement with published data.

5.5 In-situ Monitoring of Light Attenuation and Image Analysis Routines

A major achievement was the development of experimental procedures for *in-situ* monitoring of light transmission during tensile loading. Additionally, the development of image analysis routines to analyse 10000 images per test were regarded to be the most significant accomplishments of this study. It has been demonstrated that the image analysis routines were capable of identifying and tracking the imminent fracture of each fibre in the bundle or composite. It has been shown that the fibres in the bundle were fracturing even after the peak-load and the failure of individual filaments did not cause tow failure. The self-sensing fibres proved this effect in real-time. This is a very significant demonstration since the fracturing of the fibres in the bundle was monitored *in-situ* and without any external sensor or monitoring system. The fibres themselves demonstrated the fracture due to attenuation of the transmitted light by them. The use of reinforcing fibres to detect damage in the fibre bundle *in-situ* has been reported for the first time. The results from AE followed the same trend in the case of fibre bundles and composites.

6 Recommendations for Further Research

6.1 Coherent Fibre Bundles

In recent years, much effort has focussed on progressive fibre failure; the failure of one fibre initiated by the failure of neighbouring fibres. Self-sensing techniques can provide reliable results in this area. It has been demonstrated that at the onset of failure the light was significantly attenuated before complete fracture of the filament. If the spatial location of fibres is known with respect to the neighbouring fibres in an image, it can be used to predict the failure of neighbouring fibres. This can be successfully achieved if the bundles are coherent, since the spatial location of fibres will be identical at both ends of the bundle. Therefore, the light attenuation of a filament can be related to the light attenuation of its neighbours. Coherent bundles can be used to fabricate composite test coupons. The failure of a fibre in the test coupon will cause a stress concentration and the neighbouring fibres will fracture in a progressive manner. The light attenuation of the fibres can be used to predict/study these effects.

6.2 Image Analysis Routines to Identify Progressive Fibre Failures

The developed image analysis routines were capable of identifying and recording the location of each fibre. The light attenuation in all the fibres was recorded irrespective of the neighbouring fibres. A further development of these routines may lead to the identification of light attenuation in the neighbouring fibres. This can be related to the progressive fibre failure and reveal the effects of a fractured fibre on the neighbouring fibres.

6.3 Development of Intensity-based Sensors to Measure Strain

Self-sensing fibres predict the state of damage by attenuation of transmitted light intensity. The further development of reinforcing fibre light guides to measure strain and temperature will circumvent the need for embedded optical fibre sensors. For example, fibre Bragg gratings can be inscribed into the SDOF. The optical time-domain reflector-meter working principle can be used to locate the fracture point. The possibility of using the self-sensing fibres in different types of composites such as carbon fibre composites may increase the potential applicability of the technology developed.

6.4 Application of the Resin-injection Technique

The resin-injection technique can be used to fabricate composites with conventional optical fibres (125 µm) with gratings written on them. Therefore, when a composite test coupon will be loaded it can show the actual strain in the reinforcing (FBG in this case) fibres. This can be a significant demonstration since the true strain in the reinforcing fibres will be recorded.

7 References

[1] B. Harris, Engineering Composite Materials, The Institute of Materials, London 1999.

[2] D. Hull and T. W. Clyne, An Introduction to Composite Materials, Cambridge University Press, Cambridge 1996.

[3] G. Kelly and S. Hallstrom, *Strength and failure mechanisms of composite laminates subject to localised transverse loading*. Composite Structures *69,* 301-314 (2005).

[4] X. E. Gros, *Review of NDT Techniques for Detection of Low-Energy Impacts in Carbon Reinforcements*. Sampe Journal *31,* 29-34 (1995).

[5] K. L. Reifsnider, Damage in composite materials: basic mechanisms, accumulation, tolerance an introduction, American Society for Testing and Materials, Philadelphia 1982.

[6] E. M. John, Damage detection in composite materials, American Society of Testing Materials, Philadelphia 1992.

[7] K. T. V. Grattan and T. Sun, *Fiber optic sensor technology: An overview*. Sensors and Actuators *82,* 40-61 (2000).

[8] S. Hayes, T. Liu, D. Brooks, S. Monteith, B. Ralph, S. Vickers and G. F. Fernando, *In situ self-sensing fibre reinforced composites*. Smart Materials and Structures *6,* 432-440 (1997).

[9] G. F. Fernando, B. Degamber, L. Wang, C. Doyle, G. Kister and B. Ralph, *Self-sensing fibre reinforced composites*. Advanced Composites Letters *13,* 123-129 (2004).

[10] G. Kister, L. Wang, B. Ralph and G. F. Fernando, *Self-sensing E-glass fibres*. Optical Materials *21,* 713-727 (2003).

[11] G. Kister, B. Ralph and G. F. Fernando, *Damage detection in glass fibre-reinforced plastic composites using self-sensing E-glass fibres*. Smart Materials and Structures *13,* 1166-1175 (2004).

[12] S. K. Mazumdar, Composites manufacturing: materials, product, and process engineering, CRC Press, 2002.

[13] S. A. Strong, Fundamentals of Composite manufacturing: Materials, Methods and Applications, SME, 1989.

[14] D. Gay and V. H. Suong, Composite materials: Design and Applications, CRC Press, London 2002.

[15] P. K. Mallick, Fibre Reinforced Composites, Marcel Dekker, Inc., 1993.

[16] I. M. Daniel and O. Ishai, Engineering Mechanics of Composite Materials, Oxford University press, NewYork 1994.

[17] S. K. Ghosh, *Composite materials handbook.* Journal of Mechanical Working Technology *11,* 126 (1985).

[18] M. M. Barash, Composite materials handbook, pp. 381-382, McGraw-Hill, 1992.

[19] M. M. Schwartz and N. J. River, Composite materials: Processing, fabrication, and applications, Prentice Hall, London, 1997.

[20] K. Zolfaghar, N. Khan, D. Brooks, S. Hayes, T. Liu, J. Roca, J. Lander and G. F. Fernando, *Quartz and E-glass fibre self-sensing composites.* Proceedings of SPIE - The International Society for Optical Engineering *3321,* 314-328 (1996).

[21] F. C. Allard, Fibre Optics Handbook, McGraw-Hill, USA, 1989.

[22] K. Thyagarajan and A. Ghatak, Fiber optic essentials, Wiley, 2007.

[23] C. Yeh, Handbook of fiber optics: Theory and applications, Institue of Physics Publishing, Bristol 1990.

[24] J. Goure and I. Verrier, Optical fibre devices, Institute of Physics Publishing, Bristol 2002.

[25] J. A. Buck, Fundamentals of optical fibres, Wiley, 2004.

[26] U. Eric, Fibre optic sensors: An introduction for engineers and scientists, Wiley-Interscience, New York 1991.

[27] J. R. Vinson and W. Tsu, Composite materials and their use in structures, Applied Science Publishers, London, 1975.

[28] N. D. Flesher and C. T. Herakovich, *Predicting delamination in composite structures.* Composites Science and Technology *66,* 745-754 (2006).

[29] A. O. Addin, S. M. Sapuan, E. Mahdi and M. Othman, *Prediction and detection of failures in laminated composite materials using neural networks - A review*. Polymers & Polymer Composites *14,* 433-441 (2006).

[30] W. J. Cantwell and Morton J., *Detection of Impact damage in CFRP Laminates*. Composite Structure *3,* 241-257 (1985).

[31] H. Hatta, M. S. Aly-Hassan, Y. Hatsukade, S. Wakayama, H. Suemasu and N. Kasai, *Damage detection of C/C composites using ESPI and SQUID techniques*. Composites Science and Technology *65,* 1098-1106 (2005).

[32] B. Hofer, *Fibre optic damage detection in composite structures*. Composites *18,* 309-316 (1987).

[33] S. S. Kessler, S. M. Spearing and C. Soutis, *Damage detection in composite materials using Lamb wave methods*. Smart Materials & Structures *11,* 269-278 (2002).

[34] G. Nosenzo, M. P. Whelan and T. Dalton, *Damage detection in composite structures based on optical fibre strain sensing and finite element model updating*. Damage Assessment of Structures, Proceedings *245-2,* 509-516 (2003).

[35] J. Rossignol and A. Thionnet, *A novel technique for microwave detection of damage in composite materials using a microstrip resonator*. Comptes Rendus Mecanique *334,* 719-724 (2006).

[36] G. Zhou and L. M. Sim, *Damage detection and assessment in fibre-reinforced composite structures with embedded fibre optic sensors-review*. Smart Materials and Structures *11,* 925-939 (2002).

[37] W. Weibull, *A statistical distribution function of wide applicability*. Journal of Applied Mechanics *18,* 293-297 (1951).

[38] S. L. Phoenix and H. M. Taylor, *The Asymptotic Strength Distribution of a General Fiber Bundle*. Advances in Applied Probability *5,* 200-216 (1973).

[39] H. E. Daniels, *The Statistical Theory of the Strength of Bundles of Threads*. Proceedings of the Royal Society of London Series A Mathematical and Physical Sciences *183,* 405-435 (1945).

[40] C. Zweben and B. W. Rosen, *A statistical theory of material strength with application to composite materials*. Journal of the Mechanics and Physics of Solids *18,* 189-206 (1970).

[41] D. G. Harlow and S. L. Phoenix, *Probability distributions for the strength of composite materials I: two-level bounds*. International Journal of Fracture *17*, 347-372 (1981).

[42] Y. Kasai and M. Saito, *Weibull analysis of strengths of various reinforcing filaments*. Fibre Science and Technology *12*, 21-29 (1979).

[43] Z. Chi, T. Chou and G. Shen, *Determination of single fibre strength distribution from fibre bundle testing*. Journal of Materials Science *19*, 3319-3324 (1984).

[44] M. R. Wisnom, *The Relationship between Tensile and Flexural Strength of Unidirectional Composites*. Journal of Composite Materials *26*, 1173-1180 (1992).

[45] R. Hill and E. U. Okoroafor, *Surface conditions of Kevlar and glass and mechanical properties studied by Weibull statistics and acoustic emission*. Composites *25*, 913-916 (1994).

[46] C. A. Baillie and M. G. Bader, *Strength studies of single carbon fibres in model composite fragmentation tests*. Composites *25*, 401-406 (1994).

[47] A. H. Rezaifard, M. G. Bader and P. A. Smith, *Investigation of the transverse properties of a unidirectional carbon/epoxy laminate: Part 1--Matrix properties*. Composites Science and Technology *52*, 275-285 (1994).

[48] A. H. Rezaifard, M. G. Bader and P. A. Smith, *Investigation of the transverse properties of a unidirectional carbon/epoxy laminate: Part 2--Laminate properties*. Composites Science and Technology *52*, 287-295 (1994).

[49] R. Hill and E. U. Okoroafor, *Weibull statistics of fibre bundle failure using mechanical and acoustic emission testing: the influence of interfibre friction*. Composites *26*, 699-705 (1995).

[50] E. U. Okoroafor and R. Hill, *Relating acoustic emission signal parameters to the strength of fibres used in the manufacture of polymeric composites*. Ultrasonics *33*, 123-131 (1995).

[51] M. R'Mili, T. Bouchaour and P. Merle, *Estimation of Weibull parameters from loose-bundle tests*. Composites Science and Technology *56*, 831-834 (1996).

[52] N. Iyengar and W. A. Curtin, *Time-dependent failure in fiber-reinforced composites by fiber degradation*. Acta Materialia *45*, 1489-1502 (1997).

[53] Z. Wang and Y. Xia, *Experimental evaluation of the strength distribution of fibers under high strain rates by bimodal Weibull distribution*. Composites Science and Technology *57*, 1599-1607 (1998).

[54] H. Roger, B. Richard and D. Kaloedes, *Transverse cracking of fibre bundle composites studied by acoustic emission and Weibull statistics-effects of post-curing and surface treatment*. Journal of Materials Sciences *34,* 5215-5226 (1999).

[55] T. S. Creasy, *A method of extracting Weibull survival model parameters from filament bundle load/strain data*. Composites Science and Technology *60,* 825-832 (2000).

[56] T. Dooley, T. S. Creasy and A. Cuellar, *Extraction of Weibull parameters from fiber bundle experiments through Fourier deconvolution*. Composites Part A: Applied Science and Manufacturing *31,* 1255-1260 (2000).

[57] M. K. Cattell and K. A. Kibble, *Determination of the relationship between strength and test method for glass fibre epoxy composite coupons using Weibull analysis*. Materials & Design *22,* 245-250 (2001).

[58] J. Andersons, R. Joffe, M. Hojo and S. Ochiai, *Glass fibre strength distribution determined by common experimental methods*. Composites Science and Technology *62,* 131-145 (2002).

[59] B. Moser, L. Weber, A. Rossoll and A. Mortensen, *The influence of non-linear elasticity on the determination of Weibull parameters using the fibre bundle tensile test*. Composites Part A: Applied Science and Manufacturing *34,* 907-912 (2003).

[60] Y. Zhou, W. Yang, Y. Xia and P. K. Mallick, *An experimental study on the tensile behavior of a unidirectional carbon fiber reinforced aluminum composite at different strain rates*. Materials Science and Engineering A *362,* 112-117 (2003).

[61] E. N. Brown, A. K. Davis, K. D. Jonnalagadda and N. R. Sottos, *Effect of surface treatment on the hydrolytic stability of E-glass fiber bundle tensile strength*. Composites Science and Technology *65,* 129-136 (2005).

[62] M. R. Wisnom and J. W. Atkinson, *Reduction in tensile and flexural strength of unidirectional glass fibre-epoxy with increasing specimen size*. Composite Structures *38,* 405-411 (2005).

[63] E. V. Iarve, R. Kim and D. Mollenhauer, *Three-dimensional stress analysis and Weibull statistics based strength prediction in open hole composites*. Composites Part A: Applied Science and Manufacturing *38,* 174-185 (2007).

[64] D. Loidl, O. Paris, H. Rennhofer, M. Muller and H. Peterlik, *Skin-core structure and bimodal Weibull distribution of the strength of carbon fibers*. Carbon *45,* 2801-2805 (2007).

[65] M. R'Mili, M. Moevus and N. Godin, *Statistical fracture of E-glass fibres using a bundle tensile test and acoustic emission monitoring*. Composites Science and Technology *68,* 1800-1808 (2008).

[66] G. Short, F. Guild and M. Pavier, *Delaminations in flat and curved composite laminates subjected to compressive load*. Composite Structures *58*, 249-258 (2002).

[67] K. Balasubramaniam, B. V. S. Sekhar, J. V. Vardan and C. V. Krishnamurthy, *Structural health monitoring of composite structures using guided lamb waves*. Advanced Nondestructive Evaluation I, Pts 1 and 2, Proceedings *321-323*, 759-764 (2006).

[68] V. Bhatia, C. A. Schmid, K. A. Murphy, R. O. Claus, T. A. Tran, J. A. Greene and M. S. Miller, *Optical-Fiber Sensing Technique for Edge-Induced and Internal Delamination Detection in Composites*. Smart Materials & Structures *4*, 164-169 (1995).

[69] C. Scarponi and G. Briotti, *Ultrasonic detection of delaminations on composite materials*. Journal of Reinforced Plastics and Composites *16*, 768-790 (1997).

[70] S. Takeda, Y. Okabe and N. Takeda, *Delamination detection in CFRP laminates with embedded small-diameter fiber Bragg grating sensors*. Composites Part A-Applied Science and Manufacturing *33*, 971-980 (2002).

[71] A. Todoroki, Y. Tanaka and Y. Shimamura, *Delamination monitoring of graphite/epoxy laminated composite plate of electric resistance change method*. Composites Science and Technology *62*, 1151-1160 (2002).

[72] L. Hang-yin, L. Kin-tak and L. Cheng, *Determination of dynamic strain profile and delamination detection of composite structures using embedded multiplexed fibre-optic sensors*. Composite Structures *66*, (2004).

[73] R. P. Harrison and M. G. Bader, *Damage development in CFRP laminates under monotonic and cyclic stressing*. Fibre Science and Technology *18*, 163-180 (1983).

[74] M. Salvia and L. Vincent, *Modelling of flexural fatigue behaviour in UD glass-fibre-reinforced polymer*. Composites Science and Technology *56*, 797-802 (1996).

[75] P. S. Uskokovic, M. Miljkovic, M. Krivokuca, S. S. Putic and R. Aleksici, *An intensity based optical fibre sensor for flexural damage detection in woven composites*. Advanced Composites Letters *8*, 55-58 (1999).

[76] I. G. Kim, H. Y. Lee and J. W. Kim, *Impact damage detection in composite laminates using PVDF and PZT sensor signals*. Journal of Intelligent Material Systems and Structures *16*, 1007-1013 (2005).

[77] N. C. Huang and X. Y. Liu, *Debonding and fiber pull-out in reinforced composites*. Theoretical and Applied Fracture Mechanics *21*, 157-176 (1994).

[78] S. Jihan, A. M. Siddiqui and M. A. S. Sweet, *Fracture strength of E-glass fibre strands using acoustic emission*. Ndt & e International *30,* 383-388 (1997).

[79] R. O. Amir and M. Ahmadi, *Fracture Strength Distribution in E-glass Fiber Using Acoustic Emission*. Journal of Composite Materials *44,* 693-705 (2010).

[80] V. Valery and V. Evgeny, Mechanics and analysis of composites materials, Elesevier Science Limited, UK, 2001.

[81] V. V. Vasiliev and E. V. Morozov, *Mechanics of a Unidirectional Ply.* In *Advanced Mechanics of Composite Materials (Second Edition).* pp. 57-132, Elsevier Science Ltd, Oxford 2007.

[82] S. Blassiau, A. Thionnet and A. R. Bunsell, *Micromechanisms of load transfer in a unidirectional carbon fibre-reinforced epoxy composite due to fibre failures: Part 3. Multiscale reconstruction of composite behaviour.* Composite Structures *83,* 312-323 (2008).

[83] S. Blassiau, A. Thionnet and A. R. Bunsell, *Micromechanisms of load transfer in a unidirectional carbon fibre-reinforced epoxy composite due to fibre failures. Part 1: Micromechanisms and 3D analysis of load transfer: The elastic case.* Composite Structures *74,* 303-318 (2006).

[84] S. Blassiau, A. Thionnet and A. R. Bunsell, *Micromechanisms of load transfer in a unidirectional carbon fibre-reinforced epoxy composite due to fibre failures. Part 2: Influence of viscoelastic and plastic matrices on the mechanisms of load transfer.* Composite Structures *74,* 319-331 (2006).

[85] A. Bussiba, M. Kupiec, S. Ifergane, R. Piat and T. Behlke, *Damage evolution and fracture events sequence in various composites by acoustic emission technique.* Composites Science and Technology *68,* 1144-1155 (2008).

[86] G. C. Sih and A. M. Skudra, Failure mechanics of composites, Oxford University Press, North-Holland 1985.

[87] R. Hill, R. Brooks and D. Kaloedes, *Characterization of transverse failure in composites using acoustic emission*. Ultrasonics *36,* 517-523 (1998).

[88] S. Pardo, D. Baptiste, F. Decobert, J. Fitoussi and R. Joannic, *Tensile dynamic behaviour of a quasi-unidirectonal E-glass/polyester composite.* Composites Science and Technology *62,* 579-584 (2002).

[89] S. L. Ogin, P. A. Smith and P. W. R. Beaumont, *Matrix cracking and stiffness reduction during the fatigue of a (0/90)s GFRP laminate*. Composites Science and Technology *22,* 23-31 (1985).

[90] M. T. Kortschot and P. W. R. Beaumont, *Damage mechanics of composite materials. IV: The effect of lay-up on damage growth and notched strength*. Composites Science and Technology *40,* 167-179 (1991).

[91] H. L. Ganczakowski, M. F. Ashby, P. W. R. Beaumont and P. A. Smith, *The behaviour of Kevlar fibre-epoxy laminates under static and fatigue loading--Part 2: Modelling*. Composites Science and Technology *37,* 371-392 (1990).

[92] S. L. Ogin, P. A. Smith and P. W. R. Beaumont, *Matrix cracking and stiffness reduction during the fatigue of a (0/90)s GFRP laminate*. Composites Science and Technology *22,* 23-31 (1985).

[93] T. Okabe, H. Sekine, J. Noda, M. Nishikawa and N. Takeda, *Characterization of tensile damage and strength in GFRP cross-ply laminates*. Materials Science and Engineering A *383,* 381-389 (2004).

[94] M. R. Wisnom, *The effect of transverse compressive stresses on tensile failure of glass fibre-epoxy*. Composite Structures *32,* 621-626 (1995).

[95] K. Liao and E. Y. M. Tan, *In situ tensile strength degradation of glass fiber in polymer composite*. Scripta Materialia *44,* 785-789 (2001).

[96] T. Keller, T. Tirelli and A. Zhou, *Tensile fatigue performance of pultruded glass fiber reinforced polymer profiles*. Composite Structures *68,* 235-245 (2005).

[97] H. Iba, T. Chang and Y. Kagawa, *Optically transparent continuous glass fibre-reinforced epoxy matrix composite: fabrication, optical and mechanical properties*. Composites Science and Technology *62,* 2043-2052 (2002).

[98] C. Doyle and G. Fernando, *Detecting impact damage in a composite material with an optical fibre vibration sensor system*. Smart Materials and Structures *7,* 543-549 (1998).

[99] C. Doyle, A. Martin, T. Liu, M. Wu, S. Hayes, P. A. Crosby, G. R. Powell, D. Brooks and G. F. Fernando, *In-situ process and condition monitoring of advanced fibre-reinforced composite materials using optical fibre sensors*. Smart Materials & Structures *7,* 145-158 (1998).

[100] C. Doyle, A. Martin, M. Wu, T. Liu, S. Hayes, D. Brooks, R. A. Badcock and G. F. Fernando, *Intensity-based optical fibre sensors for condition monitoring of engineering materials*. SPIE - International Society of Optical Engineering 288-299 (1996).

[101] J. Abrya, S. Bocharda, A. Chateauminois, M. Salvia and G. Giraud, *In situ detection of damage in CFRP laminates by electrical resistance measurements*. Composites Science and Technology, *59,* 92-935 (1999).

[102] N. Angelidis, N. Khemiri and PE. Irving, *Experimental and finite element study of the electrical potential technique for damage detection in CFRP laminates.* Smart Materials and Structures *14,* 147-154 (2005).

[103] W. J. Cantwell and J. Morton, *The Significance of Damage and Defects and Their Detection in Composite-Materials - A Review.* Journal of Strain Analysis for Engineering Design *27,* 29-42 (1992).

[104] N. Hu, H. Fukunaga and M. Kameyama, *Identification of delaminations in composite laminates.* Journal of Intelligent Material Systems and Structures *17,* 671-683 (2006).

[105] R. Zoughi, S. Ganchev and G. W. Carriveau, *Overview of microwave NDE applied to thick composites.* Nondestructive Characterization of Materials Vii, Pts 1 and 2 *210-,* 69-75 (1996).

[106] K. T. V. Grattan and B. T. Meggitt, Optical Fibre Sensor Technology, Wiley Interscience Ltd, London 1999.

[107] H. Tsuda, *Ultrasound and damage detection in CFRP using fiber Bragg grating sensors.* Composites Science and Technology *66,* 676-683 (2006).

[108] Y. Rao, S. Yuan, X. Zeng, D. Lian and Y. Zhu, *Simultaneous strain and temperature measurement of advanced 3-D braided composite materials using an improved EFPI/FBG.* Optics and Lasers in Engineering *38,* 557-566 (2002).

[109] E. Udd, W. L. Schulz, J. Seim, M. Morrell, T. Weaver, J. Bush and G. Adamovsky, *Fiber optic distributed sensing systems for harsh aerospace environments.* Proceedings of SPIE - The International Society for Optical Engineering *3674,* 136-147 (1999).

[110] T. Chan, L. Yua, H. Y. Tam, Y. Q. Ni, S. Y. Liu, W. H. Chung and L. K. Cheng, *Fiber Bragg grating sensors for structural health monitoring of Tsing Ma bridge: Background and experimental observation.* Engineering Structures *28,* 648-659 (2006).

[111] Zhang P. and T. Hwa-Yaw, *Effects of Microstructures of Smart Fiber Composites on Embedded Fiber Bragg Grating Sensors.* Journal of Reinforced Plastics and Composites (2003).

[112] C. S. Shin and C. C. Chiang, *Embedded Fibre Bragg Grating Sensors for Internal Fatigue Damage Monitoring in Polymeric Compositesr.* International Journal of Fatigue (2008).

[113] G. P. Carman and G. P. Sendeckyj, *Review of the Mechanics of Embedded Optical Sensors.* Journal of Composites Technology & Research *17,* 183-193 (1995).

[114] D. C. Lee, Lee J., I. Kwon and K. Seo, *Monitoring of fatigue damage of composite structures by using embedded intensity-based optical fibre sensors*. Smart Materials and Structures *10,* (2000).

[115] G. Zhou and L. M. Sim, *Evaluating damage in smart composite laminates using embedded EFPI strain sensors*. Optics and Lasers in Engineering *47,* 1063-1068 (2009).

[116] A. R. Martin, G. F. Fernando and K. F. Hale, *Impact damage detection in filament wound tubes using embedded optical fibre sensors*. Smart Materials and Structures *6,* 470-476 (1997).

[117] L. Wang, G. Kister, B. Ralph, J. D. R. Talbot and G. F. Fernando, *Conventional E-glass fibre light guides: Self-sensing composite based on sol-gel cladding*. Smart Materials and Structures *13,* 73-81 (2004).

[118] L. Wang, S. Pandita, V. R. Machavaram, S. Malik, D. Harris and G. F. Fernando, *Characterisation of the cross-linking process in an E-glass fibre/epoxy composite using evanescent wave spectroscopy*. Composites Science and Technology *69,* 2069-2074 (2009).

[119] S. Ojo and S. A. Malik. Self-sensing small-diameter optical fibre composites (MRes project), 03-2010.

[120] R. Kashyap, Fibre Bragg Gratings, Academic Press, USA, 1999.

[121] M. Majumder, T. K. Gangopadhyay, A. K. Chakraborty, K. Dasgupta and D. K. Bhattacharya, *Fibre Bragg gratings in structural health monitoring--Present status and applications*. Sensors and Actuators A: Physical *147,* 150-164 (2008).

[122] L. Kin-Tak, L. Yuan, L. Zhou, J. Wu and C. Woo, *Strain monitoring in FRP laminates and concrete beams using FBG sensors*. Composite Structures *51,* 9-20 (2001).

[123] X. Zhao, J. Gou, G. Song and J. Ou, *Strain monitoring in glass fiber reinforced composites embedded with carbon nanopaper sheet using Fiber Bragg Grating (FBG) sensors*. Composites Part B: Engineering *40,* 134-140 (2009).

[124] R. A. Silva-Muoz and R. A. Lopez-Anido, *Structural health monitoring of marine composite structural joints using embedded fiber Bragg grating strain sensors*. Composite Structures *89,* 224-234 (2009).

[125] J. Degrieck, W. De Waele and P. Verleysen, *Monitoring of fibre reinforced composites with embedded optical fibre Bragg sensors, with application to filament wound pressure vessels*. Ndt & e International *34,* 289-296 (2001).

[126] J. M. Ko and Y. Q. Ni, *Technology developments in structural health monitoring of large-scale bridges*. Engineering Structures *27,* 1715-1725 (2005).

[127] S. Rupali, T. SweeChuan and Q. N. Nam, *Application of a new fiber Bragg grating based shear force sensor for monitoring civil structural components*. Smart Materials and Structures (2005).

[128] H. N. Li, D. S. Li and G. B. Song, *Recent applications of fiber optic sensors to health monitoring in civil engineering*. Engineering Structures *26,* 1647-1657 (2004).

[129] J. S. Sirkis and I. P. Lu, *On interphase modeling for optical fiber sensors embedded in unidirectional composite systems*. Journal of Intelligent Material Systems and Structures *6,* 199-209 (1995).

[130] C. Y. Wei, C. C. Ye, S. W. James, R. P. Tatam and P. E. Irving, *An experimental approach to quantify strain transfer efficiency of fibre Bragg grating sensors to host structures*. The 13th International Conference on Composite Materials (2001).

[131] G. Duck, G. Renaud and R. Measures, *Mechanical load transfer into a distributed optical fiber sensor due to a linear strain gradient: Embedded and surface bonded cases*. Smart Materials and Structures *8,* 175-181 (1999).

[132] J. Botsis, L. Humbert, F. Colpo and P. Giaccari, *Embedded fiber Bragg grating sensor for internal strain measurements in polymeric materials*. Optics and Lasers in Engineering *43,* 491-510 (2003).

[133] E. N. Barton, S. L. Ogin, A. M. Thorne and G. T. Reed, *Optimisation of the coating of a fibre optical sensor embedded in a cross-ply GFRP laminate*. Composites Part A: Applied Science and Manufacturing *33,* 27-34 (2002).

[134] T. W. Kai, K. Y. L. Christopher and G. O. Noah, *Investigation of the strain transfer for surface-attached optical fiber strain sensors*. Smart Materials and Structures *17,* 035037 (2008).

[135] S. A. Malik, M. S. Ramani, D. Harris and G. F. Fernando, *Finite element modelling of fibre Bragg grating strain sensors and experimental validation*. Proceedings of SPIE Vol 7292 *Sensors and Smart Structures Technologies for Civil, Mechanical, and Aerospace Systems,* (2009).

[136] W. Y. Li, C. C. Cheng and Y. L. Lo, *Investigation of strain transmission of surface-bonded FBGs used as strain sensors*. Sensors and Actuators A: Physical *149,* 201-207 (2009).

[137] V. R. Machavaram, R. A. Badcock and G. F. Fernando, *Fabrication of intrinsic fibre Fabry-Perot sensors in silica fibres using hydrofluoric acid etching*. Sensors and Actuators A: Physical *138,* 248-260 (2007).

[138] J. Leng and A. Asundi, *Strucural health monitoring of smart composite materials by using EFPI and FBG sensors*. Sensors and Actuators *103,* 330-340 (2003).

[139] P. T. Cole, *Using Acoustic Emission (AE) to Locate and Identify Defects in Composite Structures*. Composite Structures *3,* 59-267 (1985).

[140] M. Wevers and M. Surgeon, *Acoustic Emission and Composites.* In *Comprehensive Composite Materials*. (Ed. K. Anthony and Z. Carl) pp. 345-357, Pergamon, Oxford 2000.

[141] T. F. Drouillard, *A history of acoustic emission*. Journal of Acoustic Emission *14,* 1-34 (1996).

[142] P. Pevzner, T. Weller and A. Berkovits, *A novel fiber Bragg grating acoustic emission sensor head for mechanical tests*. Scripta Materialia *53,* 1181-1186 (2005).

[143] R. Chen, T. Bradshaw, J. Burns, P. Cole, P. Jarman, D. Pedder, R. Theobald and G. Fernando, *Linear location of acoustic emission using a pair of novel fibre optic sensors*. Measurement Science & Technology *17,* 2313-2318 (2006).

[144] M. Johnson and P. Gudmundson, *Broad-band transient recording and characterization of acoustic emission events in composite laminates*. Composites Science and Technology *60,* 2803-2818 (2000).

[145] M. Johnson, *Classification of AE transients based on numerical simulations of composite laminates*. Ndt & e International *36,* 319-329 (2003).

[146] M. Johnson and P. Gudmundson, *Experimental and theoretical characterization of acoustic emission transients in composite laminates*. Composites Science and Technology *61,* 1367-1378 (2001).

[147] V. Kostopoulos, T. Loutas and K. Dassios, *Fracture behavior and damage mechanisms identification of SiC/glass ceramic composites using AE monitoring*. Composites Science and Technology *67,* 1740-1746 (2007).

[148] M. Johnson, *Waveform based clustering and classification of AE transients in composite laminates using principal component analysis*. Ndt & e International *35,* 367-376 (2002).

[149] Physical Acoustic Manual. 2006.
       Ref Type: Catalog

[150] M. Surgeon and M. Wevers, *One sensor linear location of acoustic emission events using plate wave theories*. Materials Science and Engineering A *265,* 254-261 (1999).

[151] S. Barré and M. L. Benzeggagh, *On the use of acoustic emission to investigate damage mechanisms in glass-fibre-reinforced polypropylene*. Composites Science and Technology *52,* 369-376 (1994).

[152] J. M. Berthelot and J. Rhazi, *Acoustic emission in carbon fibre composites*. Composites Science and Technology *37,* 411-428 (1990).

[153] M. R. Bhat, M. A. Majeed and C. R. L. Murthy, *Characterization of fatigue damage in unidirectional GFRP composites through acoustic emission signal analysis*. NDT&E International *27,* 27-32 (1994).

[154] J. Bohse, *Acoustic emission characteristics of micro-failure processes in polymer blends and composites*. Composites Science and Technology *60,* 1213-1226 (2000).

[155] P. J. de Groot, P. A. M. Wijnen and R. B. F. Janssen, *Real-time frequency determination of acoustic emission for different fracture mechanisms in carbon/epoxy composites*. Composites Science and Technology *55,* 405-412 (1995).

[156] F. J. Guild, M. G. Phillips and B. Harris, *Acoustic emission studies of damage in GRP*. NDT International *13,* 209-218 (1980).

[157] F. J. Guild, D. Walton, R. D. Adams and D. Short, *The application of acoustic emission to fibre-reinforced composite materials*. Composites *7,* 173-179 (1976).

[158] S. Huguet, N. Godin, R. Gaertner, L. Salmon and D. Villard, *Use of acoustic emission to identify damage modes in glass fibre reinforced polyester*. Composites Science and Technology *62,* 1433-1444 (2002).

[159] A. Cowking, A. Attou, A. M. Siddiqui, M. A. S. Sweet and R. Hill, *Testing E-glass fibre bundles using acoustic emission*. Journal of Materials Science *26,* 1301-1310 (1991).

[160] A. Attou, A. Cowking and S. Jihan, *Strength investigation of a commercial e-glass fibre roll using acoustic emission*. NDT International *32,* 623-626 (1990).

[161] M. A. Hamstad and R. L. Moore, *Acoustic Emission from Single and Multiple Kevlar 49 Filament Breaks*. Journal of Composite Materials *20,* 46-66 (1986).

[162] G. H. Dunham and D. D. Edie, *Model of stabilisation for PAN based carbon fibre precussor bundles*. Carbon *30,* 435-450 (1992).

[163] L. Dong and J. Mistry, *Acoustic emission monitoring of composite cylinders*. Composite Structures *40,* 43-53 (1998).

[164] S. V. Lomov, D. S. Ivanov, T. C. Truong, I. Verpoest, F. Baudry, K. Vanden Bosche and H. Xie, *Experimental methodology of study of damage initiation and development in textile composites in uniaxial tensile test.* Composites Science and Technology *68,* 2340-2349 (2008).

[165] P. Henrat, A. Vautrin and B. Harris, *Mechanical and acoustic emission response of unidirectional and cross-plied GRP laminates.* Composites Science and Technology *30,* 263-277 (1987).

[166] C. R. Ramirez-Jimenez, N. Papadakis, N. Reynolds, T. H. Gan, P. Purnell and M. Pharaoh, *Identification of failure modes in glass/polypropylene composites by means of the primary frequency content of the acoustic emission event.* Composites Science and Technology *64,* 1819-1827 (2004).

[167] Y. Y. Hung, *Shearography for non-destructive evaluation of composite structures.* Optics and Lasers in Engineering *24,* 161-182 (1996).

[168] N. Angelidis and P. Irving, *Detection of impact damage in CFRP laminates by means of electrical potential techniques.* Composites Science and Technology *67,* 594-604 (2007).

[169] L. Shen, J. Li, B. Liaw, F. Delale and J. Chung, *Modelling and Analysis of the Electrical Resistance Measurement of Carbon Fiber Polymer-Matrix Composites.* Composite Science and Technology *10,* (2006).

[170] D. C. Seo and J. L. Lee, *Damage detection of CFRP laminates using electrical resistance measurement and neural network.* Composite Structures *47,* 525-530 (1999).

[171] P. Pevzner, T. Weller and A. Berkovits, *Use of heat emitted by broken optic fibers: A new approach for damage detection in composites.* Engineering Failure Analysis *12,* 860-874 (2005).

[172] S. Burke, S. Cousland and C. Scala, *Non-destructive characterisation of advanced composite materials.* Mater Forum *18,* 85-109 (1994).

[173] A. Okafor, A. Otieno, A. Dutta and V. Rao, *Detection and characterisation of high-velocity impact damage in advanced composite plates using multi-sensing techniques.* Composite Structures *54,* 289-297 (2001).

[174] N. P. Avdelidis, B. C. Hawtin and D. P. Almond, *Transient thermography in the assessment of defects of aircraft composites.* NDT&E International, *36,* 433-439 (2003).

[175] L. Toubal, M. Karama and B. Lorrain, *Damage evolution and infrared thermography in woven composite laminates under fatigue loading.* International Journal of Fatigue *28,* 1867-1872 (2006).

[176] R. Prakash, *Non-destructive testing of composites*. Composites *11,* 217-224 (1980).

[177] G. Kister, R. A. Badcock, Y. M. Gebremichael, W. J. O. Boyle, K. T. V. Grattan, G. F. Fernando and L. Canning, *Monitoring of an all-composite bridge using Bragg grating sensors*. Construction and Building Materials *21,* 1599-1604 (2007).

[178] S. A. Malik, S. Ojo and G. F. Fernando, *In-situ damage detection in glass fibre composites*. 17th International Conference on Composite Materials (2009).

[179] R. Lynsey. Characterisation of E-glass Fibres from PPG Industries (UK). 10-10-2009.

[180] V. Calard and J. Lamon, *Failure of fiber bundles*. Composites Science and Technology *64,* 701-710 (2004).

[181] E. Redmore. Deployment and characterisation of hydrofluoric acid etched optical fibre chemical sensors (UG project). 27-3-2009.

[182] M. E. Foley and J. W. Gillespie, *Modeling the effect of fiber diameter and fiber bundle count on tow impregnation during liquid molding processes*. Journal of Composite Materials *39,* 1045-1065 (2005).

[183] Photron High-speed Camera PCI-1024 Manual. 2007. Photron, UK.
Ref Type: Catalog

[184] R. J. Crawford, Plastics Engineering, Butterworth-Henimann, London 1999.

[185] ASTM Standard D636. Standard Test Method for Tensile Properties of Plastics. 2010. West Conshohocken, ASTM International.
Ref Type: Catalog

[186] W. E. Gottfried, Polymeric Materials, Hanser Garden Publications, USA, 2001.

[187] H. S. L, Introduction to Physical Polymer Science, Wiley-Inter-science, 2001.

[188] I. K. Jacqueline, Concise Encyclopaedia of Polymer Science and Engineering, pp. 629,1111, Wiley-Inter-science, 1990.

[189] N. Godin, S. Huguet, R. Gaertner and L. Salmon, *Clustering of acoustic emission signals collected during tensile tests on unidirectional glass/polyester composite using supervised and unsupervised classifiers*. Ndt & e International *37,* 253-264 (2004).

[190] J. K. Lee, *AE characteristic of the damage behavior of TiNi/Al6061 SMA composite*. Composite Structures *60,* 255-263 (2003).

[191] Y. H. Yu, J. H. Choi, J. H. Kweon and D. H. Kim, *A study on the failure detection of composite materials using an acoustic emission*. Composite Structures *75,* 163-169 (2006).

[192] W. Haselbach and B. Lauke, *Acoustic emission of debonding between fibre and matrix to evaluate local adhesion*. Composites Science and Technology *63,* 2155-2162 (2003).

[193] S. Feih, K. Manatpon, Z. Mathys, A. Gibson and A. Mouritz, *Strength degradation of glass fibers at high temperatures*. Journal of Materials Science *44,* 392-400 (2009).

[194] A. Ridruejo, C. Gonzβlez and J. LLorca, *Damage micromechanisms and notch sensitivity of glass-fiber non-woven felts: An experimental and numerical study*. Journal of the Mechanics and Physics of Solids *58,* 1628-1645 (2010).

[195] S. Barré, T. Chotard and M. L. Benzeggagh, *Comparative study of strain rate effects on mechanical properties of glass fibre-reinforced thermoset matrix composite*. Composites Part A: Applied Science and Manufacturing *27,* 1169-1181 (1996).

[196] D. G. Clarke and M. G. Bader. 7th International Conference on Composite Materials. 79-83. 1-11-1989.
Ref Type: Conference Proceeding

[197] S. Kiesel, *Behaviour of intrinsic polymer optical fibre sensor for large-strain applications*. Measurement Science & Technology *18,* 3144 (2007).

[198] S. C. Kuang, P. J. Scully and W. J. Cantwell, *An evaluation of a novel plastic optical fibre sensor for axial strain and bend measurements*. Material Science and Technology *13,* 1523 (2002).

[199] S. C. Kuang, W. J. Cantwell and Thomas C., *Crack detection and vertical deflection monitoring in concrete beams using plastic optical fibre sensors*. Measurement Science & Technology *14,* 205 (2003).

[200] M. G. Bader and J. F. Collins, *The effect of fibre-interface and processing variables on the mechanical properties of glass-fibre filled nylon 6*. Fibre Science and Technology *18,* 217-231 (1983).

[201] S. Debnath, R. Ranade, S. L. Wunder, J. McCool, K. Boberick and G. Baran, *Interface effects on mechanical properties of particle-reinforced composites*. Dental Materials *20,* 677-686 (2004).

[202] A. R. Chambers, J. S. Earl, C. A. Squires and M. A. Suhot, *The effect of voids on the flexural fatigue performance of unidirectional carbon fibre composites*

developed for wind turbine applications. International Journal of Fatigue *28,* 1389-1398 (2006).

[203]   S. F. M. de Almeida and Z. d. S. N. Neto, *Effect of void content on the strength of composite laminates*. Composite Structures *28,* 139-148 (1994).

[204]   P. Olivier, J. P. Cottu and B. Ferret, *Effects of cure cycle pressure and voids on some mechanical properties of carbon/epoxy laminates*. Composites *26,* 509-515 (1995).

[205]   J. Varna, R. Joffe, L. A. Berglund and T. S. Lundstrm, *Effect of voids on failure mechanisms in RTM laminates*. Composites Science and Technology *53,* 241-249 (1995).

[206]   M. R. Wisnom, T. Reynolds and N. Gwilliam, *Reduction in interlaminar shear strength by discrete and distributed voids*. Composites Science and Technology *56,* 93-101 (1996).

[207]   H. Yoshida, T. Ogasa and R. Hayashi, *Statistical approach to the relationship between ILSS and void content of CFRP*. Composites Science and Technology *25,* 3-18 (1986).

[208]   H. Y. Zhu, D. h. LI, D. X. Zhang, B. C. Wu and Yu. Y. Chen, *Influence of voids on interlaminar shear strength of carbon/epoxy fabric laminates*. Transactions of Nonferrous Metals Society of China *19,* s470-s475 (2009).

[209]   L. Liu, B. M. Zhang, D. F. Wang and Z. J. Wu, *Effects of cure cycles on void content and mechanical properties of composite laminates*. Composite Structures *73,* 303-309 (2006).

[210]   H. Huang and R. Talreja, *Effects of void geometry on elastic properties of unidirectional fiber reinforced composites*. Composites Science and Technology *65,* 1964-1981 (2005).

[211]   J. M. Tang, W. I. Lee and G. S. Springer, *Effects of cure pressure on resin flow, voids and mechanical properties*. Journal of Composite Materials *19,* 421-440 (1987).